

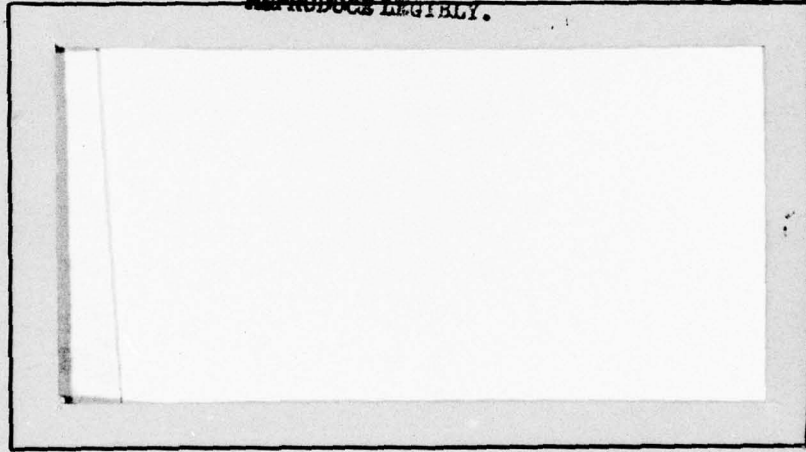
LEVEL ^{DB} ₀ _{SC}

AIR FORCE INSTITUTE OF TECHNOLOGY



**AIR UNIVERSITY
UNITED STATES AIR FORCE**

**THIS DOCUMENT IS BEST QUALITY PRACTICABLE.
THE COPY FURNISHED TO DDC CONTAINED A
SIGNIFICANT NUMBER OF PAGES WHICH DO NOT
REPRODUCE LEGIBLY.**



DDC
REPRODUCTION
JUL 3 1978
LIBRARY

Handwritten signature

SCHOOL OF ENGINEERING

**ORIGINAL CONTAINS COLOR PLATES: ALL DDC
REPRODUCTIONS WILL BE IN BLACK AND WHITE.**

WRIGHT-PATTERSON AIR FORCE BASE, OHIO

78 06 30 020

DISTRIBUTION STATEMENT A
Approved for public release
Distribution Unlimited

AD A057434

**AD No. _____
DDC FILE COPY**

DISCLAIMER NOTICE

THIS DOCUMENT IS BEST QUALITY PRACTICABLE. THE COPY FURNISHED TO DDC CONTAINED A SIGNIFICANT NUMBER OF PAGES WHICH DO NOT REPRODUCE LEGIBLY.

AD A 057434

①

AD No.
DDC FILE COPY

AN ANALYSIS OF THE STABILITY
OF AN AIRCRAFT EQUIPPED
WITH AN AIR CUSHION RECOVERY SYSTEM
THESIS

AFIT/GGC/EE/78M-5

Max A. Stafford
Captain USAF

ORIGINAL CONTAINS COLOR PLATES: ALL DDC
REPRODUCTIONS WILL BE IN BLACK AND WHITE.

DDC
REPRODUCED
JUL 3 1978
RESERVED
E

DISTRIBUTION STATEMENT A
Approved for public release;
Distribution Unlimited

78 06 30 020

14 / AFIT-GGC-EE-78M-5

6 AN ANALYSIS OF THE STABILITY
OF AN AIRCRAFT EQUIPPED
WITH AN AIR CUSHION RECOVERY SYSTEM.

9 Master's THESIS,

Presented to the Faculty of the School of Engineering
of the Air Force Institute of Technology
Air University
in Partial Fulfillment of the
Requirements for the Degree of
Master of Science

12 / 219p.

ACCESSION for	
NTIS	White Section <input checked="" type="checkbox"/>
DDC	Buff Section <input type="checkbox"/>
UNANNOUNCED	<input type="checkbox"/>
JUSTIFICATION.....	
BY.....	
DISTRIBUTION/AVAILABILITY CODES	
Dist.	AVAIL. and/or SPECIAL
A 23	

OS
EKG

10 Allen
by
Max Stafford
Captain USAF

Graduate Guidance and Control Engineering

11 Mar 1978

012 225 *Allen*

Preface

In this report I attempt to fulfill three separate needs which I perceive to exist. First, and foremost, the field of air cushion landing technology appears to me as being one which has not attracted the attention, to any great extent, of control system engineers. I sincerely hope that this thesis generates some interest in the control community for the problems are both challenging and stimulating. Secondly, this report is written to propose specific solutions to problems encountered in landing the Jindivik aircraft. While the Jindivik project was dropped during the research phase of this report, there has been renewed interest in recent weeks. Finally, this thesis has been undertaken for my own needs: not just to meet degree requirements, but to finally use some of the techniques which have been learned during my coursework.

Many people have contributed to this report directly and indirectly. Technical information and computer resources have been provided by the Air Cushion Group/AFFDL. Mr. James Steiger, Major Jack Randall (CAF), and Mr. Dave Perez, in this organization, have been most helpful and cooperative. Several members of the faculty at AFIT have been extremely helpful. Major Richard Potter provided excellent guidance and direction in the earlier stages. Professor John D'Azzo has given much needed encouragement and many helpful suggestions in the wording of the report. A very thorough reading and criticism of the rough draft of this report was rendered by Dr. Pete Maybeck. Dr. Maybeck's comments were invaluable and deeply appreciated.

The professionalism, dedication, and patience shown by Ms. Fonda Parrott in typing this thesis is sincerely appreciated and will long be remembered.

A final acknowledgement of thanks is due my family - Sherry and Scott. There is no way to recover the time which could have been shared were it not for the long hours devoted to this report. I thank you both for your patience and understanding.

Contents

	Page
Preface	ii
List of Figures	vi
List of Tables	xi
Abstract	xiii
I. Introduction	1
II. The Aerodynamic Model	14
General Description of the Jindivik Drone	15
Equations of Motion	16
Determination of Forces	21
III. Design and Analysis of a Yaw Control System	31
Simulations of Existing Aircraft and Autopilot	32
Design of a Yaw Control System	45
Simulations of Aircraft with Yaw Control	64
IV. Modeling of the ACRS Trunk	82
Experimentally Obtained Trunk Data	84
Description of the Trunk	85
Placement of the Spring-Damper Units	86
Reaction and Frictional Forces Acting on the Trunk	90
Verification of Trunk Dynamics	96
V. Analysis of the Slideout	104
Airframe with Existing Autopilot Simulation	112
Analysis of the Lateral Directional Instability	120
Design of a Lateral-Directional Control System for the Slideout	123
Verification of the Lateral-Directional Control System	126
VI. Summary and Recommendations	138
Recommended Additional Investigation (In-Flight)	139
Recommended Additional Investigation (Slideout)	140

Contents

	Page
Appendix A: Pertinent Aerodynamic Data for the Jindivik Drone Aircraft	143
Appendix B: Salient Features of the EASY Aircraft Modeling and Analysis Program	181
Bibliography	200
Vita	202

List of Figures

<u>Figure</u>	<u>Page</u>
1 The Jindivik Drone Aircraft Resting on an Air Cushion Recovery System	6
2 Typical Air Cushion Technology Components	8
3 The Pillow Braking System	10
4 The Body Axes and Notation	19
5 Relationship of Z_{a0} to Lift and Drag	27
6 The Existing Pitch Control System	29
7 The Existing Roll Control System	29
8 Time History of the Orientation of the Bare Airframe	35
9 Time Histories of Sideslip Angle and Yaw Rate for the Bare Airframe Simulation	36
10 Verification of the Adequacy of the Pitch Control System	40
11 Verification of the Adequacy of the Roll Control System	42
12 Time History of the Orientation for the Airframe/Autopilot Combination	43
13 Time Histories of Sideslip Angle and Yaw Rate for the Airframe/Autopilot Combination	44
14 The Coanda-Effect Yaw Thruster	48
15 A Yaw Thruster Installed on the Jindivik Aircraft	48
16 Geometry of the Yaw Thruster Installed on the Jindivik	50
17 Phase Plane Trajectories with No Control Inputs	58
18 Phase Plane Trajectories with Constant Control Inputs	60

List of Figures

<u>Figure</u>	<u>Page</u>
19 Block Diagram of Yaw Control System Implementation . . .	64
20 Time Histories of Sideslip Angle and Yaw Rate in Yaw Control Simulation Number 1	66
21 Time History of the Orientation of the Aircraft in Yaw Control Simulation Number 1	67
22 Phase-Plane Trajectory for Yaw Control Simulation Number 1	68
23 Time Histories of Sideslip Angle and Yaw Rate in Yaw Control Simulation Number 2	70
24 Time History of the Orientation of the Aircraft in Yaw Control Simulation Number 2	71
25 Phase-Plane Trajectory for Yaw Control Simulation Number 2	72
26 Time Histories of Sideslip Angle and Yaw Rate in Yaw Control Simulation Number 3	73
27 Time History of the Orientation of the Aircraft in Yaw Control Simulation Number 3	74
28 Phase-Plane Trajectory for Yaw Control Simulation Number 3	75
29 Time Histories of Sideslip Angle and Yaw Rate in Yaw Control Simulation Number 4	77
30 Time History of the Orientation of the Aircraft in Yaw Control Simulation Number 4	78
31 Phase-Plane Trajectory for Yaw Control Simulation Number 4	49
32 Geometry of the Jindivik ACRS Number 2	86
33 Placement of Spring Damper Units for the Trunk Model	89
34 Position Vector from an Arbitrary Point on the Surface of the Earth to a Spring-Damper Unit Point of Attachment	91

List of Figures

<u>Figure</u>	<u>Page</u>
35	Verification of Heave Mode Dynamics 99
36	Verification of Pitch Mode Dynamics 100
37	Verification of Roll Mode Dynamics 101
38	Forward Velocity and Angle of Attack Time Histories During Slideout with No Control System 107
39	Pitch Angle and Height of GC Time Histories During Slideout with No Control System 108
40	Roll Angle and Yaw Angle Time Histories During Slideout with No Control System 110
41	Sideslip Angle and Yaw Rate Time Histories During Slideout with No Control System 111
42	Lateral Versus Longitudinal Displacement During Slideout with No Control System 113
43	Forward Velocity and Angle of Attack Time Histories During Slideout with Existing Autopilot 114
44	Pitch Angle and Height of CG Time Histories During Slideout with Existing Autopilot 115
45	Roll Angle and Yaw Angle Time Histories During Slideout with Existing Autopilot 117
46	Sideslip Angle and Yaw Rate Time Histories During Slideout with Existing Autopilot 118
47	Lateral Versus Longitudinal Displacement During Slideout with Existing Autopilot 119
48	Eigenvalue Locations for Variation in Forward Velocity from 200 ft/sec to 40 ft/sec 121
49	Roll Angle and Yaw Angle Time Histories During Slideout with Optimal Controller (-3 ft/sec Gust) 127
50	Sideslip Angle and Yaw Rate Time Histories During Slideout with Optimal Controller (-3 ft/sec Gust) 128

List of Figures

<u>Figure</u>	<u>Page</u>
51 Lateral Versus Longitudinal Displacement During Slideout with Optimal Controller (-3 ft/sec Gust)	129
52 Roll Angle and Yaw Angle Time Histories During Slideout with Optimal Controller (-10 ft/sec Gust)	130
53 Sideslip Angle and Yaw Rate Time Histories During Slideout with Optimal Controller (-10 ft/sec Gust)	131
54 Lateral Versus Longitudinal Displacement During Slideout with Optimal Controller (-10 ft/sec Gust)	132
55 Roll Angle and Yaw Angle Time Histories During Slideout with Optimal Controller (-25 ft/sec Gust)	133
56 Sideslip Angle and Yaw Rate Time Histories During Slideout with Optimal Controller (-25 ft/sec Gust)	134
57 Lateral Versus Longitudinal Displacement During Slideout with Optimal Controller (-25 ft/sec Gust)	135
A-1 Lift Coefficient Versus Angle of Attack	156
A-2 Drag Coefficient Versus Angle of Attack	157
A-3 Pitching Moment Coefficient Versus Angle of Attack	159
A-4 Side Force Coefficient Versus Sideslip Angle	160
A-5 Roll Moment Coefficient Versus Sideslip Angle	161
A-6 Roll Moment Coefficient Versus Sideslip Angle	162
A-7 Roll Moment Coefficient Versus Sideslip Angle	163
A-8 Roll Moment Coefficient Versus Sideslip Angle	164
A-9 Yaw Moment Coefficient Versus Sideslip Angle	168
A-10 Yaw Moment Coefficient Versus Sideslip Angle	169
A-11 Yaw Moment Coefficient Versus Sideslip Angle	170
A-12 Yaw Moment Coefficient Versus Sideslip Angle	171

List of Figures

<u>Figure</u>	<u>Page</u>
A-13 Yaw Moment Coefficient Versus Sideslip Angle (Flaps Down)	173
A-14 Change in Lift Coefficient Versus Elevator Deflection . .	174
A-15 Change in Drag Coefficient Versus Elevator Deflection (Deg)	175
A-16 Change in Pitching Coefficient Versus Elevator Deflection	176

List of Tables

<u>Table</u>	<u>Page</u>
I Some Pertinent Characteristics of the Jindivik Drone Aircraft	16a
II Configuration and Initial Conditions for Simulations .	33
III Experimentally Obtained Data for the Jindivik ACRS Trunk Number 2	85
IV Location and Types of Spring Damper Units	89
V Values of Stiffness and Damping Coefficients for Pitch, Roll, and Heave Spring-Damper Units	90
VI Comparison of Predicted and Simulated Damping Ratios and Periods	103
VII Configurations and Initial Conditions for Slideout Simulations	105
I-A Longitudinal Aerodynamic Coefficients (Flaps-Up) . . .	145
II-A Longitudinal Aerodynamic Coefficients (Flaps Down) . .	145
III-A Lateral Directional Aerodynamic Coefficients	146
IV-A Lateral Directional Aerodynamic Coefficients	147
V-A Lateral Directional Aerodynamic Coefficients	148
VI-A Lateral Directional Aerodynamic Coefficients	149
VII-A Lateral Directional Aerodynamic Coefficients	150
VIII-A Lateral Directional Aerodynamic Coefficients	151
IX-A Lateral Directional Aerodynamic Coefficients	152
X-A Lateral Directional Aerodynamic Coefficients	153
XI-A Change in Lift Coefficient with Elevator Deflection Angle	154
XII-A Change in Drag Coefficient with Elevator Deflection Angle	154
XIII-A Change in Moment Coefficient with Elevator Deflection Angle	154

List of Tables

<u>Table</u>		<u>Page</u>
XIV-A	Parameter Values for Yaw Moment Versus Sideslip Angle Curve Fits	167
XV-A	Some Stability Derivatives from Reference	178
I-B	Description of Some of the Blocks in the EASY Modeling Program	182
II-B	Descriptions of Some of the EASY Analysis Commands . .	183

Abstract

The stability of an aircraft equipped with an air cushion recovery system (ACRS) was investigated both in-flight and during the landing (slideout) phase of flight. Digital computer simulations were used to identify unstable tendencies of a specific aircraft (the Jindivik drone). Control system designs are proposed to eliminate the instabilities.

A nonlinear, six degree of freedom, aerodynamic model is developed based on available wind-tunnel data. The model is used in a computer software package, EASY, to simulate the vehicle in flight. The vehicle is shown to be unstable in flight due to lateral-directional characteristics created by the installation of the ACRS. A time optimal control design is developed using a coanda-effect yaw thruster. The design is verified by computer simulations which indicate that the controller performs adequately for reasonably small deviations in sideslip angle.

A model of the air cushion recovery system is also developed. The model is generated by matching experimental data obtained from an actual ACRS with 14 spring/damper units. The model is verified by computer simulation, and then slideout simulations are performed. These simulations reveal a lateral-directional instability in the slideout. An optimal control design is proposed and verified, after which it is shown that the stability of the system is dramatically enhanced by the addition of an optimal controller.

I. INTRODUCTION

An attempt is made here to review the general characteristics of conventional landing gear and air cushion landing devices. Following this review is a description of some of the components that have been used (or proposed) in the air cushion technology field. A brief history of air cushion research is then presented, followed by a statement of the problem areas approached in this thesis. The final paragraph is an overview of the remainder of the thesis.

Some Prominent Characteristics of Conventional Landing Gear

Conventional landing systems have been used for so many years that, perhaps, some of the undesirable characteristics associated with these systems are traits that we have unconsciously resigned ourselves to live with. For instance, given a choice between constructing an expensive two mile asphalt runway, or a two mile grass-covered landing strip, one would likely pick the latter if planes could safely land on the grass. Thus, conventional landing systems have at least one major undesirable characteristic: they require hard surfaces for taxiing, taking off, and landing. Several other characteristics of conventional systems are given below.

For takeoffs, it is highly desirable that low frictional forces exist in the takeoff direction. Also, high frictional forces perpendicular to the takeoff direction aid in maintaining a straight ground

track. Low forward friction and high lateral friction are obtained with conventional landing systems.

For landings, however, neither low rolling friction nor high lateral friction is desirable. Wheel brakes are used to increase considerably the forward friction, while skillful pilot technique is used to circumvent the hazard created by high lateral friction in crosswind landings. Some aircraft, notably the B-52, alleviate the high lateral friction problem by adjusting the angular orientation of the landing gear to match the angle between the airplane's heading on final approach and the runway centerline (the "crab" angle).

Conventional landing systems have the very desirable quality of providing absorption of the energy at impact. The absorption is achieved primarily by the use of dampers and the natural springiness of the tires.

Both a weight and a drag penalty are incurred by conventional landing systems. The drag problem is frequently solved by making the gear retractable, but this adds considerably to the weight of the system.

Previously mentioned components include wheel brakes, dampers, and retractable landing gear. Aside from adding weight to the aircraft, these components also usually require hydraulic actuators. Hence, these components require a larger capacity (and hence, heavier) hydraulic system, and they also greatly increase the complexity of the landing gear.

One characteristic of conventional landing systems is particularly desirable: most conventional systems have an adequate steering capability. Differential braking, along with nosewheel steering on most

aircraft, allow precise control on the ground.

While conventional landing systems will undoubtedly be used for many years to come, the several undesirable traits listed above do exist. A continuing effort should be made to eliminate these shortcomings, and the use of air cushion technology appears to be the most fruitful avenue to pursue at the present time to achieve this objective. Below are some of the characteristics of air cushion devices.

Some Prominent Characteristics of Air Cushion Landing Systems

Possibly the greatest potential advantage of air cushion landing systems is the large area over which the weight is distributed. This characteristic allows landings on grass, sand, water, mud, as well as asphalt or concrete. Landings have already been made on these surfaces by the LA-4 aircraft (Ref 19). The research program involving the LA-4 went further, however, and demonstrated an ability to taxi over various surface irregularities such as ditches, stumps, and plowed fields.

For takeoffs, it has been noted that rolling friction is low with conventional landing systems. Forward friction is also very low with air cushion systems. Unlike conventional gear, however, the lateral friction is also low and this poses a problem since some steering mechanism must be devised in order to control the vehicle on the ground. Systems have been designed to allow differential braking by forcing only a portion of the underside of the air cushion system against the ground. This method, known as "pillow braking", was used by Bell Aerosystems on the LA-4 aircraft (Ref 19) with apparent success. Another method considered for controlling the ground track of air cushion vehicles is differential thrusting (Ref 12, Ref 8). Still another device, one which

is considered in some detail in this thesis, is the yaw thruster. This device holds considerable promise, as is later shown.

High forward friction is desired when landing a vehicle, as noted earlier, and effective methods of achieving this are discussed in the air cushion literature. Pillow braking is one such method. The principle is the same as discussed above, but areas on the underside of the air cushion system are symmetrically pressed against the ground rather than differentially. This method was tested successfully on the LA-4 aircraft referenced above, as well as on the CC-115 aircraft (Ref 8:141). Another method of recovery has been proposed, but has not yet been flight tested. This method uses a majority of the underside of the air cushion device as a rubber skid. A more detailed discussion of this device is presented in Chapter 4.

It was mentioned previously that dampers on conventional landing gear provide good energy absorption at touchdown. A well designed air cushion system also provides good energy absorption, but heavy dampers are not required.

The drag and weight of conventional landing systems have been noted to be undesirable traits. Well designed air cushion systems offer a significant reduction in weight. The change in drag as a result of an air cushion system varies considerably from one design to another in a takeoff or landing configuration, but can be made very small for cruise configurations.

Since an air cushion system does not require dampers, gear retraction mechanisms or wheel brakes, the complexity may be well less than that of conventional gear. It should be noted that conventional

retractable landing systems have been studied and improved upon for many years. Yet, they are very complex and require a multitude of moving parts. To demonstrate the simplicity of air cushion systems, as well as to present the common components which are referred to throughout the remainder of this report, some definitions and terminology are now given.

Air Cushion Components

Air cushion systems are frequently categorized by function. The name "Air Cushion Landing System (ACLS)" is used to denote an air cushion system which is designed for takeoffs as well as landings. The name is somewhat misleading, since no mention of takeoff capability is included, but nevertheless this is the nomenclature which is widely used (Ref 17:6). When a system has been designed for takeoffs only, the phrase "Air Cushion Takeoff System (ACTS)" is used. Similarly, when a system has been designed to be used only during recovery, the phrase "Air Cushion Recovery System (ACRS)" is used. While the major portion of this thesis is concerned only with Air Cushion Recovery Systems, the following few paragraphs discuss all three systems in order to place the ACRS in the proper perspective.

A major component of any air cushion system is the inflatable bag called the "trunk". The trunk is composed of flexible material which is attached to the underside of an aircraft fuselage for the purpose of containing a volume of air. The overall shape of the trunk (when inflated) is typically similar to an elongated torus, but the shape is sometimes altered to achieve certain desired effects. Figure 1 depicts a Jindivik drone aircraft resting on an ACLS trunk (Ref15). A cross



Fig. 1 The Jindivik Drone Aircraft Resting on an Air Cushion Recovery System

sectional view of the trunk is depicted in Figure 2 along with other typical air cushion components. From this figure it is seen that the trunk serves as a reservoir: it receives a supply of air and simultaneously exhausts air through nozzles on its underside as well as sometimes through a pressure relief valve. Before these three components are discussed, a description is first given of what is meant by the term "air cushion".

The volume of air enclosed by the underside of the fuselage, the inside surface of the trunk, and the ground is generally referred to as the air cushion. Air may be supplied directly into this volume as shown in Figure 2, or, the only flow into the air cushion might come from the jets around the underside of the trunk. A given design of an air cushion system may use either or both methods of supplying the air, but the effect which is achieved is essentially the same from either method. The air cushion serves to lift the vehicle and trunk by a fraction of an inch above the ground, which allows the vehicle to "ride" on air. The friction coefficient is reduced to a very small value.

The air supply shown in Figure 2 might be provided by a separate engine/compressor combination (as it was for the LA-4 ACLS). It might also come from the propulsion engine (as has been designed for the Jindivik ACTS).

The nozzles on the underside of the trunk are usually placed all around the trunk for ACLS and ACTS designs. For ACRS designs, however, there appears to be a good argument for "lubrication"—placing nozzles in only the forward portion of the trunk. Such a placement allows the forward area to maintain a low friction coefficient. Two specific advantages are derived from a reduced forward-area friction. First,

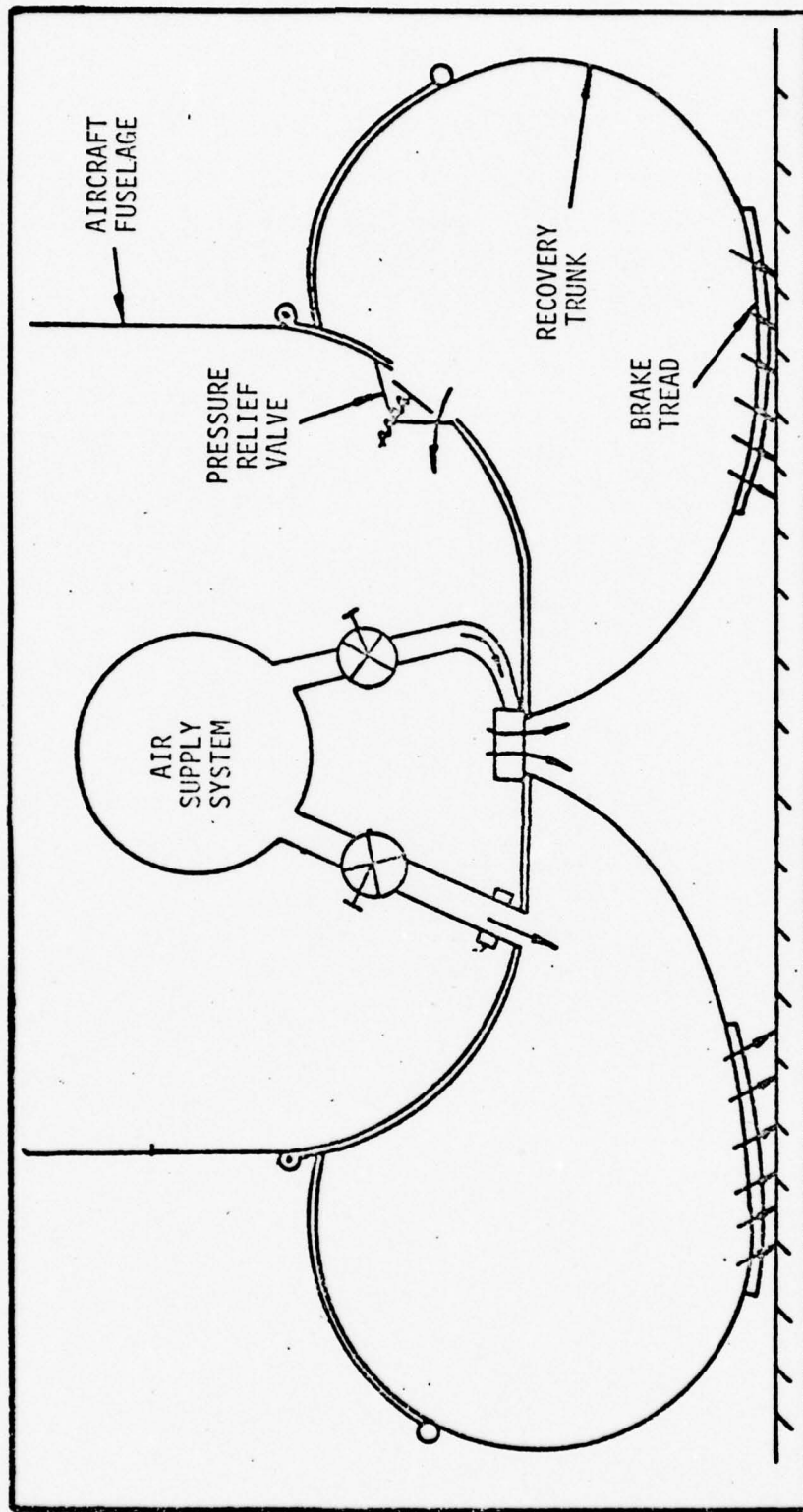


Fig. 2 Typical Air Cushion Technology Components

the directional stability is enhanced since the resultant frictional force acts more aft of the center of gravity. Second, the forward section of the trunk is acting to prevent the large nose-down pitching moments that are present during the landing.

A pressure relief valve is frequently included in the design of an air cushion system. Its purpose is to prevent the pressure in the trunk from exceeding some predetermined value. There are several possible reasons for including this component. Obviously there may be structural limitations which might be exceeded with too great a trunk pressure. This limitation is shared by the ACLS, ACRS and ACTS. The relief valve might also provide an improvement in stability by reducing fan stall (Ref 5:15). Another reason for including a pressure relief valve in the design is to provide additional damping during the landing impact (Ref 21:74). Finally, the use of a pressure relief valve might be the primary means of regulating the pressure, particularly for a direct-flow type of air supply (Ref 17:16).

One final component of air cushion systems is the brake tread. Generally the brake tread is made of rubber and is simply used to provide high frictional forces during landing. The pillow braking system discussed previously is illustrated in Figure 3. Here the brake tread is placed only on the underside of the pillows. This design is very attractive for an ACLS, while a simpler approach is often taken with air cushion recovery systems since the design objective for an ACRS is to achieve a high frictional force which, in turn, leads to short landing distances. Therefore, the entire underside of an ACRS might well be brake tread. Nozzles are drilled through the brake tread

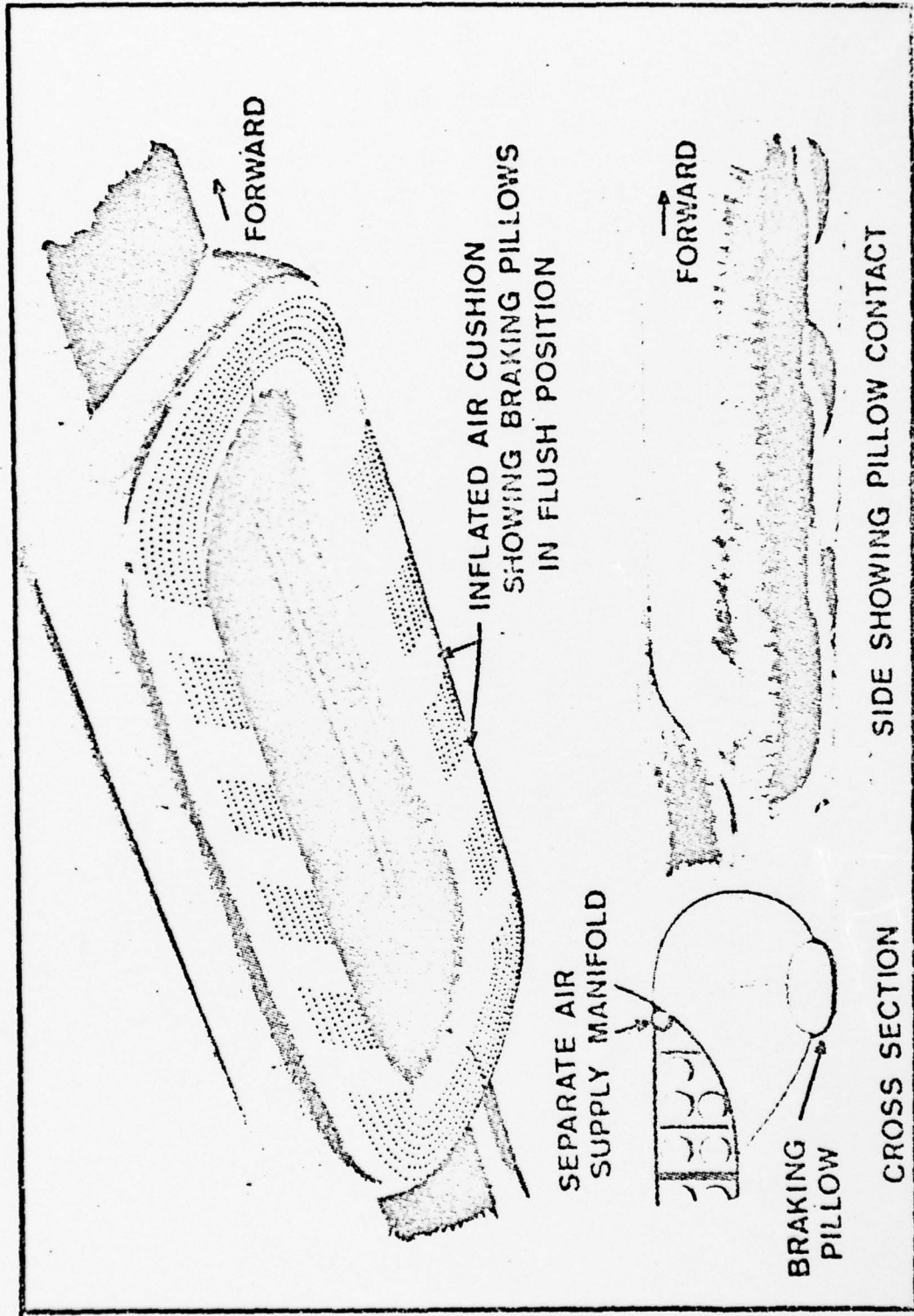


Fig. 3 The Pillow Braking System (Ref 19)

Fig. 3 The Pillow Braking System

where necessary. With this type of recovery system, the braking begins as soon as the vehicle touches down and continues until the vehicle comes to rest. Since the aircraft is sliding on the brake tread for the entire landing, the landing is often termed the "slideout".

Recent History of Air Cushion Systems

Three major programs have been initiated in attempts to demonstrate the feasibility of using air cushion technology to replace conventional landing gear in some applications. The first program was undertaken by Bell Aerospace, Division of Textron, in the mid to late 1960's. The first air-cushioned takeoff and landing was performed during this program on August 4, 1967, on a converted Lake LA-4 aircraft. Reference 19 presents highlights of a test program which Bell Aerosystems accomplished under contract to the Air Force Flight Dynamics Laboratory. The program appears to have been highly successful, but the LA-4 aircraft was in a rather lightweight class.

It was decided that another aircraft would be fitted with an ACLS to demonstrate the feasibility of air cushion technology applied to larger aircraft. Hence, in the early 1970's an advanced development program was initiated utilizing the CC-115 aircraft. The CC-115 has a gross weight of 41,000 pounds. Reference 8 presents a detailed report on the objectives, scope, and initial test results of the CC-115 program.

A third program has been underway since the early 1970's. This program has been directed towards demonstrating the feasibility of using air cushion technology for launching and recovering high performance jet aircraft. The test bed aircraft selected was the Australian-made

Jindivik drone. The program received a setback in the Summer of 1977, when the government of Australia decided against furnishing the Jindivik aircraft for a test bed.

Analysis of the Problem

While much effort has been expended on the three programs mentioned above, the vast majority of this effort has been directed along the lines of improving the air cushion systems. Certainly there was (and is) much to accomplish in this area, as air cushion landing system technology is still in its infancy. On several occasions, however, it appears that a comprehensive examination of the stability and control strategy was sorely needed. For instance, films of taxi tests with the Jindivik drone aircraft show poor directional stability, severe nose down pitching tendencies, and rather violent roll rates. A taxi accident occurred during the testing when lateral control was insufficient during a braking run (Ref 15, Appendix I).

At the request of Flight Dynamics Laboratory personnel, this thesis has been directed at analyzing the stability and control of the Jindivik aircraft during landing. The research documented by this report has come from a critical study of the existing characteristics of the Jindivik aircraft and, where needed, control strategies have been proposed and analytically tested. Three specific problems are addressed in the following four chapters: 1) in-flight lateral-directional stability with the trunk inflated, 2) lateral-directional stability during the slideout, and 3) pitch stabilization during the slideout.

Overview

Modeling of the physical situation is broken into two segments-- the aerodynamic model and the trunk model. Chapter 2 is devoted entirely to modeling the Jindivik aircraft in flight with the trunk inflated. The third chapter makes use of the aerodynamic model to demonstrate an aerodynamic lateral-directional stability problem created by the ACRS, and then gives a solution to this problem. Chapter 4 derives an ACRS model which is then incorporated into the aerodynamic model. The fifth chapter verifies the model, analyzes the yawing and rolling stability under various conditions, and finally proposes control strategies to improve the system. Chapter 6 summarizes the findings and states some conclusions based on these findings.

II. THE AERODYNAMIC MODEL

Aerodynamic forces greatly affect the motion of an aircraft during the touchdown, as well as throughout a considerable portion of the landing ground run. A mathematical description of these forces is derived in this chapter based primarily on wind tunnel data presented in Appendix A. Gravitational forces, thrust forces and moments, and aerodynamic forces and moments are combined with kinematic relationships, as well as with information on the existing autopilot, to derive what is referred to throughout this report as the "aerodynamic model".

Introduction

An aerodynamic model is necessary for two major reasons:

1) it allows an analysis of in-flight stability deficiencies with an Air Cushion Recovery System (ACRS) installed, and 2) the aerodynamic model allows computation of necessary aerodynamic forces and moments during the slideout. The second reason is obvious, but some explanation of the first reason is in order.

Every test program involving Air Cushion Recovery Systems has, thus far, been conducted on an existing aircraft to which an ACRS has been added. Hence, no thought was given during the original design of the aircraft to the control or stability with an ACRS installed. It is conceivable that an aircraft will some day be designed from the beginning to land with an ACRS; but, until such

time, whenever an ACRS is used to replace conventional gear on an existing vehicle, the stability of the system must be considered. An analysis of the in-flight aerodynamic characteristics of the Jindivik aircraft is presented in Chapter III. This analysis not only demonstrates some of the detrimental effects that an ACRS can produce when installed on an existing aircraft, but further, it serves to confirm the first reason given above for the necessity of an aerodynamic model.

Four general areas are covered in the development of the aerodynamic model of the Jindivik drone. The first of these is a general description of the Jindivik, since this aircraft has some unique characteristics. Secondly, the equations of motion are presented in both the inertial frame and the body frame. The equations of motion require a mathematical description of the forces which act upon the aircraft; thus, the third area is a development of these forces. The final area consists of a description of the autopilot which is presently installed on the Jindivik.

General Description of the Jindivik Drone

The Government Aircraft Factories (GAF) of Australia produced the Jindivik drone aircraft in the 1950's. Several excellent reasons for selecting the Jindivik as a test-bed aircraft are given in Reference 17, and among the most significant of these reasons are, 1) the engine inlet on this vehicle is above the fuselage and hence ingestion of debris should not be a problem, and 2) the aircraft normally lands on a metal skid and thus little modification of the landing procedure is anticipated.

Several physical characteristics of the Jindivik are presented in Table I. These characteristics are used throughout this chapter in the derivation of the model. Two entries in Table I are of special note. First, the approach speed of 130 knots is considerably higher than the approach speed of either the LA-4 or the CC-118 aircraft. This is significant since important information will be obtained in the Jindivik program concerning the recovery of high speed ACRS-equipped aircraft. Secondly, the lateral control consists of ailerons only, i.e., there is no movable rudder. This fact is significant in any control system design, since whatever control strategies are developed may well be useful only for the Jindivik. Thus, a clear distinction is made throughout this report between solutions which are specific to the Jindivik and solutions which are considered to be appropriate for a more general class of problems.

Equations of Motion

Any of the standard textbooks on aircraft stability and control can be consulted for a derivation of the equations of motion (References 14, 16, or 4, for instance). Hence, the equations of motion are stated here with only some preliminary remarks concerning reference systems, notation, and assumptions. The assumptions are introduced as necessary to simplify the problem.

The first assumptions made here are those commonly made in stability and control analyses, and are not very restrictive:

- 1) Newton's laws of mechanics are assumed to hold,
- 2) an earth-fixed reference frame is assumed to be an inertial frame,
- 3) the earth is assumed to be flat over trajectories of the vehicle which are of

Table I

SOME PERTINENT CHARACTERISTICS OF THE JINDIVIK DRONE AIRCRAFT

Parameter	Value	Source
Landing Weight	2620 lbs	Ref 5
Approach Speed	130 knots	Ref 5
Surface Area, S	76 ft ²	Ref 6
Wing Span, b	19 ft	Ref 6
Chord, c	4 ft	Ref 6
z_p - coordinate of the thrust vector, z_t	-.375 ft	Ref 1
Center of gravity location	20% of MAC	Ref 6
Tail Area, A_t	13 ft ²	Ref 18
Tail Aspect Ratio	2.89	Ref 18
Moment of Inertia about x_b , I_{xx}	1150 slug-ft ²	Ref 5
Moment of Inertia about y_b , I_{yy}	1800 slug-ft ²	Ref 5
Moment of Inertia about z_b , I_{zz}	2840 slug-ft ²	Ref 5
Longitudinal Control	Conventional Elevator	Ref 5
Lateral Control	Conventional Ailerons Fixed Vertical Stabilizer	Ref 5
Propulsion	Single Jet Engine	Ref 5

interest, and 4) the aircraft mass is assumed to be constant. These assumptions greatly simplify the equations of motion. A description of the earth frame mentioned in the second and third assumptions is now in order.

The earth frame consists of a right-hand, 3-dimensional Cartesian coordinate system whose origin is any arbitrary point on the surface of the earth. The third (or z_e) axis is perpendicular to a plane tangent to the earth's surface and points towards the center of the earth. The first (or x_e) axis lies in an arbitrary direction in the tangent plane but is fixed with respect to the earth. The second (or y_e) axis completes the orthogonal system. It is seen to be convenient in later chapters to fix the x_e axis such that it is parallel to the runway, but for this chapter and the next the direction remains arbitrary.

To simplify the problem still further, it is assumed that the vehicle is a rigid body. This is also a commonly made assumption, although there are many instances where this is totally unrealistic. Since gross vehicular motion is of interest in this report, as opposed to aeroelastic phenomena, and since the aerodynamic loads are relatively light throughout the approach and landing phase, the neglect of structural deformation is considered reasonable.

The equations which describe the motion of a rigid body in the (assumed) inertial earth frame are as follows:

$$F = m A \quad (1)$$

$$M = \frac{dH}{dt} \quad (2)$$

where

F - vector force sum acting on the body

m - mass of the body

A - acceleration of the body

M - vector moment sum acting on the body

H - angular momentum of the body

$\frac{d}{dt}$ - differentiation with respect to time

While mathematically correct, the above equations are not efficient computationally, and therefore, the body-frame axis system is introduced in order to remedy this situation. This axis system is defined in the following manner for the purposes of this report: the first (or x_b) axis extends from the origin, the center of mass of the body, through the nose of the aircraft, parallel to the fuselage reference line. The second (or y_b) axis is perpendicular to the first axis and passes through the right wing, while the third (z_b) axis completes the right-hand, orthogonal axis system towards the underside of the vehicle. Figure 4 illustrates this axis system, along with notation for velocities, forces, and moments. With this notation the vector equations (1) and (2) can be expanded to the following set of six scalar equations (Ref 16):

$$m(\dot{U} + QW - RV) = \Sigma X \quad (3)$$

$$m(\dot{V} + RU - PW) = \Sigma Y \quad (4)$$

$$m(\dot{W} + PV - QU) = \Sigma Z \quad (5)$$

$$\dot{P}I_x - \dot{R}I_{xz} + QR(I_z - I_y) - PQI_{xz} = \Sigma L \quad (6)$$

$$\dot{Q}I_y + PR(I_x - I_z) - R^2I_{xz} + P^2I_{xz} = \Sigma M \quad (7)$$

$$\dot{R}I_z - \dot{P}I_{xz} + PQ(I_y - I_x) + QR I_{xz} = \Sigma N \quad (8)$$

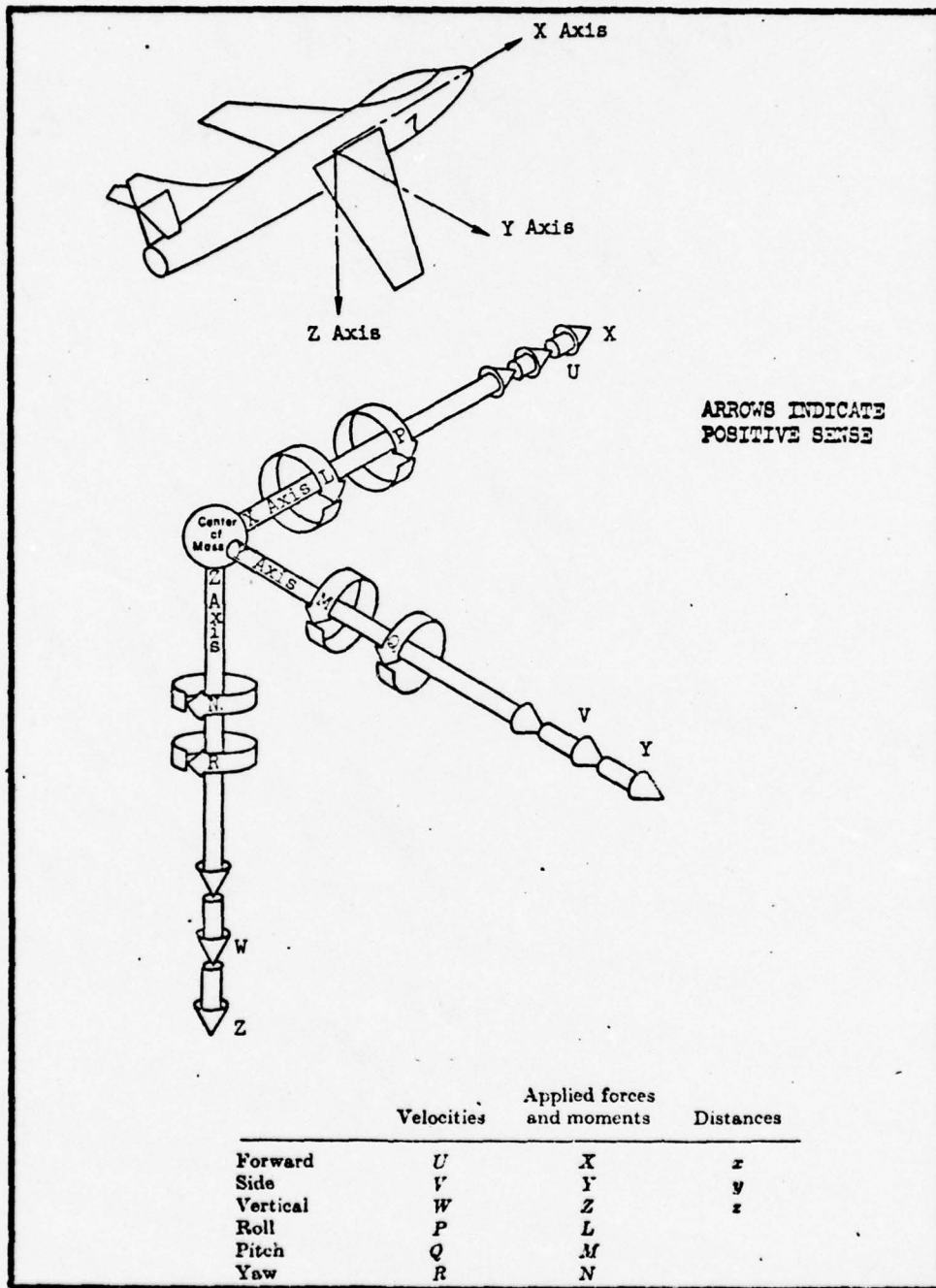


Fig. 4 The Body Axes and Notation (Ref 14)

where

I_x = moment of inertia about x_b

I_y = moment of inertia about y_b

I_z = moment of inertia about z_b

I_{xz} = product of inertia

The I_{xy} and I_{yz} products of inertia are usually negligible since most aircraft are symmetric about the $x_b - z_b$ plane (Ref 4:5). As a first approximation in this report, I_{xz} is neglected also since no value for this product of inertia could be found. A more refined analysis should include this term, although its magnitude is usually much less than that of the moments of inertia.

The equations of motion and the reference frames have been presented, but an additional set of equations are valuable when a vector in one frame is to be represented in another frame. The desired transition from one frame to another is usually accomplished by an Euler angle transformation. The Euler angles are typically denoted by ψ , θ , and ϕ , which represent the yaw, pitch, and roll angles, respectively. The angles must often be determined numerically since they are related to the inertial angular rates P , Q , and R by three coupled, nonlinear differential equations. These equations are

$$\dot{\phi} = P + Q \sin \phi \tan \theta + R \cos \phi \tan \theta \quad (9)$$

$$\dot{\theta} = Q \cos \phi - R \sin \phi \quad (10)$$

$$\dot{\psi} = (Q \sin \phi + R \cos \phi) \sec \theta \quad (11)$$

If values of these angles are known at a particular time, then the appropriate transformation matrix for going from the earth frame to the body frame (or vice versa) can be determined. Let C_b^e represent

a transformation matrix such that if a vector expressed in body-frame coordinates is multiplied by this matrix, the product is a representation of the same vector in earth-frame coordinates. In terms of the Euler angles, this matrix is

$$C_b^e = \begin{bmatrix} \cos \psi \cos \theta & \cos \psi \sin \phi \sin \theta & \sin \psi \sin \phi \\ & -\sin \psi \cos \phi & +\cos \psi \sin \theta \cos \phi \\ \sin \psi \cos \theta & \cos \psi \cos \phi & \sin \psi \sin \theta \cos \phi \\ & +\sin \psi \sin \phi \sin \theta & -\cos \psi \sin \phi \\ -\sin \theta & \cos \theta \sin \phi & \cos \theta \cos \phi \end{bmatrix} \quad (12)$$

Conversely, given a vector expressed in earth-frame coordinates, one can find a transformation matrix, C_e^b , which can transform those coordinates to yield a body-frame representation of the vector. It can be shown that

$$C_e^b = \left[C_b^e \right]^T \quad (13)$$

Thus far, the equations of motion have been developed along with the mathematical relationships necessary to transform vector coordinates expressed in one frame to another frame. In the next section the forces and moments which appear on the right-hand side of equations 3 through 8 are developed for the in-flight configuration.

Determination of Forces

All forces discussed in this report arise from one of five different sources: thrust, gravity, control, aerodynamic, or ground contact. These sources are identified by the subscripts t, g, c, a, and f, respectively. For example, suppose it is desired to discuss the force produced by a control input in the y_b direction, then it is

represented as Y_C . Similarly, a torque arising from an aerodynamic source about the z_b axis is denoted as N_a . A discussion of control forces produced by the existing autopilot is given in the last section of this chapter, while the ground friction and reaction forces are covered in the fourth chapter. The remainder of this section is devoted to gravitational, thrust, and aerodynamic forces and moments.

Gravity. In vector notation the gravitational force can be written as

$$G = mg\hat{e}_3 \quad (14)$$

where g is the local gravitational acceleration, and \hat{e}_3 is a unit vector in the direction of the third earth axis, z_e . By the transformation matrix, C_e^b , this force can easily be represented in body-frame coordinates:

$$\begin{bmatrix} X_g \\ Y_g \\ Z_g \end{bmatrix} = \begin{bmatrix} C_e^b \end{bmatrix} \begin{bmatrix} G \end{bmatrix}^e = C_e^b \begin{bmatrix} 0 \\ 0 \\ mg \end{bmatrix} \quad (15)$$

or, by use of the definition of C_b^e in equation 12,

$$\begin{bmatrix} X_g \\ Y_g \\ Z_g \end{bmatrix} = \begin{bmatrix} -mg \sin \theta \\ mg \cos \theta \sin \phi \\ mg \cos \theta \cos \phi \end{bmatrix} \quad (16)$$

This equation can be used directly for computation of the gravitational forces acting on the aircraft.

Thrust. The Jindivik has a single jet engine which lies in the $X_b - Z_b$ plane. The thrust vector is assumed to be parallel to

the fuselage reference line but displaced from the center of gravity by a distance z_T . Thus, there is only one force component and one moment component:

$$X_T = F_T \quad (17)$$

$$M_T = z_T F_T \quad (18)$$

where F_T represents the magnitude of the thrust.

Aerodynamic Forces and Moments. In contrast with the straightforward determination of the gravitational and thrust forces, the aerodynamic forces are difficult to obtain with great precision. Two primary sources are relied upon for data which is necessary for the computation of these forces (Refs 1, 15), but the data is less than exhaustive. In several instances extrapolations are necessary, but no claim is made as to the accuracy of such extrapolations.

A method commonly used to obtain expressions for the aerodynamic forces and moments is that of forming a first-order Taylor series expansion about some operating point (Refs 14, 16). This method is explained below in general terms, after which an example is presented.

Let F represent a function which is analytic in some region of interest, and furthermore let F be dependent upon a set of m variables: $(\Lambda_1, \Lambda_2, \dots, \Lambda_m)^T = \Lambda$. Define Λ^* to be the values of the dependent variables which make up Λ at some point within the region of interest, and call this point the equilibrium point. Then the Taylor series expansion of F to first order, denoted by $F^*(\Lambda)$, is given by the formula

$$F(\Lambda) \doteq F^*(\Lambda) = F(\Lambda^*) + (\Lambda_1 - \Lambda_1^*) \left. \frac{\partial F(\Lambda)}{\partial \Lambda_1} \right|_{\Lambda^*} + (\Lambda_2 - \Lambda_2^*) \left. \frac{\partial F(\Lambda)}{\partial \Lambda_2} \right|_{\Lambda^*} + \dots + (\Lambda_m - \Lambda_m^*) \left. \frac{\partial F(\Lambda)}{\partial \Lambda_m} \right|_{\Lambda^*} \quad (19)$$

The wind tunnel data presented in Appendix A is used to provide the value of each function at the equilibrium points (i.e., the $F(\Lambda^*)$ values), while a combination of given, derived, and wind-tunnel data is used in determining the partial derivatives indicated in equation 19. Furthermore, while many dependent variables affect the individual forces or moments, physical insight and experience have been used in the past to limit the number of these variables to those few which are most significant (Refs 4, 14, and 16). A tabular listing of the relative importance of different dependent variables can be seen indirectly in Reference 16, page 4.114, where each of 24 "stability derivatives" are given a score based on their relative importance. Stability derivatives are directly related to the partial derivatives indicated in equation 19. In order to illustrate the Taylor series expansion method, an example of a force expansion is now given.

Consider the aerodynamic force in the z_b direction, Z_a . The dependent variables which have been determined to be the most significant contributors to Z_a are, 1) rate of change of angle of attack, $\dot{\alpha}$, 2) pitching velocity, q , and 3) the elevator deflection angle, δ_E . Thus, in equation 19 the variables represented by Λ are

$$\Lambda = (\dot{\alpha}, q, \delta_E) \quad (20)$$

The reader may well wonder why angle of attack, α , and forward velocity, U , have been omitted from the listing of independent variables since Z_a obviously changes when either of these variables are changed. The reason for the omission is that these variables are included in the computation of the equilibrium forces in each iteration of a digital computer program. In effect, a new

equilibrium point is established during each iteration of the program, with the Taylor series expansion being used only to compute the effects of the control forces and the "dynamic variables". The dynamic variables are defined in this report as variables which are either inertial angular velocities (P, Q, R), or rates of change of the attitude of the aircraft with respect to the relative wind (i.e., rate of change of angle of attack, $\dot{\alpha}$, or rate of change of sideslip angle, $\dot{\beta}$).

The independent variables identified by equation 20 are now substituted for Λ in equation 19, and F in equation 19 is replaced by Z_a , to yield

$$Z_a(\dot{\alpha}, q, \delta_E) = Z_a(*) + (\dot{\alpha} - \dot{\alpha}^*) \left. \frac{\partial Z_a}{\partial \dot{\alpha}} \right|_{(*)} + (q - q^*) \left. \frac{\partial Z_a}{\partial q} \right|_{(*)} + (\delta_E - \delta_E^*) \left. \frac{\partial Z_a}{\partial \delta_E} \right|_{(*)} \quad (21)$$

In this equation, as well as throughout this chapter, the symbol "*" is used to indicate that the function is evaluated at the equilibrium point. Also, throughout this report the control variables and the dynamic variables are assigned a value of zero at every equilibrium point. Hence, in Equation 21, $\dot{\alpha}^* = q^* = \delta_E^* = 0$, and the equation can be written in a more compact form

$$Z_a = Z_{a_0} + Z_{\dot{\alpha}} \dot{\alpha} + Z_q q + Z_{\delta_E} \delta_E \quad (22)$$

where the definitions of Z_{a_0} , $Z_{\dot{\alpha}}$, Z_q , and Z_{δ_E} are obvious. If the coefficients of $\dot{\alpha}$, q , and δ_E are divided by the moment of inertia about the Z_b axis, I_{zz} , the familiar "dimensional stability derivatives" are obtained (Refs 4, 16). A brief description of how the equilibrium force Z_{a_0} and the values of $Z_{\dot{\alpha}}$, Z_q , and Z_{δ_E} are actually computed is presented next.

In static wind tunnel testing, as was performed in Reference 15, the data is obtained by subjecting a model to the flow in the tunnel and measuring the resultant forces while the model is placed systematically in different attitudes and configurations. The resulting data is expressed in terms of "static" aerodynamic coefficients which are defined as follows:

$$C_L = \frac{L}{qS} \quad (23)$$

$$C_D = \frac{D}{qS} \quad (24)$$

$$C_M = \frac{M}{qSc} \quad (25)$$

$$C_y = \frac{Y}{qS} \quad (26)$$

$$C_l = \frac{L_l}{qSb} \quad (27)$$

$$C_n = \frac{N}{qSb} \quad (28)$$

where,

q = dynamic pressure, $\frac{\rho V_T^2}{2}$

S = planform surface area

c = mean aerodynamic chord

b = wing span

L = lift

D = drag

M = pitching moment

Y = side force

L_l = rolling moment

N = yawing moment

It has been necessary here to change the symbol for rolling moment given in Figure 4 (L) to L_l , so as to distinguish between the usual

symbol for lift and the symbol for rolling moment. Both lift and rolling moment are symbolized by L throughout the remainder of this report whenever there is no ambiguity. The first two coefficients above are necessary to compute the value of Z_{a_0} .

The relationship between Z_{a_0} , L , and D can be seen from Figure 5 below. Clearly, Z_{a_0} can be computed as follows:

$$\begin{aligned} Z_{a_0} &= -L \cos \alpha - D \sin \alpha \\ &= -qS(C_L \cos \alpha + C_D \sin \alpha) \end{aligned} \quad (29)$$

Thus, a knowledge of C_L , C_D , q , and α is all that is necessary to compute Z_{a_0} . Appendix A presents analytic approximations of C_L and C_D (as well as the other static aerodynamic coefficients) as functions of α , β , and the flap setting. Thus, a computer program calculation of Z_{a_0} (or any other equilibrium force or moment) during any one iteration requires only the flap setting, the true velocity, and the

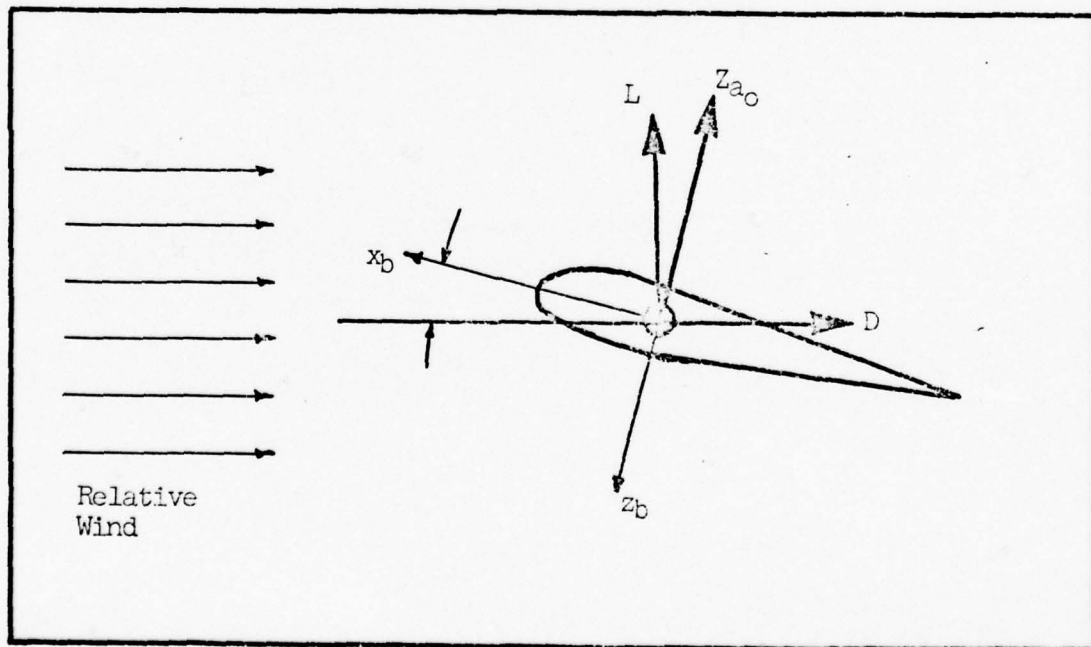


Fig. 5 Relationship of Z_{a_0} to Lift and Drag

orientation of the aircraft to the flow (i.e., angle of attack and sideslip angle). The computer program used for all simulations in this report performs calculations of equilibrium forces and moments in the manner just described.

Wind tunnel data for the dynamic variable coefficients ($Z_{\dot{\alpha}}$ and Z_q in Equation 22) are not available. Approximate values for these two coefficients are derived in the second section of Appendix A.

The elevator control coefficient is also needed in Equation 22, and there is sufficient wind tunnel data to establish this coefficient. Both the data (Tables XI-A, XII-A, and XIII-A) and analytic approximations of the data are given in Appendix A.

An example of how one aerodynamic force, Z_a , is computed has been given. The other aerodynamic forces and moments are computed in the same manner, but some coefficients in the other expansions have been taken directly from Reference 1. These coefficients are given in Table XV-A, Appendix A. The final step in setting up the mathematical in-flight model is the conversion of the algebraic relationships into the computer program which has been previously mentioned. Much of the tedium of writing such a program was avoided by the use of a software applications package created by Boeing Computer Services, EASY (Ref 6). A brief description of EASY and portions of the computer program which have been used to simulate and analyze the Jindivik are given in Appendix B.

Existing Autopilot. There are two primary flight control surfaces on the Jindivik: the elevator and the ailerons. Block diagrams of the existing autopilots which drive each control surface are presented in Figures 6 and 7. Consider the simpler of the two

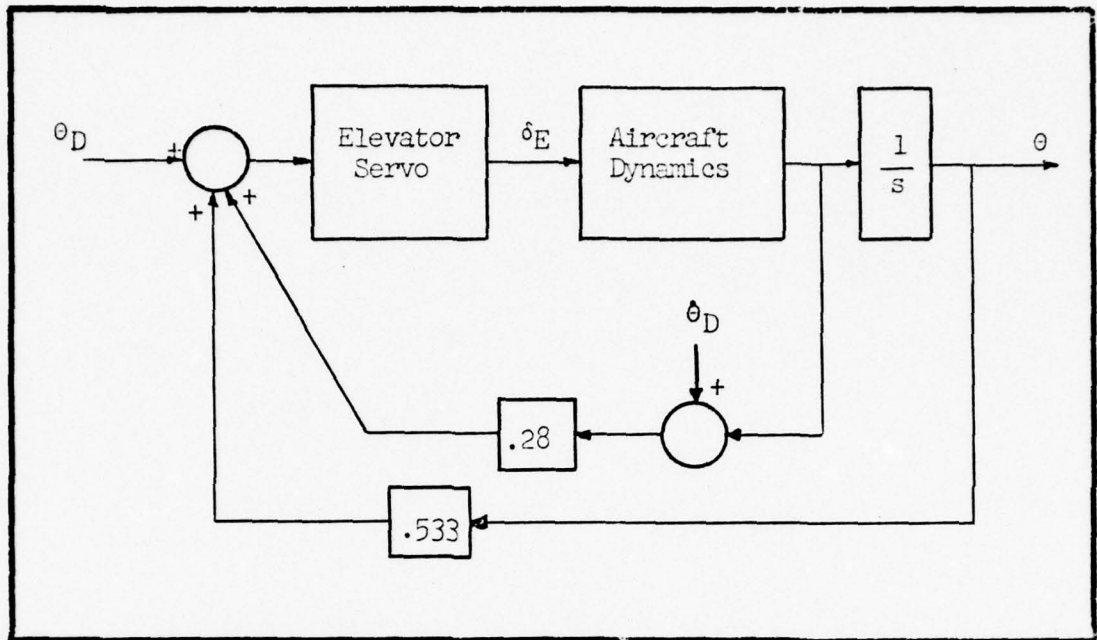


Fig. 6 The Existing Pitch Control System

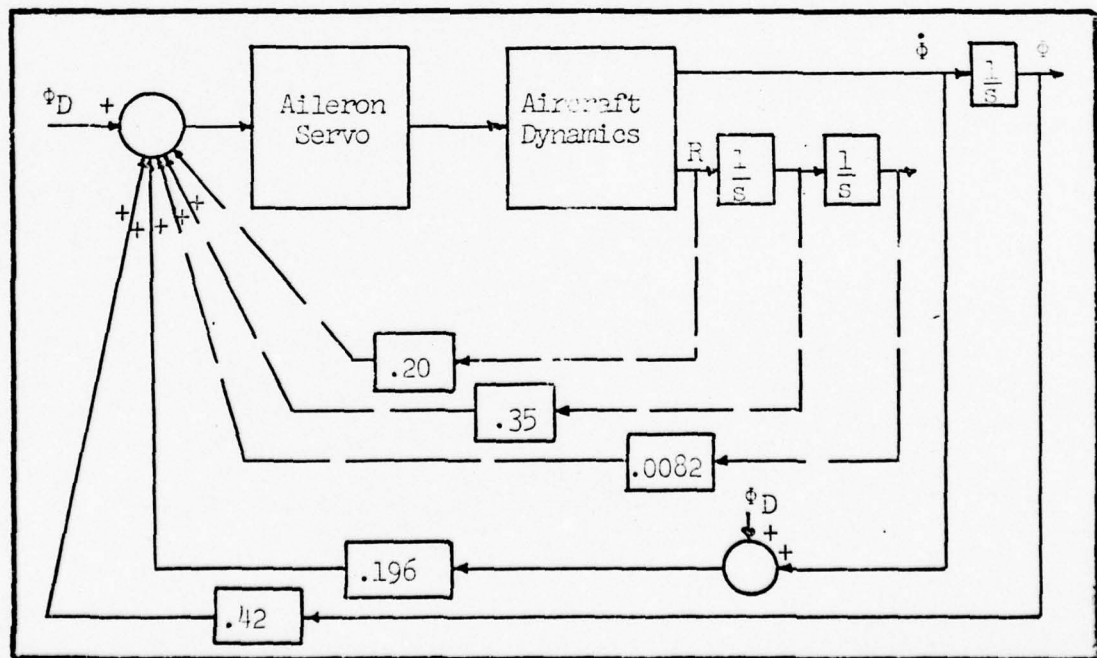


Fig. 7 The Existing Roll Control System

first — the pitch autopilot. The pitch autopilot, also referred to as the pitch control system, has the combined purposes of allowing a ground crewman 1) to command a desired pitch rate and pitch attitude and, 2) to achieve and hold that rate and/or attitude until receiving another command. The use of pitch and pitch-rate feedback is very common, and furthermore, it is shown by simulations in Chapter III that the pitch control system is adequate.

The roll autopilot, or roll control system, is similar in structure to the pitch autopilot. Roll angle and roll angle rate can be commanded and regulated by a ground crewman. The outer loops (connected with dashed lines in Figure 7) were apparently designed to stabilize the heading of the rudderless vehicle. Simulations were run with the outer loops engaged, but this configuration was found to be unstable. Other simulations were made with these loops disengaged (see Chapter III), but the vehicle was found to be laterally unstable in this configuration as well. Since an unacceptable situation is achieved in either arrangement, the outer loops were eliminated in all subsequent simulations. It is demonstrated in Chapter III that the roll autopilot using only roll and roll-rate feedback is acceptable if yawing motion is controlled.

III. DESIGN AND ANALYSIS OF A YAW CONTROL SYSTEM

The development of an aerodynamic model of the Jindivik in Chapter II allows considerable information to be obtained by performing dynamic simulations. Several simulation results are presented in this chapter which serve to demonstrate the existence of a lateral stability problem. The instability is shown to be one which can occur whenever an Air Cushion Recovery System is installed on an existing aircraft. Since the problem is of a general nature, an effective solution to the problem is highly desirable. Therefore, a considerable portion of this chapter is devoted to developing a yaw control system. Although the system proposed in this chapter is designed specifically to the Jindivik, the basic structure can be used in a wide variety of situations.

Introduction

In-flight simulations of the Jindivik aircraft equipped with an inflated Air Cushion Recovery System are examined early in this chapter to identify any instabilities, or other undesirable dynamic characteristics, which may be caused by the installation of an ACRS. Simulation results are also exploited toward the end of the chapter to validate a yaw control system design. Since simulation results are a vital part of this chapter, two caveats are given at the outset. First, the scope of the simulations is very limited, since the

intent of this report is not to conduct a detailed investigation of the entire flight envelope of the Jindivik. Secondly, simulation results are only as accurate as the model which produces those results. The simulations in this chapter sometimes rely upon extrapolated wind tunnel data as well as somewhat crude estimates of some of the stability derivatives. In spite of these shortcomings, however, the simulations provide some very useful information, as will be seen shortly.

The remainder of this chapter is divided into three main sections. The first section consists of results obtained from simulating both the bare airframe and the airframe and autopilot combination. The second section develops a yaw control system to stabilize the Jindivik in flight. Verification of this yaw control system is achieved in the third section by simulating the aerodynamic model with the yaw controller added.

Simulations of Existing Aircraft and Autopilot

The first simulation results to be considered are those of the bare airframe. These results serve as a baseline to which the dynamics of all other configurations can be compared. Another reason for simulating the bare airframe is to isolate undesirable aerodynamic characteristics which may be attenuated, or even exacerbated, by the existing control system.

The configuration and initial conditions for the bare airframe simulation are given in Table II. A gross weight of 2620 lbs is used since this is a typical landing weight. The airspeed is chosen to be 300 ft/sec (180 knots), since the present landing speed is

Table II

CONFIGURATION AND INITIAL CONDITIONS FOR SIMULATIONS

Flaps	Up
ACRS	Deployed
Gross Weight	2620 lbs
True Velocity, V_T	300 ft/sec
Altitude	Mean Sea Level
Thrust	807 lbs
Equilibrium Pitch Angle	2.07°
Equilibrium Elevator Deflection	3.26°

217 ft/sec (130 knots) and the Jindivik would fly a pattern airspeed somewhat faster. Equilibrium conditions were computed by hand for angle of attack, thrust setting, and elevator deflection angle. Aileron deflection angle and rate are set to zero for the start of the simulation. The flap setting is chosen arbitrarily to be 0° and this setting is maintained throughout all in-flight simulations. By choosing an initial pitch angle equal to the equilibrium angle of attack (2.07°), a velocity vector is established which is parallel to the earth's surface. While some lengthy simulations were run (up to 20 seconds), shorter simulations are chosen for analysis since excessive extrapolation of the available wind tunnel data is required for long runs. Thus, a simulation time of three seconds is used for the bare airframe simulations, which diverge quickly, while longer runs are used for analysis later in the chapter for more stable configurations.

Simulation results for the bare airframe are presented in Figures 8 and 9. The variables displayed in Figure 8 are the Euler angles--roll (ϕ), pitch (θ), and yaw (ψ). These angles represent the orientation of the vehicle with respect to the earth. Roll angle is the angle between the y_b axis of the aircraft and the surface of the earth, with right wing down being the positive direction. Pitch angle is the angle between the vehicle x_b axis and the surface of the earth, with a nose-up direction being positive. The yaw angle is the angle between the x_b axis of the vehicle and an arbitrary $x_e - z_e$ plane in the earth frame, where the positive direction for yaw is to the right.* The most notable aspect of these simulation results is the roll angle--in less than 3 seconds the roll angle reaches a value of -100° . The pitch angle reaches -6° in 3 seconds and is decreasing. The yaw angle of the aircraft has veered -18° off the original heading.

Figure 9 displays the time history of the sideslip angle, β , and the angular velocity about the z_b axis, R . The sideslip angle is the angle between the velocity vector of the vehicle and the longitudinal axis. The reason for presenting the sideslip angle is that the abrupt changes in orientation of the vehicle shown in Figure 8 are intimately related to the sideslip angle. The following paragraphs describe this relationship in some detail.

While most aircraft are symmetric about the $x_b - z_b$ plane, the wind tunnel data presented in Appendix A show that this is not true

*These descriptions of the Euler angles are given only for the benefit of the reader who is unfamiliar with flight dynamics. They are not intended to be rigorous definitions. Precise definitions can be found in References 4, 14, and 16.

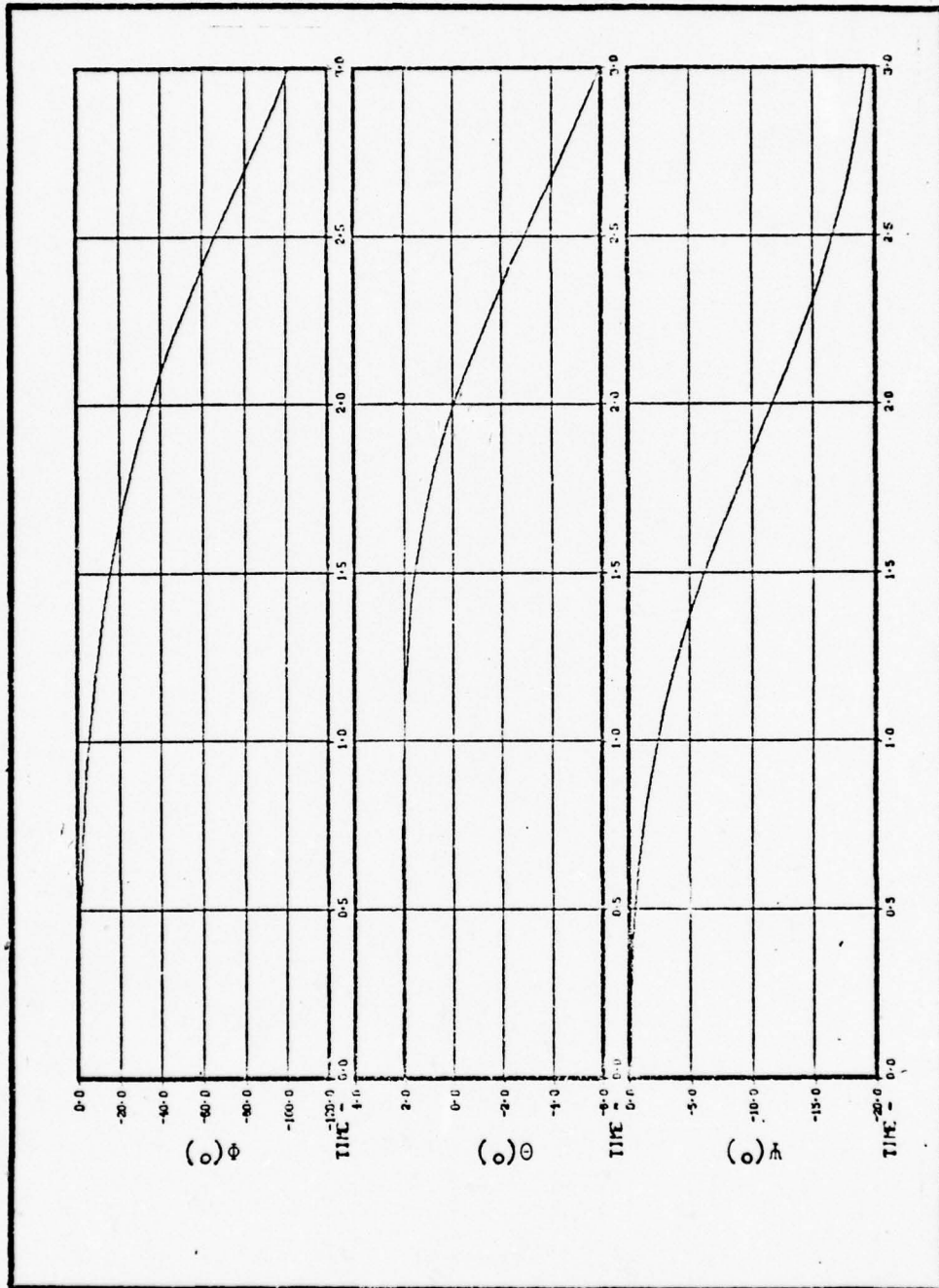


Fig. 8 Time History of the Orientation of the Bare Airframe

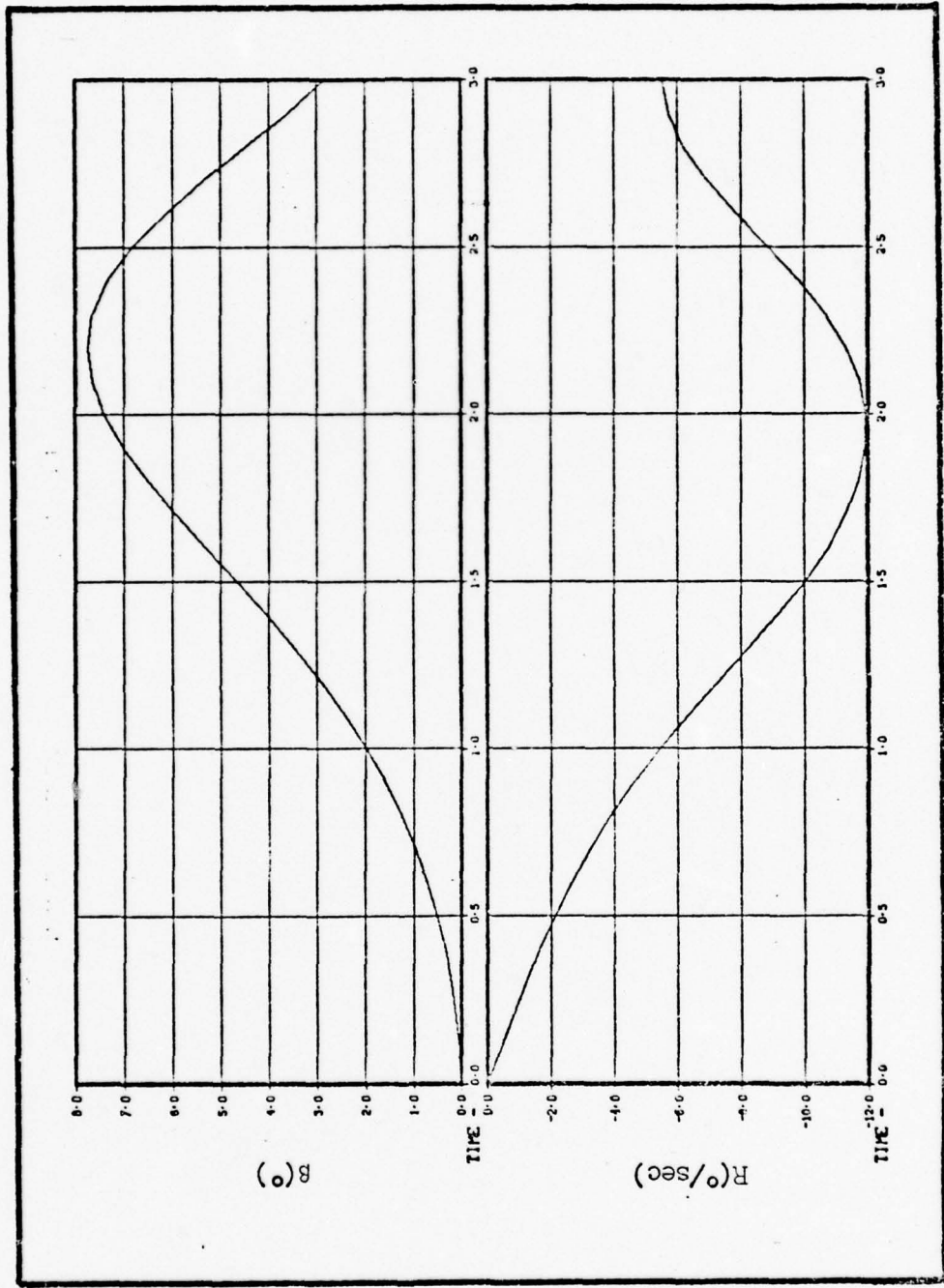


Fig. 9 Time Histories of Sideslip Angle and Yaw Rate for the Bare Airframe Simulation

of the Jindivik. The side force coefficient (Fig. A-4), roll moment coefficient (Fig. A-6), and yaw moment coefficient (Fig. A-10), all have nonzero values when $\beta = 0$. The yawing moment is of particular interest since the slope of the yaw moment coefficient, C_n , versus sideslip angle is negative at $\beta = 0^\circ$ for all values of angle of attack. Whenever the slope of the C_n vs β curve is negative, the aircraft is statically unstable (Ref 4:113).

Static stability can be defined as a condition wherein the aircraft tends to return to an equilibrium point when it has been displaced from that point. This definition is not well suited for nonlinear systems since the size of the displacement can affect the stability. Thus, for the purposes of this report, a restriction on the size of the displacement is required. For all values of angle of attack, the yaw moment coefficient slope (with flaps up) is seen to be negative within the range $-2^\circ \leq \beta \leq +2^\circ$ (Figs. A-9 through A-12). To see why a negative slope results in static instability, it is necessary only to consider the consequences of either an increase or a decrease in β . If β were increased slightly from 0° , a more negative yawing moment would be produced. But a more negative yawing moment would eventually produce a more negative yaw angle, and consequently a further increase in β .

Returning to the simulation results in Figure 9, the effect of lateral static instability can be seen directly. The values of C_n at $\beta = 0^\circ$ is negative. This results in a negative torque about the z_b axis which in turn produces a yaw acceleration and rate. The value of the yaw rate after one second is seen to be about $-5.5^\circ/\text{sec}$. A value of 2° has been reached by β and consequently an even higher

value of C_n is produced. After the first two seconds the results of the simulation cannot be so easily interpreted since the relationships become very nonlinear. However, some general trends produced by increases in sideslip angle can be noted. When β increases, the rolling moment, C_l , becomes more negative as can be seen in Figure A-6. The rolling moment produces a rolling acceleration which brings about a roll rate and a roll angle change. The abrupt change in roll angle (from 0° to -100° in less than 3 seconds) has already been noted in Figure 8. The roll angle variation can account for changes in pitch, since the pitching moment (which acts about the y_b axis of the vehicle) depends upon angle of attack. A roll angle other than 0° results in the lift vector of the vehicle no longer being aligned with the force of gravity. Hence, an unbalanced vertical force is produced which eventually results in a change in angle of attack. The change in yaw angle in Figure 8 is the result of both the yaw rate, R , and the roll angle, ϕ . It should be noted here that all variations in the variables presented in Figures 8 and 9 can be explained in terms of either the lack of lateral symmetry or, more importantly, the lack of lateral static stability.

Now that the bare airframe has been simulated and discussed, simulations of the airframe augmented by the autopilot can be described. In order to examine the pitch autopilot and roll autopilot separately, the equations of motion are decoupled into longitudinal equations (equations involving forces along the x_b and z_b axes, and moments about y_b) and lateral equations (forces along y_b and moments about the x_b and z_b axes).

The pitch autopilot, as mentioned in Chapter II, makes use of pitch angle and pitch angle rate feedback. An initial angle of attack of 3.07° (1° higher than the equilibrium angle of attack) is used to check the longitudinal dynamics. This angle of attack could be considered to have come about from an instantaneous gust along the z_0 axis. A desired characteristic of the pitch autopilot is that it be able to return the aircraft to a desired pitch angle after a perturbation. The purpose of this simulation is to verify this characteristic.

Figure 10 portrays the results of this simulation. The initial angle of attack, α , is seen to be 3.07° , but in about 2.5 seconds α has returned to the equilibrium value of 2.07° . The pitch angle drops sharply and then returns to a value of about 2.04° . Although the reference pitch attitude is 2.07° , the autopilot has not achieved this value after 5 seconds. One possible explanation is that there is a slight drop in velocity during the simulation, and this changing velocity might have produced the slightly low value of pitch angle. The difference is very slight, however, and the pitch autopilot appears to be performing satisfactorily.

A simulation of the roll autopilot is also of interest as roll control of the vehicle is necessary. Since the vehicle is statically unstable about the yaw axis, yaw rate and angle are excluded from the simulation. This simulation is intended only to verify that the roll autopilot can restore and maintain a desired roll angle when all states other than roll angle, ϕ , roll rate, P , and the roll autopilot internal states are fixed.

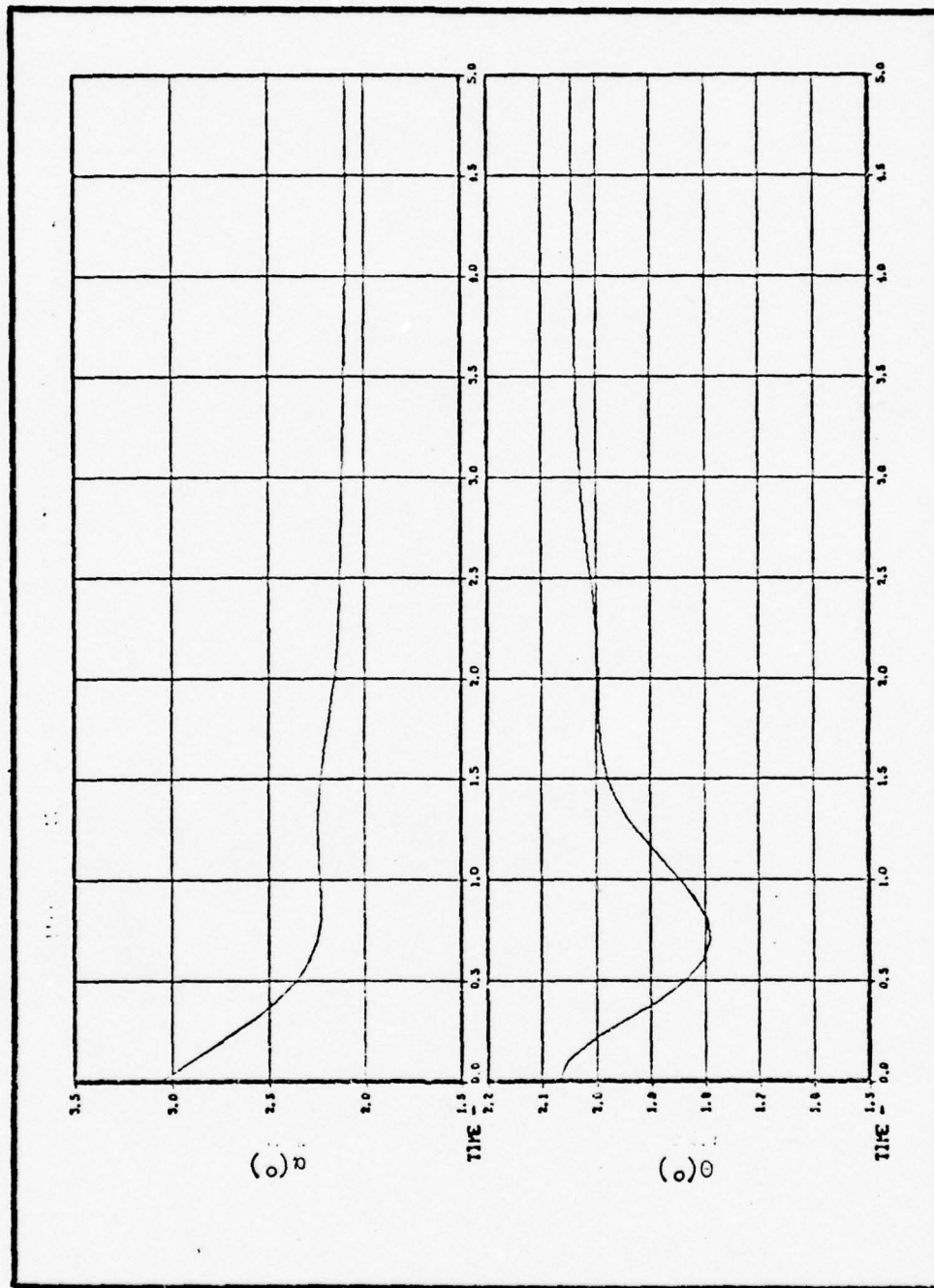


Fig. 10 Verification of the Adequacy of the Pitch Control System

Figure 11 demonstrates the adequacy of the roll axis autopilot. The autopilot brings the vehicle to a 0° (commanded) roll angle after having been displaced by an initial roll angle of 5° . The roll rate is returned to $0^\circ/\text{sec}$ and the aileron deflection undergoes a slightly underdamped oscillation before settling down to 0° .

A full six-degree of freedom simulation is now presented. The only purpose of this simulation is to demonstrate the inadequacy of the existing autopilot. The same initial conditions are used for this simulation as are given in Table II.

The simulation results of the airframe and autopilot combination are presented in Figures 12 and 13. Roll and pitch angles in Figure 12 can be compared with the bare airframe simulation results in Figure 8. A much improved situation is apparently obtained in these two variables, but both angles are still decreasing after 3 seconds. The peak yaw angle magnitude is seen to be even greater than in the bare airframe simulation. Figure 13 reveals that the lateral static instability exhibited by the bare airframe causes the deviations. Thus, neither the aileron controller nor the elevator controller are effective means of controlling yaw position or rate. The lateral static stability of the aircraft has been destroyed by the installation of the ACRS and the existing autopilot is not equipped to handle such a situation.

Before proceeding to the next section, a list of conclusions may prove useful:

1. The Jindivik airframe equipped with a particular ACRS is statically unstable.

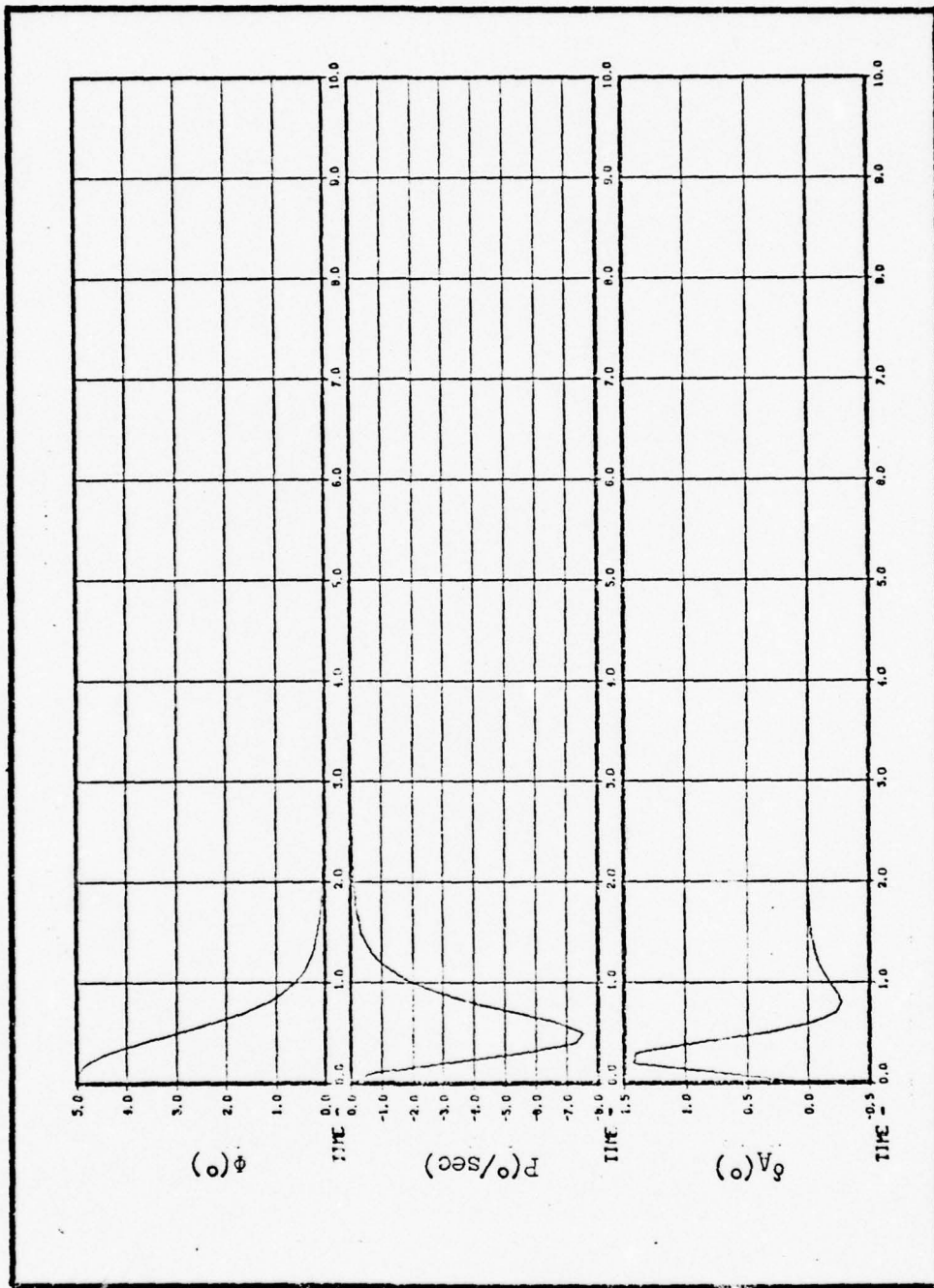


Fig. 11 Verification of the Adequacy of the Roll Control System

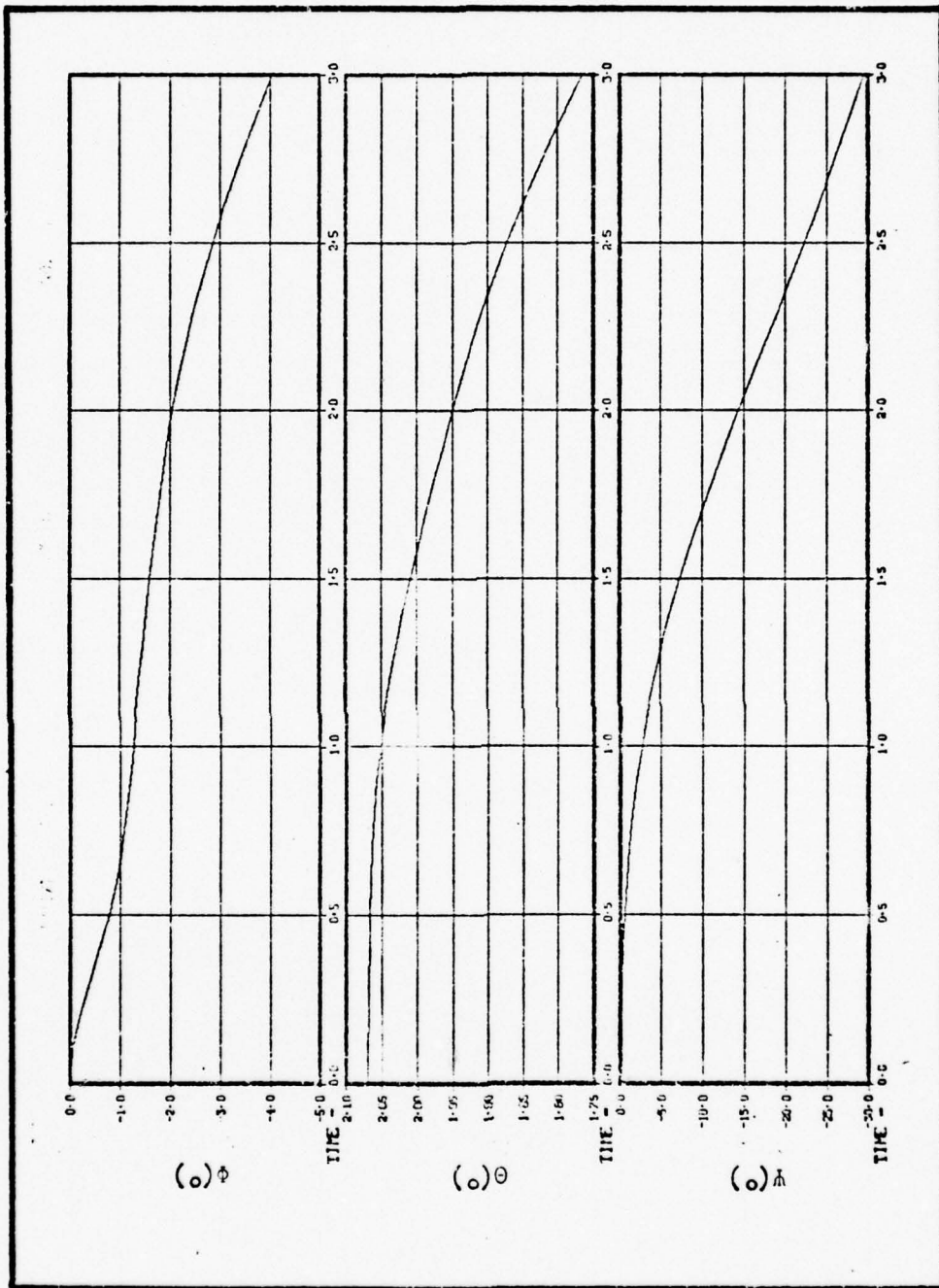


Fig. 12 Time History of the Orientation for the Airframe/Autopilot Combination

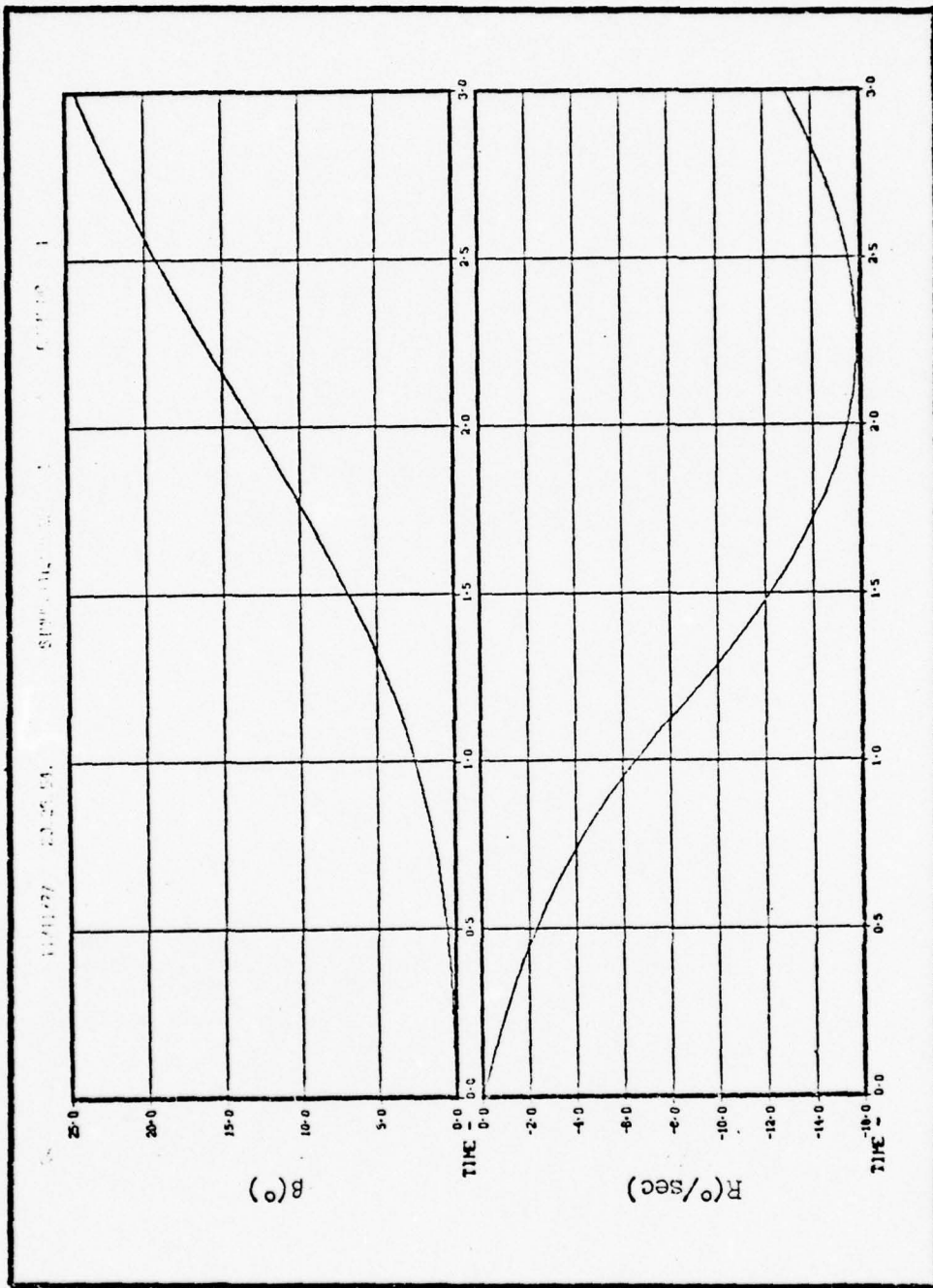


Fig. 13 Time Histories of Sideslip Angle and Yaw Rate for the Airframe/Autopilot Combination

2. The existing pitch controller adequately controls pitch rate and pitch angle.
3. The existing roll controller adequately controls roll rate and roll angle.
4. The performance of the Jindivik with the existing autopilot system is inadequate.

The use of the term "adequate" in these conclusions is meant to imply only that the system does not appear to be divergent for the conditions considered. Furthermore, while a detailed aerodynamic analysis of the Jindivik is not within the scope of this report, a physical reason for the statically unstable condition can be given.

The vertical stabilizer on conventional aircraft provides ample area aft of the center of gravity to create lateral static stability. An ACRS installed on the Jindivik results in a considerable addition of surface area forward of the center of gravity which offsets, to some extent, stabilizing effects of the tail. Since this particular stability problem can occur whenever an ACRS is placed on an existing airframe, it is reasonable to seek a general solution to this problem. While the next section is devoted to solving the lateral stability problem of the Jindivik aircraft, the same procedures can be applied in many other situations.

Design of a Yaw Control System

A fundamental question which must be answered before beginning any design process is, "What is the purpose of the design?" In light of conclusions stated in the previous section, a statement of the purpose of a yaw control system for the Jindivik can be made:

The purpose of the yaw control system is to provide lateral stabilization of the vehicle such that the vehicle is stable when the ACRS is deployed.

While many different designs are possible, only three are given here as possible alternatives. While these three approaches are certainly not exhaustive, they serve to illustrate the wide range of possibilities. The approaches considered are 1) increasing the area of the vertical stabilizer, 2) changing the aileron control law, and 3) devising a control law for the yaw thrusters.

The most straightforward solution to the problem is to increase the area of the vertical stabilizer. The main advantages of this approach are simplicity and reliability. The disadvantages are numerous: 1) the added tail area increases total drag throughout the entire mission, even though the additional area is needed only briefly (while the ACRS is deployed), 2) structural modification of the tail may be rather expensive, 3) the larger tail surface is easier to detect by both radar and visual means (with obvious implications for military use), and 4) while the increase in area increases stability, no means of control is added.

Changing the aileron control law is another alternative which could be used to meet the stated purpose. The approach would essentially be that of a single input (aileron deflection) multiple output (sideslip angle and roll angle) control problem. Modern optimal control theory could possibly be applied to determine a feedback law which would stabilize the vehicle and allow some control over both sideslip angle and roll angle. A big advantage is inexpensive implementation, but there is a disadvantage also.

Although requirements of controllability are met (i.e., an aileron deflection produces both a yaw and a roll moment), the yawing moment is only weakly affected by an aileron deflection. Additional analysis is required to ascertain the adequacy of this design approach, however.

The third approach mentioned above is that of designing a control law for yaw thruster devices which would stabilize the vehicle. The term "yaw thruster device" has been used to denote a broad range of mechanisms which are capable of producing a torque about the z_b axis. In order to enumerate advantages and disadvantages, however, a more specific description must be given. A particular type of yaw thruster has been designed for directional control of the Jindivik which makes use of the "Coanda effect".

The Coanda effect was discovered in 1910 by Henri Coanda (Ref 7 :1). While a full description of the Coanda effect yaw thruster can be found in Reference 7 , page 1, a brief discussion of its operating characteristics is sufficient for the purposes of this report.

Coanda effect yaw thrusters create a torque about the vehicle z_b axis by deflecting a portion of the exhaust flow produced by the jet propulsion engine (see Figure 14). The deflected portion of the flow becomes attached to a metal plate on either the port or starboard side of the exhaust nozzle. The deflection takes place very rapidly and, therefore, it is assumed to occur instantaneously for the purposes of this report. Control of the device is achieved by small solenoid operated valves which affect the pressure behind the ports shown in Figure 14. Figure 15 is a photograph of a yaw

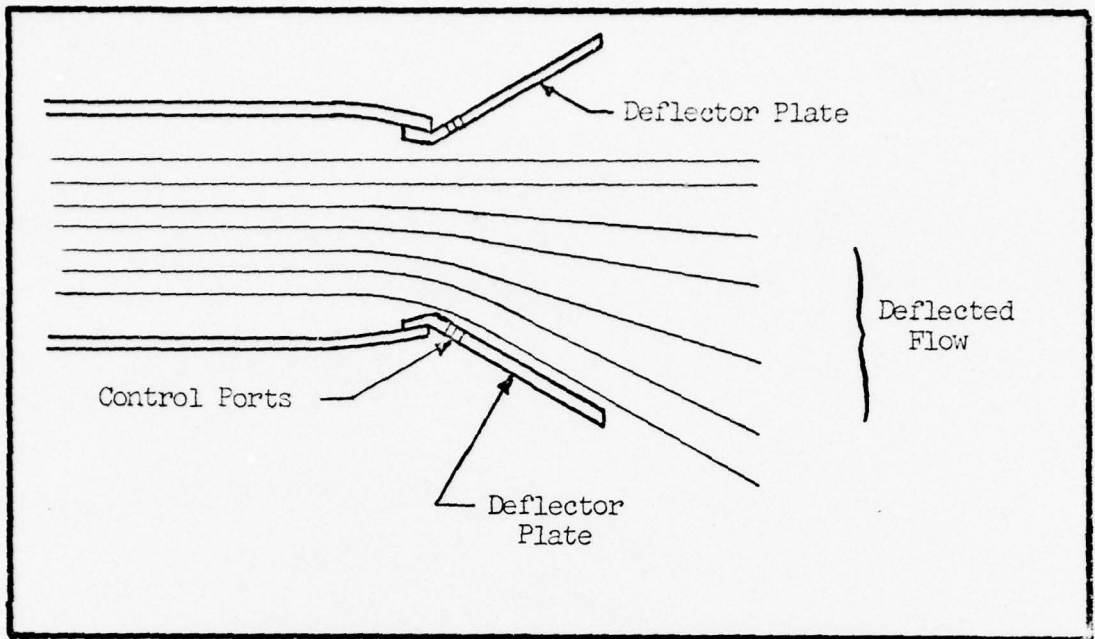


Fig. 14 The Coanda - Effect Yaw Thruster

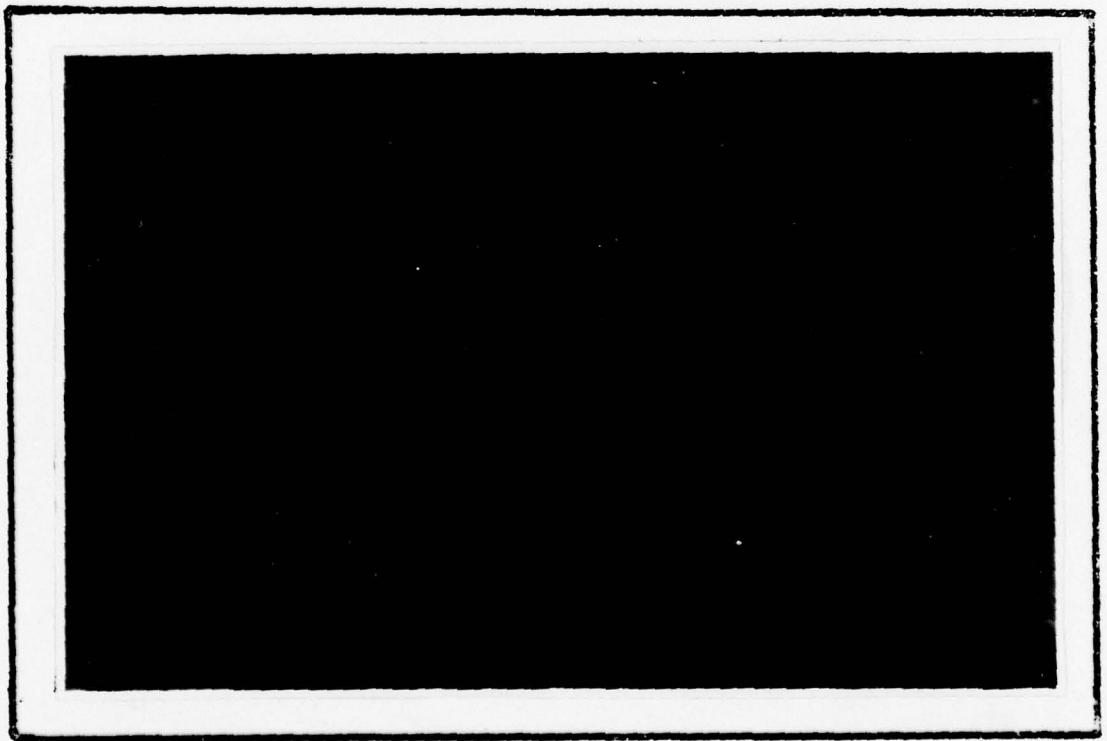


Fig. 15 A Yaw Thruster Installed on the Jindivik Aircraft

thruster installed on the Jindivik aircraft. A mathematical model of the yaw thrust device which has been designed for the Jindivik is given later in this chapter, but first the advantages and disadvantages of this device are presented.

The biggest disadvantage of the coanda-effect yaw thruster is that the magnitude of the output of the device is dependent upon the thrust level of the propulsion engine. Hence, for takeoff operations the device produces its maximum torque, while during the slideout only a fraction of the maximum torque is produced since the thrust is usually at an idle setting. During cruise portions of a mission the thrust level will vary somewhere between these extremes. Some preliminary test data (Reference 15) indicates that the range of yaw torque available is roughly 100 ft-lb (at idle) to 450 ft-lb (at maximum thrust).

Advantages of the yaw thruster for stabilization of the Jindivik in flight are numerous. Since the device is to be used for control during the takeoff phase, no additional modification of the Jindivik is necessary, except for the control circuitry. It is claimed, therefore, that low cost is an advantage of using this method for stabilizing the vehicle. Also, the weight of added control circuitry is much less than the additional weight required by an increase in tail area. A final advantage is that yaw thrusters could be used for control of the vehicle as well as for stabilization. A brief description of how the yaw controllers could be used for control in a turn is given later in this chapter.

Before any details of the design procedure are discussed, a mathematical model of the coanda-effect yaw thruster is developed.

Figure 16 depicts the geometry of the situation. The yaw thruster produces a net force, F_{yt} , parallel to the y_b axis by deflecting part of the exhaust flow from the jet engine. The direction of F_{yt} is positive when the net force acts in the positive y_b direction. Hence, the following force and moment equations can be written:

$$Y_c(\text{yaw thruster}) = F_{yt} \quad (30)$$

$$N_c(\text{yaw thruster}) = -l_{yt} F_{yt} \quad (31)$$

where Y_c and N_c represent a control input force along the y_b axis and a control input torque about the z_b axis respectively.

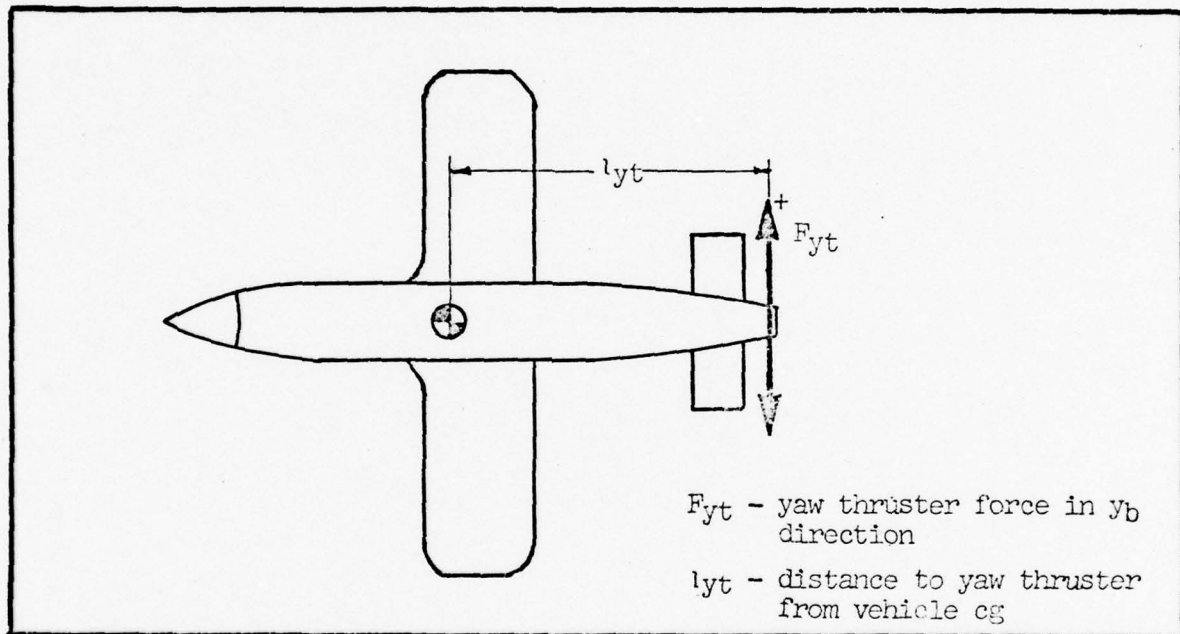


Fig. 16 Geometry of the Yaw Thruster Installed on the Jindivik

It should be noted here that the coanda-effect yaw thruster cannot provide a continuous range of forces. Instead, it can provide a maximum net force in either the positive y_b direction or the negative y_b direction, or no net force in the y_b direction.

Since the output of this control device is maximum effort in one direction or another, it appears that it should be well suited for use in a time optimal, bounded input control design. This design approach was undertaken and the main features of this design are now presented.

Analyses of the stability of the Jindivik early in this chapter imply that the negative C_n versus β slopes of Figures A-9 through A-13 in Appendix A are responsible for unacceptable performance in the simulations. Yaw moment coefficient, C_n , is strongly related to yaw angle acceleration, \dot{R} . Furthermore, sideslip angle, β , is closely related to lateral velocity, $V(\beta \equiv \sin^{-1}(V/V_T))$, where V_T is the magnitude of the inertial velocity of the vehicle. Therefore, it is reasonable to expect that the side force and yaw moment equations (equations 4 and 8, Chapter 2) are closely related. Thus, these two equations are chosen in an attempt to simplify the problem. The equations are repeated here for convenience:

$$m(\dot{V} + RU - PW) = \Sigma Y \quad (4)$$

$$\dot{R}I_z - P I_{xz} + PQ(I_y - I_x) + QR I_{xz} = \Sigma N \quad (8)$$

It is assumed that the pitch and roll autopilots are restricting Q , P , and \dot{P} to small values (i.e., these values are kept small in comparison with V , R , \dot{V} , and \dot{R}), such that the following terms can be neglected: WP , $\dot{P}I_{xz}$, $PQ(I_y - I_x)$, and $QR I_{xz}$. Equations (4) and (8) then become

$$m(\dot{V} + RU) = \Sigma Y \quad (32)$$

$$\dot{R}I_z = \Sigma N \quad (33)$$

To simplify the problem further, linear approximations for ΣY and

ΣN can be made. By techniques described in Chapter 2, these summations can be written as

$$\Sigma Y = Y_g + Y_t + Y_a + Y_c + Y_f \quad (34)$$

$$\Sigma N = N_t + N_a + N_c + N_f \quad (35)$$

where the subscripts g, t, a, c, and f are defined in Chapter II.

For wings-level, in-flight conditions, equations 34 and 35 reduce to

$$\Sigma Y = Y_a + Y_c \quad (36)$$

$$\Sigma N = N_a + N_c \quad (37)$$

The aerodynamic side force can be written as

$$Y_a = \bar{q} S C_y = \bar{q} S [C_{y_0} + C_{y_\beta} \Delta\beta] = \bar{q} S C_{y_0} + \bar{q} S C_{y_\beta} \Delta\beta \quad (38)$$

or more compactly,

$$Y_a = Y_{a_0} + Y_{\beta\Delta\beta} \quad (39)$$

Definitions of the parameters used in equation 38 are

\bar{q} = dynamic pressure

S = surface area

C_y = side force coefficient

C_{y_0} = side force coefficient at an equilibrium point

$C_{y_\beta} = \frac{\partial C_y}{\partial \beta}$ evaluated at an equilibrium point

A similar treatment of the aerodynamic yaw moment, N_a , yields

$$N_a = \bar{q} S b [C_n(\alpha, \beta)] + N_{R\Delta R} + N_{P\Delta P} + N_{\delta A \Delta \delta A} \quad (40)$$

where

b = wing span

C_n = yaw moment coefficient

$N_R = \frac{\partial N_a}{\partial R}$ evaluated at an equilibrium point

$N_P = \frac{\partial N_a}{\partial P}$ evaluated at an equilibrium point

$N_{\delta A} = \frac{\partial N_a}{\partial \delta A}$ evaluated at an equilibrium point

Although C_n is a function of both α and β , the pitch autopilot can be assumed to keep variations in α small such that $C_n(\alpha, \beta) \doteq C_n(\beta)$.

Further simplification results from a linearization of $C_n(\beta)$:

$$C_n(\beta) \doteq C_{n_0} + C_{n_\beta} \Delta\beta \quad (41)$$

where C_{n_0} is the value of C_n at the equilibrium point and C_{n_β} is the partial derivative of $C_n(\beta)$ with respect to β evaluated at the equilibrium point. Thus, equation (40) can be written as

$$N_a \doteq \bar{q} S b C_{n_0} + \bar{q} S C_{n_\beta} \Delta\beta + N_{R\Delta R} + N_{P\Delta P} + N_{\delta A \Delta \delta A} \quad (42)$$

Typically the last two terms are small when compared with the other terms, so these are neglected. Then the complete simplified expression for N_a is written compactly as

$$N_a \doteq N_{a_0} + N_{\beta} \Delta\beta + N_{R\Delta R} \quad (43)$$

with the definitions of the terms being obvious by comparison of equation 43 with 42.

The control terms Y_c and N_c have been defined in equations 30 and 31, so the complete expressions for ΣY and ΣN can be written:

$$\Sigma Y \doteq Y_{a_0} + Y_{\beta} \Delta\beta + F_{yt} \quad (44)$$

$$\Sigma N \doteq N_{a_0} + N_{\beta} \Delta\beta + N_{R\Delta R} - l_{yt} F_{yt} \quad (45)$$

Returning to equations 32 and 33, the side force and yaw moment equations are now approximated by

$$m(\dot{V} + RU) = Y_{a_0} + Y_{\beta} \Delta\beta + F_{yt} \quad (46)$$

$$\dot{R}I_z = N_{a_0} + N_{\beta} \Delta\beta + N_{R\Delta R} - l_{yt} F_{yt} \quad (47)$$

If the equilibrium point is specified to some extent, the equations can be further simplified. Assuming that, 1) U is nearly constant, 2) the equilibrium point is always taken with $\beta = 0$, and 3) the equilibrium point is always taken with $R = 0$, the following statements can be made

$$U = U_0, \text{ a constant} \quad (48)$$

$$\Delta\beta = \beta = \sin^{-1}V/V_T \doteq \left(\frac{1}{V_T}\right)V \quad (49)$$

$$\Delta R = R \quad (50)$$

Rewriting equations 46 and 47 using the stated equilibrium conditions and definitions,

$$m(\dot{V} + RU_0) = Y_{a_0} + (Y_{\beta}\frac{1}{V_T})V + F_{yt} \quad (51)$$

$$\dot{R}I_Z = N_{a_0} + (N_{\beta}\frac{1}{V_T})V + N_{RR} - l_{yt}F_{yt} \quad (52)$$

These two equations can be solved for the first derivatives of V and R, producing

$$\dot{V} = \left(\frac{Y_{\beta}}{mV_T}\right)V + (-U_0)R + \frac{1}{m}F_{yt} + \frac{Y_{a_0}}{m} \quad (53)$$

$$\dot{R} = \left(\frac{N_{\beta}}{I_Z V_T}\right)V + \left(\frac{N_{RR}}{I_Z}\right)R + \left(\frac{-l_{yt}}{I_Z}\right)F_{yt} + \frac{N_{a_0}}{I_Z} \quad (54)$$

In state variable format, these equations are expressed as

$$\begin{bmatrix} \dot{V} \\ \dot{R} \end{bmatrix} = \begin{bmatrix} a_{11} & a_{12} \\ a_{21} & a_{22} \end{bmatrix} \begin{bmatrix} V \\ R \end{bmatrix} + \begin{bmatrix} b_1 \\ b_2 \end{bmatrix} F_{yt} + \begin{bmatrix} C_1 \\ C_2 \end{bmatrix} \quad (55)$$

where definitions of the terms in equation 55 are

$$a_{11} = \frac{Y_{\beta}}{mV_T} \quad a_{12} = -U_0$$

$$a_{21} = \frac{N_{\beta}}{I_Z V_T} \quad a_{22} = \frac{N_{RR}}{I_Z}$$

$$b_1 = \frac{1}{m} \quad C_1 = \frac{Y_{a_0}}{m}$$

$$b_2 = \frac{-l_{yt}}{I_Z} \quad C_2 = \frac{N_{a_0}}{I_Z}$$

The constant terms C_1 and C_2 above represent the contributions of C_y and C_n at $\beta = 0^\circ$. These terms exist due to either a lack of symmetry in the one-quarter scale model used in determining the wind tunnel data, or possibly they exist due to misalignment of the model in the wind tunnel. Another possibility is that the model

represents the actual aircraft very well, the model was not misaligned, and the actual aircraft is really not symmetric about the $x_b - z_b$ plane. As mentioned in Appendix A, a 3-inch pipe extends several feet along the upper, port side of the vehicle for the purpose of supplying bleed air to the ACRS. It is conceivable that this asymmetric object produces the values of C_{y_0} and C_{n_0} , but it is beyond the scope of this report to attempt to confirm or dispute this possibility. Another simplifying assumption is now made: the constant terms are assumed to be zero, which is equivalent to saying that the aerodynamics of the aircraft are adjusted so as to balance the side force and yaw moment when $\beta = 0$.

With the assumption that $(C_1, C_2) = (0, 0)$, equation 55 is of the form

$$\dot{x} = Ax + bu \quad (56)$$

where the control, u , is bounded. If the problem is now to find an extremal control, u^* , which transfers an arbitrary initial state at $t = 0$ to the final state $x(t_f) = 0$ in minimum time, then the problem is referred to as a stationary, linear regulator, minimum-time problem (Ref 13:249). Certain theorems which pertain to this problem are proven in the literature and presented here for convenience (Ref 13:249).

Theorem 1 (Uniqueness)

If an extremal control exists, then it is unique.

Theorem 2 (Number of Switchings)

If the order of the system described by equation 56 is n , if the eigenvalues of A are all real, and if a time-optimal control exists, then each control component can switch at most $(n-1)$ times.

Furthermore, for a much broader class of minimum-time problems with bounded controls, the form of the control is maximum effort (bang-bang) throughout the interval of operation (Ref 13:247). To find the optimal control solution to the problem at hand, the optimal control theory results stated above, and a linear transformation of the state variables in equation 56 are all that are necessary.

Although the time response of equation 56 can easily be found, a convenient closed-form solution for x_2 (or R) in terms of x_1 (or V) is not readily obtained. Such a relationship is very useful for finding an extremal control. A convenient method for obtaining a closed form solution is to decouple the two states in equation 56 such that the following form is obtained

$$\dot{z} = \begin{bmatrix} \dot{z}_1 \\ \dot{z}_2 \end{bmatrix} = \begin{bmatrix} \lambda_1 & 0 \\ 0 & \lambda_2 \end{bmatrix} \begin{bmatrix} z_1 \\ z_2 \end{bmatrix} + \begin{bmatrix} 1 \\ 1 \end{bmatrix} u \quad (57)$$

where λ_1 and λ_2 are the eigenvalues of A in equation 56. The above form allows z_2 to be written in terms of z_1 by the following manipulations

$$\frac{\dot{z}_2}{z_1} = \frac{\lambda_2 z_2 + u}{\lambda_1 z_1 + u} \quad (\lambda_1 z_1 + u \neq 0) \quad (58)$$

or

$$(\lambda_2 z_2 + u) \left(\frac{dz_1}{dt} \right) = (\lambda_1 z_1 + u) \frac{dz_2}{dt} \quad (59)$$

which implies

$$(\lambda_2 z_2 + u) dz_1 = (\lambda_1 z_1 + u) dz_2 \quad (60)$$

or, more conveniently,

$$\frac{dz_1}{\lambda_1 z_1 + u} = \frac{dz_2}{\lambda_2 z_2 + u} \quad (61)$$

Definite integration can be performed in equation 61 from an initial state, $(z_{10}, z_{20}) = z_0$:

$$\frac{1}{\lambda_1} \int_{z_{10}}^{z_1} \frac{\lambda_1 d\zeta_1}{\lambda_1 \zeta_1 + u} = \frac{1}{\lambda_2} \int_{z_{20}}^{z_2} \frac{\lambda_2 d\zeta_2}{\lambda_2 \zeta_2 + u} \quad (62)$$

Note that u is treated as a constant in the above development. This is possible due to the optimal control theory result stated earlier which assures that the form of the solution is maximum effort (i.e., constant along a trajectory) throughout the interval of operation.

Performing the integration indicated in equation 62,

$$\frac{1}{\lambda_1} \ln(\lambda_1 \zeta_1 + u) \Big|_{z_{10}}^{z_1} = \frac{1}{\lambda_2} \ln(\lambda_2 \zeta_2 + u) \Big|_{z_{20}}^{z_2} \quad (63)$$

which, after some algebraic manipulation, yields z_2 in terms of z_1 as desired:

$$z_2 = \frac{-u}{\lambda_2} + \left(z_{20} + \frac{u}{\lambda_2} \right) \left(\frac{z_1 + u/\lambda_1}{z_{10} + u/\lambda_1} \right)^{\lambda_2/\lambda_1} \quad (64)$$

It is often useful to examine the functional relationship defined by equation 64 in terms of the "phase plane". The phase plane is a 2-dimensional representation of values of z versus z . The relationship between these two variables appears as a set of curves which are frequently referred to as phase trajectories. Reference 10, pages 470 to 479, and reference 9, pages 447 to 457, can be consulted by the interested reader for complete descriptions of linear, time-invariant second order systems in the phase plane. In this report only one of several general cases is considered, that being the case of real eigenvalues (λ_1 and λ_2) with one positive and the other negative.

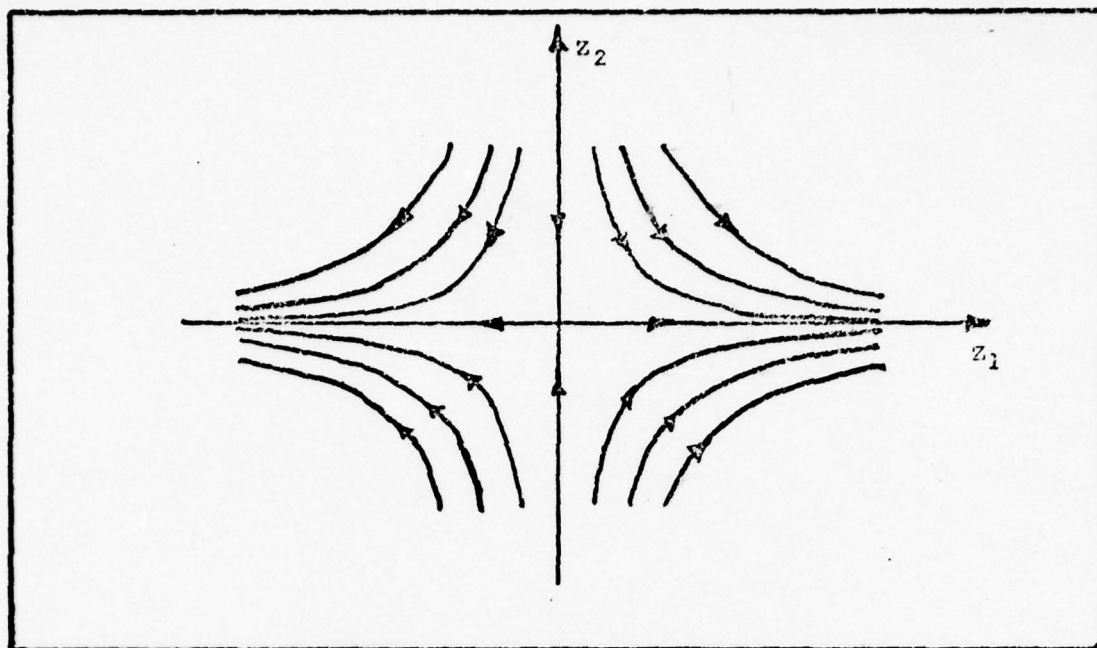


Fig. 17 Phase Plane Trajectories with no Control Inputs

Whenever the state variables of a second-order system are decoupled, as in equation 57, and when the eigenvalues are both real with one positive and one negative, the phase plane trajectories for an unforced system have the form depicted in Figure 17. The origin is referred to as a saddle point, and the z_1, z_2 axes separate the phase plane into four regions of interest. These regions are important because the behavior of the system can be determined from a knowledge of the particular region in which the initial state vector lies. For example, if the initial state of the system is such that z_1 and z_2 are both positive, the system will diverge to the right (i.e., to the condition $z_2 \rightarrow 0$ and $z_1 \rightarrow \infty$). It is important to note that the trajectories are centered at the origin for the *unforced* case, i.e., for $u = 0$ in equation 64. This fact can be seen by inspection of equation 64 directly. Also of interest is the shape of the trajectories when u is not zero but some arbitrary constant.

Rearranging equation 64 slightly is helpful in determining the shapes of the forced trajectories:

$$\left(z_2 + \frac{u}{\lambda_2}\right) = \left(z_{20} + \frac{u}{\lambda_2}\right) \left(\frac{z_1 + u/\lambda_1}{z_{10} + u/\lambda_1}\right)^{\lambda_2/\lambda_1} \quad (65)$$

The form of this equation suggests that an axis translation could be helpful. Letting $z'_2 = (z_2 + u/\lambda_2)$ and $z'_1 = (z_1 + u/\lambda_1)$, equation 65 becomes

$$z'_2 = \left(z_{20} + u/\lambda_2\right) \left(\frac{z'_1}{z_{10} + u/\lambda_1}\right)^{\lambda_2/\lambda_1} \quad (66)$$

The form of this equation is the same as that of 64 except that the constant term multiplying $(z'_1)^{\lambda_2/\lambda_1}$ is different. Thus, these trajectories have the same overall trends as those in Figure 17, but the exact shapes and the location of the origin of these trajectories will vary depending upon the value of u .

Consider now the trajectories in Figure 18, where families of trajectories are sketched for three values of u : $u = +\Omega$, $u = 0$, and $u = -\Omega$. The term Ω is used here to denote the maximum magnitude of the control u . Also shown in Figure 18 is a portion of two particularly important trajectories ($A - 0$, $B - 0$)—those which pass through the origin. Since the optimal control solution must take the state of the system to the origin, these two curves constitute the final trajectory of all solutions. Furthermore, since the optimal solution can have at most $(n - 1)$ switches of the control element, the only task remaining is to determine a scheme which will take an arbitrary initial state to one of these two trajectories with no control switching. When such a trajectory is found, the solution is complete, for, as stated previously in Theorem 1, if an extremal

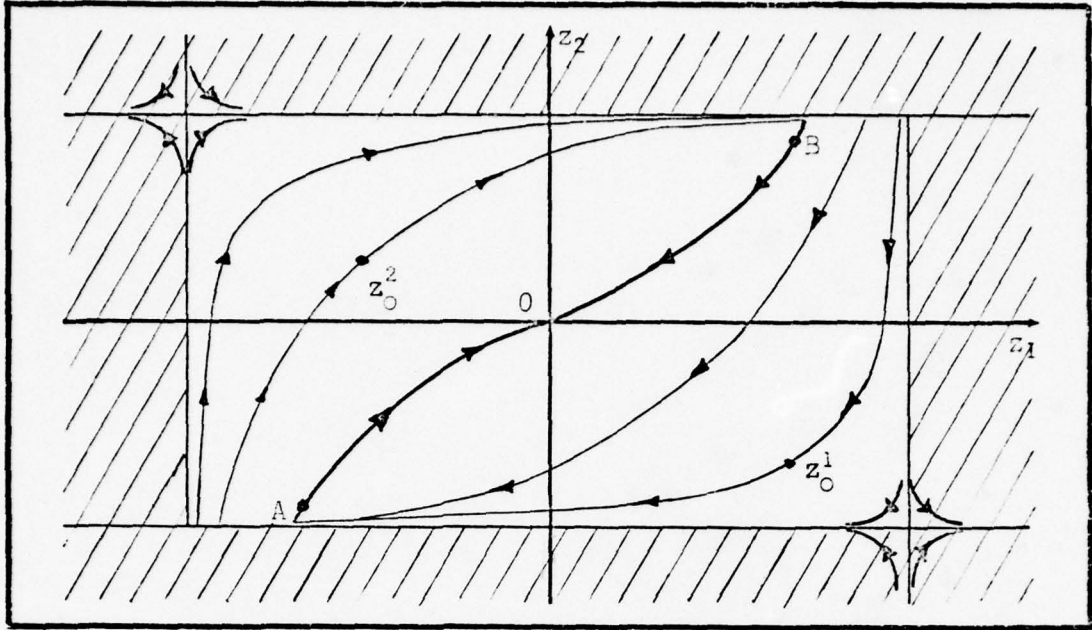


Fig. 18 Phase Plane Trajectories with Constant Control Inputs

control exists it is unique. From the sketch the strategy to be followed is obvious--for an initial state to the left of the combined curves A - O - B, a positive value of u , $+\Omega$, should be applied, while for an initial state to the right of A - O - B, a negative value of u , $-\Omega$, should be applied. Examples of this strategy are shown in the figure by the trajectories which begin at z_0^1 and z_0^2 . A mathematical statement of the foregoing is now developed.

Let the combined curves A - O and O - B be denoted by $S(z_{10})$. In order to determine S as a function of the states, consider the set of initial conditions such that $(z_1, z_2) = (z_{10}, z_{20}) = 0$, and $u = \pm\Omega$. Then equation 65 becomes

$$\frac{\pm\Omega}{\lambda_2} = (z_{20} \pm \frac{\Omega}{\lambda_2}) \left(\frac{\pm\Omega}{z_{10} \pm \frac{\Omega}{\lambda_1}} \right)^{\lambda_2/\lambda_1} \quad (67)$$

which when solved for z_{20} yields

$$z_{20} = \frac{\mp\Omega}{\lambda_2} \pm \frac{\Omega}{\lambda_2} \left(\frac{z_{10} \pm \frac{\Omega}{\lambda_1}}{\pm\Omega} \right)^{\lambda_2/\lambda_1} \quad (68)$$

A more explicit determination of $S(z_{1_0})$ can be made only after values of λ_1 and λ_2 are known. It is a simple matter to define S , given values for Ω , λ_1 , and λ_2 , as is shown later. With $S(z_{1_0})$ determined, the optimal control strategy is

$$\begin{aligned}
 u &= +\Omega : \text{for } z_0 \text{ on A - O portion of S} \\
 u &= +\Omega : \text{for all } z_0 \text{ such that } z_{2_0} > S(z_{1_0}) \\
 u &= -\Omega : \text{for } z_0 \text{ on B - O portion of S} \\
 u &= -\Omega : \text{for all } z_0 \text{ such that } z_{2_0} < S(z_{1_0}) \\
 u &= 0 : \text{if } (z_{1_0}, z_{2_0}) = (0, 0)
 \end{aligned} \tag{69}$$

The technique which has just been developed is now used to develop an optimal control law for the Jindivik. The required steps are: 1) decoupling of the state equations (see equation 55) into the form of equation 57, and 2) derivation of the control law by use of equations 68 and 69.

When all values for the elements in the A and b matrices of equation 56 are computed, the resulting equation is

$$\begin{bmatrix} \dot{V} \\ \dot{R} \end{bmatrix} = \begin{bmatrix} -.188 & -5.23 \\ -.735 & -.267 \end{bmatrix} \begin{bmatrix} V \\ R \end{bmatrix} + \begin{bmatrix} .0123 \\ -.2018 \end{bmatrix} u \tag{70}$$

The values of A were derived in two ways. First, the values were computed directly from the definitions determined earlier in this report for the elements of A. These values were checked by the use of the "LINEAR ANALYSIS" feature of EASY (described in Appendix B), and all values were found to agree within 1%. The b matrix is computed from the definitions for the elements of the matrix which are given immediately following equation 55.

Verification of the simplifying assumptions made in the derivation of this simple state model is achieved to some degree by comparing the eigenvalues of the full 16-state model with those of the A matrix of the 2-state model. Two eigenvalues of the full-state model closely correspond to the 2-state eigenvalues, as shown below:

	2-State Model Eigenvalues	Full-State Model Eigenvalues	Percent Deviation
λ_1	1.734	1.677	3.4%
λ_2	-2.188	-2.302	5.0%

Decoupling of the state equations is now performed by standard techniques (Ref 9:160-163). It is readily verified that the matrix T, whose elements are

$$T = \begin{bmatrix} .2754 & -.2631 \\ -.1012 & -.1006 \end{bmatrix}$$

transforms the coupled equations implied in equation 70 into decoupled equations of the form given in equation 57. The vector z is simply a linear combination of the elements of x:

$$z = T^{-1}x$$

It should be noted here that a decoupled form can always be obtained if the eigenvalues of A are distinct.

The control law is now relatively simple to determine. From equation 68 and the 2-state model eigenvalues, equations for the phase-plane trajectory initial conditions can be written:

$$u = +\Omega : z_{20}^+ = \frac{\Omega}{2.188} - \frac{\Omega}{2.188} \left(\frac{z_{10} + \frac{\Omega}{1.734}}{\Omega} \right)^{-1.262} \quad (71)$$

$$u = -\Omega : z_{20}^- = \frac{\Omega}{2.188} + \frac{\Omega}{2.188} \left(\frac{z_{10} - \frac{\Omega}{1.734}}{\Omega} \right)^{-1.262} \quad (72)$$

The switching curve, S, is now defined for this specific problem:

$$S = \begin{array}{ll} z_{20}^+ & z_{10} < 0 \\ z_{20}^- & z_{10} > 0 \end{array} \quad (73)$$

The optimal control strategy is now explicitly determined:

$$\begin{array}{ll} z_2 = z_{20}^+ & : u = +\Omega \\ z_2 = z_{20}^- & : u = -\Omega \\ z_2 > S & : u = +\Omega \\ z_2 < S & : u = -\Omega \end{array} \quad (74)$$

Since the system is unstable and the control is bounded, there are initial states from which it is impossible to reach the origin. The location of these states is depicted by the shaded areas in Figure 18. Mathematically, a solution to the time optimal control problem is seen to be impossible whenever the initial condition, z_{10} , and the magnitude of the control, u , are such that the values inside the parentheses in equations 71 and 72 are negative.

There are many ways to implement the control law stated in equation 74, but for the purposes of this report the most direct and straightforward method of implementation is sufficient. Figure 19 depicts a block diagram of the simulation model with the yaw control system added.

The same conditions as are used for the bare airframe and airframe with autopilot simulations (see Table II) are used for the yaw control simulations. The purpose of these simulations is to verify that the design of the yaw controller is sufficient to stabilize the Jindivik in flight. Since the purpose here is to demonstrate the validity of the design, only a limited number of simulations are presented.

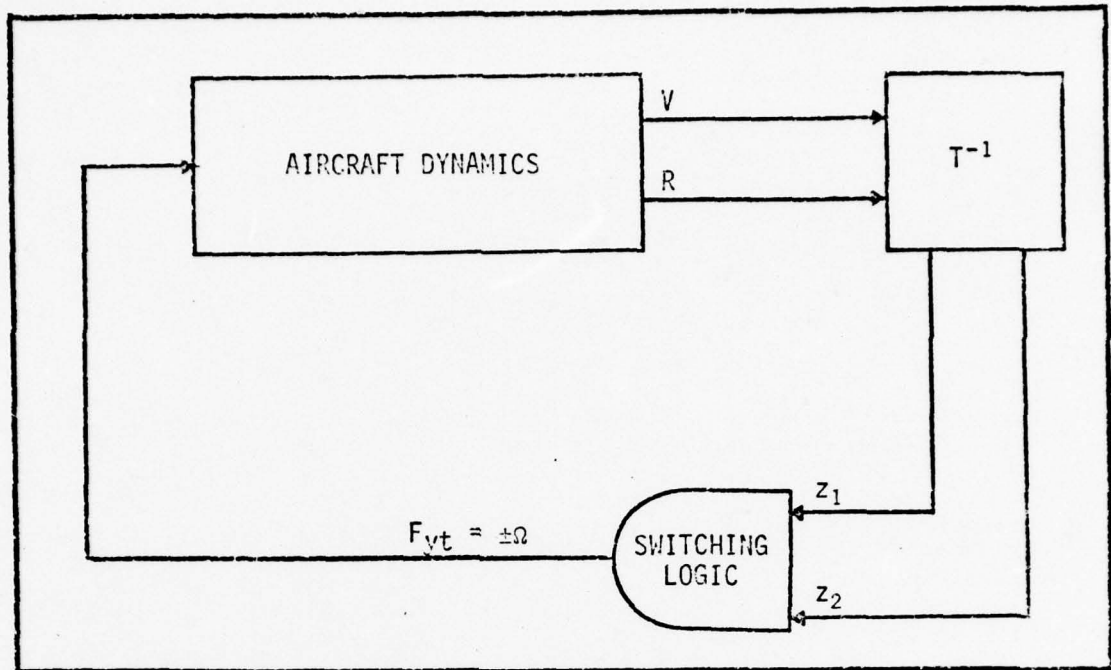


Fig. 19 Block Diagram of Yaw Control System Implementation

The magnitude of the thrust available from the yaw thrusters is assumed to be 50 lbs. It is acknowledged that this value may be somewhat optimistic based upon the information given in Reference 15, but the purpose here is merely to verify the design procedure. Additional simulations can be performed after more extensive information is obtained on the Jindivik yaw thrusters.

The simulations presented here cover four different situations as shown below:

Simulation Number	Initial Sideslip Angle, $\beta(^{\circ})$	Status of Lateral-Directional Coefficients
1	+2	Symmetric
2	+2	Unsymmetric
3	+7	Symmetric
4	+7	Unsymmetric

The meaning of the terms "symmetric," and "unsymmetric," is that the

curves representing the lateral-directional coefficients C_y , C_l , and C_n are all shifted so as to pass through the origin in the symmetric simulation, while these curves represent the actual wind tunnel data in the unsymmetric simulations. Although the controller is designed for the symmetric case, the simulations demonstrate that the controller functions adequately even when the vehicle is in an unsymmetric configuration, so long as the initial sideslip angle is not too large.

Initial conditions of 2° and 7° for sideslip angle, β , are used to illustrate, 1) the effects of the nonlinear C_n vs β characteristics on the performance of the yaw controller, and 2) that there is an upper limit on the value of sideslip angle which the controller can tolerate.

The first simulation results are presented in Figures 20 through 22. Figure 20 demonstrates the immediate return of sideslip angle, β , to a stable value of 0° and the accompanying build-up of yaw rate. This figure illustrates the dramatic improvement of the stability of the system accomplished by the yaw controller. The basic airframe simulation, and the airframe/autopilot combined simulation, (Figures 9 and 13) indicate a value of β of 7.5° and 12.5° respectively at $t = 2$ sec, whereas the sideslip angle with yaw control is zero for all $t > 1$. sec.

Figure 21 is presented here to demonstrate that the orientation of the aircraft with respect to the earth is well behaved. Unlike the simulation results in Figures 8 and 12, the roll, pitch, and yaw angles are reasonably constant with the yaw control system engaged.

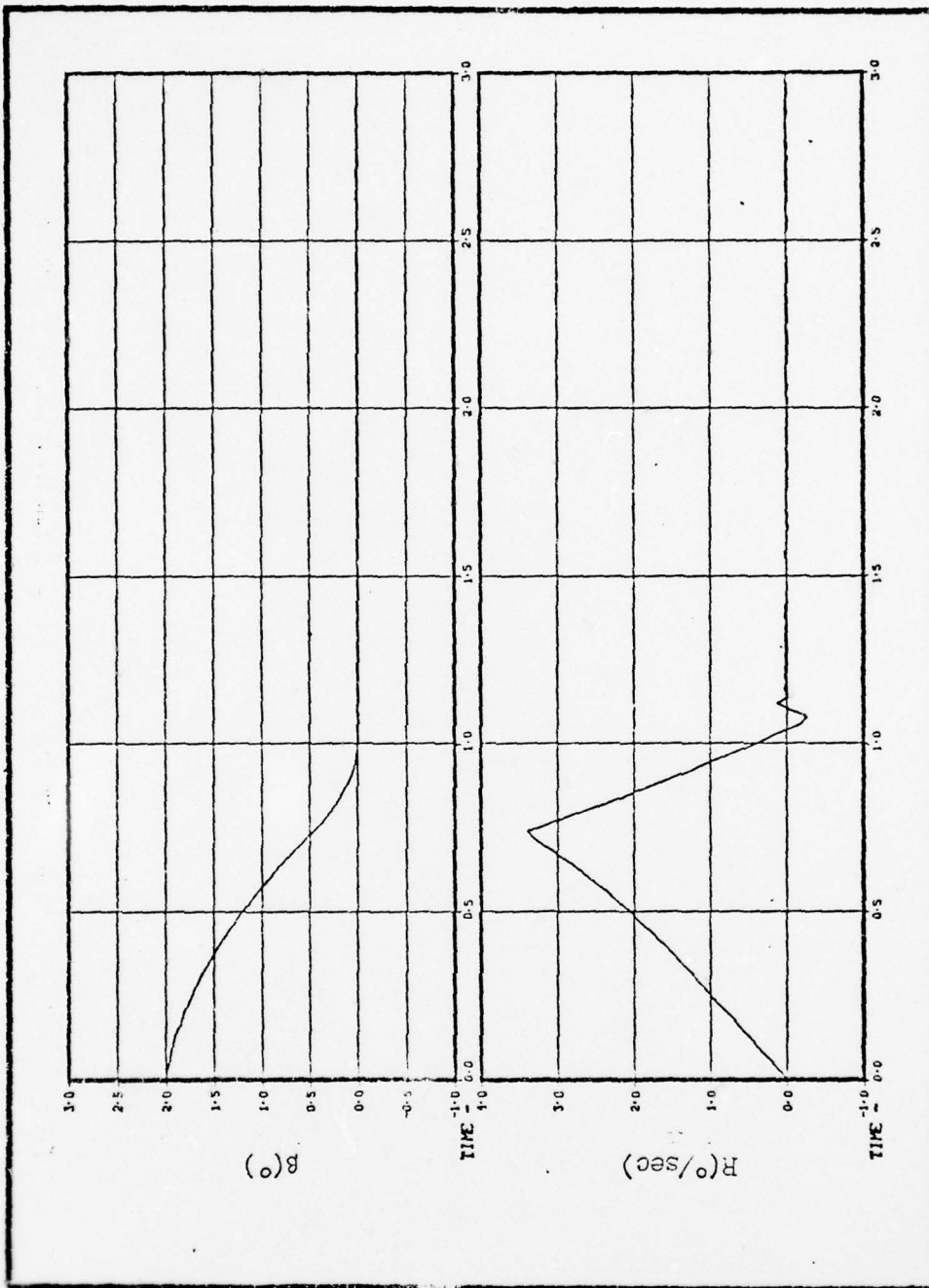


Fig. 20 Time Histories of Sideslip Angle and Yaw Rate in Yaw Control Simulation Number 1

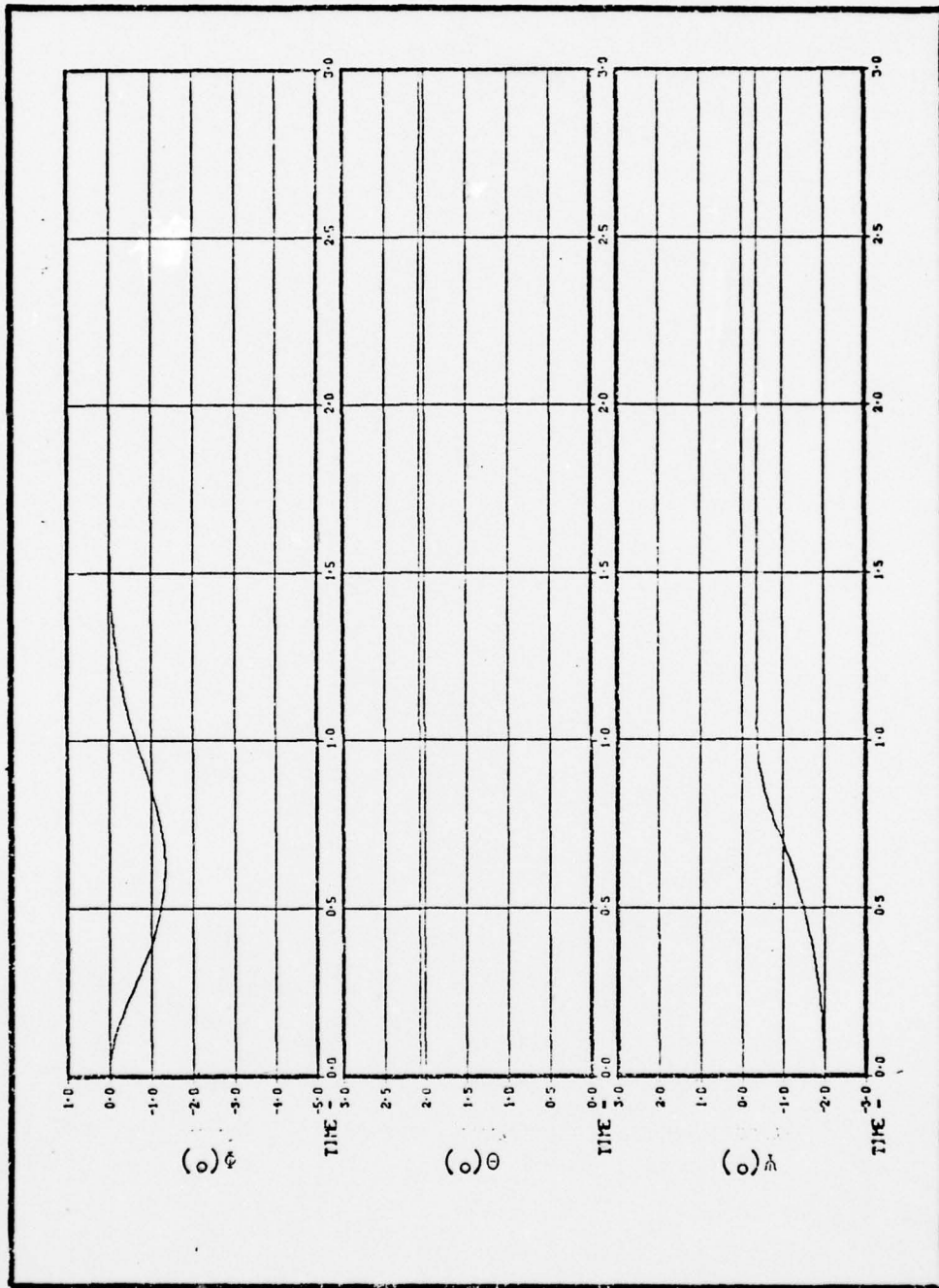


Fig. 21 Time History of the Orientation of the Aircraft
 in Yaw Control Simulation Number 1

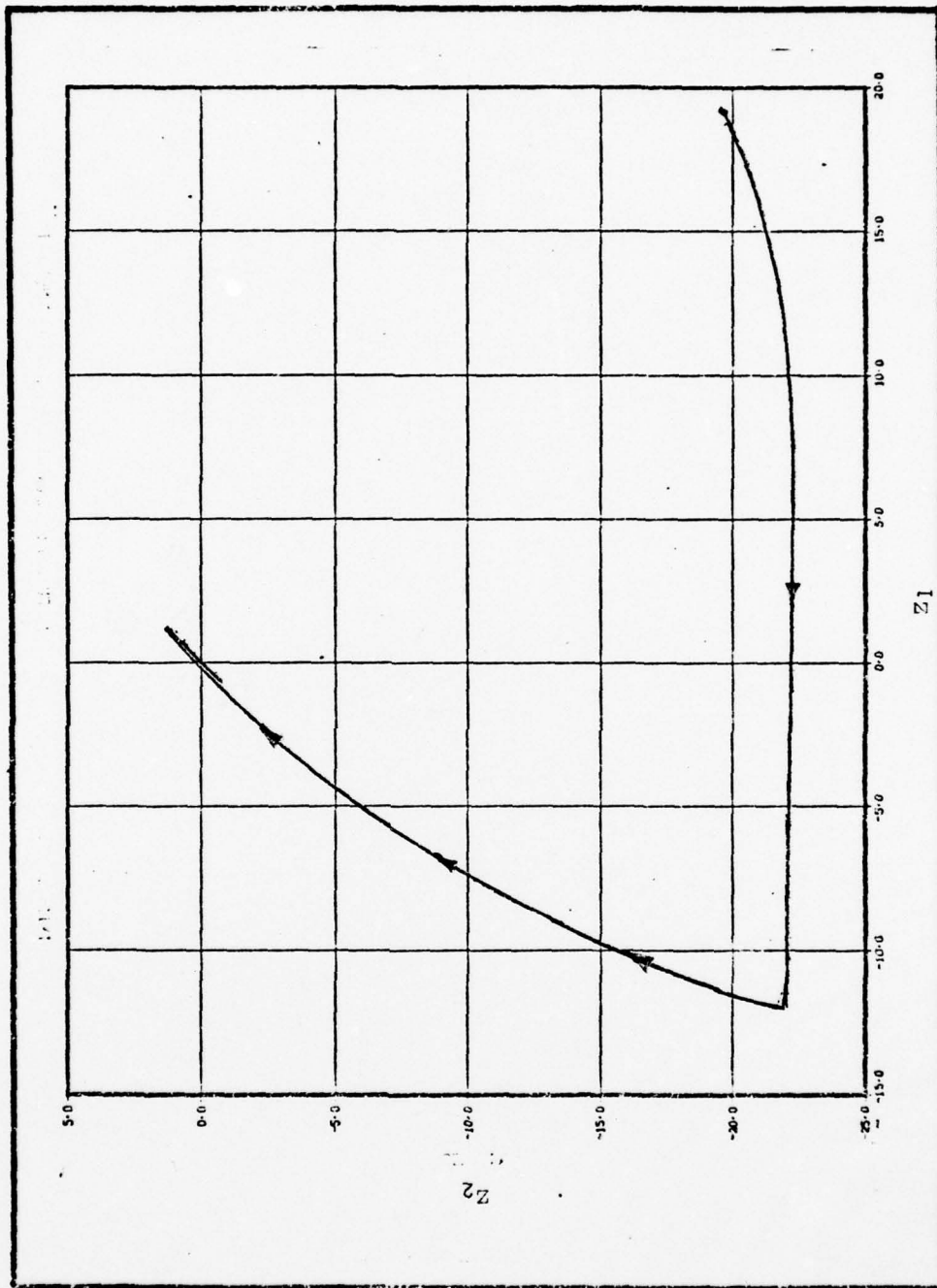


Fig. 22 Phase-Plane Trajectory for Yaw Control Simulation Number 1

Figure 22 depicts the phase-plane trajectory for this simulation. The variables z_2 and z_1 in this figure represent elements of the vector z which is defined earlier in the design phase by

$$z = T^{-1}x$$

The initial state of z , z_0 , is below the switching curve, S , and therefore a negative yaw thruster force is commanded. The state changes along a trajectory towards the switching curve until the switching curve is encountered, at which time the yaw thruster force is switched to a positive value. While the 2-static linear model is designed to yield no overshoot of the origin, the 16-state nonlinear model does overshoot the origin slightly.

The results of the second simulation are presented in Figures 23 through 25. The unsymmetric model is used in this simulation to illustrate the effects of non-zero values of C_y , C_l , and C_n at $\beta = 0^\circ$. Although a stable situation is reached at $t = 2.6$ sec, the constant side force, rolling moment, and yawing torques significantly reduce the effectiveness of the yaw control system. The orientation of the aircraft, as depicted in Figure 24, appears to be entirely acceptable in this simulation. Figure 25 is the phase-plane portrait for this simulation.

For simulation number 3 a larger initial value of β is chosen such that the C_n versus β curve is well out of the linear range ($-2^\circ \leq \beta \leq 2^\circ$). The nonlinearity does not significantly degrade the effectiveness of the yaw control system, as β steadily decreases to 0° and both β and R are stabilized with 2.5 sec. The aircraft orientation can be seen to be well controlled in Figure 27. The phase plane portrait is shown in Figure 28.

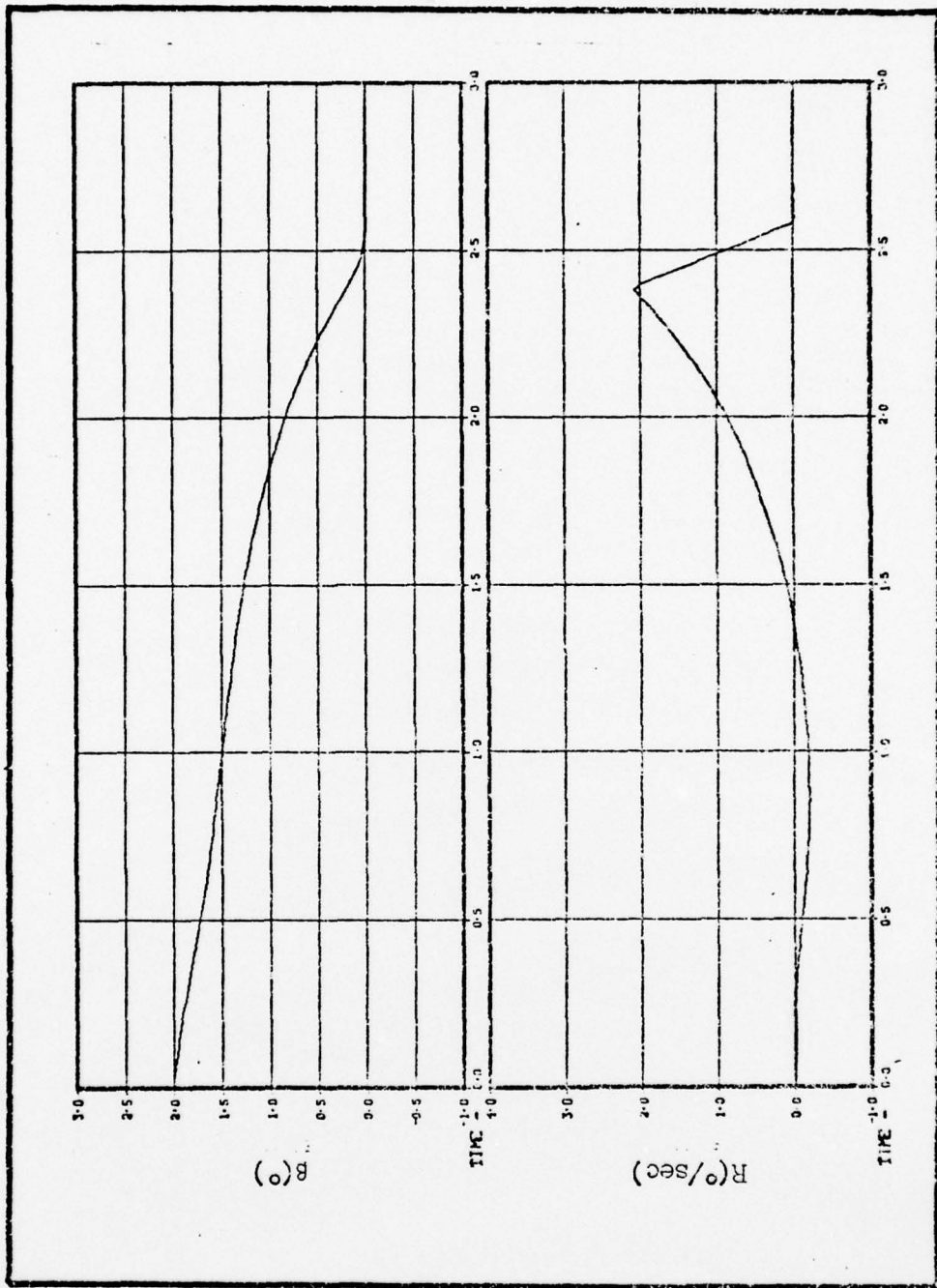


Fig. 23 Time Histories of Sideslip Angle and Yaw Rate in Yaw Control Simulation Number 2

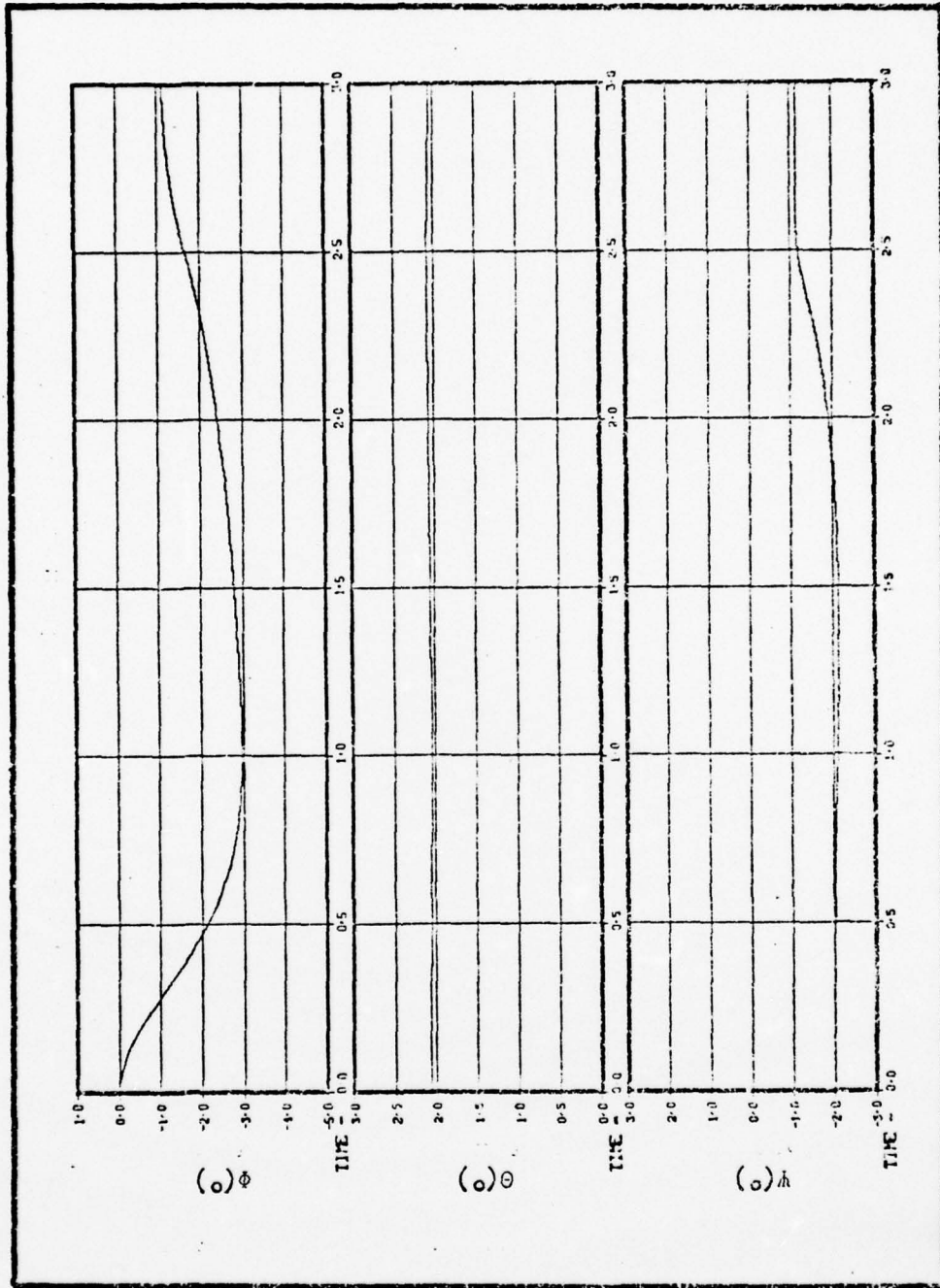


Fig. 24 Time History of the Orientation of the Aircraft
in Yaw Control Simulation Number 2

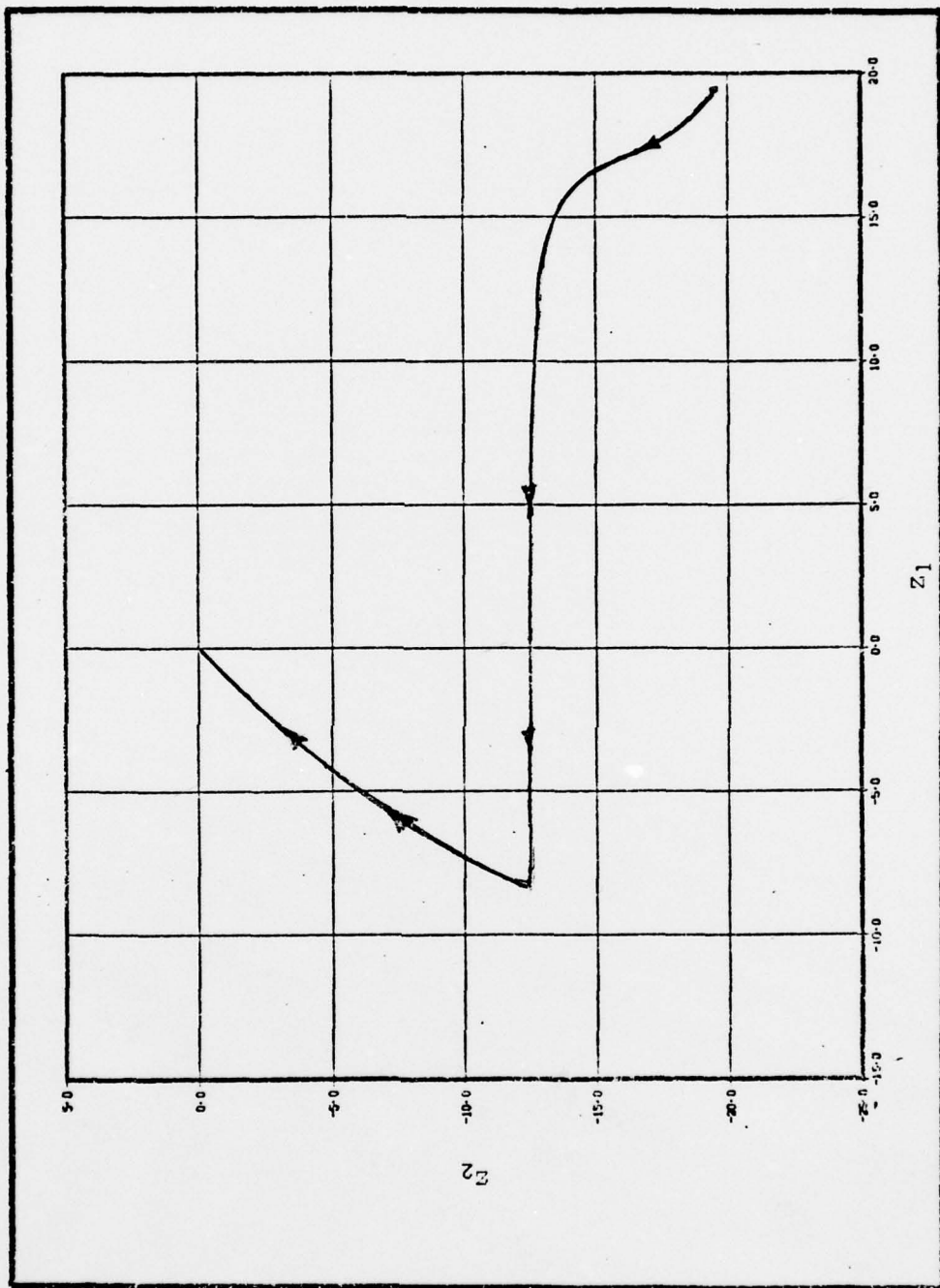


Fig. 25 Phase-Plane Trajectory for Yaw Control Simulation Number 2

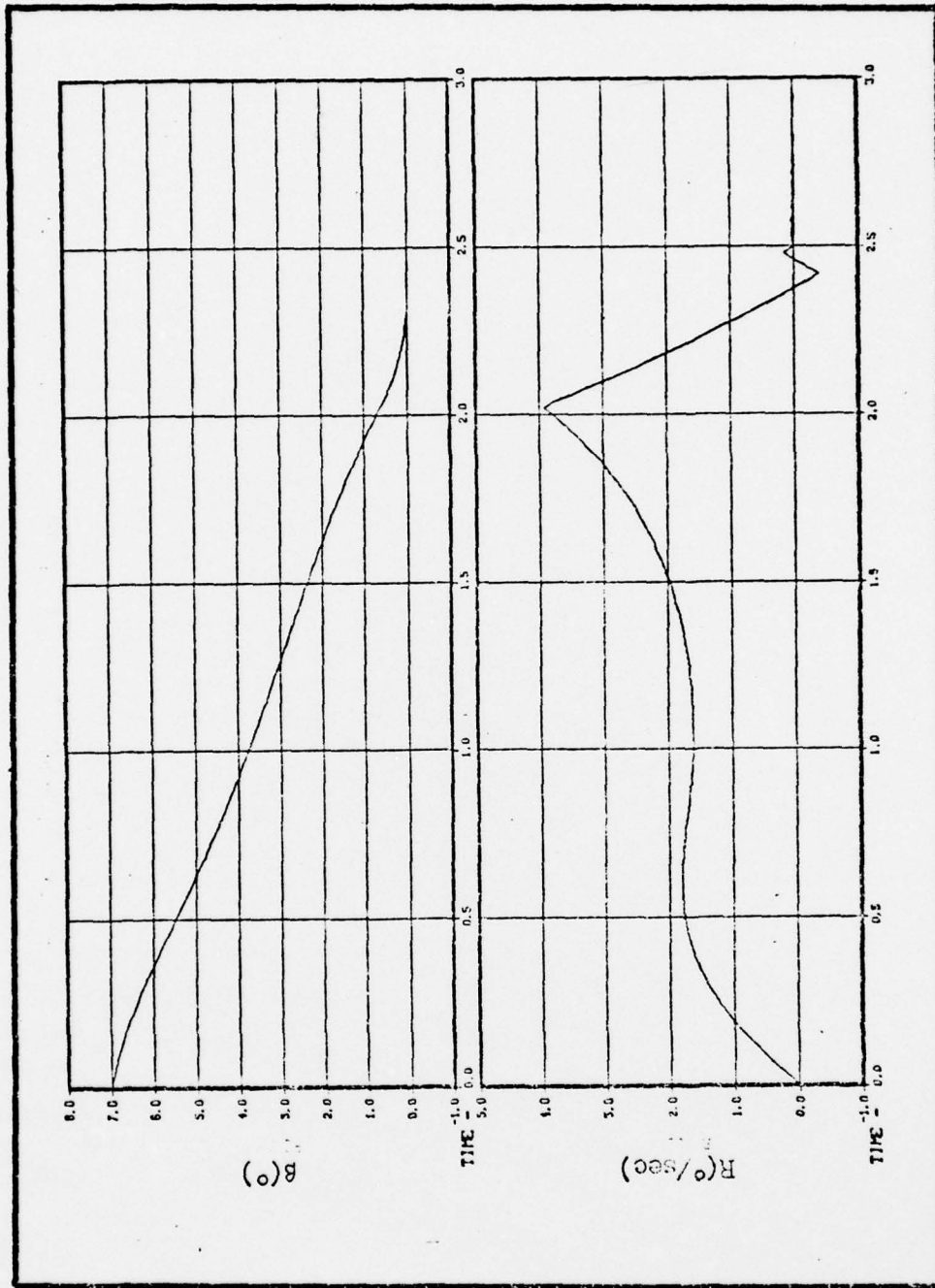


Fig. 26 Time Histories of Sideslip Angle and Yaw Rate in Yaw Control Simulation Number 3

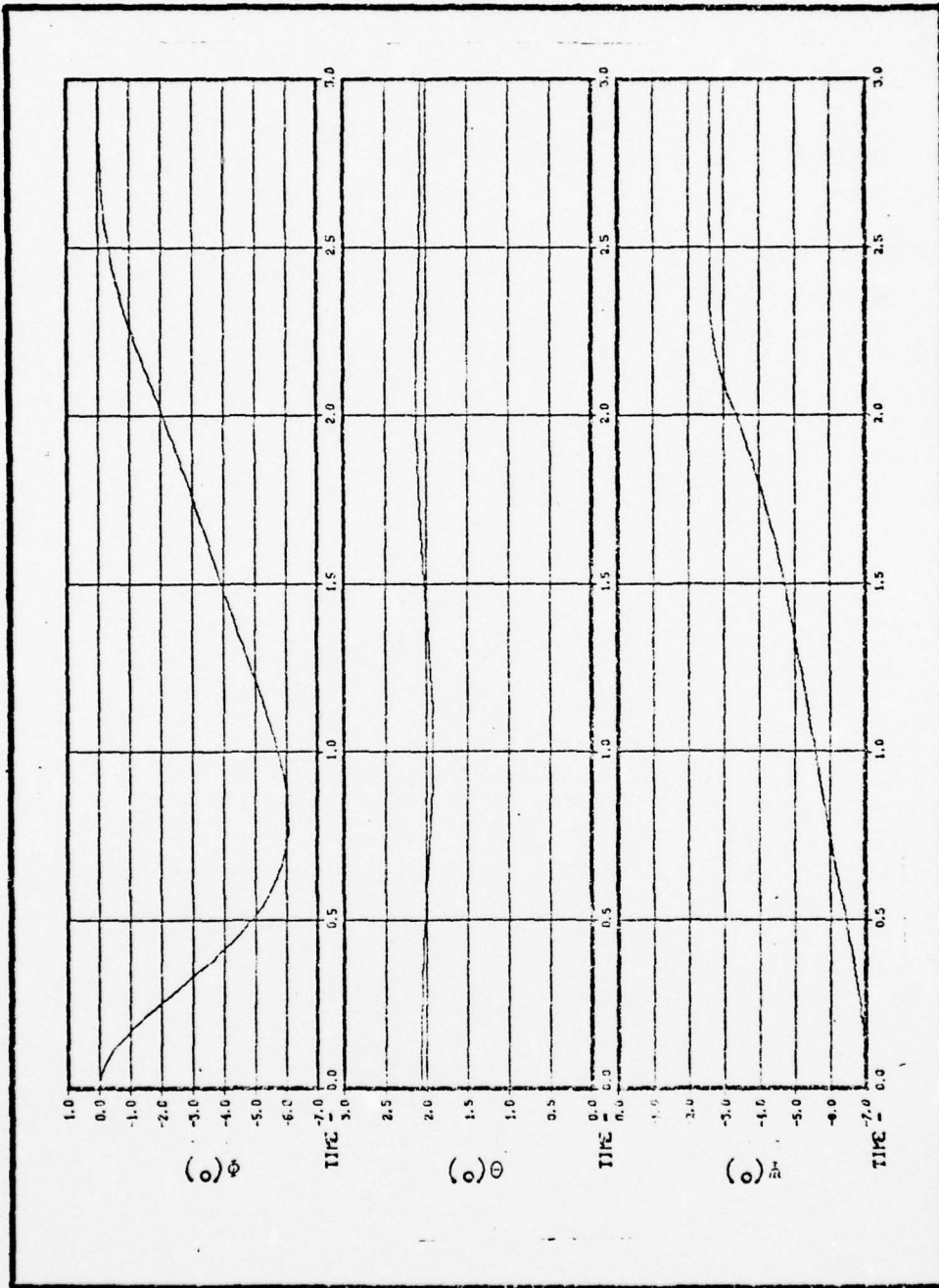


Fig. 27 Time History of the Orientation of the Aircraft in Yaw Control Simulation Number 3

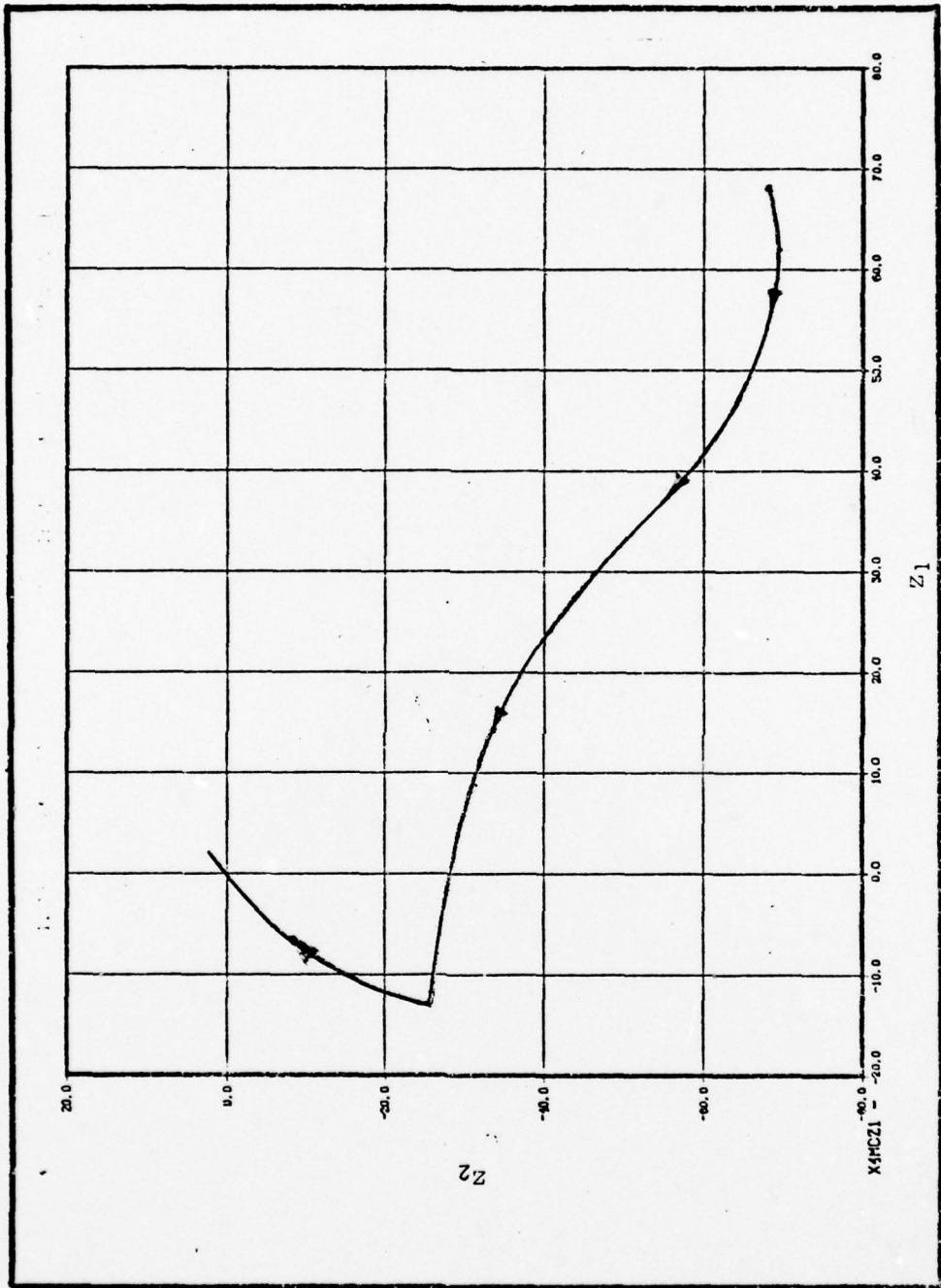


Fig. 28 Phase-Plane Trajectory for Yaw Control Simulation Number 3

The final simulation results are presented in Figures 29 through 31. An initial value of $\beta = 7^\circ$ is used for this simulation, as it is for simulation number 3, but the unsymmetric model is simulated here. The shift in the C_n versus β curves (Figures A-9 through A-12) are such that a higher value of C_n is prevalent for any given value of β . This increase is too large for the yaw control system to tolerate, even though the correct control is commanded by the control system ($u = -\Omega$). Sideslip angle begins to decrease in Figure 29, but upon reaching a value of approximately 5.5° the value of C_n is near its minimum value (see Figure A-10). At the value of velocity chosen for this simulation, 300 ft/sec, the minimum value of C_n is approximately given by

$$C_{n_{\min}} = \bar{q} S b C_{n_{\alpha}} = 2.2^\circ = (107)(76)(19)(-.004) = -618 \text{ ft-lb} \quad (76)$$

which is 118 ft-lb greater in magnitude than the maximum magnitude of the yaw controller (500 ft-lb). Figures 30 and 31 further describe the unfortunate situation which results from having too little control authority to meet the destabilizing yaw characteristics of the Jindivik.

Conclusions

The simulation results depicted in Figures 8, 9, 12, and 13 vividly illustrate a lack of stability in both the bare airframe and the airframe combined with the existing autopilot. There is certainly no reason to have expected the existing autopilot to cope with the new aerodynamic characteristics which have resulted from the addition of an ACRS. The existing autopilot performs well, however, if the yaw is controlled, as illustrated by the simulation results in Figures 10 and 11.

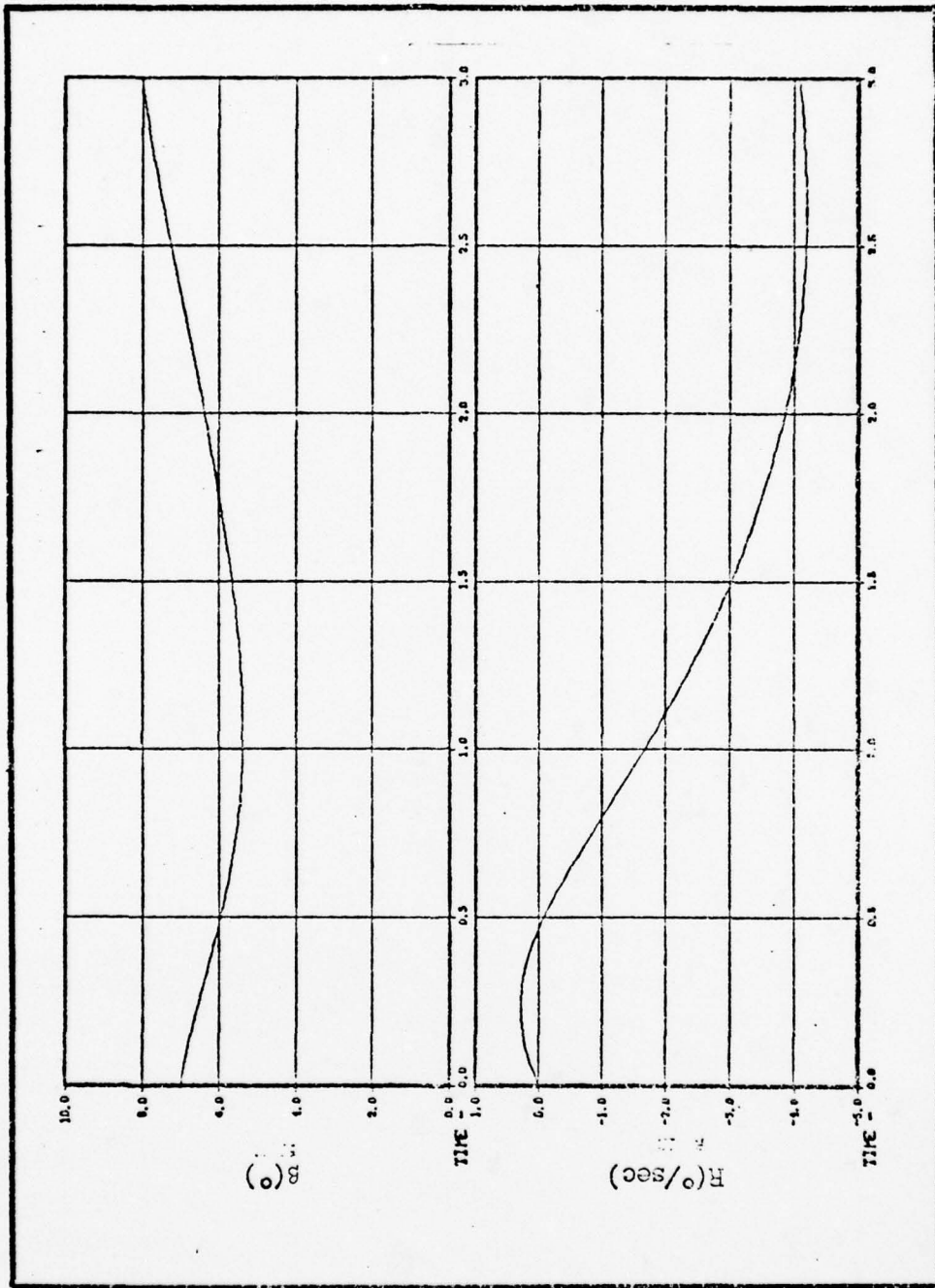


Fig. 29 Time Histories of Sideslip Angle and Yaw Rate in Yaw Control Simulation Number 4

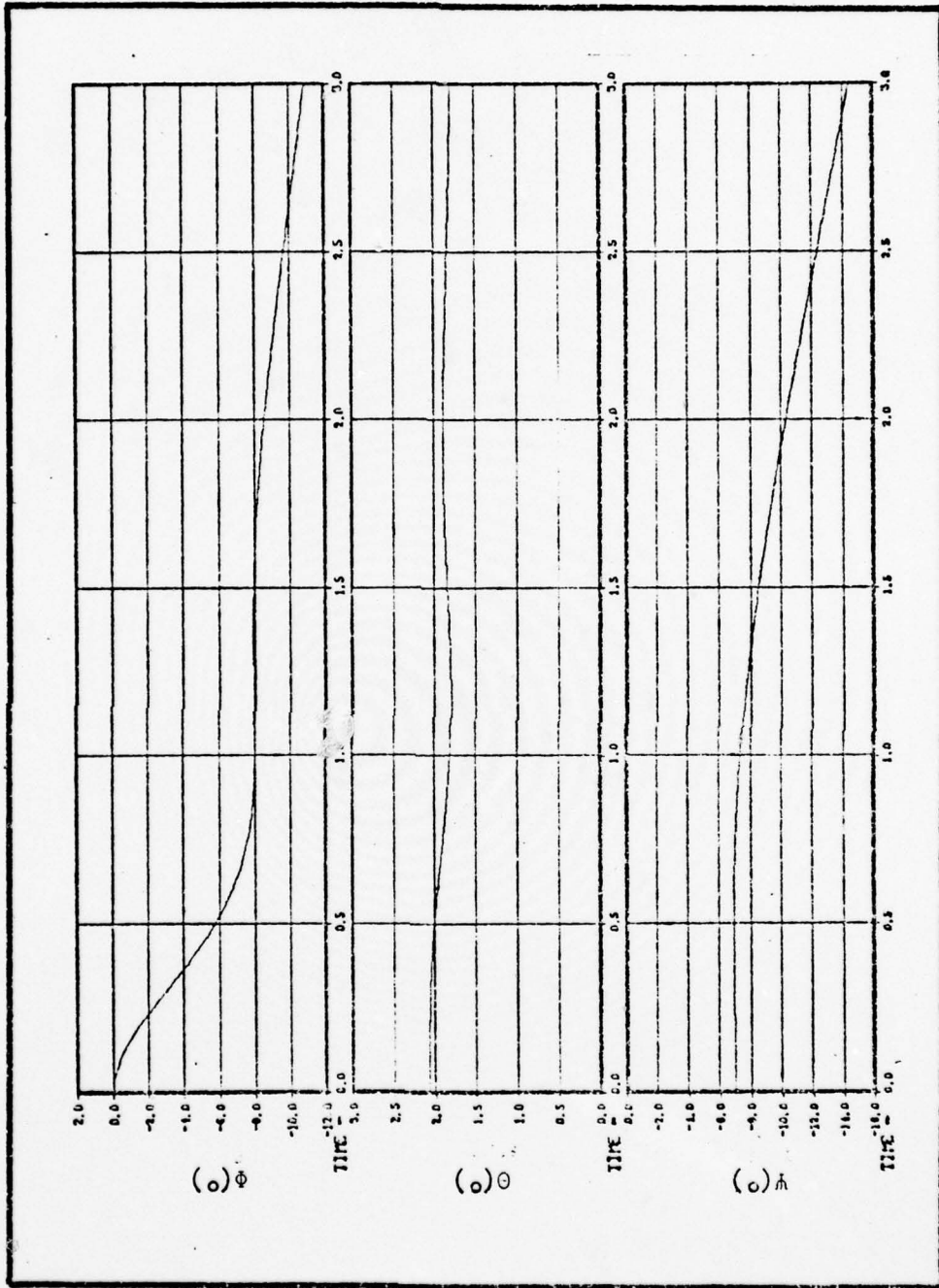


Fig. 30 Time History of the Orientation of the Aircraft
in Yaw Control Simulation Number 4

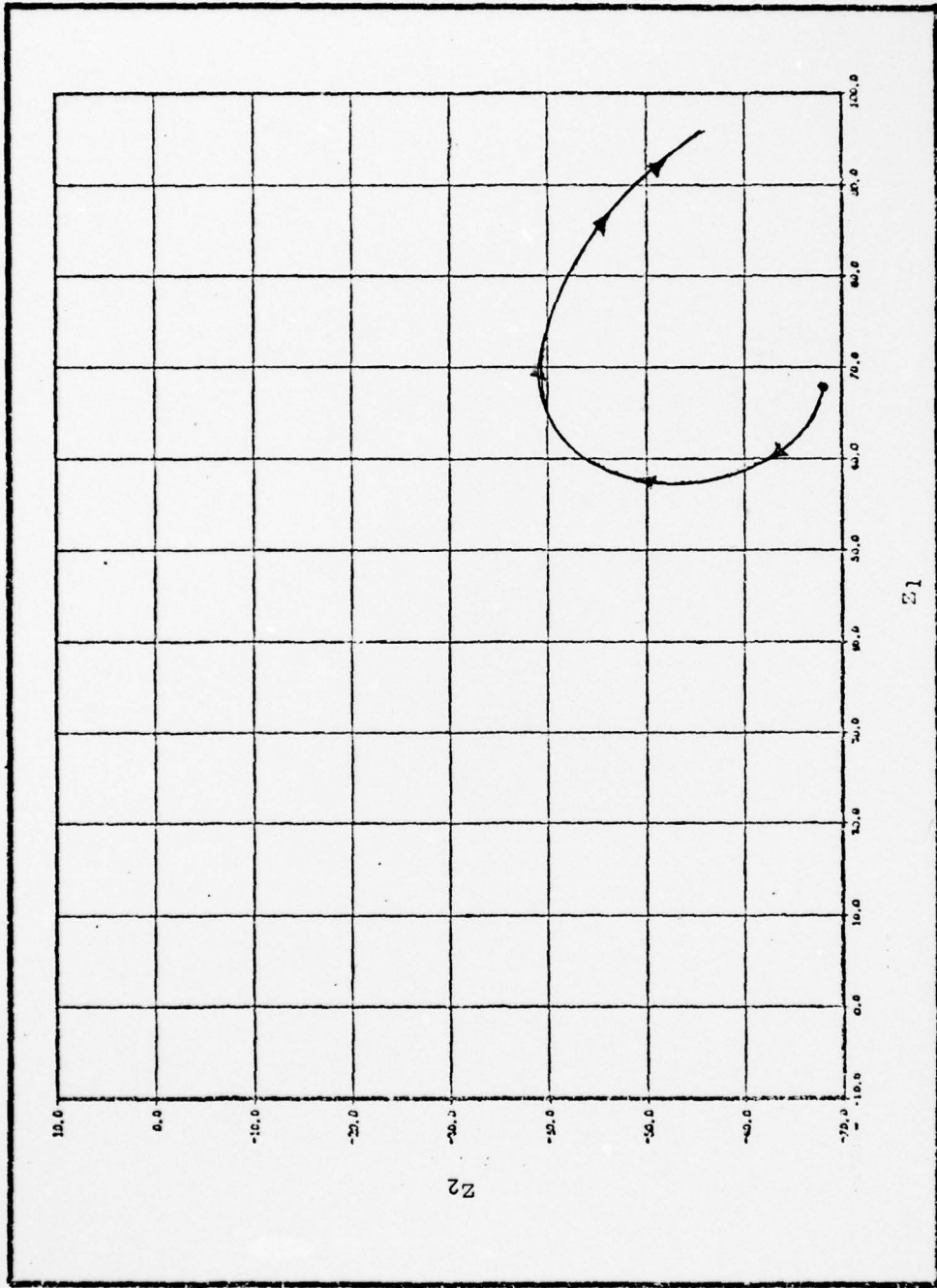


Fig. 31 Phase-Plane Trajectory for Yaw Control Simulation Number 4

AD-A057 434

AIR FORCE INST OF TECH WRIGHT-PATTERSON AFB OHIO SCH--ETC F/G 1/3
AN ANALYSIS OF THE STABILITY OF AN AIRCRAFT EQUIPPED WITH AN AI--ETC(U)
MAR 78 M A STAFFORD

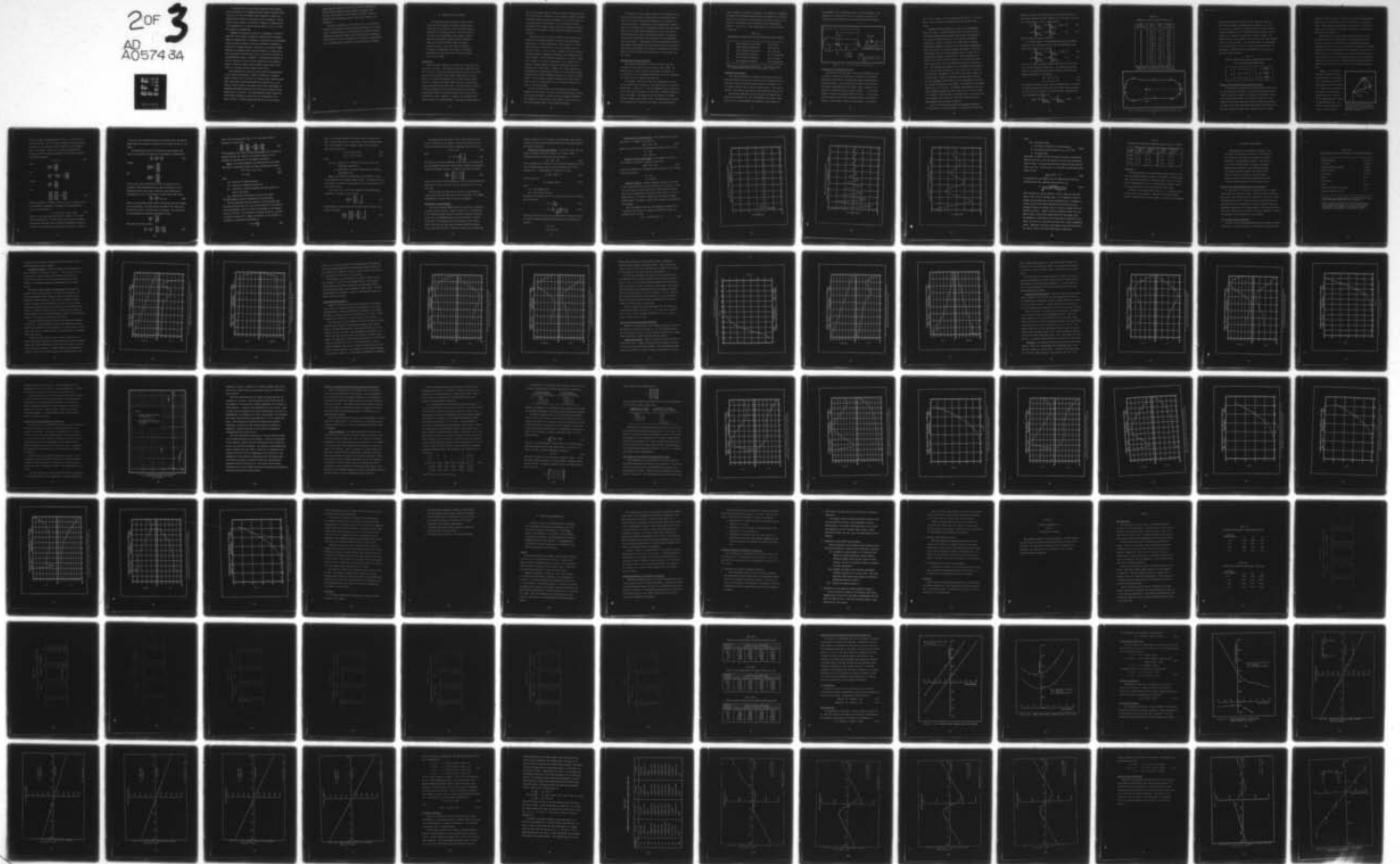
AFIT-GGC-EE-78M-5

NL

UNCLASSIFIED

2 OF 3

AD A0574 34



To control the yaw, a yaw control system has been designed which, when added to the original autopilot design (original except for the R , \dot{R} , and \ddot{R} feedback loops discussed in Chapter II) stabilize the aircraft at one specific set of conditions. Limitations do exist, however, as depicted in Figures 29 through 31, but if the magnitude of β is kept relatively small ($-2^\circ \leq \beta \leq 2^\circ$) the yaw controller performs well.

Although the simulation results are encouraging, it should be noted that a full range of operating conditions must be examined before an implementation is attempted. Particularly, the performance of the yaw control system in turns and at different airspeeds is likely to be somewhat degraded. Since there is a specific angular velocity, \dot{R} , associated with a given bank angle in a steady state turn, a provision for achieving a value of \dot{R} should be included in an implementation design. Variation in airspeed will probably be less of a problem for the yaw control system since the variation cannot be very much (from a typical traffic pattern speed of 300 ft/sec to a typical touch-down speed of 200 ft/sec).

Other applications of the yaw control system design discussed in this chapter are possible. While the Jindivik is a somewhat unusual aircraft due to its lack of a movable rudder, aircraft which have conventional rudder systems might also profitably use a yaw thruster control system. The addition of an ACRS could produce undesirable aerodynamic characteristics which are too severe for the rudder alone to cope with. The design procedure herein would need to be modified somewhat to account for the contribution of the rudder, however. Another possible application of the yaw control

design discussed herein is in the case of vertical takeoff and landing (VTOL) aircraft and short takeoff and landing (STOL) aircraft. These types of aircraft need yaw control at very low airspeeds where conventional means of yaw control (rudders) are ineffective.

The major contributions of this chapter are, 1) the identification of an aerodynamic problem caused by the addition of an ACRS, and 2) a proposed solution to this problem for a specific aircraft. Problem areas might also exist in the slideout phase of operation; thus, Chapters IV and V are devoted to, 1) building a landing model, and 2) investigating the Jindivik's stability during the slideout.

IV. MODELING OF THE ACRS TRUNK

The aerodynamic model developed in Chapter II provides a means of computing aerodynamic forces during simulations of the slideout. These aerodynamic forces constitute an appreciable portion of the total force on the vehicle at the beginning of the slideout. Ground reaction and frictional forces, however, predominate toward the end of the slideout where the dynamic pressure is small. Thus, this chapter is devoted to developing a mathematical model capable of computing ground friction and reaction forces which act through the trunk of an ACRS.

Introduction

Several different approaches to developing a trunk model have been used in the past. The simplest models have assumed the trunk to act as a set of two linear torsional springs (one for roll motion and one for pitch motion) and a single linear spring (for heave motion, i.e., vertical translation of the center of mass) (Refs 3 and 21). A slightly more complex model has also been used which assumed nonlinear springs (Ref 17:86). The most elaborate attempts to model the dynamics of an air cushion device are those which mathematically describe the pressure distribution and air flow in and around the trunk. Reference 5, pages 3 to 13, presents the salient features of several attempts to describe the trunk pressure

and air flow mathematically in order to predict the dynamics of the air cushion system. Reference 5 also presents a sophisticated ACRS model which takes into account deformation of the trunk as well as air supply system characteristics. As in many other modeling problems, the more complex models tend to have enhanced predictive capability at the expense of time and effort required to generate the model.

While there often is need for a precise model, there is good motivation for using the simplest of models, the linear spring/damper model, in certain applications. The slideout of an ACRS-equipped vehicle is claimed to be one such application for the following reasons. First, the rate of change of vehicle orientation is typically small throughout the slideout, except during and just after touchdown. Certain external conditions could produce a rapid rate of change of the vehicle orientation (e.g., severe gusts or irregular landing surfaces), and these conditions should not be analyzed with a linear model. Secondly, if a control system is to be designed for an ACRS-equipped vehicle, the most dominant characteristics of the ACRS are probably sufficient to design the control system. Once the control system is designed, the control system could be used in a simulation with a more elaborate trunk model in order to verify the design.

Due to the limited amount of time available for conducting research for this report, the scope of the research has been limited to slideouts beginning at a point just after touchdown transients have damped out. This portion of the slideout allows the use of a linear spring-damper model in the slideout simulation.

The remainder of this chapter consists of the development of a linear trunk model which is combined with the aerodynamic model in Chapter V in order to analyze the performance of the Jindivik in the slideout phase. A description of some experimentally obtained data is the starting point for building the model, since the dynamic behavior of the model should resemble that of the actual system. After presenting this data some pertinent geometry is introduced, followed by an explanation of the placement of the spring-damper units in the model. A description of the forces produced by spring displacement, displacement rate, and sliding friction is then given. Finally, the model dynamics are shown to be essentially the same as those of the actual ACRS-vehicle combination in heave, pitch, and roll modes.

Experimentally Obtained Trunk Data

Unpublished, experimentally obtained trunk data was made available for this report by the Air Cushion Group, AFFDL. The methods used to obtain this data are described in Reference 21. As a value for the heave damping coefficient, C_H , was not available, the value of C_H for a similar trunk was used.

In addition to the data in Table III, representative values for the coefficient of friction, μ , were supplied by the Air Cushion Group/AFFDL. A value of $\mu = .3$ was recommended for the forward 1/3 of the trunk since this portion of the trunk is partially supported by an air cushion. The purpose of the air cushion is to reduce friction forward of the center of mass. By shifting the frictional force towards the aft portion of the trunk, a more directionally

stable situation is obtained in slideouts. This increase in stability is derived from restoring yaw moments which are produced by frictional forces aft of the center of mass whenever the velocity vector of the vehicle is not aligned with the longitudinal axis during ground contact. A value of $\mu = .8$ was recommended for the aft 2/3 portion of the trunk.

Table III

EXPERIMENTALLY OBTAINED DATA FOR THE JINDIVIK ACRS TRUNK NUMBER 2

K_H	Heave Stiffness Coefficient	12,300 lb/ft
C_H	Heave Damping Coefficient*	480 lb-sec/ft
K_P	Pitch Stiffness Coefficient	1252 ft-lb/deg
C_P	Pitch Damping Coefficient	24.7 ft-lb-sec/deg
K_R	Roll Stiffness Coefficient	90.4 ft-lb/deg
C_R	Roll Damping Coefficient	8.65 ft-lb-sec/deg

*Value was not calculated for ACRS No. 2. This value is taken as a representative value based on data given in Ref 21.

Description of the Trunk

The trunk is constructed of neoprene coated nylon fabric with tire tread rubber 3/8 inch thick along the entire underside (Ref 17). Nozzles are drilled through the brake tread in the forward 1/3 of the trunk to provide the air cushion discussed above. The trunk is mounted on the Jindivik such that the equilibrium pitch angle is 0°.

The pertinent dimensions of the trunk given in Figure 32 are obtained from Reference 18. The curve formed by the center of the brake tread is used throughout the remainder of this report for

the placement of all spring-damper units, with one exception. The exception is a spring-damper unit that supplies a portion of the total heave force, and which is located at the center of pressure.

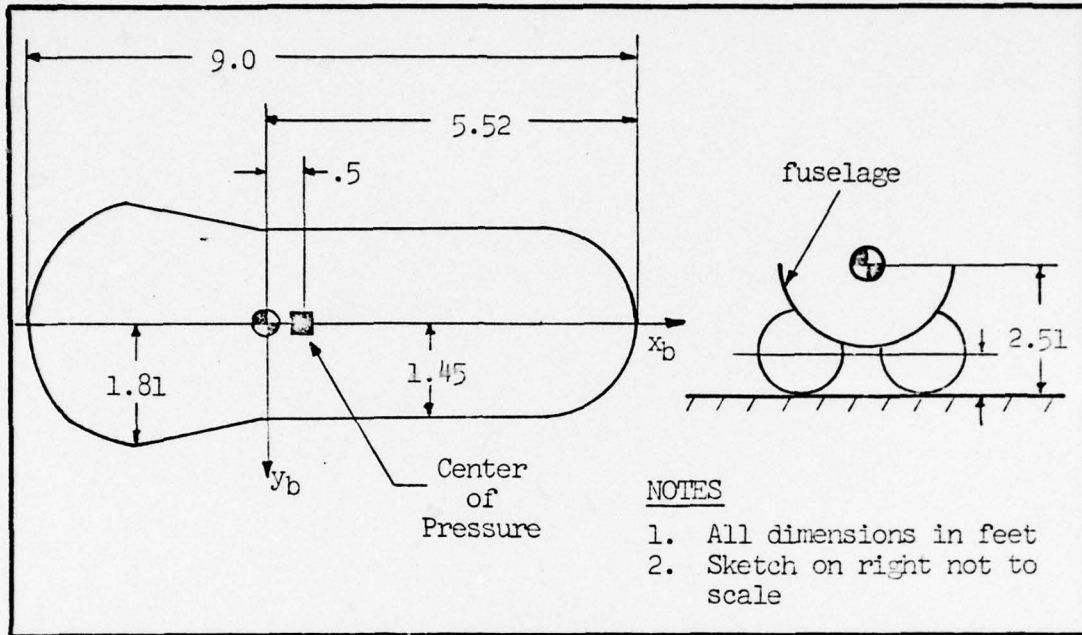


Fig. 32 Geometry of the Jindivik ACRS Number 2

Placement of the Spring-Damper Units

Although there are many ways to place the spring-damper units in order to represent the ACRS-vehicle combination, any specific arrangement should have the following particular characteristics. First and foremost, the arrangement must exhibit the same static and dynamic characteristics as the actual ACRS. Secondly, there should be a sufficient number of units in order to represent adequately the shape of the brake-tread center line, since distances from the center of mass affect the torques acting on the vehicle. Finally, a representative number of spring-damper units must be

used for the forward 1/3 of the tread area and the aft 2/3 of tread area in order to account for differences in the friction coefficients.

Following the above guidelines, a total of 14 spring-damper units was chosen. In order to meet both roll and pitch stiffness and damping coefficients, individual units around the periphery of the trunk are allowed to have one of two stiffness and damping coefficients. Seven of the units are located near the extreme forward and extreme aft portions of the trunk--these spring-damper units are referred to as "pitch" springs and dampers. Another six spring-damper units are located primarily along the sides of the trunk and are referred to as "roll" units. The fourteenth unit is located at the static center of pressure of the trunk (that point through which all of the force produced by pressure is assumed to act). The stiffness and damping of this fourteenth unit, referred to as the heave spring-damper unit, are chosen so as to bring the total stiffness and damping of all units to the correct values for the heave mode. Figure 33 describes a placement which satisfies all the requirements stated above, and this arrangement is used for all slideout simulations in this report. The labeling of the spring damper units is as follows: 1) peripheral spring-damper units are given increasing numbers from fore to aft, 2) a P or an S is added to the number to identify port or starboard units, 3) the heave unit is designated as unit number 88. The exact locations of these spring-damper units are given in Table IV.

Values for stiffness coefficients and damping coefficients are obtained in the following manner. If angular deflections are

assumed to be small, the following set of equations describes the relationships between stiffness coefficients of the pitch, roll, and heave springs (k_p , k_r , and k_h , respectively):

$$k_p \Sigma x_i^2 \left. \begin{array}{l} \text{pitch} \\ \text{springs} \end{array} \right\} + k_r \Sigma x_i^2 \left. \begin{array}{l} \text{roll} \\ \text{springs} \end{array} \right\} + k_h x_{88}^2 = K_P \quad (77)$$

$$k_p \Sigma y_i^2 \left. \begin{array}{l} \text{pitch} \\ \text{springs} \end{array} \right\} + k_r \Sigma y_i^2 \left. \begin{array}{l} \text{roll} \\ \text{springs} \end{array} \right\} = K_R \quad (78)$$

where K_P and K_R are given in Table III.

In a similar manner, the relationships between pitch damping coefficient, roll damping coefficient, and the individual spring damping coefficients can be written

$$c_p \Sigma x_i^2 \left. \begin{array}{l} \text{pitch} \\ \text{springs} \end{array} \right\} + c_r \Sigma x_i^2 \left. \begin{array}{l} \text{roll} \\ \text{springs} \end{array} \right\} + c_h x_{88}^2 = C_P \quad (79)$$

$$c_p \Sigma y_i^2 \left. \begin{array}{l} \text{pitch} \\ \text{springs} \end{array} \right\} + c_r \Sigma y_i^2 \left. \begin{array}{l} \text{roll} \\ \text{springs} \end{array} \right\} = C_R \quad (80)$$

where c_p , c_r , and c_h represent damping coefficients for the pitch, roll, and heave dampers, respectively. Two additional equations express the relationships between the stiffness coefficients and damping coefficients of the springs:

$$7k_p + 6k_r + k_h = K_H \quad (81)$$

$$7c_p + 6c_r + c_h = C_H \quad (82)$$

An additional constraint arises from the requirement that the center of pressure (the point through which all reaction force is assumed to act) lie 0.5 ft forward of the center of mass. Mathematically this requirement is expressed as

$$x_{c_p} K_H = k_p \Sigma x_i \left. \begin{array}{l} \text{pitch} \\ \text{springs} \end{array} \right\} + k_r \Sigma x_i \left. \begin{array}{l} \text{roll} \\ \text{springs} \end{array} \right\} + k_h x_{88} \quad (83)$$

Table IV

LOCATION AND TYPES OF SPRING DAMPER UNITS

Unit Designator	x_b (ft)	y_b (ft)	Type of Unit
11	5.52	0.00	Pitch
28	5.33	-.73	Pitch
25	5.33	.73	Pitch
3P	2.96	-1.45	Roll
3S	2.96	1.45	Roll
4P	1.39*	-1.45	Roll
4S	1.39*	1.45	Roll
5P	-2.00	-1.81	Roll
5S	-2.00	1.81	Roll
6P	-3.37	-.773	Pitch
6S	-3.37	.773	Pitch
7P	-3.45	-.40	Pitch
7S	-3.45	.40	Pitch
88	.50	0.00	Heave

*These values were computed - the method of computation is described later in the chapter.

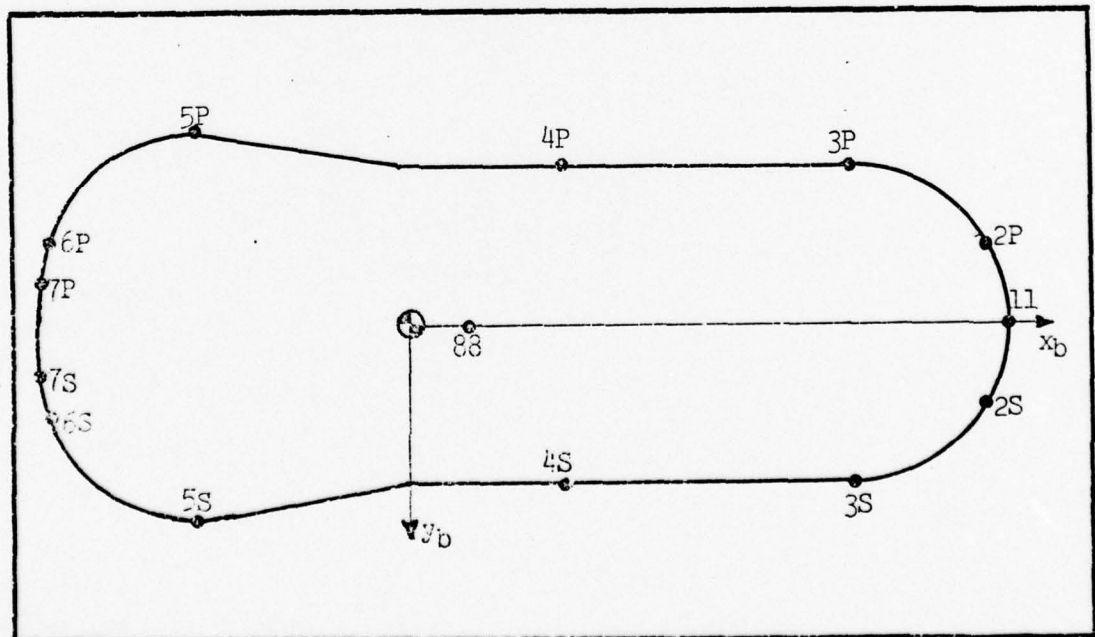


Fig. 33 Placement of Spring Damper Units for the Trunk Model

Considering equations 77 through 83 it is noted that there are seven linear algebraic equations with six unknowns: k_p , k_r , k_h , c_p , c_r , and c_h . Equations 77 through 82 lead to a unique solution for these variables, but the solution does not necessarily satisfy equation 83. Therefore, an additional variable is added. The variable chosen is the x-distance for one pair of roll spring-damper units, the 4P and 4S units. The values for these two spring-damper units in Table IV are a result of solving the seven equations (77 through 83). Solutions for the six variables k_p , k_r , k_h , c_p , c_r , and c_h are given in Table V.

Table V
VALUES OF STIFFNESS AND DAMPING COEFFICIENTS FOR PITCH,
ROLL, AND HEAVE SPRING-DAMPER UNITS

k_p	463.53 lb/ft	c_p	2.96 $\frac{\text{lb-sec}}{\text{ft}}$
k_r	264.75 lb/ft	c_r	32.47 $\frac{\text{lb-sec}}{\text{ft}}$
k_h	7466.8 lb/ft	c_h	264.5 $\frac{\text{lb-sec}}{\text{ft}}$

Reaction and Frictional Forces Acting on the Trunk

In developing the reaction and frictional forces on the trunk, two assumptions are necessary concerning the spring-damper units. First, the units are assumed to be rigid in all directions except the direction perpendicular to the surface of the earth. This assumption makes sense physically since the flexible structure of the ACRS is such that the pressure distribution under a portion of the brake tread acts normal to the landing surface. A second

assumption is that no force is created by a particular spring-damper unit whenever the spring displacement alone results in a negative force. This situation is interpreted to mean that the spring is no longer touching the ground and, hence, is incapable of transmitting any force to the vehicle.

The method used to obtain trunk forces and moments acting on the vehicle consists of three steps: 1) transformation of body position, velocity, and angular rates into spring displacements, displacement rates, and $x_e - y_e$ velocities, 2) calculation of spring reaction and frictional forces from the information obtained in the first step, and 3) transformation of the forces and moments acting on the vehicle into the body coordinate system from the information obtained in the second step. Mathematical relationships needed for each of these steps are developed below for a typical spring-damper unit.

Step 1. Let R_0 represent the position vector from some arbitrary point on the surface of the (assumed flat) earth to the center of mass of the vehicle. Further, let r_0 represent the position vector from the center of mass of the vehicle to the attachment point of any one spring-damper unit. The sum of these two position vectors is itself a position

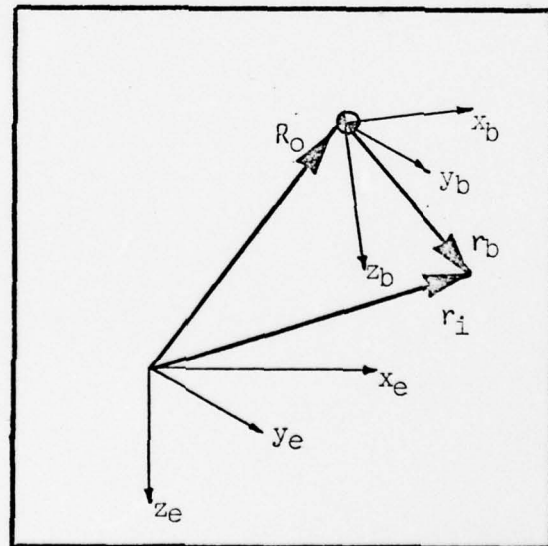


Fig. 34 Position Vector from an Arbitrary Point on the Surface of the Earth to a Spring-Damper Unit Point of Attachment

vector, r_i , from the arbitrary point in the $x_e - y_e$ plane to the point on the body. If this vector is expressed in the earth frame, the third (or z_e) component is the coordinate of the attachment point of the spring. Figure 34 is a sketch representing this situation, and the following mathematical relationships summarize the preceding comments:

$$r_i = R_o + r_b \quad (84)$$

where

$$\begin{bmatrix} R_o \end{bmatrix}^e = \begin{bmatrix} x_e \\ y_e \\ z_e \end{bmatrix}$$

and

$$\begin{bmatrix} r_b \end{bmatrix}^e = C_b^e \begin{bmatrix} r_b \end{bmatrix}^b = C_b^e \begin{bmatrix} x_b \\ y_b \\ z_b \end{bmatrix}$$

Letting

$$\begin{bmatrix} r_i \end{bmatrix}^e = \begin{bmatrix} r_x \\ r_y \\ r_z \end{bmatrix}$$

then

$$\begin{bmatrix} r_x \\ r_y \\ r_z \end{bmatrix} = \begin{bmatrix} x_e \\ y_e \\ z_e \end{bmatrix} + C_b^e \begin{bmatrix} x_b \\ y_b \\ z_b \end{bmatrix} \quad (85)$$

The only component of interest, however, is the r_z component, since this component is necessary to determine the spring deflection.

Hence, r_z is expressed as

$$r_z = z_e + c_{31}x_b + c_{32}y_b + c_{33}z_b \quad (86)$$

where c_{31} , c_{32} , and c_{33} are the third row elements of the transformation matrix, C_b^e . All terms except z_b on the RHS of equation 86 are known quantities since z_e and C_b^e are determined during each iteration of a simulation run, and x_b and y_b are given in Table IV.

A value for z_b is arbitrarily chosen as zero feet; hence, the spring-damper units are assumed to be attached to the vehicle at the $x_b - y_b$ plane.

The displacement rates of the springs are also required and these can be obtained by taking the time derivative of equation 84:

$$\frac{dr_i}{dt} = \frac{dR_o}{dt} + \frac{dr_b}{dt} \quad (87)$$

Letting

$$\left[\frac{dr_i}{dt} \right]^e = \begin{bmatrix} \dot{r}_x \\ \dot{r}_y \\ \dot{r}_z \end{bmatrix}$$

and

$$\left[\frac{dR_o}{dt} \right]^e = \begin{bmatrix} \dot{x}_e \\ \dot{y}_e \\ \dot{z}_e \end{bmatrix}$$

then the last term in equation 87 is the only term left to be evaluated. The differentiation of r_b must be carried out in the (assumed inertial) earth frame, and this is most expeditiously accomplished by use of the theorem of Coriolis (Ref 23:437, 438):

$${}^e \frac{dr_b}{dt} = \frac{{}^b dr_b}{dt} + W \times r_b \quad (88)$$

where W is the angular velocity vector of the body frame with respect to the earth frame. The first term on the RHS of 88 is zero since the position vector in the body frame is constant. The second term is now determined by recalling from Chapter II that

$$[W]^b = \begin{bmatrix} P \\ Q \\ R \end{bmatrix}$$

Then the cross product becomes

$$[W \times r_b]^b = \begin{bmatrix} Qz_b - Ry_b \\ Rx_b - Pz_b \\ Py_b - Qx_b \end{bmatrix} \quad (89)$$

which, when pre-multiplied by C_b^e , is in a form which allows an evaluation of equation 87:

$$\begin{bmatrix} \dot{r}_x \\ \dot{r}_y \\ \dot{r}_z \end{bmatrix} = \begin{bmatrix} \dot{x}_e \\ \dot{y}_e \\ \dot{z}_e \end{bmatrix} + C_b^e \begin{bmatrix} Qz_b - Ry_b \\ Rx_b - Pz_b \\ Py_b - Qx_b \end{bmatrix} \quad (90)$$

The displacement rate of any specific spring-damper unit is given by equation 90 since all variables on the RHS of equation 90 are available in each iteration of the computer simulation.

Step 2. The forces produced by the deflection and the deflection rate of a particular spring are easily calculated as follows:

$$F_d = -k(r_z - r_{z_0}) + F_{d_0} \quad (91)$$

$$F_r = -c\dot{r}_z \quad (92)$$

where

F_d - force due to spring deflection

F_r - force due to damper deflection rate

r_{z_0} - coordinate of spring attachment point with vehicle at rest on the ground

F_{d_0} - spring force with vehicle at rest on the ground

The spring-damper forces are expressed in the earth frame.

The only remaining force to consider is the frictional force. The total reaction force, $F_d + F_r$, and the direction of the velocity of the spring-damper point of contact are necessary in the computation of this force. The components of velocity in the $x_e - y_e$ plane are given in equation 90. Hence, the direction of the velocity in this plane is conveniently determined by

$$\gamma = \tan^{-1} \left(\frac{\dot{y}_e}{\dot{x}_e} \right) \quad (93)$$

where γ is the angle between the velocity vector and the x_e axis with a rotation from the x_e to the y_e axis being the positive direction. The components of the frictional force on a given spring damper unit are given by

$$F_{f_x} = -\mu(F_d + F_r)\cos\gamma \quad (94)$$

$$F_{f_y} = -\mu(F_d + F_r)\sin\gamma \quad (95)$$

where

F_{f_x} , F_{f_y} - components of frictional force in the x_e and y_e directions, respectively

μ - coefficient of friction associated with a specific spring-damper unit

Step 3. The reaction and frictional forces derived in step 2 are all expressed in the earth reference frame. The purpose of step 3 is eventually to transform these forces into forces and moments in the body reference frame.

The forces in step 2 are first expressed as earth-referenced coordinates of a vector, F_f , as follows:

$$[F_f]^e = \begin{bmatrix} F_{f_x} \\ F_{f_y} \\ F_r + F_d \end{bmatrix} \quad (96)$$

Transformation of these forces into the body frame is easily accomplished as follows:

$$[F_f]^b \equiv \begin{bmatrix} X_f \\ Y_f \\ Z_f \end{bmatrix} = C_e^b \begin{bmatrix} F_{f_x} \\ F_{f_y} \\ F_r + F_d \end{bmatrix} \quad (97)$$

The moments about the center of mass of the vehicle are computed by forming the cross product of the position vector to the point where each spring contacts the ground, and the force vector:

$$M = r_t \times f_f \quad (98)$$

where

$$r_t = r_b + C_e^b \begin{bmatrix} 0 \\ 0 \\ -r_{i_3} \end{bmatrix} \quad (99)$$

The term r_{i_3} is the third component of the vector r_i in equation 84 and, furthermore, this value in earth-frame coordinates is available during each computer iteration. Expansion of equation 98 yields

$$[M]^b = \begin{bmatrix} y_t Z_f - z_t Y_f \\ z_t X_f - x_t Z_f \\ y_t Y_f - y_t X_f \end{bmatrix} \quad (100)$$

where X_f , Y_f , and Z_f are the coordinates of F_f in the body frame (see equation 97), and x_t , y_t , and z_t are the coordinates of r_t in the body frame.

This concludes the three steps involved in calculating the trunk reaction and frictional forces in the body frame. The FORTRAN implementation of these results is given in Appendix B.

Verification of Trunk Dynamics

The three individual dynamic modes for which data is available are heave, pitch, and roll, as given in Table III. A verification of the computer program with the trunk model included is desired to ensure that no programming errors have been committed. Computer simulations of each dynamic mode are presented in this section, which verify that the trunk model accurately reflects the given heave, pitch, and roll data. The data is first used to predict the

damping coefficient, ζ , and period, T , for each mode, after which a comparison is made between these predictions and the values obtained by computer simulation.

Prediction of heave mode dynamics. In the heave mode, the only degree of freedom is vertical motion of the center of mass. A differential equation which describes this mode is

$$m\ddot{h} = -K_H h - C_H \dot{h} \quad (101)$$

where h represents the deflection of the spring attachment point from its equilibrium position and the positive direction of h is the opposite of z_e . A rearrangement of equation 101 yields

$$\ddot{h} + \frac{C_H}{m} \dot{h} + \frac{K_H}{m} h = 0 \quad (102)$$

which has the form

$$\ddot{h} + 2\zeta_H \omega_{nH} \dot{h} + \omega_{nH}^2 h = 0 \quad (103)$$

where

ζ_H - heave damping ratio

ω_{nH} - heave natural frequency

Equation 102 is readily solved for ζ_H and T_H (the period of the heave mode oscillation):

$$\zeta_H = \frac{C_H}{2\sqrt{mK_H}} \quad (104)$$

$$T_H = \frac{2\pi}{\omega_{dH}} = \frac{2\pi}{\sqrt{\frac{K_H}{m}(1 - \zeta_H^2)}} \quad (105)$$

Inserting the values for each of the parameters in equations 104 and 105, the following experimentally-derived values for ζ_H and T_H are obtained:

$$\zeta_H = 0.24$$

$$T_H = 0.53 \text{ sec}$$

Prediction of pitch mode dynamics. The equation for the pitch mode dynamics is similar to equation 101:

$$I_{yy}\ddot{\theta} = -K_p\theta - C_p\dot{\theta} \quad (106)$$

Equation 106 is solved in the same manner as equation 101 to yield

$$\zeta_p = .062$$

$$T_p = .995 \text{ sec}$$

Prediction of roll mode dynamics. The equation for the roll mode dynamics is similar to equations 101 and 106:

$$I_{xx}\ddot{\phi} = -K_r\phi - C_r\dot{\phi} \quad (107)$$

Solving this equation for the damping ratio and period, the following values are obtained:

$$\zeta_r = .102$$

$$T_r = 2.98 \text{ sec}$$

Simulation results. Computer simulation results of the model in each dynamic mode are presented in Figures 35, 36, and 37. These plots are treated as underdamped, simple, second-order system responses and are graphically evaluated for the period, T' , and the damping ratio, ζ' , which are compared with the predicted values computed above. The manner in which this evaluation is performed is now described.

With the assumption that the time responses in Figures 35 to 37 represent the outputs of unforced, second-order systems, the responses are of the form

$$C(t) = Ae^{-\zeta\omega_n t} \sin(\omega_d t + \phi) \quad (108)$$

FIG. 35 VERIFICATION OF NERVE MODE DYNAMICS

02/27/73 11.19.29. CASE NO. 1

SIMULATION DISPLAY 1

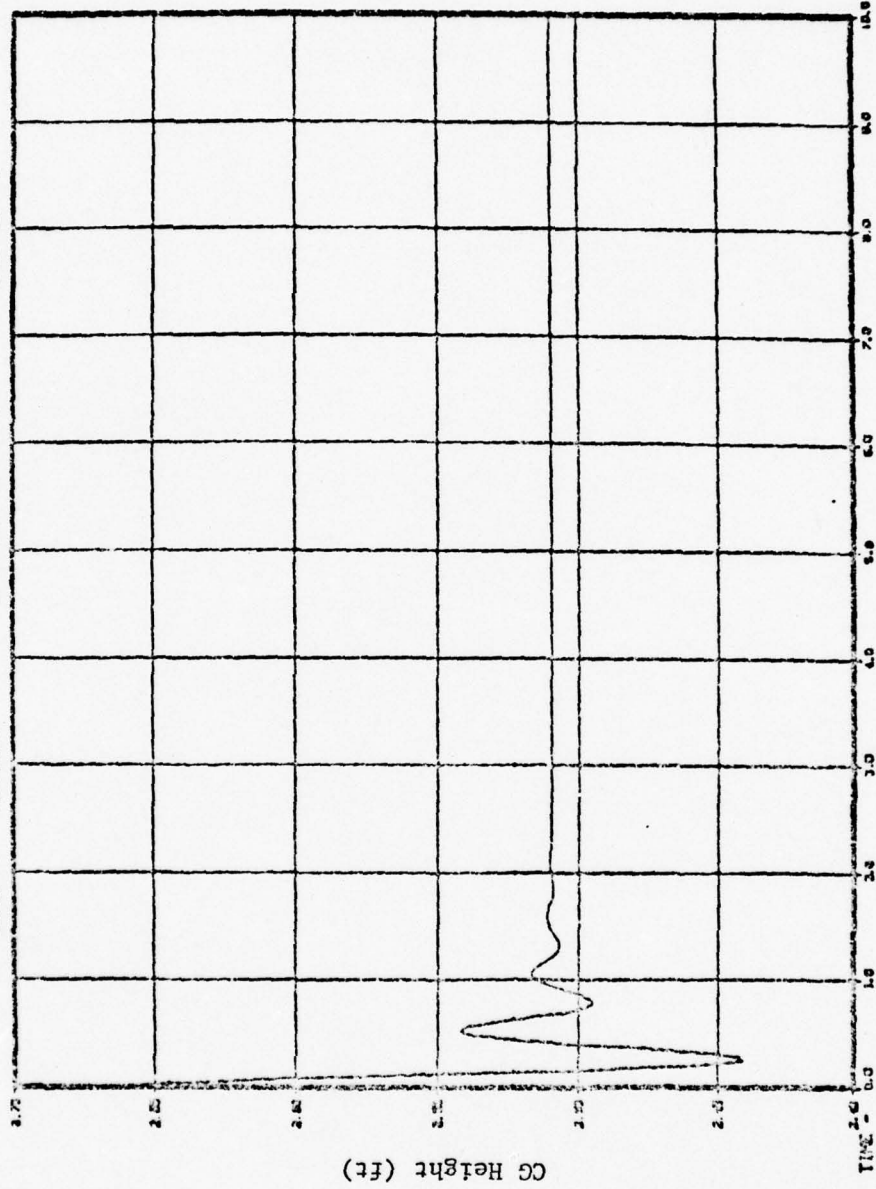


FIG. 35 VERIFICATION OF PITCH MODE DYNAMICS

02/25/78 14.01.28.

SIMULATION DISPLAY 2

CASE NO. 1

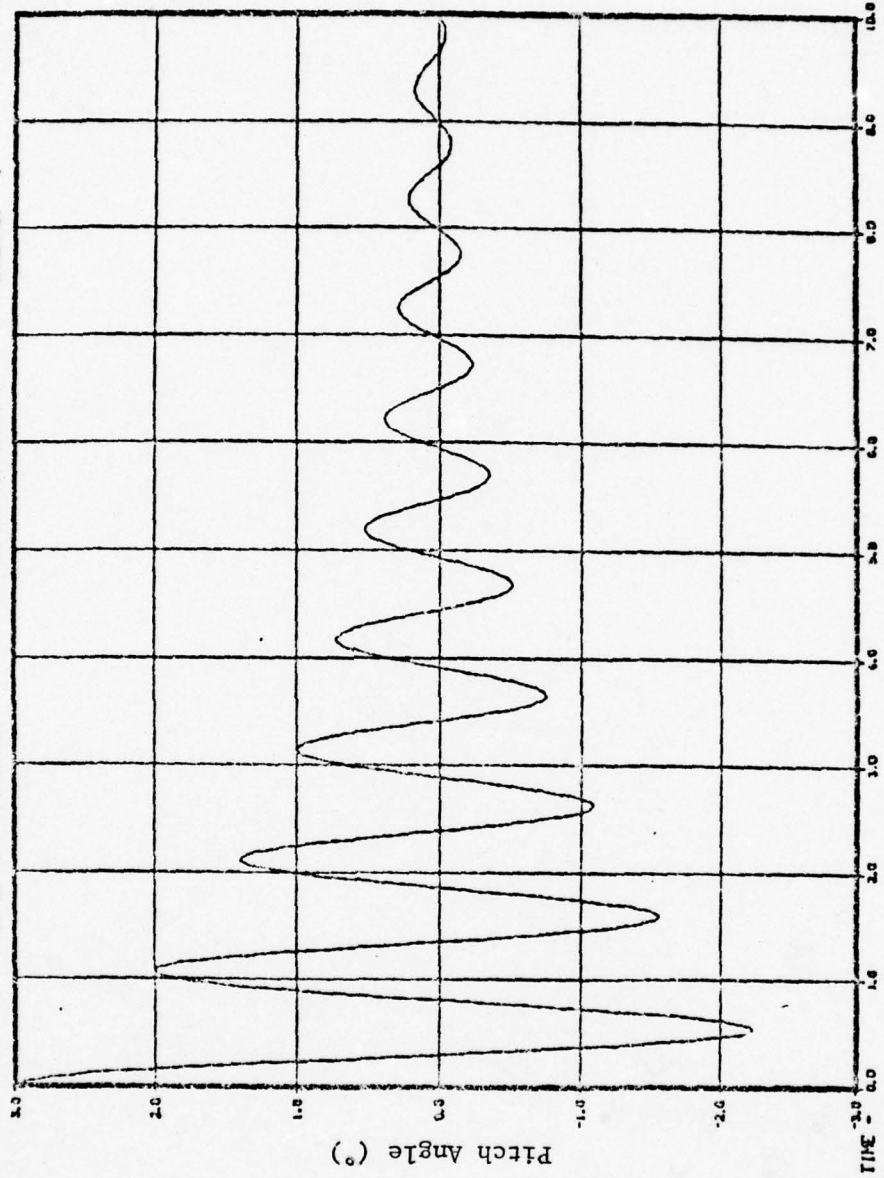
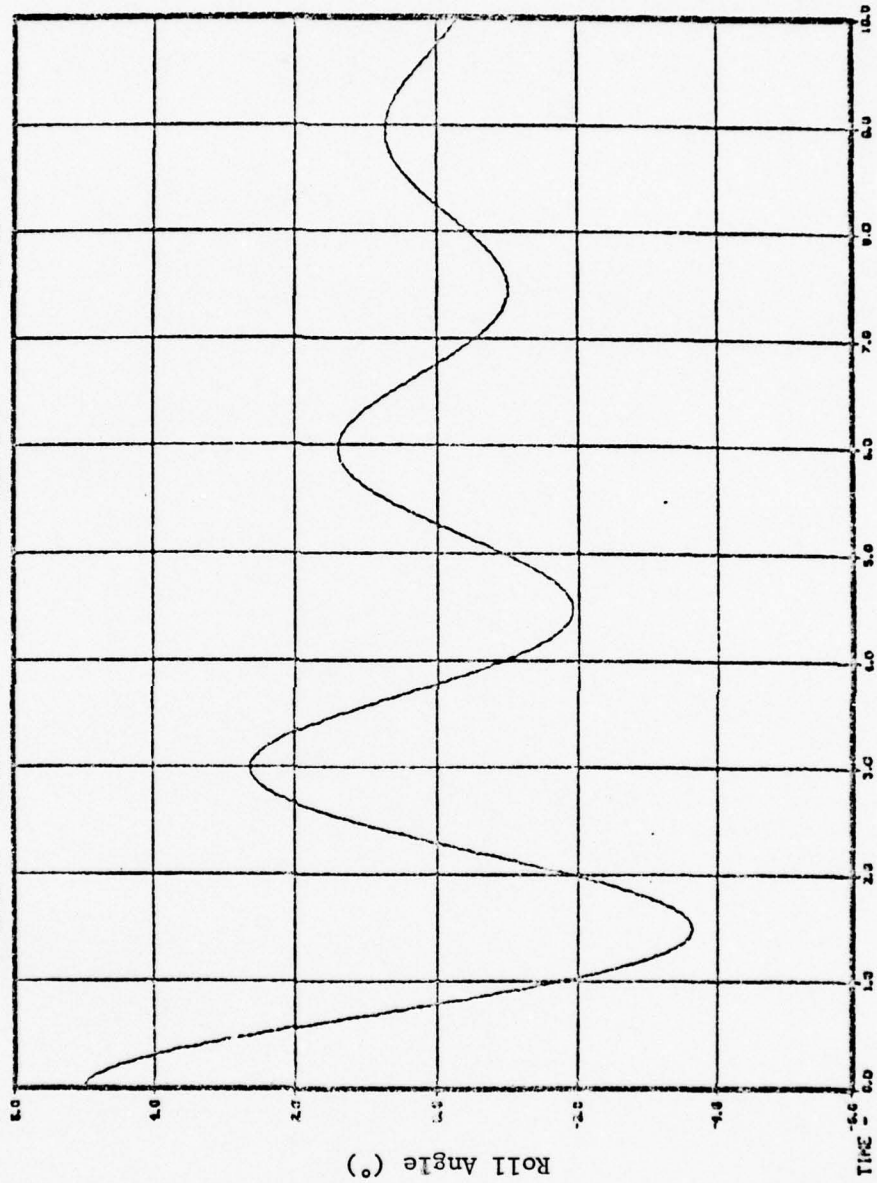


FIG. 37 VERIFICATION OF ROLL MODE DYNAMICS

02/25/78 13:44:57.

SIMULATION DISPLAY 3

CASE NO. 1



where

$C(t)$ - the system output

A - a constant determined by system parameters

ω_d - the damped natural frequency ($\omega_d = \omega_n \sqrt{1 - \zeta^2}$)

ϕ - the phase angle

(108a)

The product of $Ae^{-\zeta\omega_n t}$ and the sine function results in peak values whenever the value of the sine function is near ± 1 and the damping ratio is small. If any two positive peak values are taken from the plots, say $C(t_1) = C_1$ and $C(t_2) = C_2$, then the following approximate equation holds:

$$\frac{C_2}{C_1} \doteq e^{-\zeta\omega_n(t_2 - t_1)} \quad (109)$$

An expression for the damping ratio is determined by using this relationship and the expression given above for ω_d :

$$\zeta \doteq \frac{\ln(C_1/C_2)}{\sqrt{\ln(C_1/C_2)^2 + \frac{4\pi^2(t_2 - t_1)^2}{T}}} \quad (110)$$

This expression is used to evaluate ζ several times for each simulation, after which an average value, ζ' , is computed in order to compare the predicted value and the simulation value. Furthermore, several values of the period computed for each simulation were averaged to obtain an average value, T' , which is compared with the predicted period, T . Table VI lists the predicted versus the simulation values of period and damping ratio for each dynamic mode. The agreement is sufficiently close (less than 5% deviation in each case), to lead to the conclusion that there are no major programming errors. Therefore, the model trunk reaction forces are essentially the same as those of the actual ACRS-vehicle combination.

Table VI

COMPARISON OF PREDICTED AND SIMULATED DAMPING RATIOS AND PERIODS

Dynamic Mode	Predicted Damping Ratio	Simulation Damping Ratio	Predicted Period (sec)	Simulation Period (sec)
HEAVE	.24	.24	.53	.53
PITCH	.062	.060	.995	1.03
ROLL	.102	.102	2.98	2.98

Conclusion

A reasonable model of the trunk reaction and frictional forces has been developed which is claimed to be realistic for small angles. Since test results in Table VI are based on peak values of roll and pitch of approximately 5° and 3°, respectively, simulation results are not guaranteed to be accurate outside of these ranges.

Analysis of the dynamic characteristics of the Jindivik in the slideout phase is now possible. Chapter V uses the aerodynamic model in conjunction with the trunk model to perform such an analysis.

V. ANALYSIS OF THE SLIDEOUT

The aerodynamic model developed in Chapter II and the trunk model developed in Chapter IV are combined in this chapter for the purpose of analyzing the slideout stability of an ACRS-equipped aircraft. Simulations of the Jindivik aircraft during a slideout are analyzed which serve to illustrate a basic stability problem. Some general comments concerning the nature of this problem are made, followed by a proposed solution. Finally, simulation results are presented which serve to verify the effectiveness of the proposed solution.

Analysis of the ACRS-Equipped Vehicle in the Slideout

Two simulations were initially performed in order to identify instabilities in the slideout phase. Simulation results presented in this section were obtained with the configuration and initial conditions given in Table VII. The pitch and roll control systems were omitted from the first simulation in order to establish a baseline performance capability of the landing system. The existing pitch and roll control systems were included in the second simulation to observe the adequacy of these controllers in the slideout.

Bare Airframe Slideout Simulation

Results of the bare airframe simulation are presented in Figures 38 through 42. The overall motion of the vehicle is best described

Table VII

CONFIGURATION AND INITIAL CONDITIONS FOR SLIDEOUT SIMULATIONS

Forward Velocity	200 ft/sec
CG Height ¹	2.4977 ft
Elevator Deflection Angle ¹	-1.1354°
Angle of Attack ¹	-2.1302°
Pitch Angle ¹	-2.1302°
Thrust	300. lb
Flap Setting	UP
Weight	2620 lb
Friction Coefficient (Forward) ²	0.3
Friction Coefficient (Aft) ²	0.8

¹These values were computed using the "STEADY STATE" feature of the computer program, EASY (see Appendix B).

²These values were increased for the individual springs since a significant portion of the total reaction force is supported by the spring at the center of pressure, which does not contribute to the frictional force.

by separately considering the longitudinal-related dynamics and the lateral-directional related dynamics.

Longitudinal Dynamics. Figure 38 depicts the time histories of the x_b velocity, U , and angle of attack, α . The x_b velocity is seen to decrease at a fairly constant rate from the initial value of 200 ft/sec to a value of 50 ft/sec, where the simulation is terminated. The average deceleration is approximately 16.67 ft/sec (.52 g).

The angle of attack gradually decreases during the first 6.4 seconds for the following reason. As the velocity decreases, the pitch-up aerodynamic moment decreases, while the nose-down moment produced by sliding frictional forces remains relatively constant. After 6.5 seconds, large fluctuations in α occur due to roll angle variations which are discussed in the section on lateral-directional dynamics. Neither the deceleration of the vehicle nor the angle of attack variation with time are objectionable, except for the divergent tendency of the angle of attack after five seconds.

The pitch angle and center of gravity (cg) height are presented in Figure 39. A steady decrease in pitch angle results for the same reason that the angle of attack decreases. The final decrease in pitch angle occurs due to a large deviation in roll angle which is discussed in the next section.

Although the pitch angle is not less than -3° until the roll angle becomes quite large, the nose-down attitude is cause for concern, since only a slight perturbation could result in the nose of the aircraft contacting the runway. A control system could be designed to maintain a desired pitch attitude during the initial portion of the

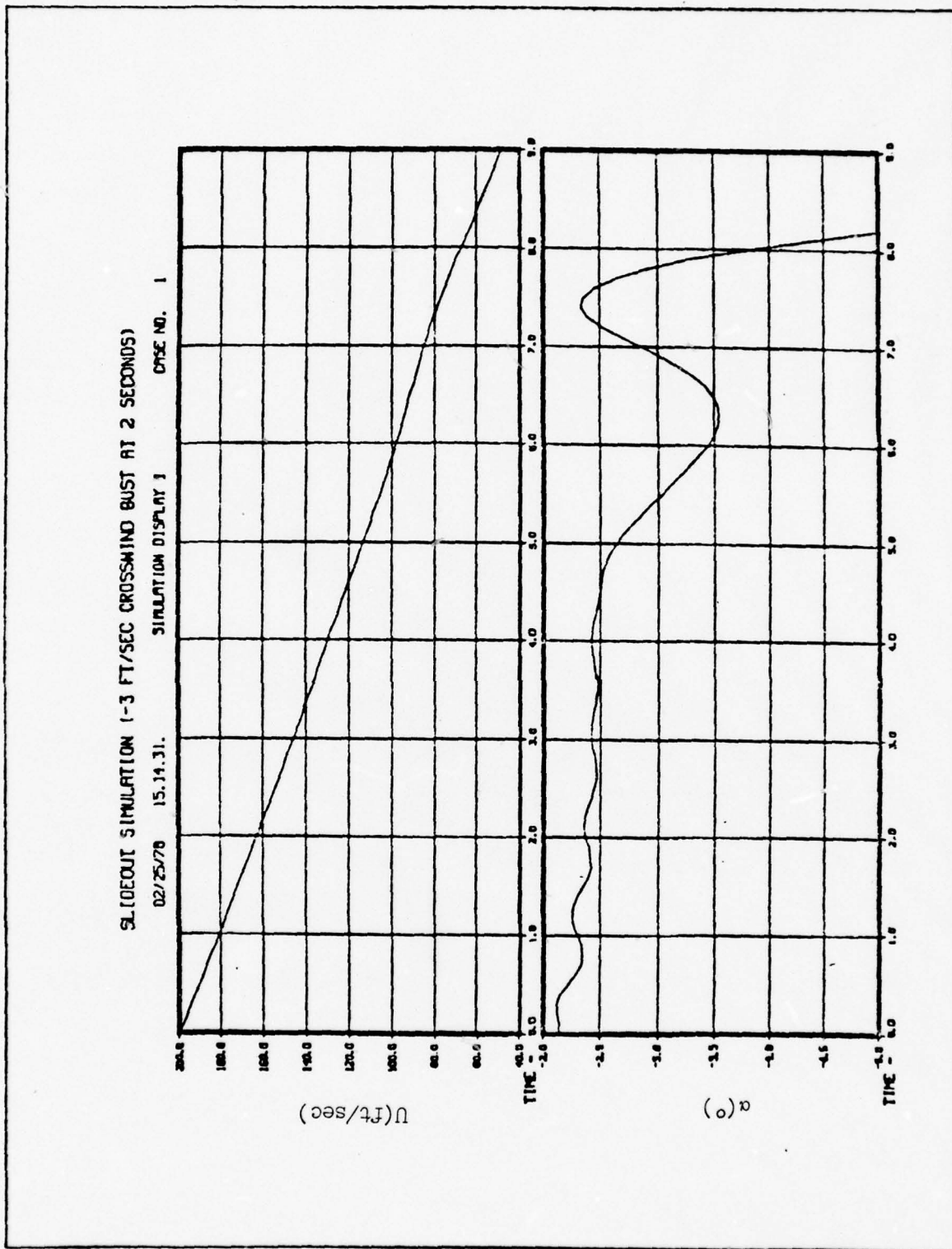


Fig. 38 Forward Velocity and Angle of Attack Time Histories
 During Slideout with no Control System

SLIDEOUT SIMULATION (-3 FT/SEC CROSSWIND GUST AT 2 SECONDS)
 02/25/78 15.14.31. SIMULATION DISPLAY 2 CASE NO. 1

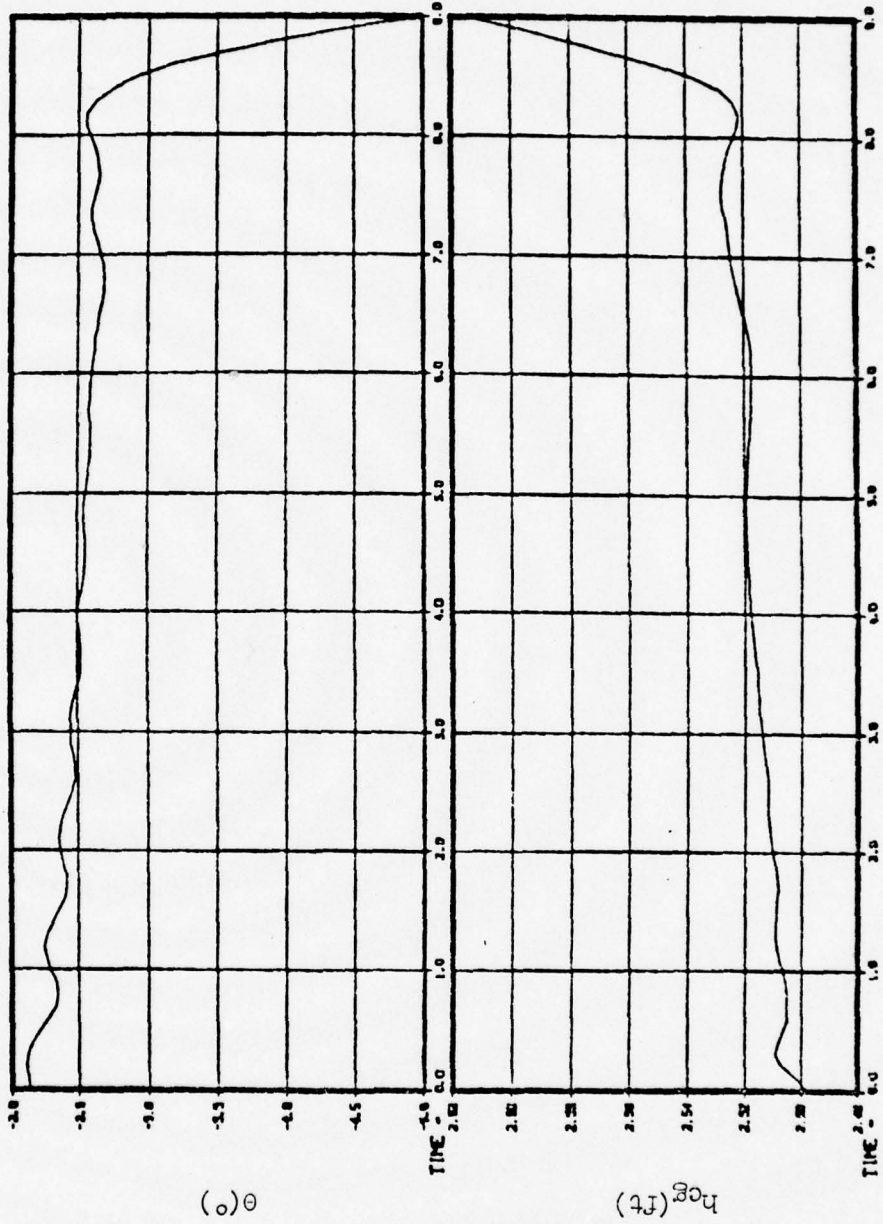


Fig. 39 Pitch Angle and Height of CG Time Histories During Slideout with No Control System

slideout, but the largest negative pitch deviations occur toward the end of the slideout where there is insufficient dynamic pressure for the elevator to be effective. Hence, no specific design is developed for controlling the pitch angle in this report.

The cg height, h_{cg} , is initially lower than the static equilibrium height of 2.51 ft due to aerodynamic forces. The springs of the trunk model are initially compressed, but they extend toward their equilibrium values as the aerodynamic forces lessen. The final large increase in cg height is a result of the large roll angle discussed in the next section.

Lateral-Directional Dynamics

A small (-3 ft/sec) crosswind gust was included in the simulations in order to excite the unstable characteristics of the ACRS-equipped vehicle. The gust was applied two seconds into the simulation when the forward velocity was approximately 160 ft/sec. Figure 40 depicts time histories of the roll angle, ϕ , and yaw angle, ψ .

The roll angle is seen to remain at 0° until the gust is applied. Since the gust produces an instantaneous increase in the sideslip angle, a negative rolling moment is also produced which causes the aircraft to roll to the left. The aerodynamic characteristics of the Jindivik are such that an increase in β produces a negative yawing moment. The negative roll angle increases the reaction and frictional forces on the left (port) side of the vehicle which also cause a negative yaw moment about the cg. These yaw moments produce the yaw rate, R , shown in Figure 41, which results in the negative increase in yaw angle in Figure 40. As the velocity decreases the aerodynamic

SLIDEOUT SIMULATION (-3 FT/SEC CROSSWIND GUST AT 2 SECONDS)
 02/25/78 15.14.31. SIMULATION DISPLAY 3 CASE NO. 1

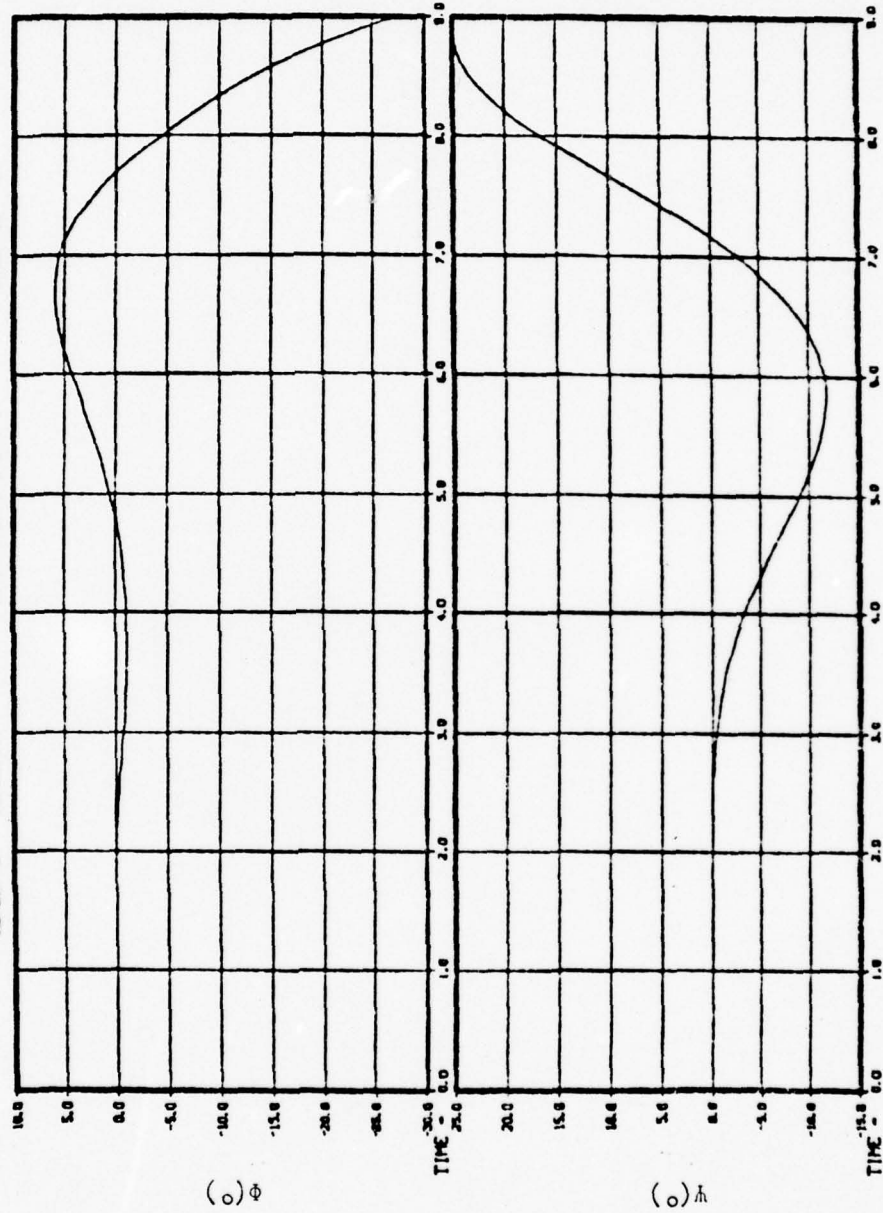


Fig. 40 Roll Angle and Yaw Angle Time Histories
 During Slideout with No Control System

SLIDEOUT SIMULATION 1-3 FT/SEC CROSSWIND BUST AT 2 SECONDS)

02/25/78 15.14.31. SIMULATION DISPLAY 4 CASE NO. 1

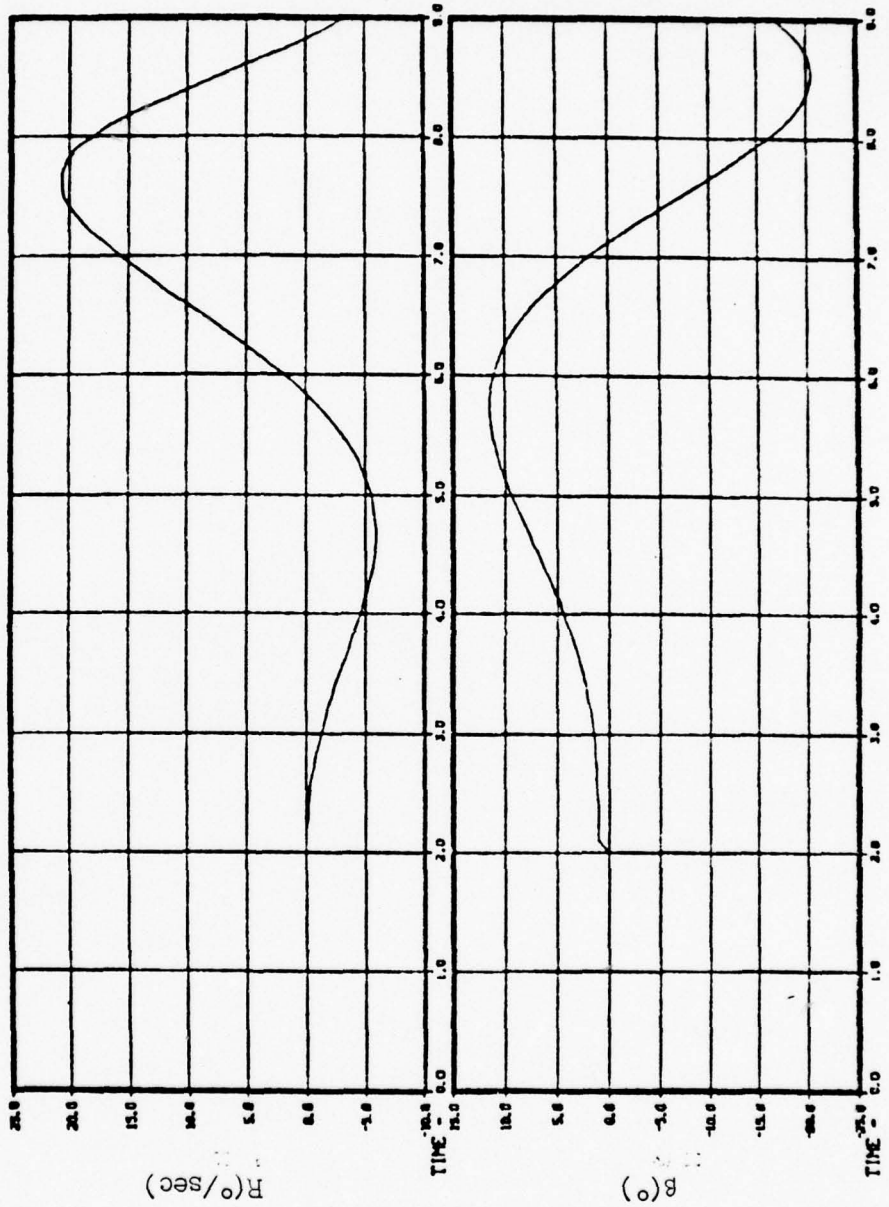


Fig. 41 Sideslip Angle and Yaw Rate Time Histories
During Slideout with No Control System

yawing moment decreases, while the yawing effect of unbalanced frictional forces remains relatively constant. Thus, the yaw rate tends to follow the roll angle throughout the slideout and the shape of the curves for ϕ and R are seen to be very similar.

The roll angle influences yaw rate, but the roll angle itself is influenced by both lateral frictional forces and spring reaction forces. Thus, as the yaw angle increases negatively, the frictional forces are acting to produce a positive rolling moment. This moment, along with trunk reaction forces causes the roll angle to increase from its negative value of -1.5° at 4 seconds, to 7° at 6.7 seconds. The reaction torque becomes larger than the roll torque produced by lateral frictional forces just after 6 seconds and the roll angle begins to decrease sharply at this point.

Figure 42 depicts the lateral displacement of the vehicle, y_e , versus distance "down the runway", x_e . It is seen that a sidewind gust of only -3 ft/sec produces a deviation of -13 feet from the runway centerline (the x_e axis).

Airframe with Existing Autopilot Simulation

Results of the simulation of the airframe and existing autopilot are presented in Figures 43 through 47. The longitudinal dynamics are very similar to those of the bare airframe, while there are significant differences in the lateral-directional dynamics.

Longitudinal Dynamics. Figure 43 presents the same variables as Figure 38 — U and α . These two figures may be compared to see that the trend is the same for both variables. The few differences which do exist are primarily a result of smaller fluctuations in the roll

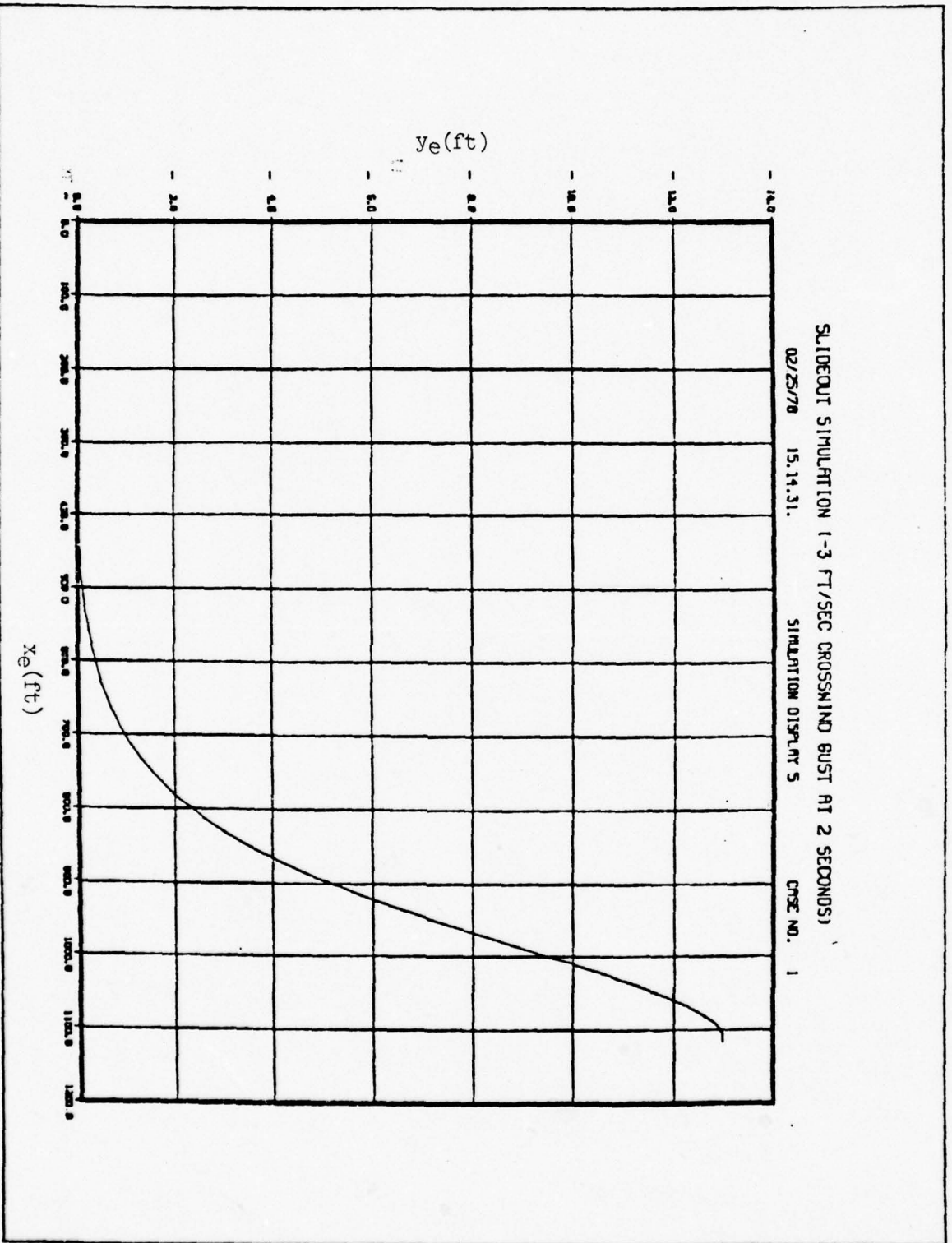


Fig. 42 Lateral Versus Longitudinal Displacement During Slidecut with No Control System

SLIDEOUT SIMULATION WITH EXISTING AUTOPILOT (1-3FT/SEC GUST)
 02/25/78 16.41.50. SIMULATION DISPLAY 1 CASE NO. 1

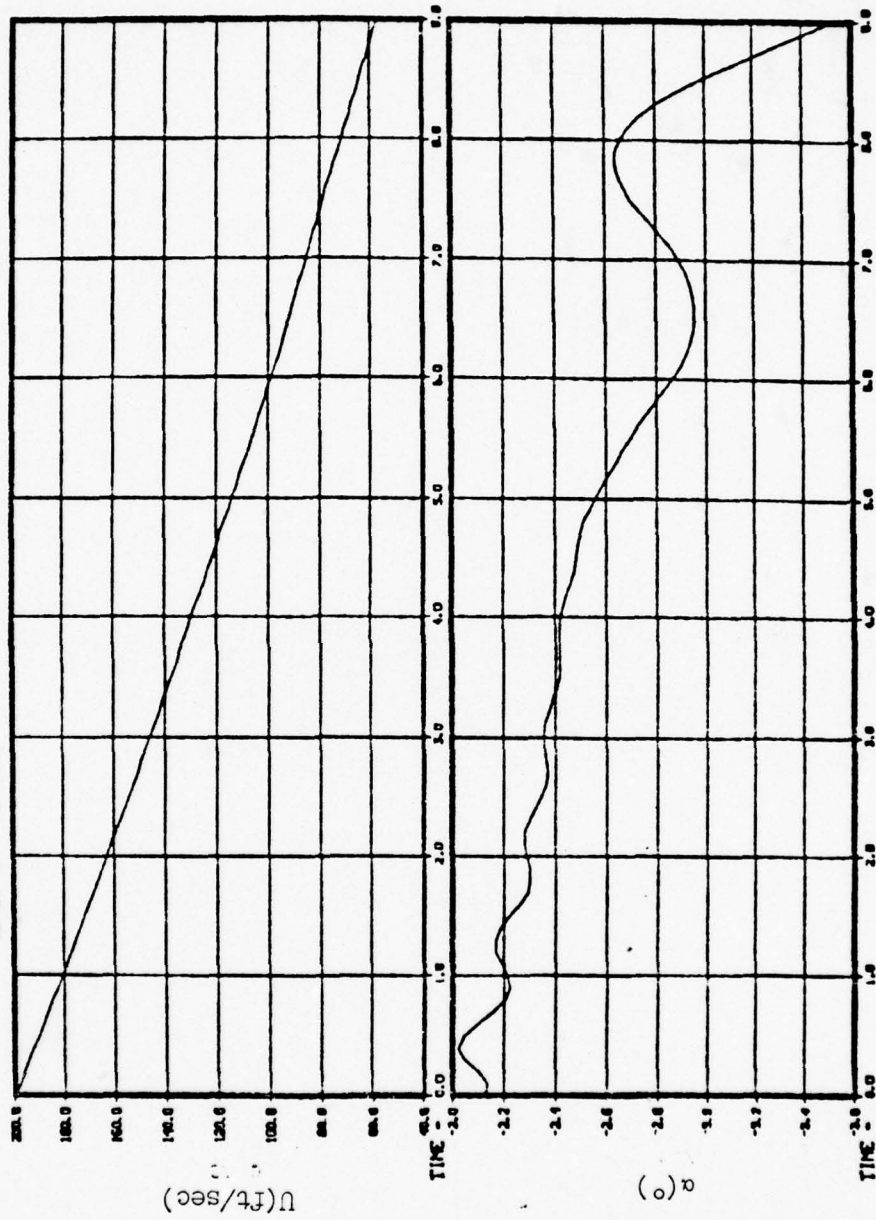


FIG. 43 Forward Velocity and Angle of Attack Time Histories
 During Slideout with Existing Autopilot

SLIDEOUT SIMULATION WITH EXISTING AUTOPILOT 1-3FT/SEC GUST)
 02/25/78 16.41.50. SIMULATION DISPLAY 2 CASE NO. 1

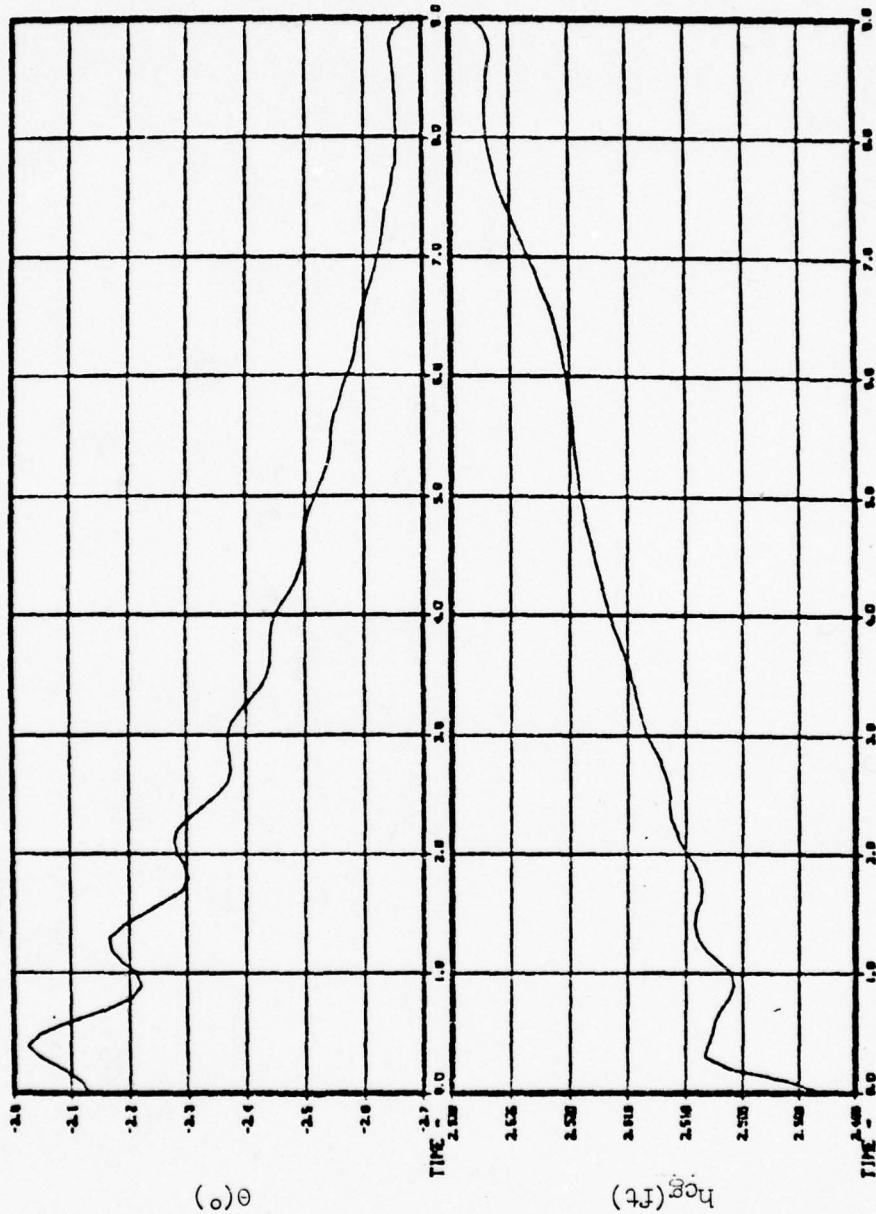


Fig. 44 Pitch Angle and Height of CG Time Histories During Slideout with Existing Autopilot

angle. These differences are, 1) a more linear rate of change in U near the end of the simulation, and 2) a more stable time history of α , although α is still somewhat erratic towards the end of the simulation.

The pitch angle and cg height depicted in Figure 44 are seen to fluctuate considerably less with the pitch and roll control systems engaged than in the bare airframe simulation. As in the case of U and α , the fluctuations are less severe primarily because the roll angle deviations are smaller.

Lateral-Directional Dynamics. While the shape of the roll angle curve in Figure 45 is similar to the roll angle curve in Figure 40, the magnitudes are considerably smaller in Figure 45 due to the action of the roll control system. A dramatic decrease in yaw angle, yaw rate, and sideslip angle deviations is also noted in Figures 45 and 46.

Figure 47 presents the lateral versus longitudinal displacements of the vehicle for the autopilot-engaged simulation. While most other variables in this simulation deviate less from their nominal values than they do in the bare airframe simulation, the final lateral displacement is only mildly reduced (from -13 ft to -12 ft). The primary reason for the small difference in the two cases is that the large positive yaw angle near the end of the autopilot-off simulation curtails the lateral displacement rate. Due to this large roll angle, however, the accuracy of the simulation is questionable in this area.

Conclusions. Two primary conclusions are drawn from these simulations. First, both configurations are unacceptable due to the divergent tendency of the roll angle. Although in the latter simulation the roll angle achieves a final value of only -6° , it is

SLIDEOUT SIMULATION WITH EXISTING AUTOPILOT (-3FT/SEC GUST)
 02/25/78 16.41.50. SIMULATION DISPLAY 3 CASE NO. 1

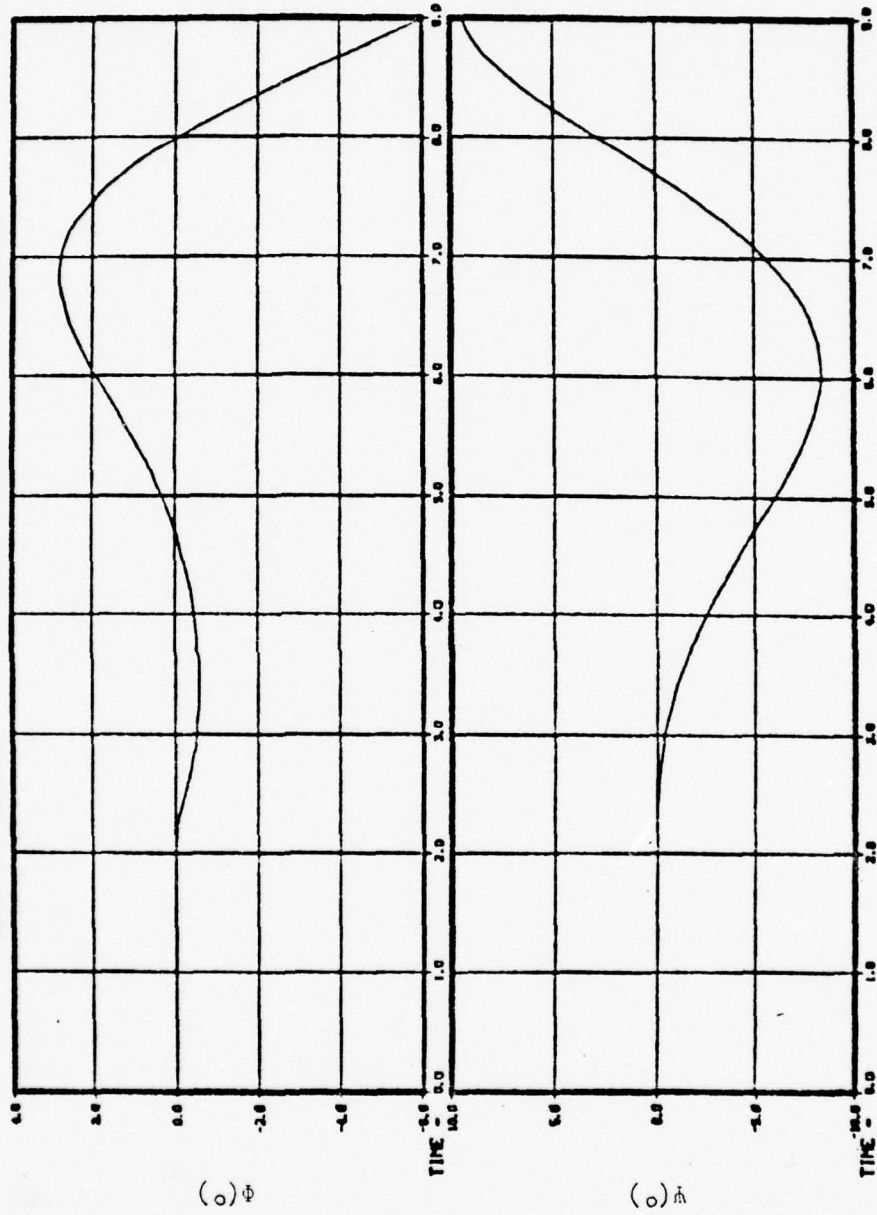


Fig. 45 Roll Angle and Yaw Angle Time Histories
 During Slideout with Existing Autopilot

SLIDEOUT SIMULATION WITH EXISTING AUTOPILOT (1-3FT/SEC GUST)

02/25/78 16.41.50.

SIMULATION DISPLAY 4

CASE NO. 1

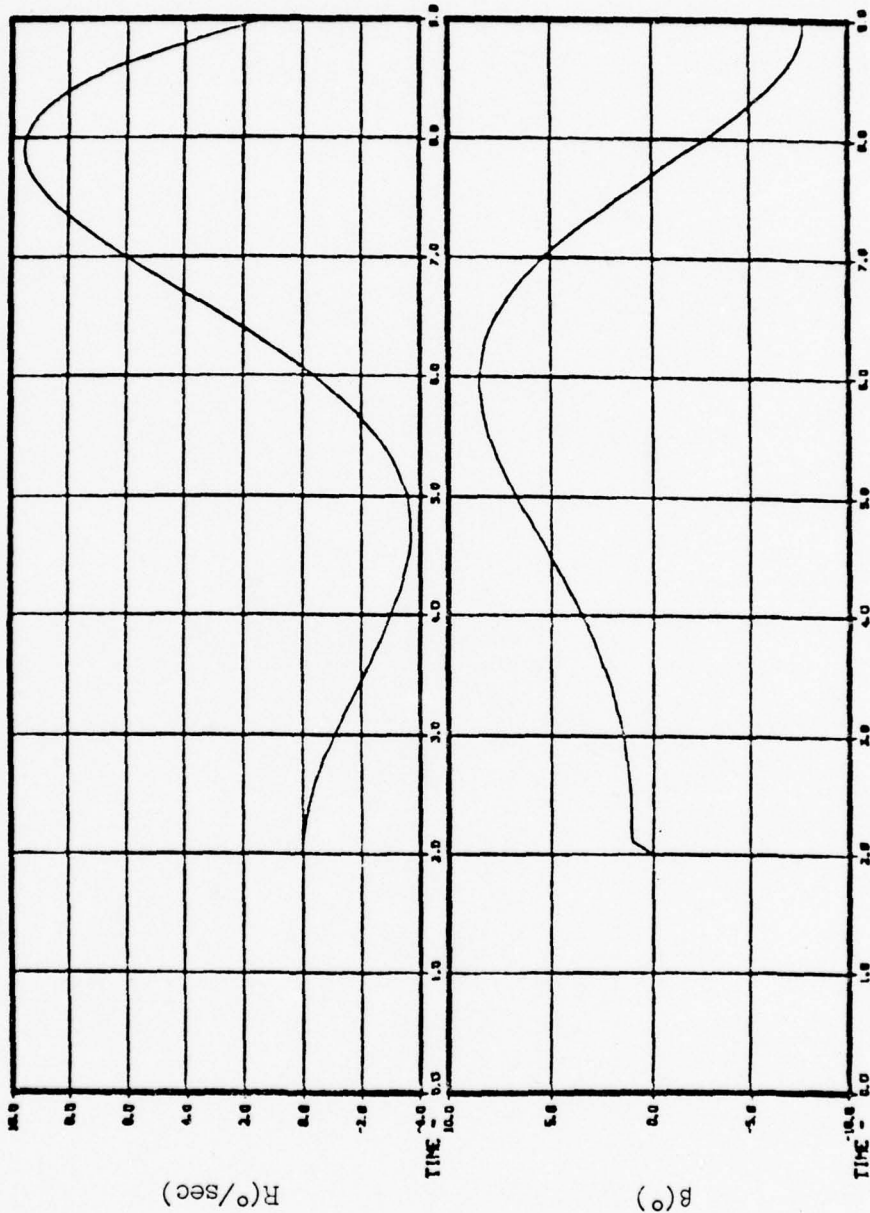


Fig. 46 Sideslip Angle and Yaw Rate Time Histories During Slideout with Existing Autopilot

SLIDEOUT SIMULATION WITH EXISTING AUTOPILOT (-3FT/SEC GUST)

02/25/78 16.41.50.

SIMULATION DISPLAY 5

CRSE NO. 1

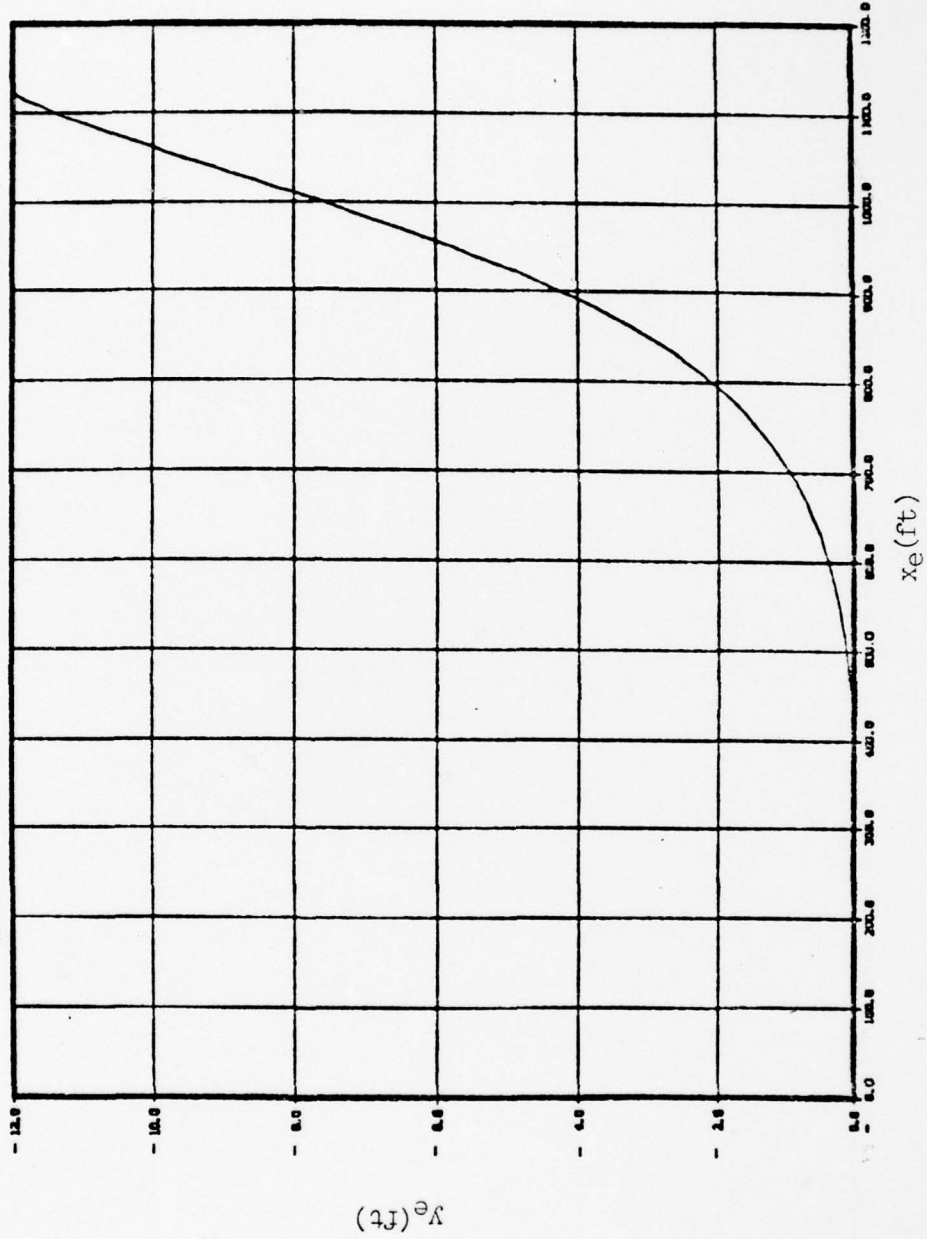


Fig. 47 Lateral Versus Longitudinal Displacement During Slideout with Existing Autopilot

decreasing at the rate of -1.5 /sec. Since the magnitude of the crosswind gust is only -3 ft/sec, it is highly probable that a larger gust will cause the roll angle to become unacceptably large.

A second conclusion is that the roll angle, roll rate, yaw angle, yaw rate, and side velocity are all important in the lateral-directional dynamics. The descriptions given above of the simulation results necessarily involve each of these variables to explain the behavior of the system. Hence, in order to control the lateral-directional dynamics of an ACRS-equipped vehicle, these variables must all be taken into account.

Analysis of the Lateral-Directional Instability

In order to gain an understanding of the cause of the instability discussed in the previous section, a linearized analysis of the slideout was performed. The analysis was carried out on a digital computer by using the LINEAR ANALYSIS feature of EASY (see Appendix B). The computer program produced a linearized approximation of the state model, as well as the eigenvalues of this linear model, at forward velocities of 200, 160, 120, 80, and 40 ft/sec. A sketch of the location of these eigenvalues in the complex plane is presented in Figure 48.

From this sketch the following observations are made: 1) the eigenvalues do not vary greatly with velocity, 2) three eigenvalues are near the origin, and, 3) one complex pair of eigenvalues has a positive real part. Elaboration of each of these observations is in order.

The first observation is used in the next section in designing an optimal controller for the landing phase. Since the variation of

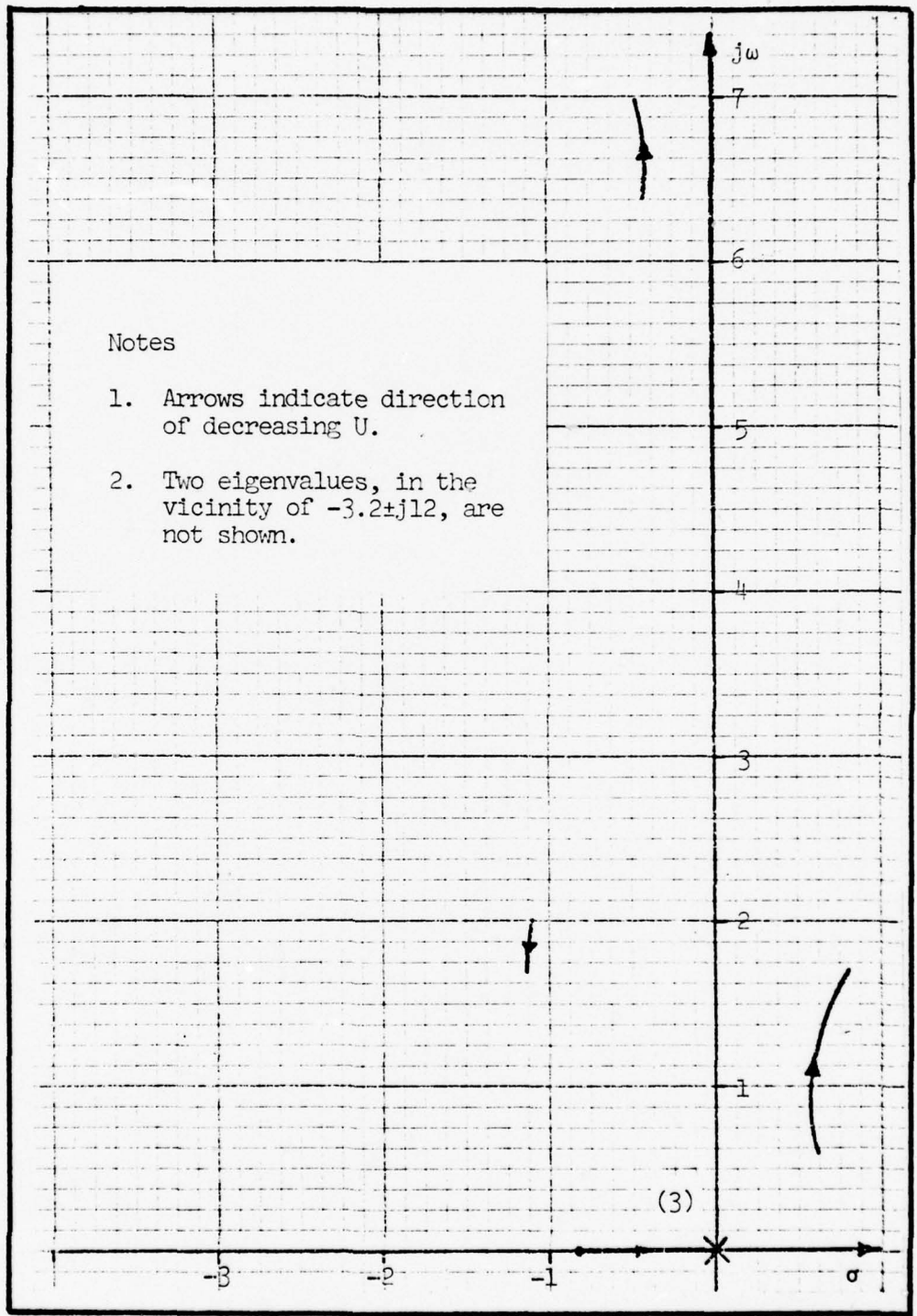


Fig. 48 Eigenvalue Locations for Variation in Forward Velocity from 200 ft/sec to 40 ft/sec

eigenvalues is small, a single set of constant feedback gains can be used for the entire slideout, thus greatly reducing the complexity of the controller.

The three eigenvalues near the origin are associated with the variables x_e , y_e , and ψ . This conclusion is based on the fact that the dynamics of the system are virtually independent of the values of these variables. Another way of expressing this is as follows: since x_e and y_e are the integrals of \dot{x}_e and \dot{y}_e , respectively, and since ψ is approximately the integral of R , a free s would appear in the denominator of any transfer function involving x_e , y_e , or ψ as output variables. This association of particular variables with specific eigenvalues is used in the next section, where it is desired to construct a reduced state model for the purpose of designing a lateral-directional control system.

The third observation stated above is the most important result of the linearized analysis of the slideout. The pair of eigenvalues in the right-half complex plane are associated with the instability noted in the slideout simulations. The location of these eigenvalues must be modified such that either 1) there are no eigenvalues with positive real parts, or 2) the magnitude of the real parts of any eigenvalues in the right-half complex plane are sufficiently small such that the slideout is terminated before the system deviates excessively from the desired state. The optimal control design developed later in this chapter effectively relocated these eigenvalues into the left half of the complex plane.

Design of a Lateral-Directional Control System for the Slideout

Due to time constraints in the research phase of this report, only one design technique has been attempted. While the magnitude of the problem has been significantly reduced by the development of a slideout model, much work remains to be done in order to develop a practical controller. The optimal control design presented below is only one approach to the problem, and while it appears to be highly successful, other design approaches as well as variations to this design should be pursued.

Continuous optimal control theory is used in designing a lateral-directional control system. As this theory is well developed in the literature (Refs 13 and 2), only a brief description of this method is discussed.

Problem Formulation. The overall objectives to be met in the design process are 1) to keep the vehicle within the confines of some (as yet) unspecified landing area, and 2) to maintain an acceptable orientation of the vehicle during the entire slideout. It is assumed at the outset that a human controller on the ground is to have some control of the vehicle. Hence, the design of a control scheme need meet only the second objective stated above, provided a sufficient means for controlling the system on the ground is available. Therefore, direct control of lateral displacement, y_e , is not attempted in the design of a control system, since it is assumed that lateral displacement can be controlled by controlling the roll angle. This appears to be a reasonable assumption in light of the slideout results presented earlier, but this assumption should be verified.

While the entire system could be treated as a multiple-input/multiple-output system, it is possible to decompose the system into longitudinal and lateral-directional reduced-state models. Each of these systems can be treated as a single-input/multiple-output system, and this approach is taken here.

Four longitudinal states were selected on physical grounds: θ , Q , W , and h_{cg} (altitude of the center of gravity). These four states, two of the three states associated with eigenvalues equal to zero (x_e and y_e), and U were all eliminated from the full 12-state system in an attempt to identify the lateral-directional dominant states. The remaining states are ϕ , ψ , V , P , and R . Various attempts to reduce the lateral-directional states further were fruitless. These five states may well be the minimum number of states which can be used to design an effective control system. Fortunately each of these five states is capable of being sensed onboard the vehicle, although sensor accuracy must be considered. A linear analysis was performed using the digital computer program, EASY (see Appendix B), at $U = 120$ ft/sec in order to verify that the 5 states chosen are the dominant lateral-directional states. The linearized state equation at this velocity is

$$\dot{x} = \begin{bmatrix} 0. & 0. & 0. & 1. & 0. \\ 0. & 0. & 0. & 0. & 1. \\ .0367 & .3600 & -.0770 & .0052 & -2.090 \\ -3.050 & -3.580 & -.0675 & -1.110 & .7150 \\ 3.433 & -1.030 & -.0500 & .2784 & -.1572 \end{bmatrix} x + \begin{bmatrix} 0 \\ 0 \\ 0 \\ -82. \\ 6.6 \end{bmatrix} u \quad (110)$$

where $x^T = [\phi, \psi, V, P, R]$, and $u = \delta_A$.

The eigenvalues of this state model are given below, along with the nearest corresponding full-state eigenvalues for comparison.

5 State Lateral- Directional Eigenvalues	Corresponding Full-State Eigenvalues
-.09015	-.008596
.7447±j1.505	.6460±j1.341
-1.372±j1.822	-1.220±j1.808

Although the agreement is not excellent, the locations of the 5-state system roughly approximate the dominant lateral-directional dynamics.

The system in equation 110 is in a form which allows optimal control theory to be applied. Since the immediate objective is to regulate the system (i.e., maintain the system states near the origin of the state space), the problem is properly termed a linear, time-invariant, optimal regulator problem. A mathematical description is given by first defining a quadratic performance index, J , for the problem at hand:

$$J = \frac{1}{2} \int_{t_0}^{\infty} [x^T Q x + u^2] dt \quad (111)$$

where Q is a weighting matrix. The solution to the optimal linear regulator problem with this performance index is in the form of a control law with a constant feedback gain matrix, F :

$$u^* = -F x \quad (112)$$

where the "*" symbol is used to denote the optimal control. A feedback gain matrix was determined by using OPTCON, a digital computer program (Ref 22). For reasons discussed later, the weighting matrix was chosen to be

$$Q = \begin{bmatrix} 0.1 & 0 & 0 & 0 & 0 \\ 0 & 1 & 0 & 0 & 0 \\ 0 & 0 & 1 & 0 & 0 \\ 0 & 0 & 0 & 1 & 0 \\ 0 & 0 & 0 & 0 & 1 \end{bmatrix}$$

which resulted in the feedback matrix

$$F = \begin{bmatrix} -3.6156 \\ -1.7124 \\ -.2919 \\ -1.2103 \\ -2.1646 \end{bmatrix}$$

The use of these feedback gains results in a new set of eigenvalues for the 5-state system as shown below.

Eigenvalues of 5-State System without Control	Eigenvalues of 5-State System with Optimal Control
-.09015	-.166
.7477±j1.505	-1.52
-1.372±j1.822	-82.24
	-1.19±j1.85

The elements of the weighting matrix were chosen such that all state deviations are penalized equally except for roll angle. The choice of the weighting matrix is arbitrary so long as Q is positive semi-definite, but the performance of the system is significantly affected by the elements of Q. While the particular values chosen for the Q matrix in this control design provide a stable system, a more refined design process would involve a tuning of Q to provide even better dynamic characteristics.

Verification of the Lateral-Directional Control System

Three simulation runs were performed with varying crosswind magnitudes introduced two seconds into the simulation. The existing pitch control system, and the lateral-directional control system designed above were used. Results of these simulations are shown in Figures 49 through 57. The longitudinal states are not shown since

SLIDEOUT SIMULATION WITH OPTIMAL CONTROLLER (-3 FT/SEC GUST)

03/03/70 17.13.16.

SIMULATION DISPLAY 3

CASE NO. 1

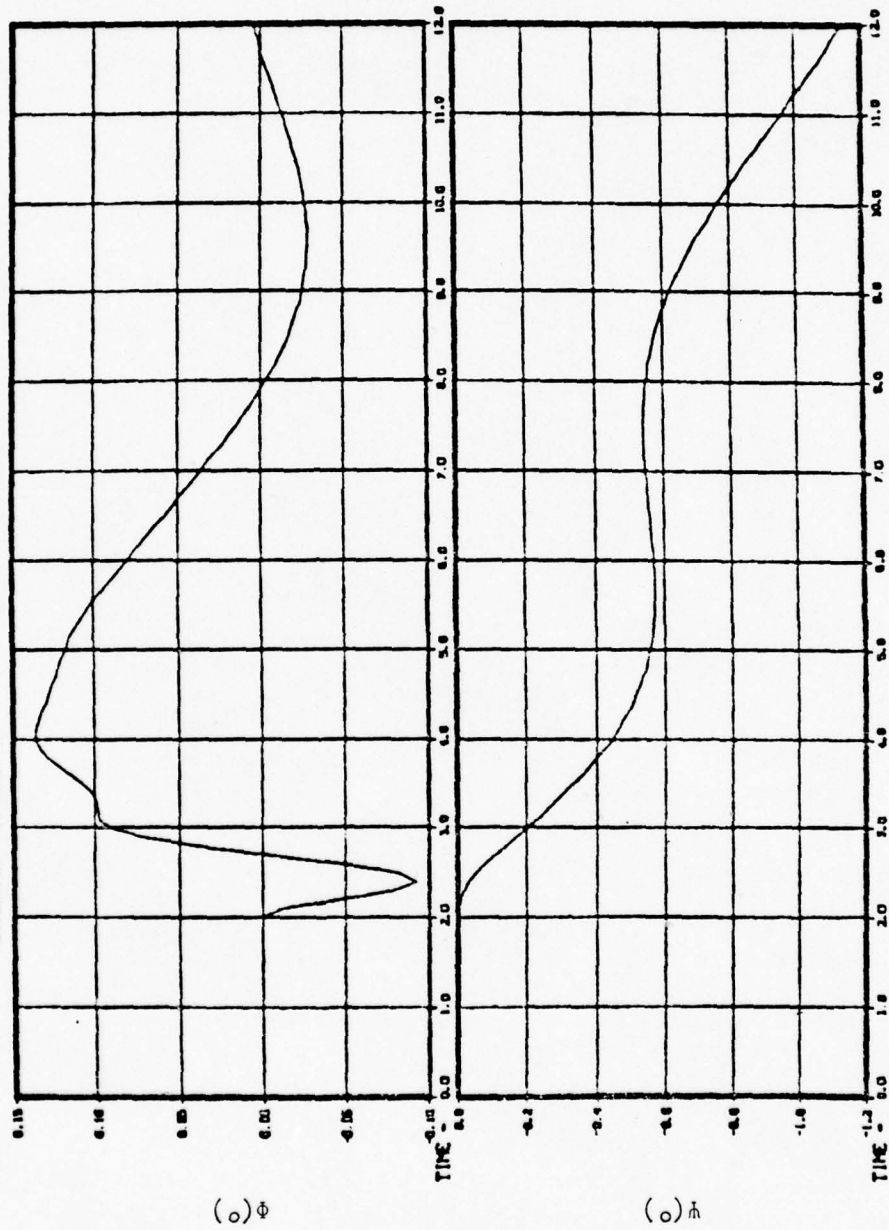


Fig. 49 Roll Angle and Yaw Angle Time Histories During Slideout with Optimal Controller (-3 ft/sec Gust)

SLIDEOUT SIMULATION WITH OPTIMAL CONTROLLER (-3 FT/SEC BUST)

CASE NO. 1

SIMULATION DISPLAY 4

03/03/78 17.13.16.

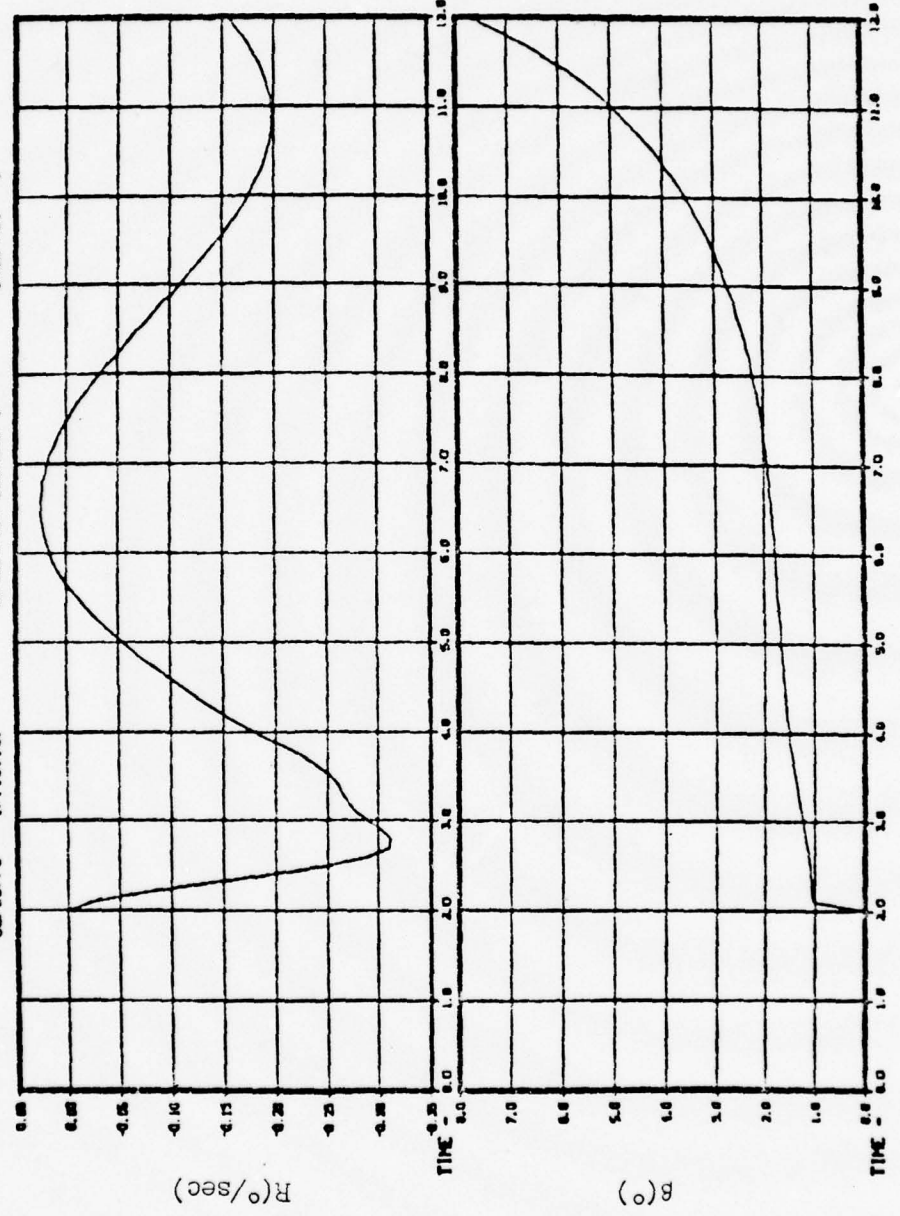


Fig. 50 Sideslip Angle and Yaw Rate Time Histories During Slideout with Optimal Controller (-3 ft/sec Gust)

SLIDEOUT SIMULATION WITH OPTIMAL CONTROLLER (-3 FT/SEC GUST)

03/03/78 17.13.16.

SIMULATION DISPLAY 5

CYCLE NO. 1

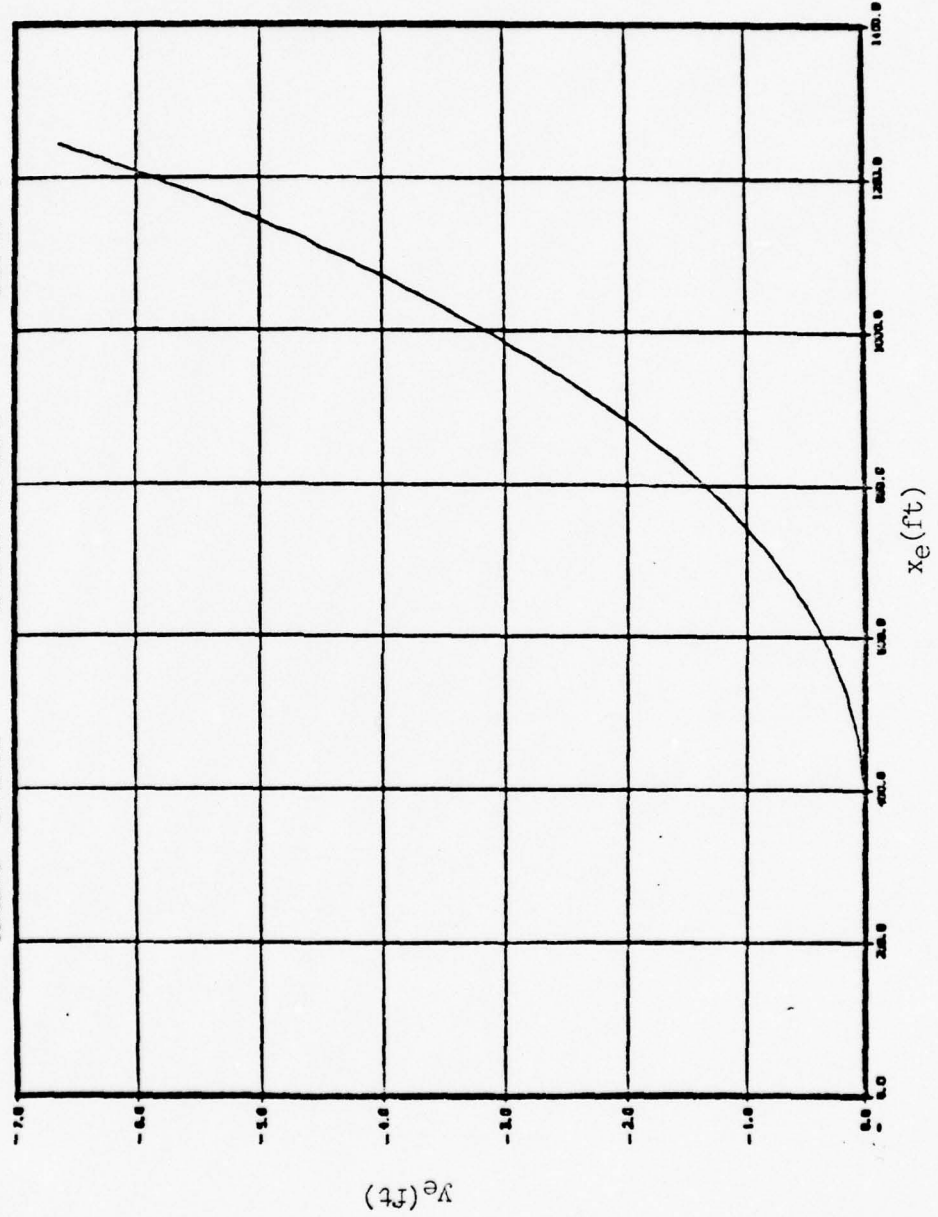


Fig. 51 Lateral Versus Longitudinal Displacement During Slideout with Optimal Controller (-3 ft/sec Gust)

SLIDEOUT SIMULATION WITH OPTIMAL CONTROLLER (-10 FT/SEC GUST)
 03/02/78 17.53.30. SIMULATION DISPLAY 3 CASE NO. 1

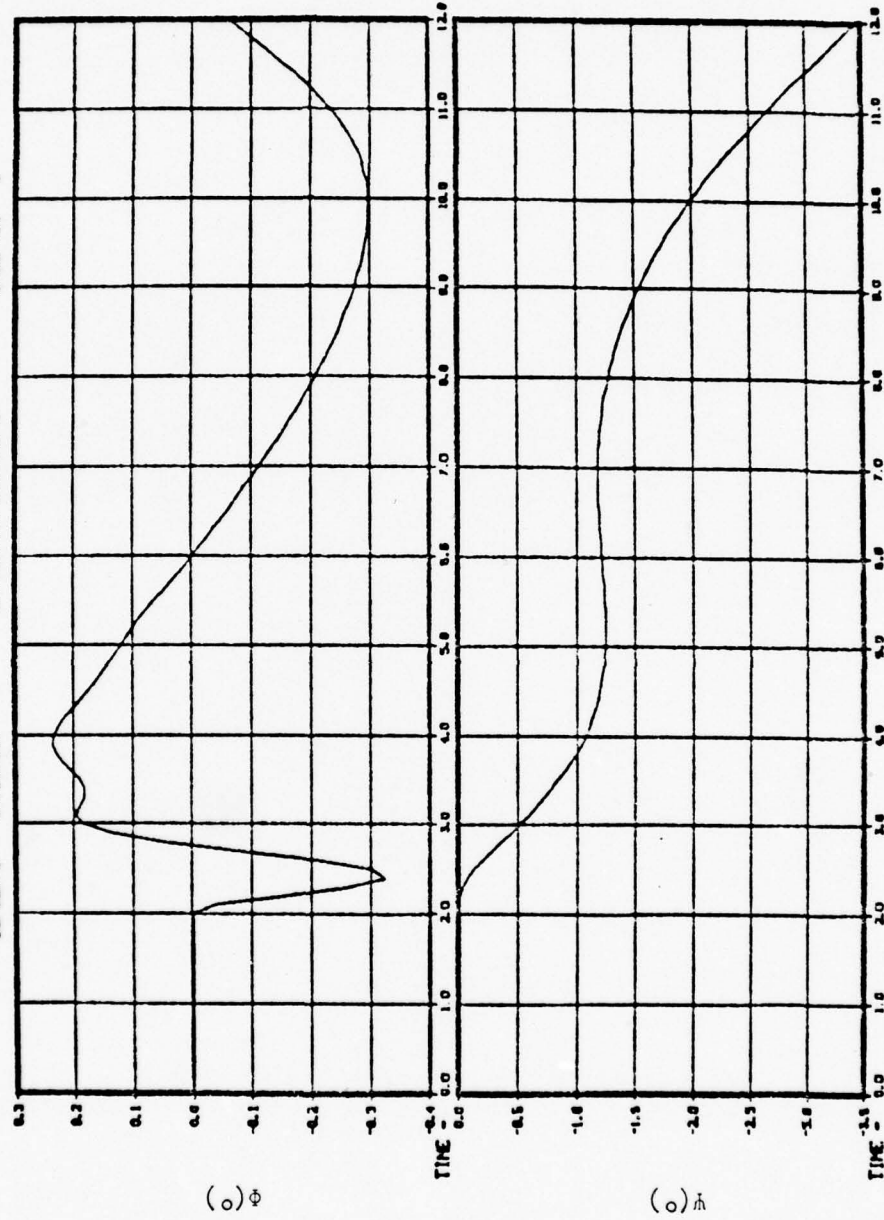


Fig. 52 Roll Angle and Yaw Angle Time Histories
 During Slideout with Optimal Controller (-10 ft/sec Gust)

SLIDEOUT SIMULATION WITH OPTIMAL CONTROLLER (-10 FT/SEC GUST)
 03/02/78 17:53:30. SIMULATION DISPLAY 4 CASE NO. 1

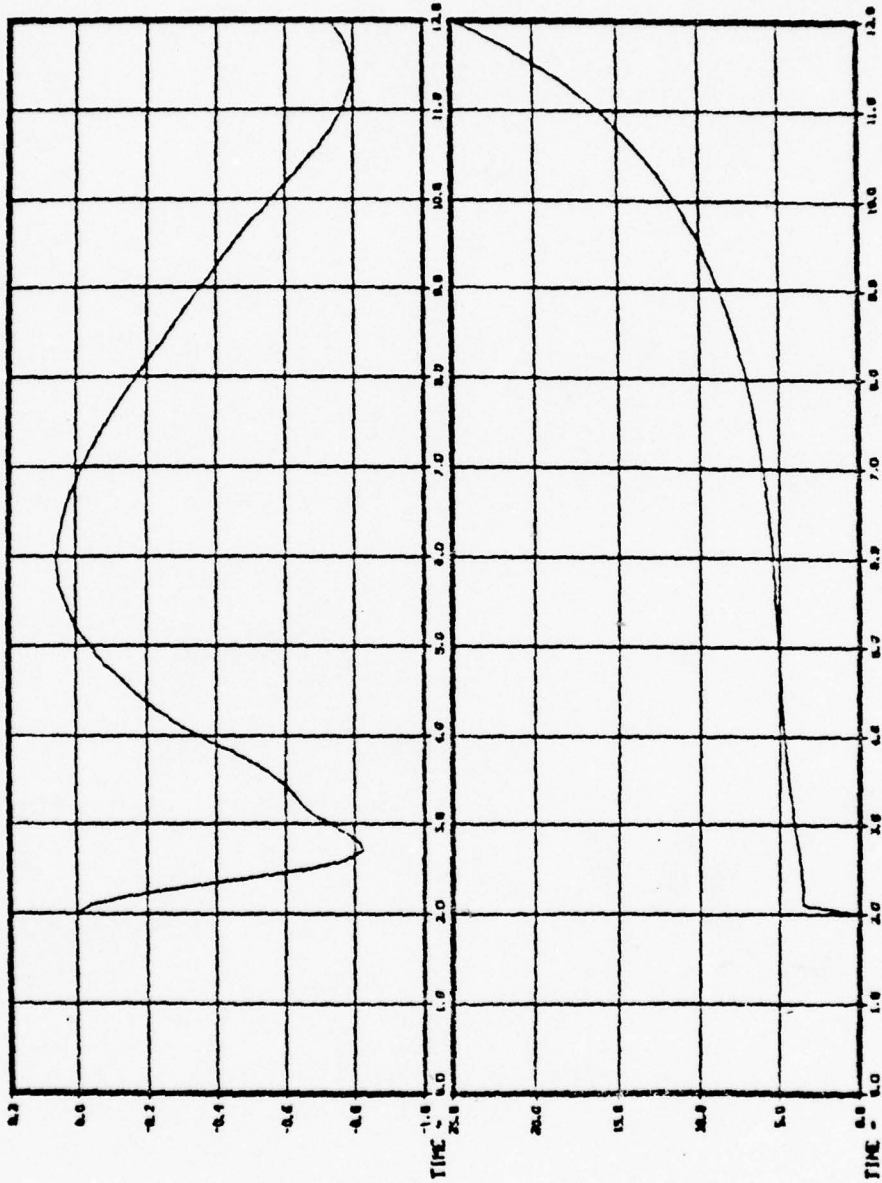


Fig. 53 Sideslip Angle and Yaw Rate Time Histories
 During Slideout with Optimal Controller (-10 ft/sec Gust)

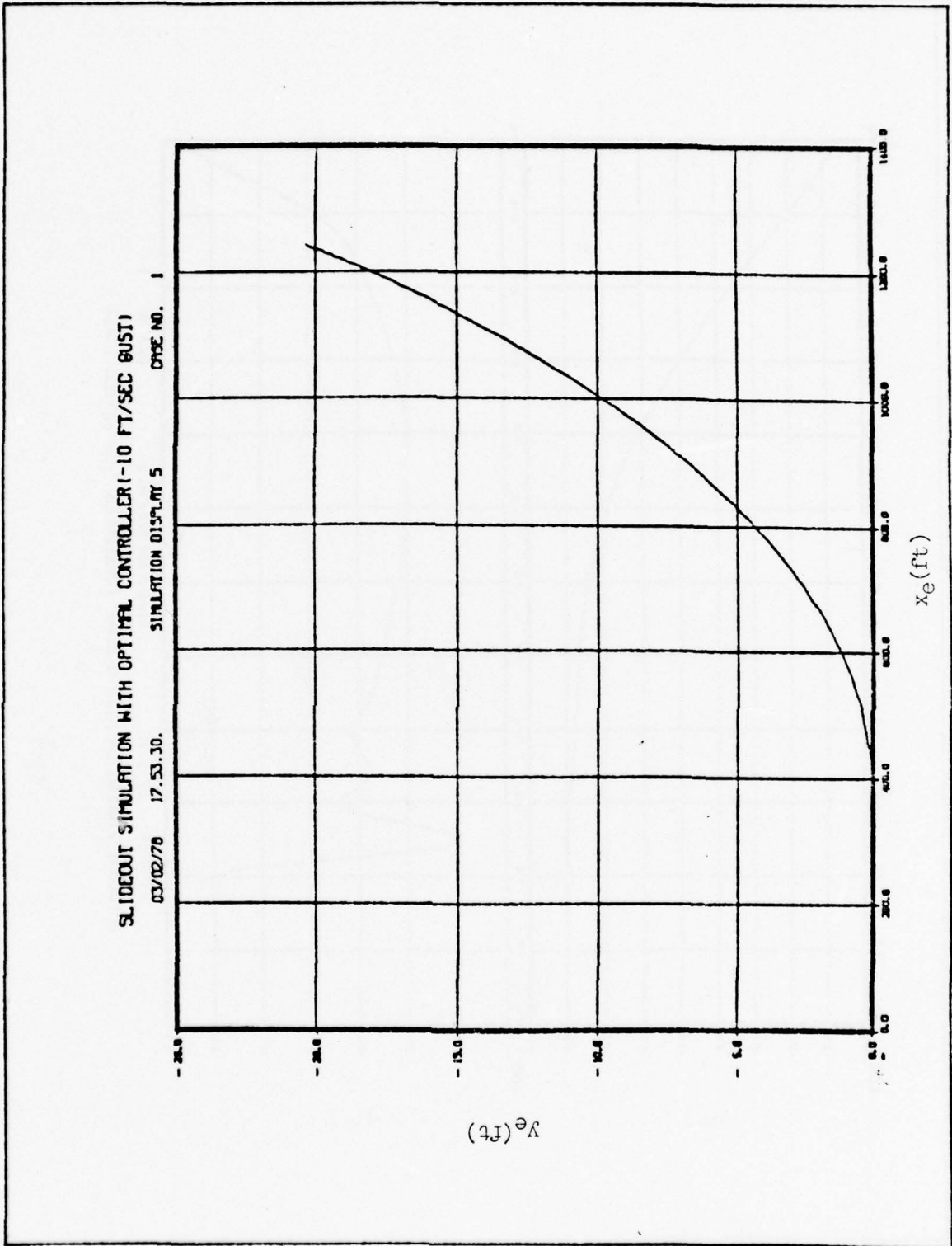


Fig. 54 Lateral Versus Longitudinal Displacement During Slideout with Optimal Controller (-10 ft/sec Gust)

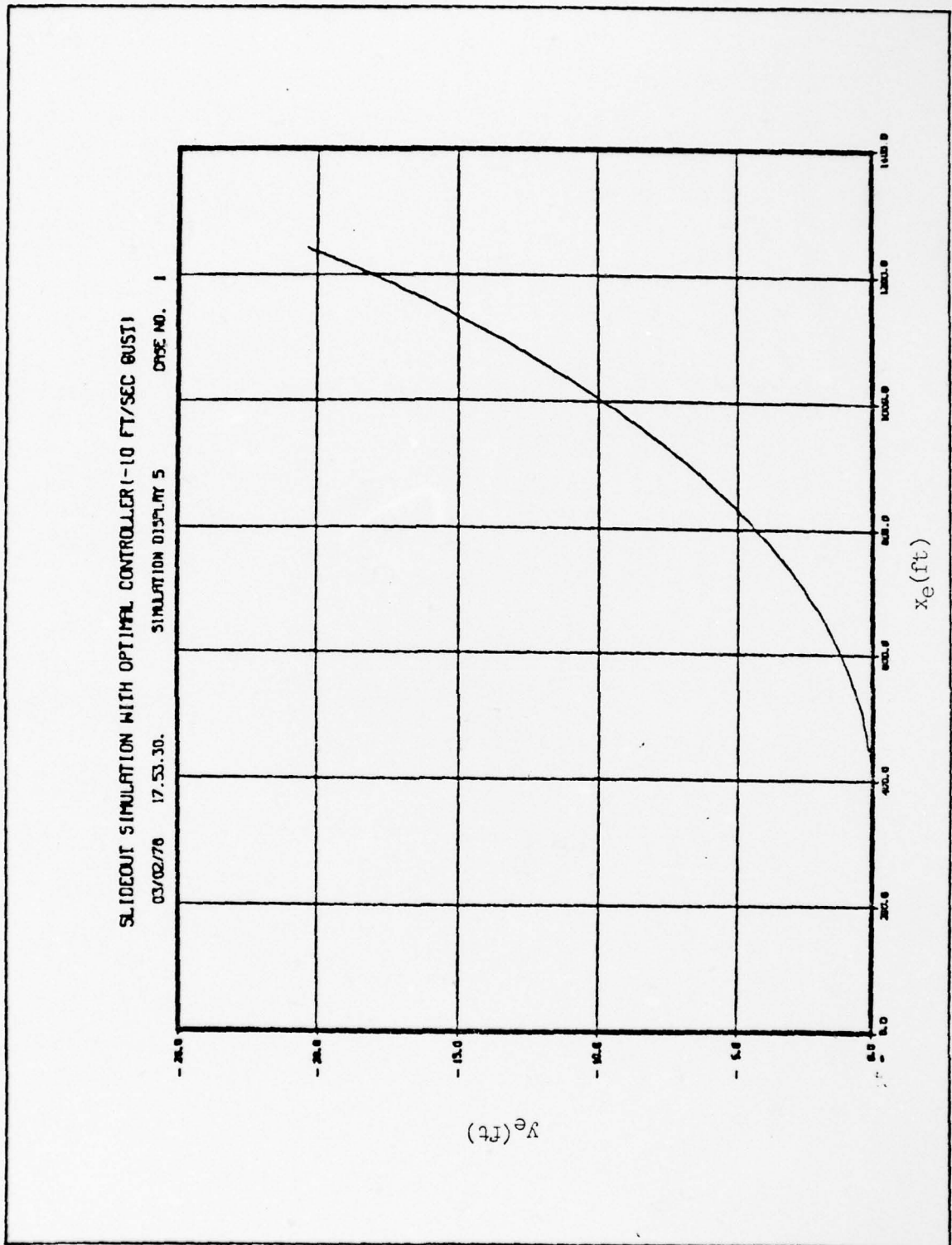


Fig. 54 Lateral Versus Longitudinal Displacement During Slideout with Optimal Controller (-10 ft/sec Gust)

SLIDEOUT SIMULATION WITH OPTIMAL CONTROLLER (-25 FT/SEC GUST)

03/02/78 10.07.31. SIMULATION DISPLAY 3 CASE NO. 1

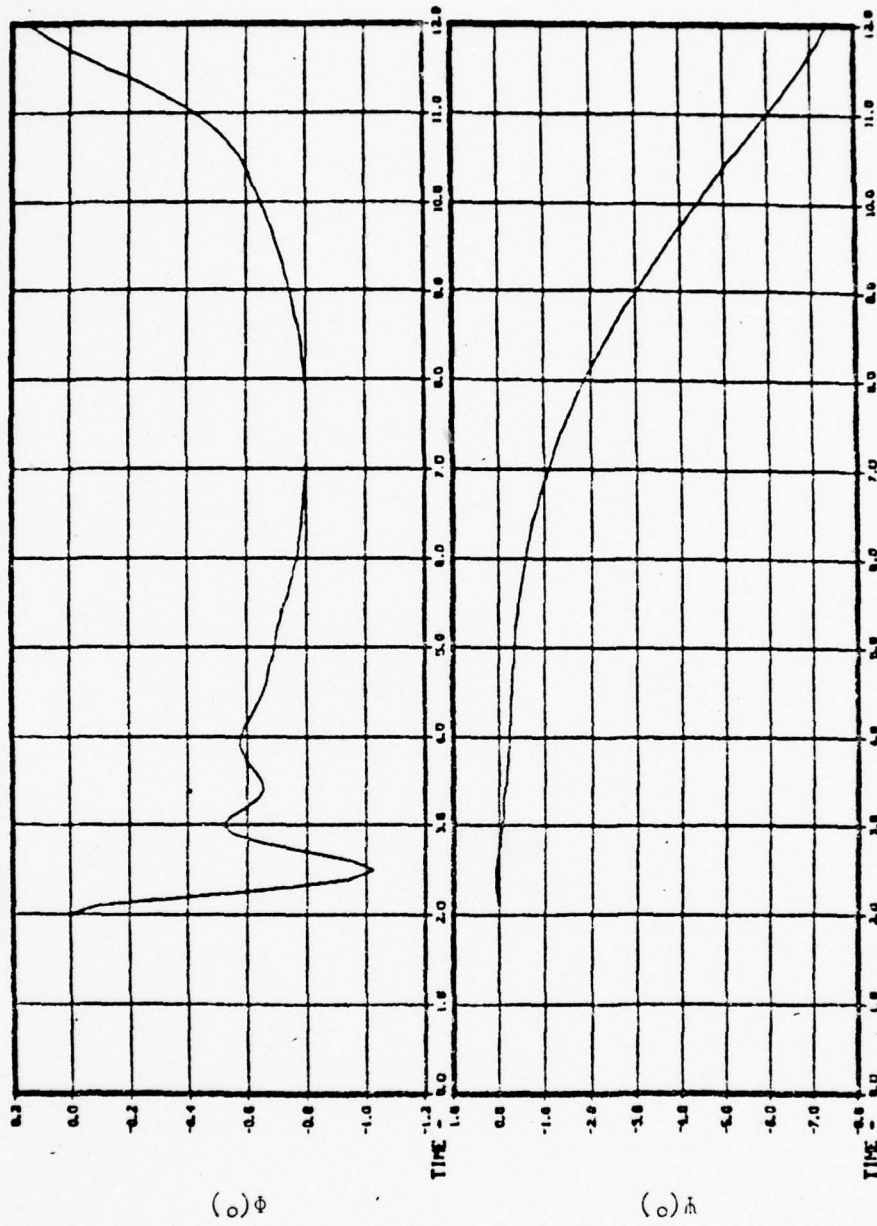


Fig. 55 Roll Angle and Yaw Angle Time Histories
During Slideout with Optimal Controller (-25 ft/sec Gust)

SLIDEOUT SIMULATION WITH OPTIMAL CONTROLLER (-25 FT/SEC GUST)
 03/02/78 18.07.31. SIMULATION DISPLAY 4 PAGE NO. 1

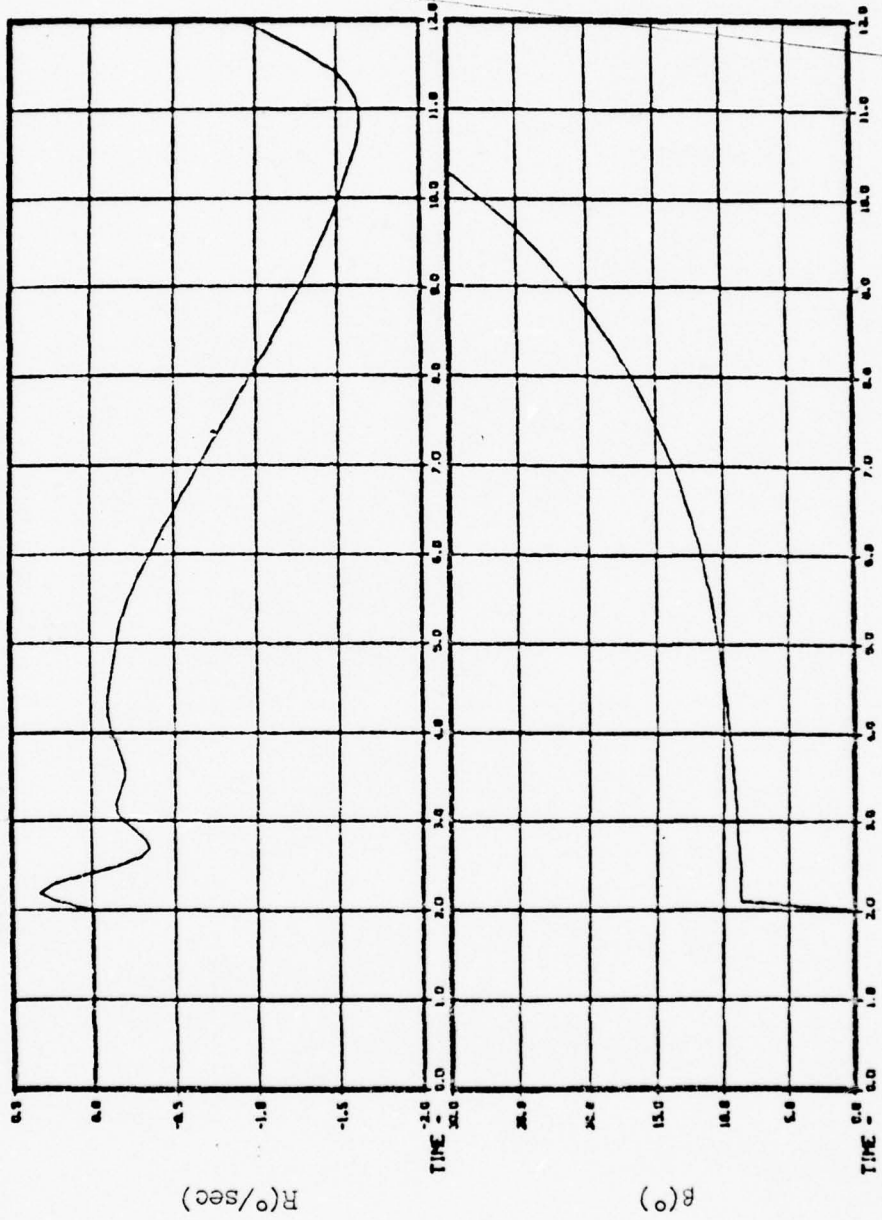


Fig. 56 Sideslip Angle and Yaw Rate Time Histories During Slideout with Optimal Controller (-25 ft/sec Gust)

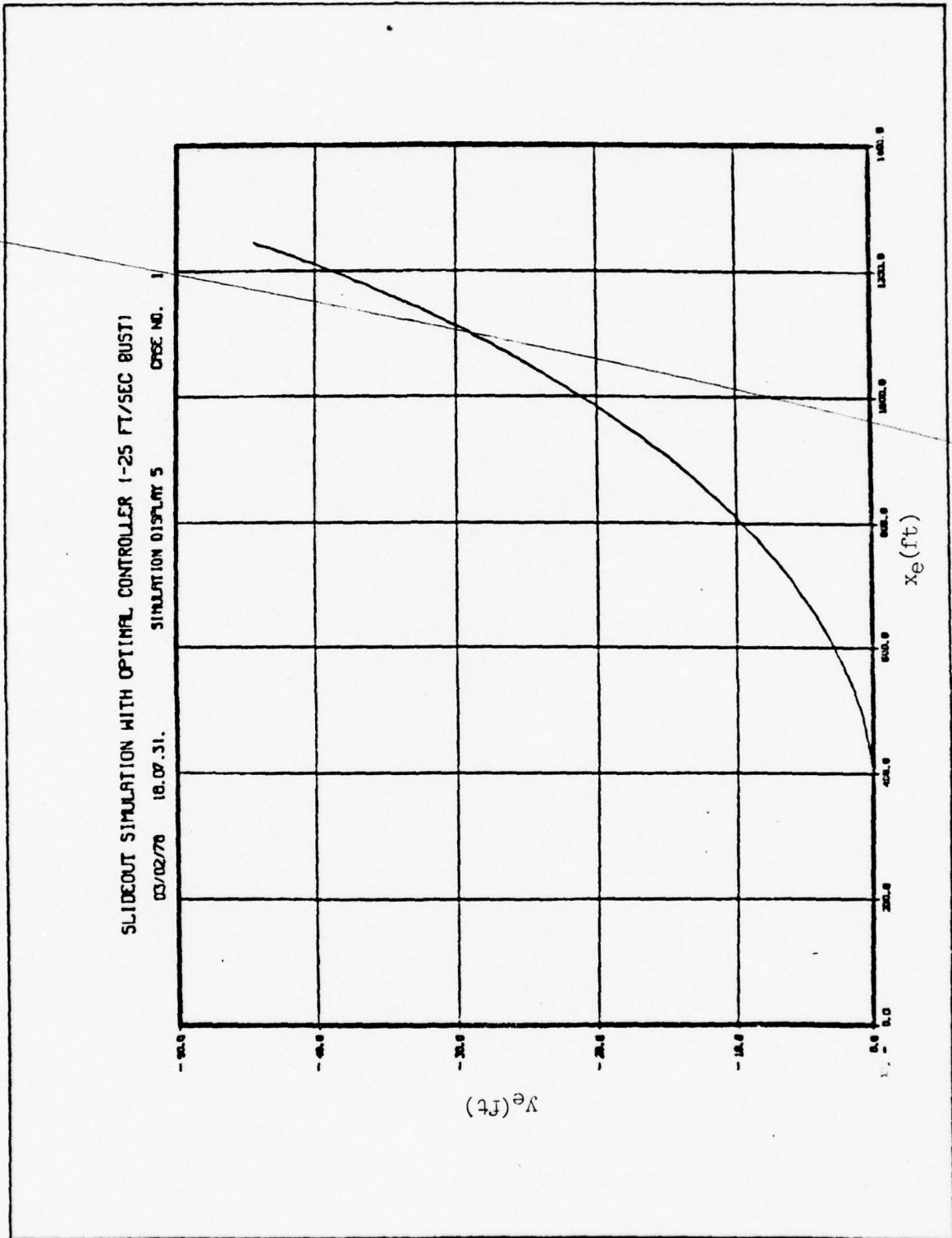


Fig. 57 Lateral Versus Longitudinal Displacement During Slideout with Optimal Controller (-25 ft/sec Gust)

their time responses are very similar to those in the case of the slideout with the existing autopilot.

The dramatic improvement in stability is readily apparent. The lateral deviation, y_e , is -4.7 ft with a -3 ft/sec constant crosswind gust at 2 seconds, which is less than 50% of the deviation achieved without the optimal controller. The deviations are considerably higher for crosswind gusts of -10 ft/sec and -25 ft/sec (-20 ft and -44 ft, respectively), but it is believed that the stability of the vehicle is such that a human operator with control of the roll angle could effectively control the ground track.

Although the magnitude of the aileron deflection angle and angular rate are much less than their maximum values ($\pm 10^\circ$, $53^\circ/\text{sec}$, respectively) during the entire slideout with crosswind values of -3 ft/sec and -10 ft/sec, the deflection angle did exceed its limit in the -25 ft/sec gust simulation at a forward velocity of approximately 60 ft/sec. Thus, there is a need for low speed roll control since the ailerons become ineffective at low speeds.

Low speed roll control can be achieved through the use of roll thrusters. The output of these devices is similar to the yaw thruster output in that the forces are constant in either direction. A design of a low speed roll control system is not undertaken here, but a design procedure very similar to that given in Chapter III would likely be very fruitful.

Conclusions

The following conclusions are made based on research efforts presented in this chapter:

1. The ACRS-equipped Jindivik is unstable during slideout with the existing control system engaged or disengaged.
2. A single complex pair of eigenvalues lies in the right half complex plane which is a result of the lateral-directional state variable relationships.
3. A reduced-state optimal control design is effective in stabilizing the full-state system.
4. Some method of roll control at low speed is required.

VI. SUMMARY AND RECOMMENDATIONS

In this, the sixth and concluding chapter, highlights of the preceding five chapters are summarized, and areas for further research are recommended. In the summary section, some comments on the generality of the findings of this report are given. The recommendations for further research are given in two sections: 1) recommendations for additional in-flight study, and 2) recommendations for further investigation of the slideout.

Summary

Following the introductory chapter, which provides background information on air cushion recovery systems, a nonlinear, six degree of freedom aerodynamic model is derived. The aerodynamic model includes the existing autopilot control laws. Furthermore, the model allows selection of thrust and flaps setting.

Chapter III provides 1) an analysis of the bare airframe, 2) an analysis of the existing autopilot, 3) an aerodynamic instability, 4) a proposed solution to the stability problem, and 5) a verification of the proposed solution. Although the analyses in Chapter III are based on the Jindivik aircraft in particular, the yaw instability discovered is primarily attributable to the addition of an ACRS. Hence, the problem is of a general nature, and is likely to occur again in the development of air cushion recovery systems.

The fourth chapter provides a spring-damper approach to modeling ground reaction and frictional forces which are transmitted to the ACRS trunk during a slideout. A specific trunk model for the Jindivik aircraft is achieved, but the approach taken can be applied to other ACRS-equipped vehicles. While experimentally obtained data is used in Chapter IV to model the trunk, new ACRS designs may be analytically evaluated by the use of models which calculate the pressure distribution and deformation of the trunk. The results of these simulations could provide sufficient information on the roll, pitch, and heave characteristics of the ACRS-vehicle combination to allow a spring-damper model to be developed.

Chapter V presents a cursory analysis of the Jindivik aircraft, equipped with an ACRS, during the slideout. A stability problem is identified by both simulations of the slideout and by analysis of linearized models at different forward velocities. It is not known at this time whether the cause of this instability is peculiar to the Jindivik, or if this is a more general trait of air cushion recovery systems.

Recommended Additional Investigation (In-Flight)

Additional aerodynamic data on the Jindivik equipped with an air cushion recovery system is highly recommended. An interesting thesis for an aerodynamics student might well be an analytical study of the effects of an ACRS on the aerodynamic characteristics of an aircraft. Wind tunnel testing is also needed, especially for the lateral-directional aerodynamic coefficients.

The yaw controller design in Chapter III requires considerably more attention than could be given in this report. The following areas are specifically recommended for future investigation:

1. Development of a control law for the yaw thruster when the aircraft is in a turn.
2. Determination of the effects of varying airspeed on the performance of the yaw controller.
3. Implementation problems which might arise, such as, 1) sensor accuracy required versus present capabilities, and 2) minimum sampling time required for digital implementation.

Recommended Additional Investigation (Slideout)

Many challenging and stimulating control problems arise from the development of the aerodynamic and trunk models. Some of the more important problems which require additional investigation are given below.

1. Eigenvalue sensitivity to parameter variation.

While considerable effort has been expended in modeling the aerodynamic and trunk forces, some of the parameters needed could not be calculated with great precision. Since the location of the eigenvalues is instrumental in designing a controller, a knowledge of how the eigenvalues vary with certain parameters is needed.

2. Sensitivity of optimal controller performance to eigenvalue variations.

The optimal control technique described in Chapter V may be very sensitive to errors in the eigenvalue locations. Specifically, if the optimal controller acts so as to cancel the eigenvalues in the right-half complex plane, inexact cancellation might occur and, thus, the system might still be unstable.

3. Variations in the optimal control design.

Several variations in the optimal control problem formulation could be analyzed. Among the most promising of these are

- (i) Allowing the control matrix, B , to vary with time.

(Since the lateral-directional control (aileron deflection angle) varies with the square of total velocity, the use of a constant B matrix in Chapter V is rather unrealistic.)

- (ii) Changing the limits on the quadratic performance integral (equation 111) to a finite time. (The feedback gains would become time varying, but improved performance might be obtained.)

- (iii) Tuning the weighting matrix, Q .

4. Evaluation of other means of control during the slideout.

The yaw thruster is capable of delivering a small force (approximately 10 lbs) and a yaw moment (approximately 100 lbs) with the engine at idle. This force and moment might be used effectively at lower speeds.

Also, if a thrust reverser were to be utilized, the engine could be operated at a higher thrust level, and a significant yawing moment would be available from the yaw thruster.

While the ailerons have been shown to be effective in controlling the vehicle over a wide range of velocity, roll control is needed at low speeds. The use of roll thrust devices is a recommended area for further investigation.

5. Analysis of the landing transient.

While the trunk model described in this report is not suitable for simulating the landing transient, a nonlinear formulation of spring damping and stiffness coefficients might be all that are necessary to produce a reasonable model. For example, the spring forces could be modeled as being proportional to the cube of the spring displacement (in compression).

6. Recommendations for pitch control techniques.

As mentioned in Chapter V, the sliding friction force produces a large nose-down pitching moment during slideout. A successful means of controlling this pitch is needed.

Conclusion

Clearly there are many problems remaining to be solved before air cushion landing gear can be considered as an effective replacement for conventional gear. The problems, however, do not in any way appear to be insurmountable.

Appendix A

Pertinent Aerodynamic Data

for the

Jindivik Drone Aircraft

This appendix consists of two main sections. The first section contains tabular listings of the wind tunnel data and curve fits to this data. The second section presents certain aerodynamic data provided by the manufacturer of the Jindivik, as well as some derived aerodynamic parameters.

SECTION I

Wind Tunnel Data

All wind tunnel data was taken by the Government Aircraft Factories of Australia (Ref 15). A one-quarter scale model was used. The vehicle was configured with an ACRS trunk and a 3-inch (full scale) pipe on the port side. The pipe was added to the vehicle to supply bleed air from the turbine engine to the trunk of the ACRS.

Pertinent wind tunnel data is presented in the following tables. Table I-A is a listing of the longitudinal aerodynamic coefficients (C_L , C_D , and C_M) versus angle of attack, α , for a flaps-up configuration. Table II-A is a listing of the same coefficients but with the flaps down. Variations in these coefficients with sideslip angle are available, but these variations are small and are therefore neglected.

Tables III-A through VI-A consist of lateral-directional aerodynamic coefficients versus sideslip angle, β , for the flaps-up configuration. The same information is given in Tables VII-A through X-A but for a flaps-down configuration. These tables show a variation in the lateral-directional coefficients with angle of attack for both flap settings.

Tables XI-A through XIII-A consist of changes in the longitudinal aerodynamic coefficients with elevator deflection angle, δ_E , for the flaps-up configuration. The flaps-down configuration is not significantly different from the flaps-up configuration and, hence, is not shown here.

Table I-A

LONGITUDINAL AERODYNAMIC COEFFICIENTS (Flaps-Up)

ANGLE OF ATTACK (DEGREES)	C_L	C_D	C_M
.09	.1430	.0940	.0562
2.19	.3143	.1027	.0415
4.30	.4982	.1114	.0367
6.41	.6770	.1585	.0336

Table II-A

LONGITUDINAL AERODYNAMIC COEFFICIENTS (Flaps-Down)

ANGLE OF ATTACK (DEGREES)	C_L	C_D	C_M
-1.75	.4096	.1609	-.0063
.33	.5443	.1650	-.0071
2.45	.7310	.1884	-.0122
4.55	.9107	.2218	-.0222

TABLE III-A
 LATERAL DIRECTIONAL AERODYNAMIC COEFFICIENTS
 FLAPS-UP ALPHA = 0.1 DEGREES

BETA	CY	CLL	CN
-7.0	.0320	.0061	-.0015
-5.0	.0345	.0034	-.0007
-3.0	.0338	.0007	-.0002
-2.0	.0252	-.0003	-.0006
-1.0	.0139	-.0016	-.0002
0.0	.0124	-.0033	-.0009
1.0	-.0174	-.0035	-.0009
2.0	-.0182	-.0044	-.0010
3.0	-.0208	-.0055	-.0010
5.0	-.0569	-.0079	-.0005
7.0	-.0869	-.0106	.0003

TABLE IV-A
 LATERAL DIRECTIONAL AERODYNAMIC COEFFICIENTS
 FLAPS-UP ALPHA = 2.2 DEGREES

BETA	CY	CLL	CN
-7.0	.0003	.0000	.0025
-5.0	.0503	.0003	.0022
-3.0	.0555	.0027	.0027
-2.0	.0657	.0015	.0003
-1.0	.0154	.0000	-.0006
0.0	.0042	-.0015	-.0010
1.0	.0016	-.0026	-.0024
2.0	-.0061	-.0040	-.0033
3.0	- - - NO DATA AVAILABLE - - -	- - -	- - -
5.0	-.0593	-.0085	-.0033
7.0	-.0703	-.0118	-.0030

TABLE V-9
 LATERAL DIRECTIONAL AERODYNAMIC COEFFICIENTS
 FLAPS-UP ALPHA = 4.5 DEGREES

DE IN	CY	CIL	CN
-7.0	.0355	.0119	.0012
-5.0	.0506	.0020	.0023
-3.0	.0314	.0059	.0023
-2.0	.0314	.0019	.0011
-1.0	.0153	.0001	-.0000
0.0	.0050	-.0017	-.0018
1.0	.0120	-.0033	-.0033
2.0	.0305	-.0053	-.0040
3.0	-.0088	-.0072	-.0044
5.0	-.0213	-.0165	-.0041
7.0	-.0596	-.0145	-.0023

TABLE VI-A
 LATERAL DIRECTIONAL AERODYNAMIC COEFFICIENTS
 FLAPS-UP ALPHA = 6.4 DEGREES

BETA	CY	CLL	CH
-7.0	.0002	.0149	.0015
-5.0	.0542	.0101	.0019
-3.0	.0308	.0052	.0021
-2.0	.0234	.0030	.0013
-1.0	.0157	.0015	.0000
0.0	.0076	-.0016	-.0016
1.0	.0057	-.0035	-.0014
2.0	-.0010	-.0058	-.0022
3.0	-.0113	-.0002	-.0020
5.0	-.0334	-.0129	-.0024
7.0	-.0537	-.0177	-.0014

TABLE VII-R
 LATERAL DIRECTIONAL AERODYNAMIC COEFFICIENTS
 FLAPS-DOWN ALPHA = -1.75 DEGREES

BETA	CY	CLL	CN
-7.0	.1019	.0112	-.0004
-5.0	.0813	.0083	-.0001
-3.0	.0592	.0051	-.0003
-2.0	.0478	.0033	-.0009
-1.0	.0329	.0021	-.0010
0.0	.0000	.0000	-.0019
1.0	.0119	.0001	-.0052
3.0	.0334	-.0014	-.0049
5.0	.0651	-.0027	-.0042
7.0	.0710	-.0025	-.0025
		-.0012	-.0014

TABLE VIII-A
 LATERAL DIRECTIONAL AERODYNAMIC COEFFICIENTS
 FLAPS-DOWN ALPHA = .30 DEGREES

BETA	CY	CLL	CN
-7.0	.0806	.0133	.0318
-5.0	.0553	.0091	.0092
-3.0	.0333	.0000	.0121
-2.0	.0205	.0003	.0014
-1.0	.0037	.0002	.0022
0.0	-.0023	.0000	.0007
1.0	-.0045	-.0003	.0004
2.0	-.0124	-.0022	-.0004
3.0	-.0185	-.0046	-.0010
5.0	-.0379	-.0090	-.0015
7.0	-.0646	-.0145	-.0014

TABLE IX-A
 LATERAL DIRECTIONAL AERODYNAMIC COEFFICIENTS
 FLAPS-DOWN ALPHA = 2.45 DEGREES

BETA	CY	CLL	CH
-7.0	.0791	.0103	.0002
-5.0	.0511	.0103	.0026
-3.0	.0251	.0003	.0001
-2.0	.0108	.0000	.0004
-1.0	-.0027	.0007	.0043
0.0	-.0113	.0013	.0007
1.0	-.0055	-.0011	.0000
2.0	-.0141	-.0007	.0003
3.0	-.0201	-.0003	.0011
5.0	-.0358	-.0104	.0000
7.0	-.0591	-.0187	-.0004

TABLE X-A
 LATERAL DIRECTIONAL AERODYNAMIC COEFFICIENTS
 FLAPS-DOWN ALPHA = 4.55 DEGREES

BETA	CY	CLL	CH
-7.0	.0297	.0195	-.0010
-5.0	.0231	.0148	-.0003
-3.0	.0082	.0055	.0003
-2.0	.0237	.0069	.0002
-1.0	.0194	.0048	-.0002
0.0	.0131	.0013	-.0016
1.0	.0142	-.0011	-.0022
2.0	.0051	-.0037	-.0027
3.0	-.0072	-.0053	-.0021
5.0	-.0226	-.0119	-.0003
7.0	-.0597	-.0168	.0010

Table XI-A

CHANGE IN LIFT COEFFICIENT WITH ELEVATOR DEFLECTION ANGLE

ELEVATOR DEFLECTION (DEGREES)	CHANGE IN LIFT COEFFICIENT			
	ALPHA = .1°	ALPHA = 2.2°	ALPHA = 4.3°	ALPHA = 6.4°
-15.0	-.0800	-.0816	-.0837	-.0765
-10.0	-.0507	-.0578	-.0477	-.0476
-5.0	-.0232	-.0259	-.0242	-.0211
0.0	0.0000	0.0000	0.0000	0.0000
5.0	.0238	.0208	.0165	.0198
10.0	.0487	.0467	.0399	.0420

Table XII-A

CHANGE IN DRAG COEFFICIENT WITH ELEVATOR DEFLECTION ANGLE

ELEVATOR DEFLECTION (DEGREES)	CHANGE IN DRAG COEFFICIENT			
	ALPHA = .1°	ALPHA = 2.2°	ALPHA = 4.3°	ALPHA = 6.4°
-15.0	-.0183	-.0266	-.0344	-.0341
-10.0	-.0201	-.0227	-.0268	-.0268
-5.0	-.0115	-.0147	-.0142	-.0149
0.0	0.0000	0.0000	0.0000	0.0000
5.0	.0164	.0165	.0175	.0188
10.0	.0346	.0382	.0385	.0407

Table XIII-A

CHANGE IN MOMENT COEFFICIENT WITH ELEVATOR DEFLECTION ANGLE

ELEVATOR DEFLECTION (DEGREES)	CHANGE IN MOMENT COEFFICIENT			
	ALPHA = .1°	ALPHA = 2.2°	ALPHA = 4.3°	ALPHA = 6.4°
-15.0	.1947	.2060	.2047	.1943
-10.0	.1256	.1401	.1293	.1264
-5.0	.0580	.0679	.0614	.0596
0.0	0.0000	0.0000	0.0000	0.0000
5.0	-.0602	-.0526	-.0529	-.0532
10.0	-.1291	-.1224	-.1234	-.1203

Approximating the Aerodynamic Coefficients with Curve Fits

In Chapter 2 an aerodynamic model of the Jindivik is developed. The development relies upon the existence of functional relationships between the orientation of the aircraft to the air flow and the aerodynamic coefficients. One method of deriving these relationships is to curve fit the tabular data with combinations of polynomials, and this is the approach taken in this section. For simplicity, the lowest order polynomial which appears to represent the overall shape of the data is used, and the polynomial coefficients are determined by least squares curve fits. A computer subroutine, PLSQ (Reference 11), was used to generate the polynomial coefficients for all second-order and higher polynomials, as well as some first-order polynomials (lift coefficient with flaps up, side force coefficient, and roll moment coefficients).

Lift Coefficient

Figure A-1 depicts the lift coefficient data for both the flaps-up and flaps-down configurations, along with the straight line curve fits of the data. The algebraic relationships are

$$\text{flaps-up } C_L = .08476\alpha + .132 \quad (\text{A-1})$$

$$\text{flaps-down } C_L = .08476\alpha + .532 \quad (\text{A-2})$$

Drag Coefficient

The coefficient of drag data is shown in Figure A-2 along with the curve fits for both the flaps-up and flaps-down configurations. The algebraic relationship for the flaps-up configuration is

$$C_D = .001506\alpha^2 + .00045\alpha + .09196 \quad (\text{A-3})$$

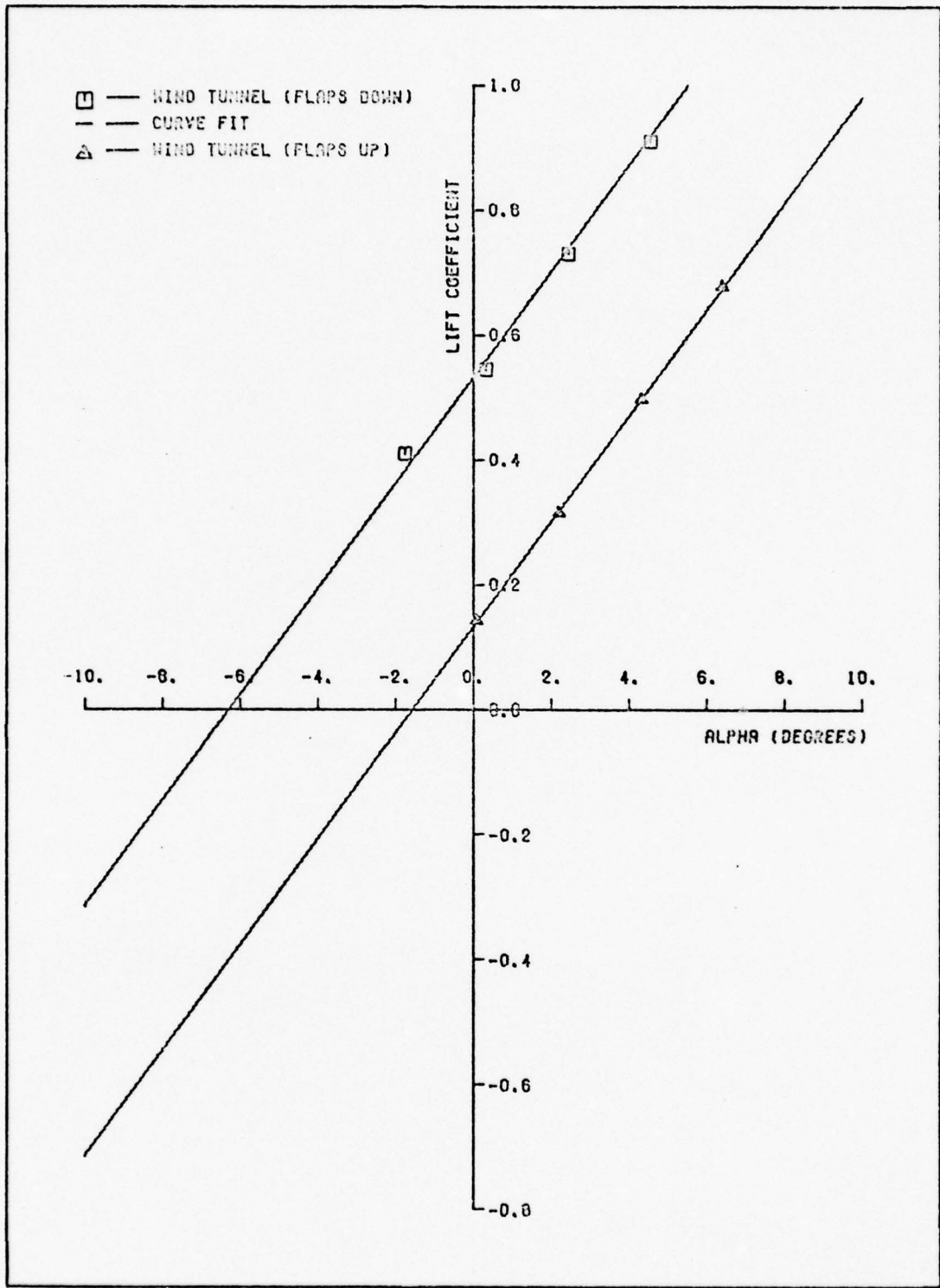


FIG. A-1 LIFT COEFFICIENT VERSUS ANGLE OF ATTACK

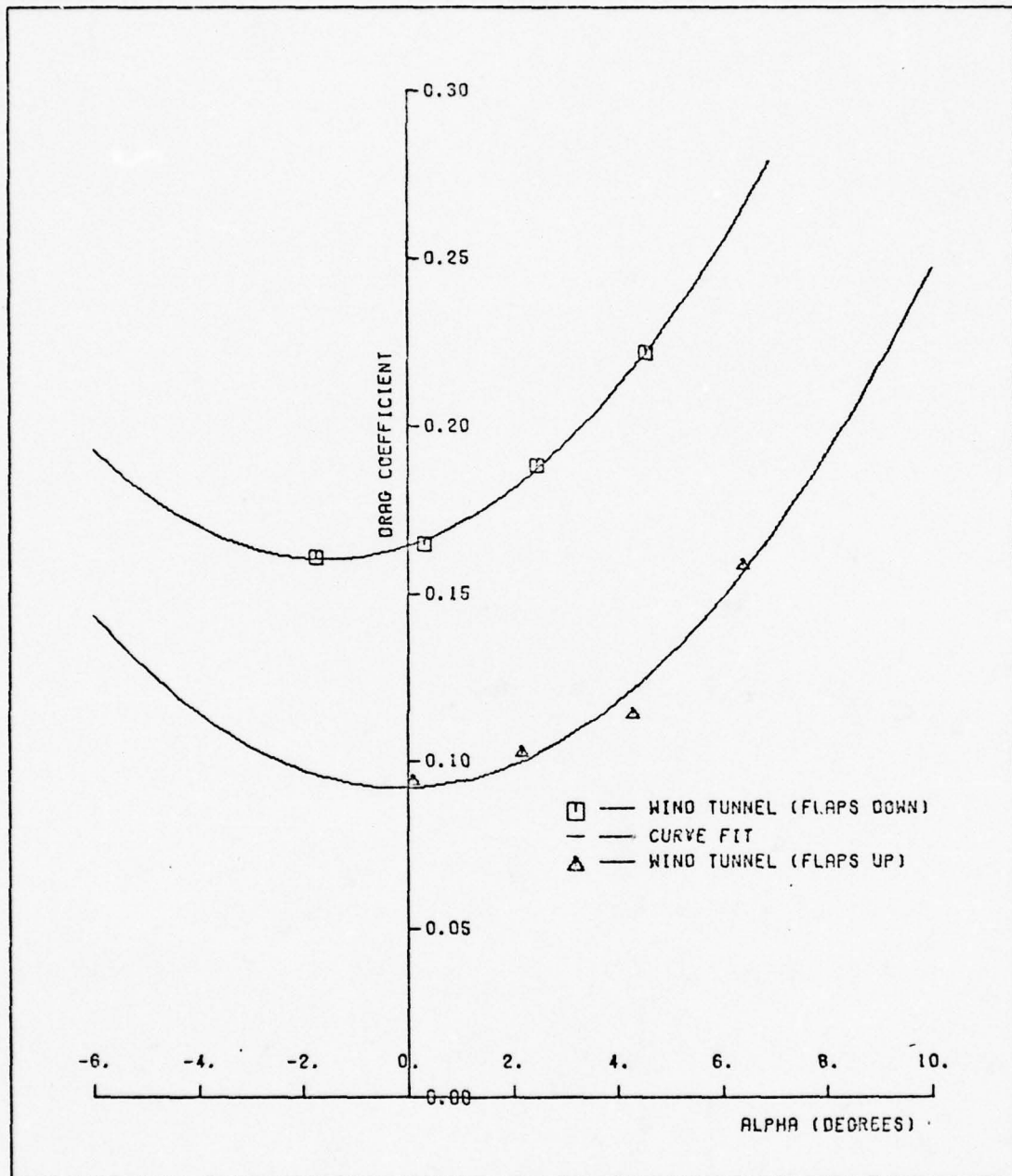


FIG. A-2 DRAG COEFFICIENT VERSUS ANGLE OF ATTACK

For the flaps-down configuration, the expression is

$$C_D = .001653\alpha^2 + .00518\alpha + .16445 \quad (A-4)$$

Pitching Moment Coefficient

Figure A-3 shows the pitching moment coefficient data for flaps up and flaps down, along with the curve fits. The defining relationship for C_M with flaps up is

$$\begin{aligned} \alpha < 0^\circ & : C_M = -.01103\alpha + .0572 \\ 0^\circ \leq \alpha \leq 6^\circ & : C_M = -1.4738 \times 10^{-4}\alpha^3 + 2.0921 \times 10^{-3}\alpha^2 \\ & \quad -1.1033 \times 10^{-2}\alpha + .0572 \\ \alpha > 6^\circ & : C_M = -.001848\alpha + .0453 \end{aligned} \quad (A-5)$$

The flaps-down curve fit is simply two straight lines

$$\begin{aligned} \alpha < .33^\circ & : C_M = 4.3 \times 10^{-4}\alpha - .0062 \\ \alpha > .33^\circ & : C_M = -3.4 \times 10^{-3}\alpha - .005 \end{aligned} \quad (A-6)$$

Side Force Coefficient

The variation in side force coefficient, C_y , is shown in Figure A-4 for flaps up. Changes in angle of attack and flap setting do not significantly affect C_y , hence a single straight line curve fit is used to approximate this coefficient

$$C_y = -.0101\beta + .00792 \quad (A-7)$$

Roll Moment Coefficient

The roll moment coefficient, C_l (CLL in FORTRAN to distinguish between lift coefficient and roll coefficient), varies linearly with sideslip angle, β , as well as with lift coefficient. The wind tunnel data for this coefficient is given in Figures A-5 through

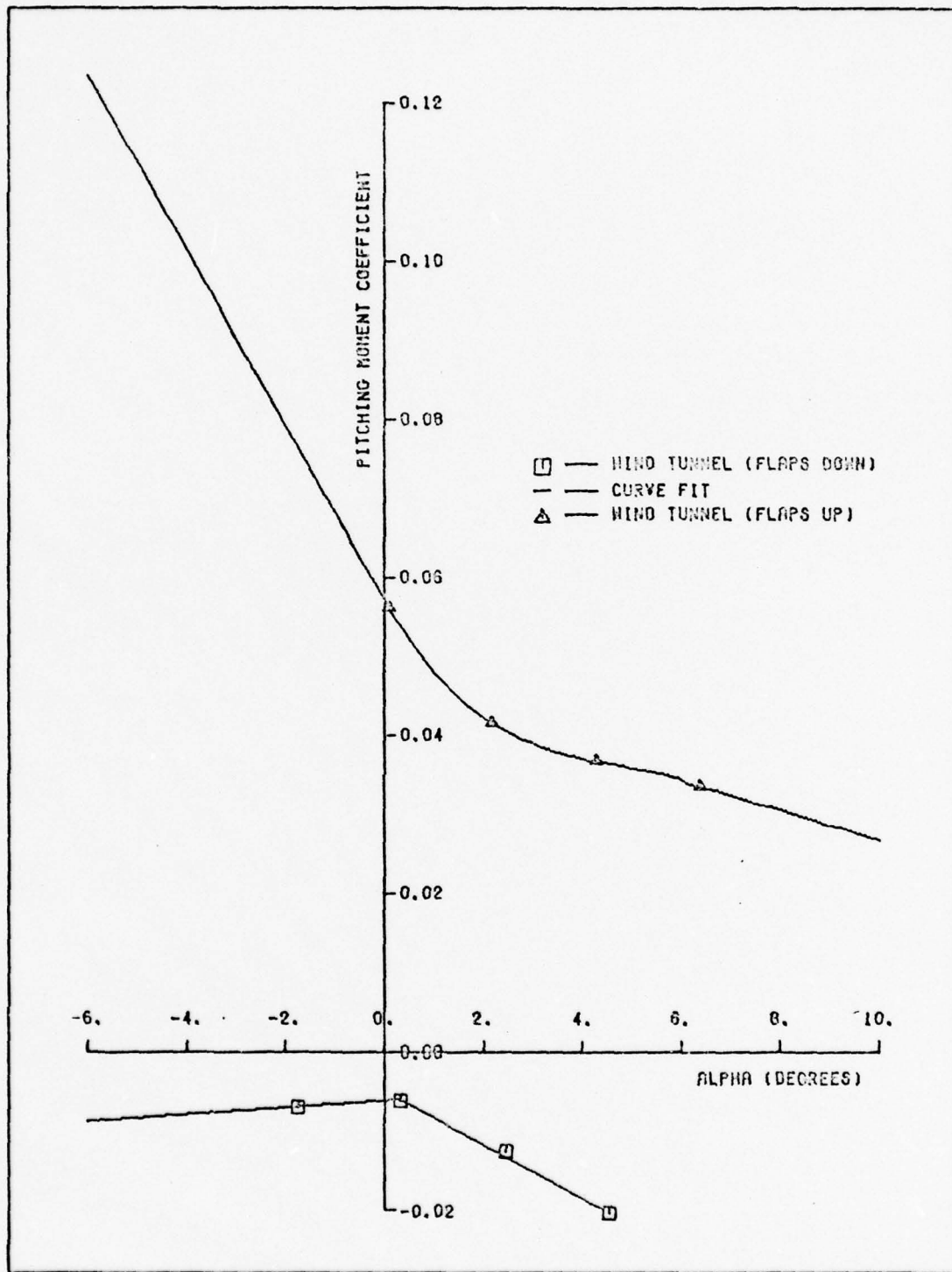


FIG. A-3 PITCHING MOMENT COEFFICIENT
VERSUS ANGLE OF ATTACK

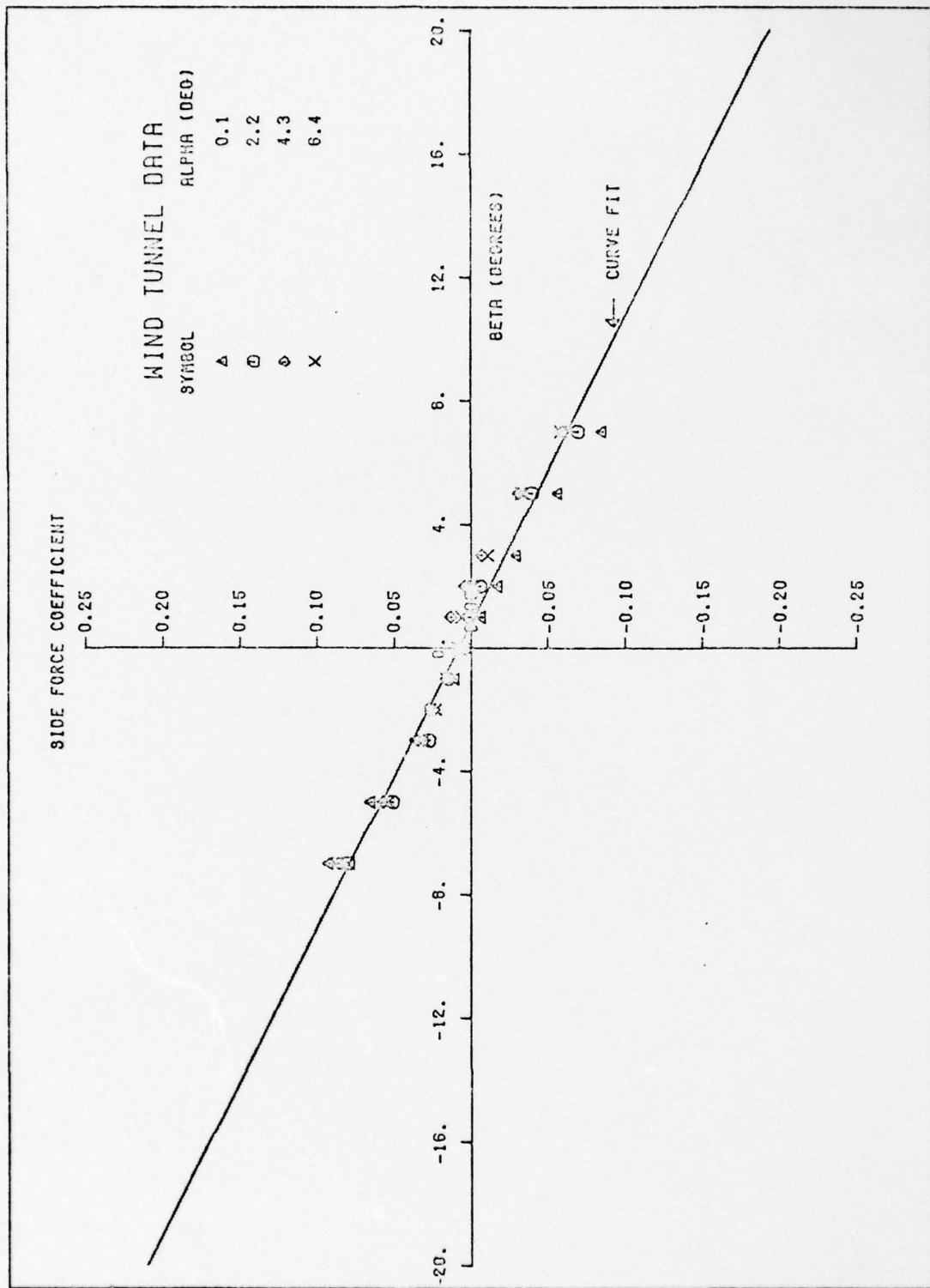


FIG. A-4 SIDE FORCE COEFFICIENT VERSUS SIDESLIP ANGLE

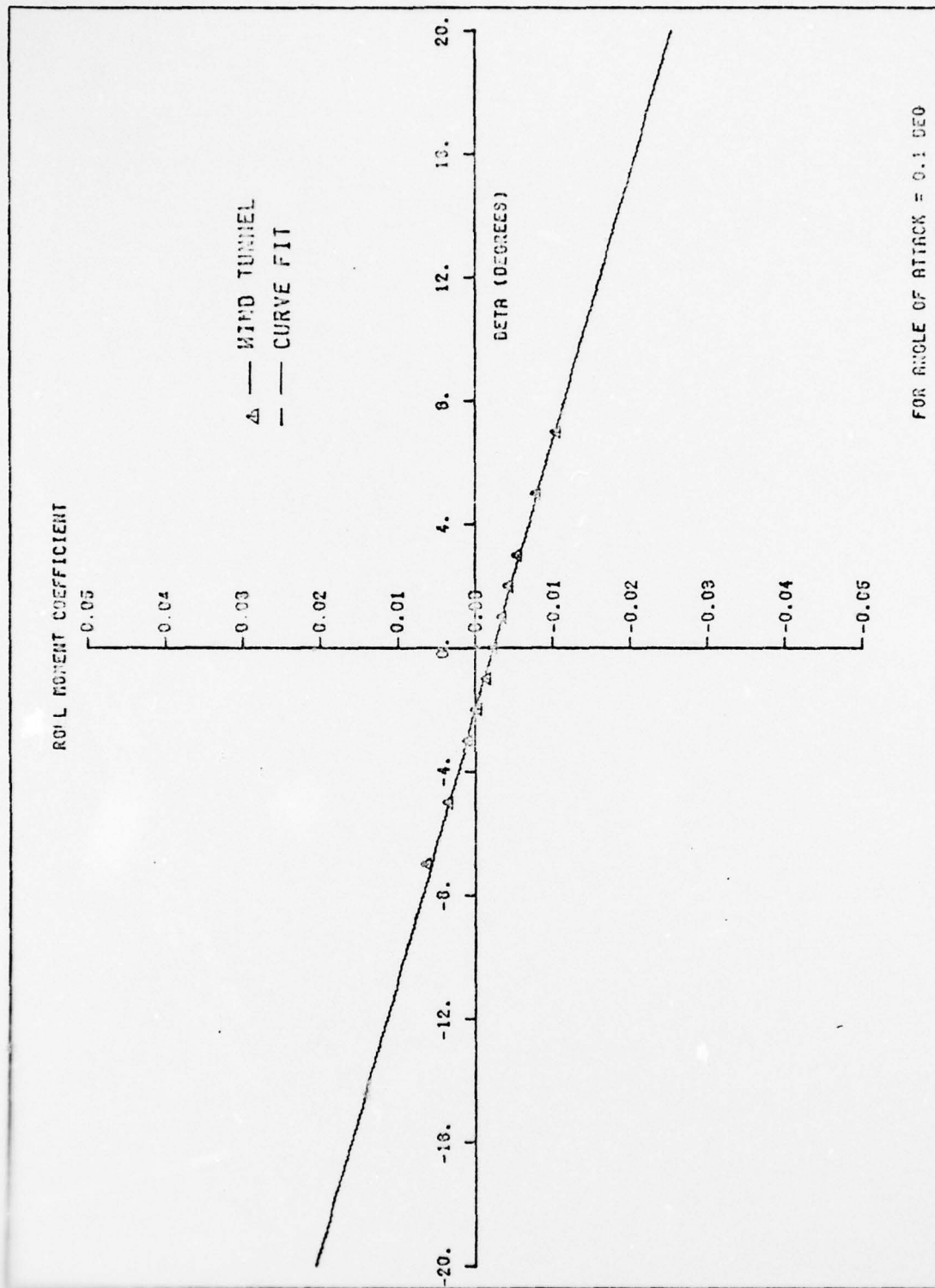
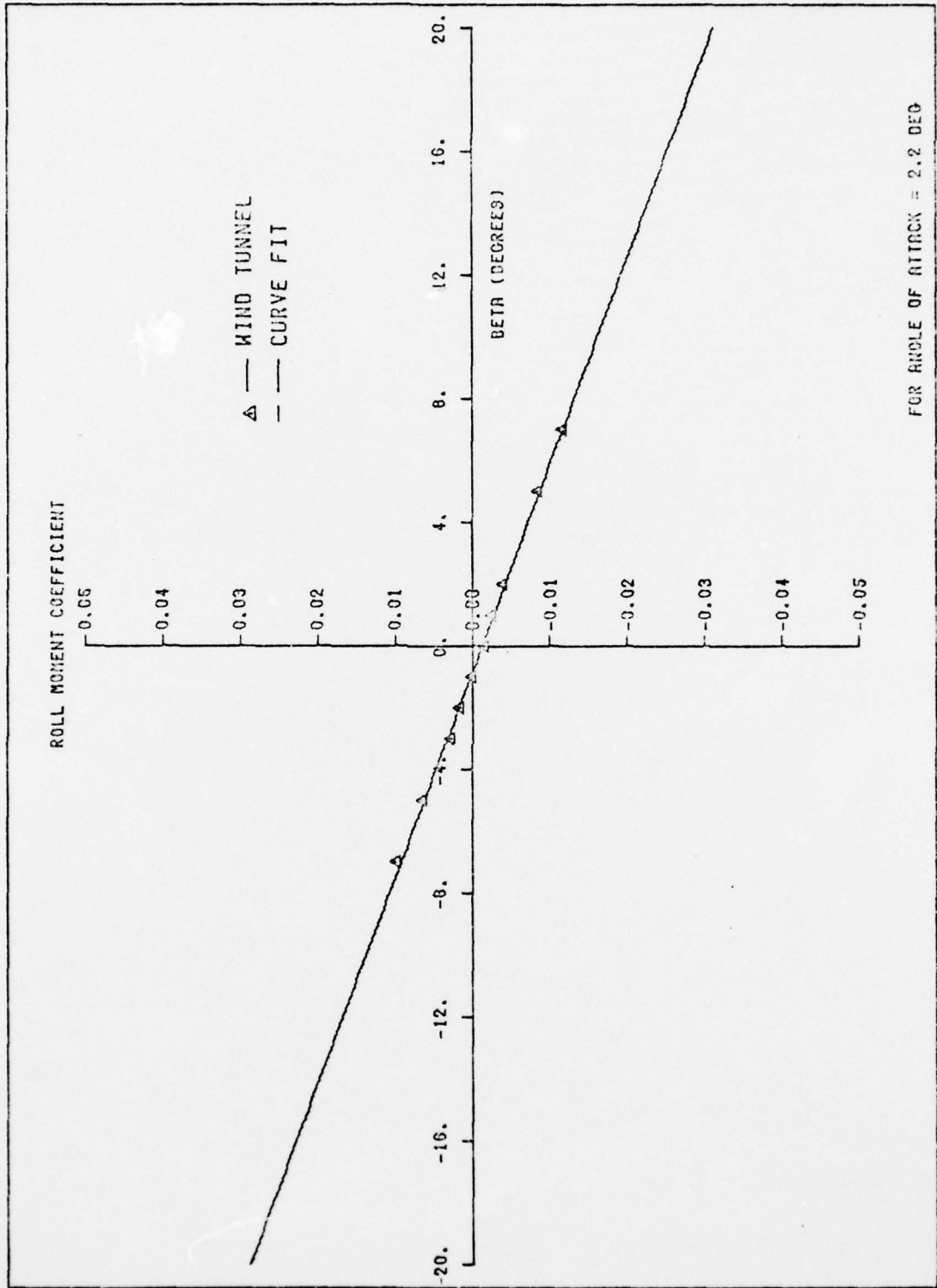


FIG. 9-5 ROLL MOMENT COEFFICIENT VERSUS SIDESLIP ANGLE



FOR ANGLE OF ATTACK = 2.2 DEG

FIG. A-6 ROLL MOMENT COEFFICIENT VERSUS SIDESLIP ANGLE

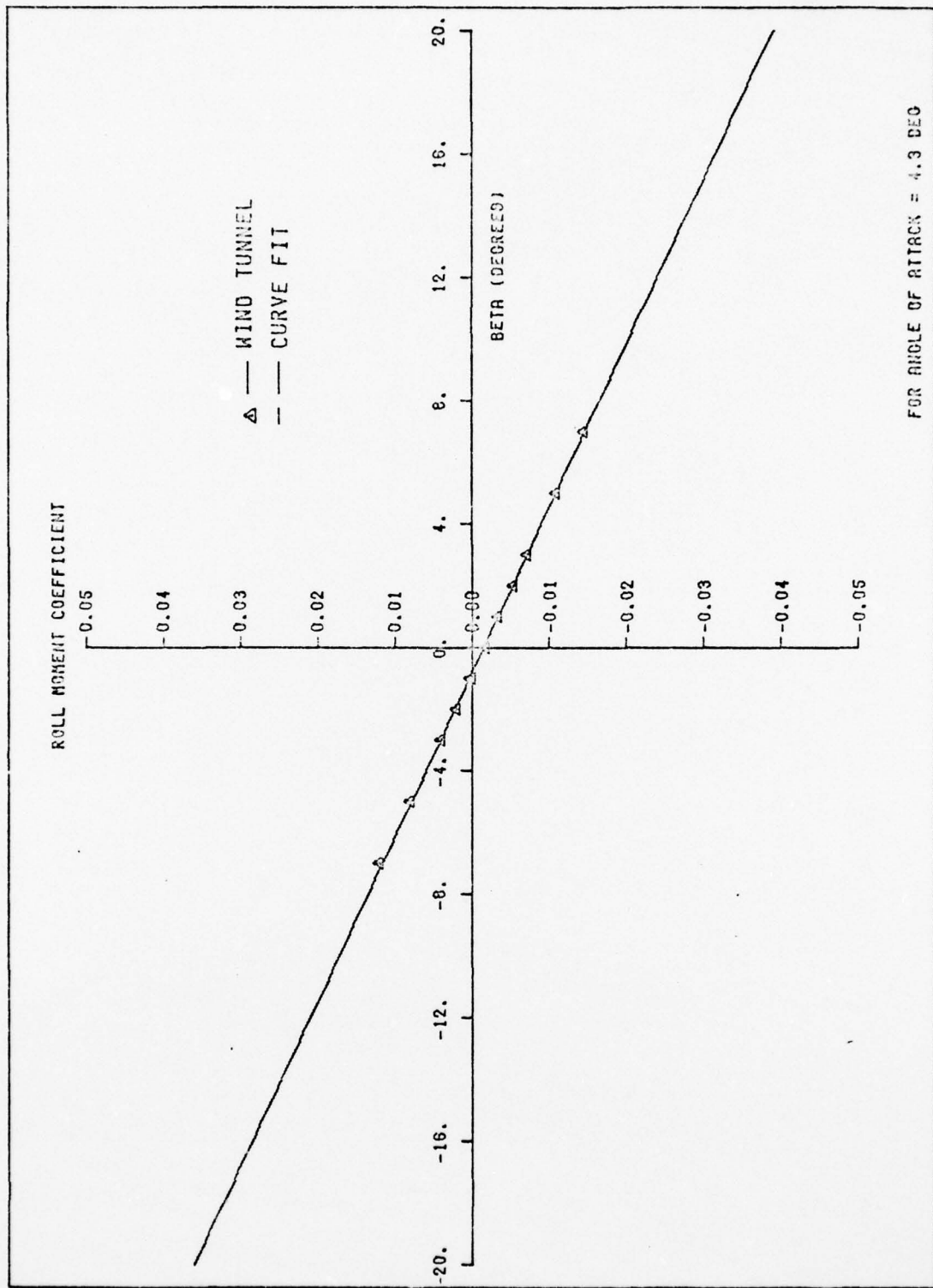
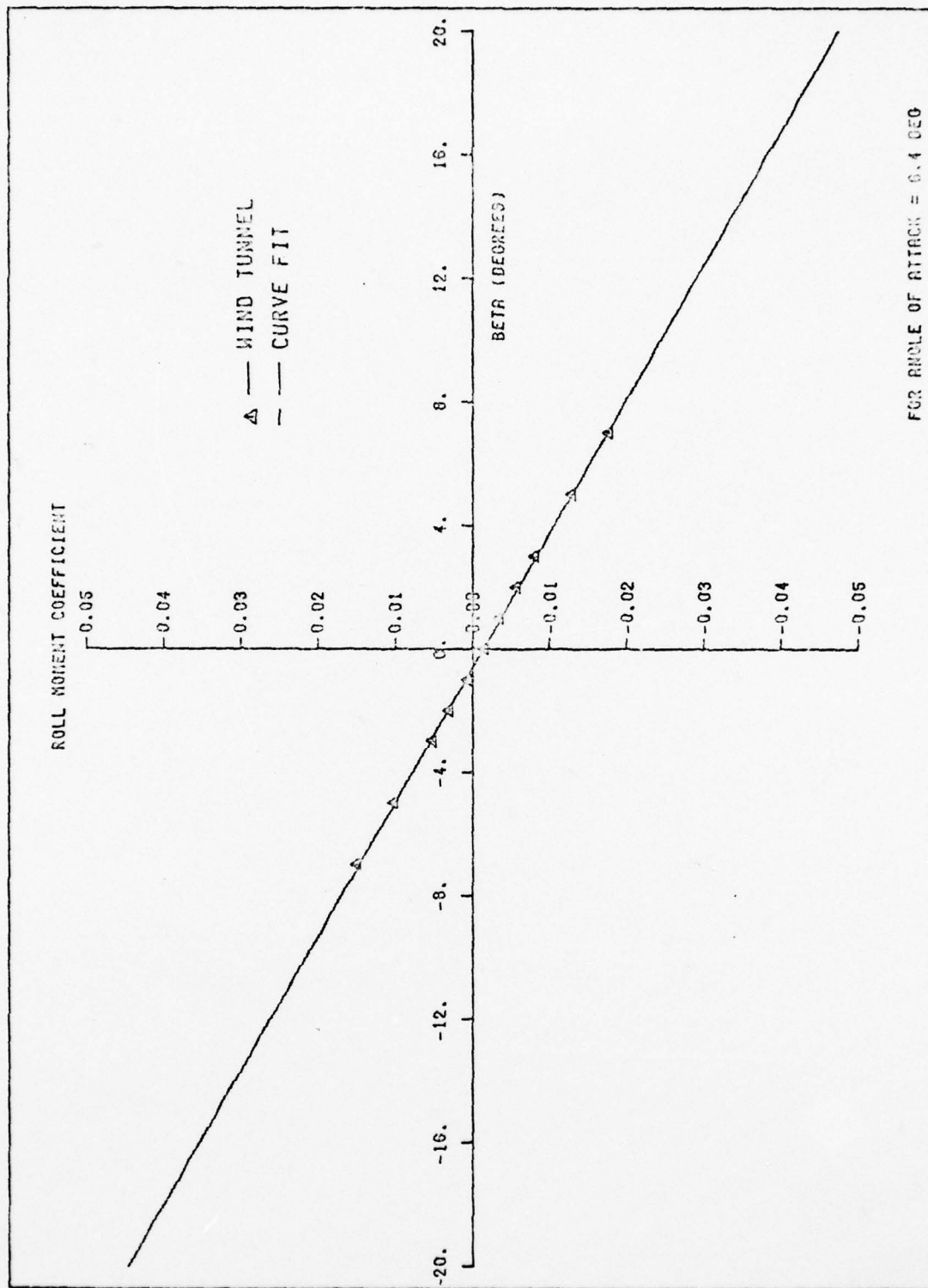


FIG. A-7 ROLL MOMENT COEFFICIENT VERSUS SIDESLIP ANGLE



FOR ANGLE OF ATTACK = 0.4 DEG

FIG. A-8 ROLL MOMENT COEFFICIENT VERSUS SIDESLIP ANGLE

A-8 for the flaps-up configuration. The defining relationships for this configuration are

$$\begin{aligned}\alpha = .1^\circ & : C_l = -1.48 \times 10^{-3}\beta - 2.355 \times 10^{-3} \\ \alpha = 2.2^\circ & : C_l = -1.501 \times 10^{-3}\beta - 1.260 \times 10^{-3} \\ \alpha = 4.3^\circ & : C_l = -1.877 \times 10^{-3}\beta - 1.555 \times 10^{-3} \\ \alpha = 6.4^\circ & : C_l = -2.302 \times 10^{-3}\beta - 1.445 \times 10^{-3}\end{aligned}\tag{A-8}$$

For an arbitrary value of α between $.1^\circ$ and 6.4° , an interpolation is made between appropriate curves. For the flaps-down case, a slightly different approach is taken. Since the slopes of the straight line curve fits vary with angle of attack, an expression for these slopes is formulated. Thus, an algorithm is obtained that computes C_l for any angle of attack and sideslip angle combination. The equation for the roll moment coefficient is

$$C_l = K_l(\alpha) \beta + .0012\tag{A-9}$$

where

$$K_l(\alpha) = .1365\alpha + 1.239\tag{A-10}$$

Yaw Moment Coefficient

Figures A-9 through A-12 show the variation in yaw moment coefficient, C_n , with sideslip angle at different angles of attack. These figures depict the flaps-up configuration: the flaps-down configuration will be covered shortly.

The yaw moment coefficient is a highly nonlinear parameter which is clearly dependent upon both sideslip angle and angle of attack. Several different polynomial curve fits of the given data were attempted. While higher order polynomials result in closer fits to the data, fifth order curve fits are used since they

adequately represent the overall shapes of the wind tunnel data. Since no data is available for sideslip angles less than -7° or greater than $+7^\circ$, straight line extrapolations are made. The slopes for these extrapolations are arbitrarily chosen to be identical at each angle of attack. Furthermore, the slopes of the straight line extrapolations match the fifth order polynomials at the "transition points". The transition points (denoted by subscript tp) are the points where the straight line extrapolations and the fifth order curve fits merge. The general form of the modeled relationships between β and C_n for the flaps-up case is

$$\begin{aligned} \beta \leq \beta_{tp}^- & : C_n = a^-\beta + b^- \\ \beta_{tp}^- \leq \beta \leq \beta_{tp}^+ & : C_n = C_1\beta^5 + C_2\beta^4 + C_3\beta^3 + C_4\beta^2 + C_5\beta + C_6 \quad (A-11) \\ \beta \geq \beta_{tp}^+ & : C_n = a^+\beta + b^+ \end{aligned}$$

Table XIV-A below lists all of the above parameters for each value of angle of attack. Linear interpolation is made for $.1^\circ \leq \alpha \leq 6.4^\circ$. For angles outside this range, the appropriate extreme curve is used (e.g., for $\alpha < .1^\circ$, the $\alpha = .1^\circ$ curve for C_n versus β is used to determine C_n).

The data for yaw moment coefficient with flaps down is not nearly as predictable as it is for the flaps-up configuration. In order to obtain a crude model for this configuration, an average value was taken from the values of C_n at $\alpha = .33^\circ$ and $\alpha = 2.45^\circ$. Three straight lines were used to roughly approximate the yaw moment coefficient versus sideslip angle. The averaged values of C_n are

Table XIV-A
 PARAMETER VALUES FOR YAW MOMENT VERSUS SIDESLIP ANGLE CURVE FITS

Parameter	$\alpha \leq 0.1^\circ$	$\alpha = 2.2^\circ$	$\alpha = 4.3^\circ$	$\alpha \geq 6.4^\circ$
a-	4.42×10^{-4}	4.3×10^{-4}	4.5×10^{-4}	4.24×10^{-4}
b-	2.243×10^{-3}	6.9776×10^{-3}	6.6688×10^{-3}	5.3769×10^{-3}
β_{Tp}	-6.2°	-5.915°	-6.5°	-5.585
C ₁	-5.8187×10^{-8}	-2.1348×10^{-7}	-4.142×10^{-7}	-2.3415×10^{-7}
C ₂	1.2552×10^{-7}	-9.655×10^{-7}	-7.8671×10^{-7}	-6.1189×10^{-7}
C ₃	1.063×10^{-5}	2.9057×10^{-5}	4.3616×10^{-5}	2.7003×10^{-5}
C ₄	1.9791×10^{-6}	6.8406×10^{-5}	6.538×10^{-5}	4.7378×10^{-5}
C ₅	-2.09735×10^{-4}	-1.3031×10^{-3}	-1.471×10^{-3}	-9.6721×10^{-4}
C ₆	-7.0296×10^{-4}	-1.3046×10^{-3}	-1.8538×10^{-3}	-8.4685×10^{-4}
a+	4.42×10^{-4}	4.3×10^{-4}	4.5×10^{-4}	4.24×10^{-4}
b+	-1.94×10^{-4}	-4.5854×10^{-3}	-3.9312×10^{-3}	-3.4532×10^{-3}
β_{Tp}^+	10.4°	6.05°	6.367°	5.5°

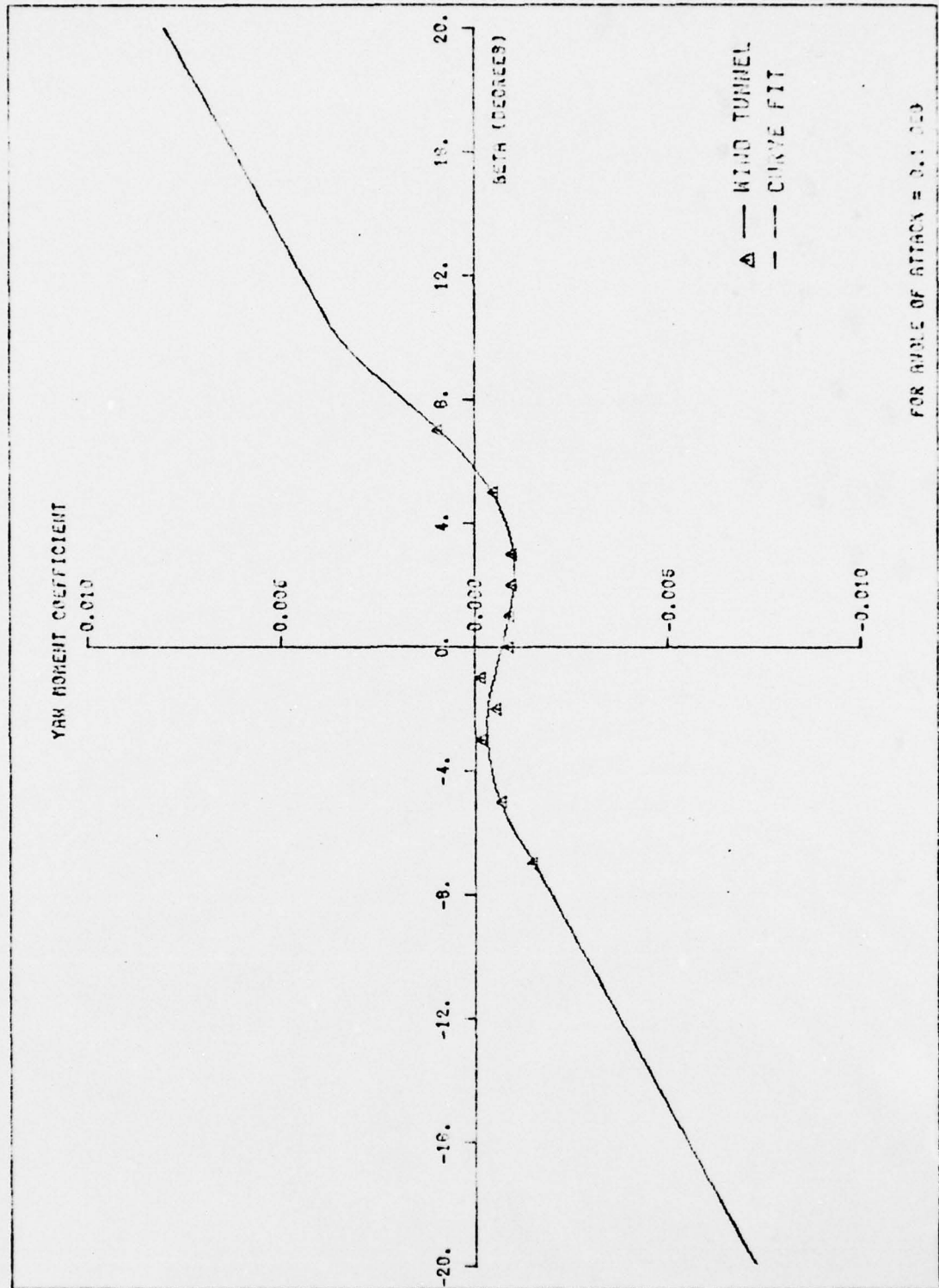


FIG. A-9 YAW MOMENT COEFFICIENT VERSUS SIDESLIP ANGLE

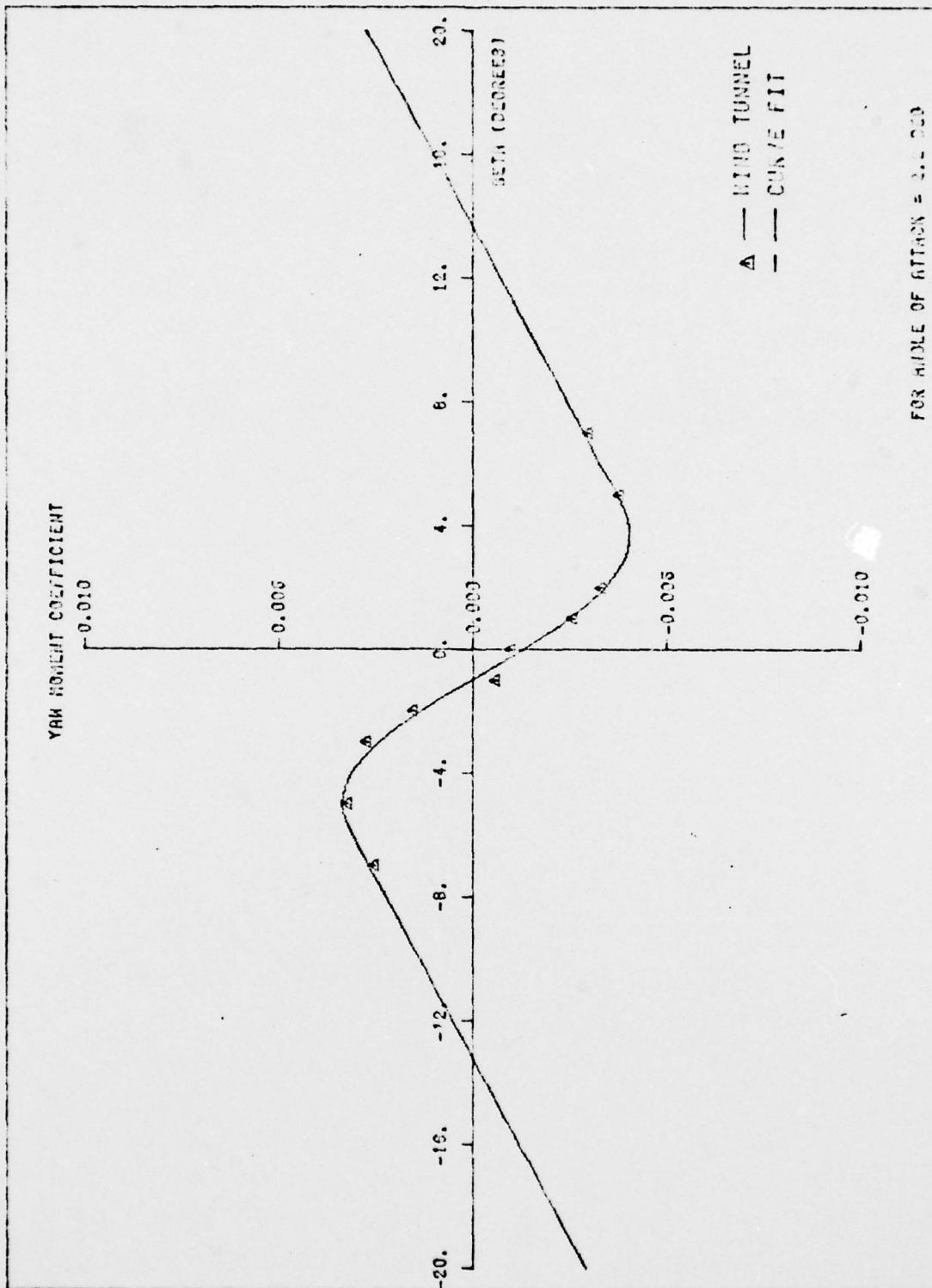


FIG. A-10 YAW MOMENT COEFFICIENT VERSUS SIDESLIP ANGLE

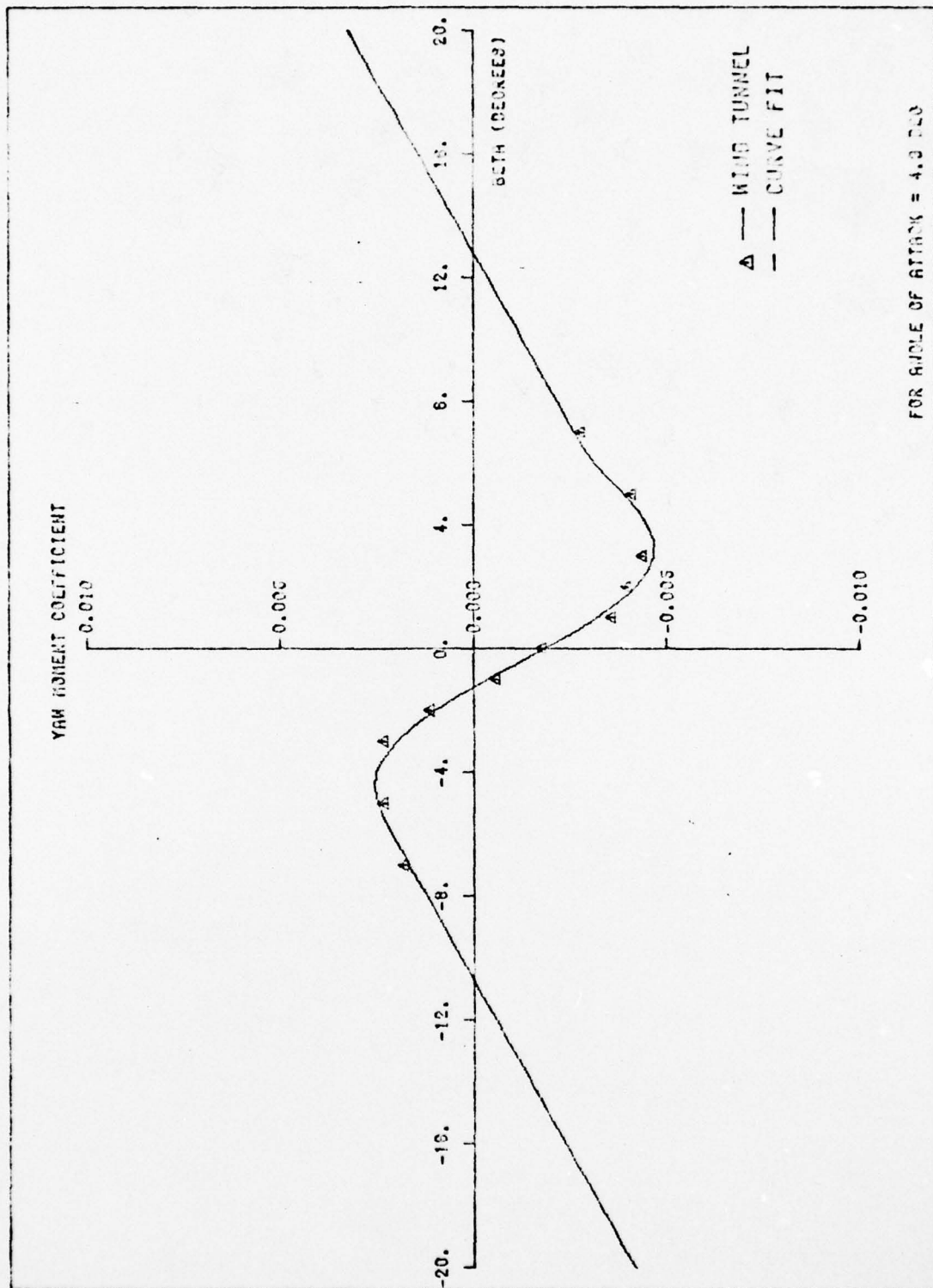


FIG. A-11 YAW MOMENT COEFFICIENT VERSUS SIDESLIP ANGLE

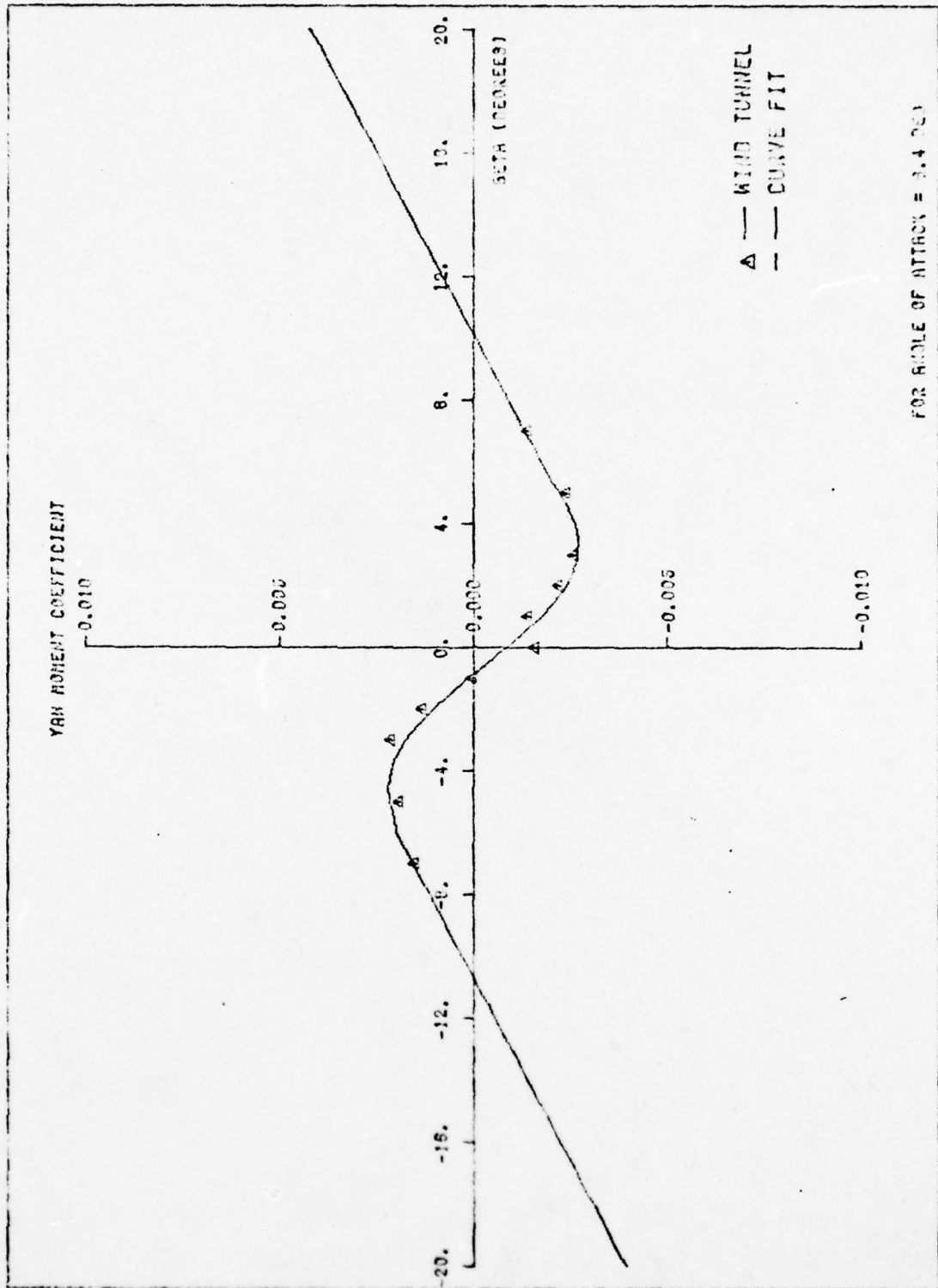


FIG. 8-12 YAW MOMENT COEFFICIENT VERSUS SIDESLIP ANGLE

given in Figure A-13, along with the curve fits. The equations for the straight lines are

$$\begin{aligned}\beta < -1.05 & : C_n = 2.25 \times 10^{-4}\beta + .003525 \\ -1.05 \leq \beta \leq 5 & : C_n = -7.75 \times 10^{-4}\beta + .002475 \quad (A-12) \\ \beta > 5 & : C_n = 2.25 \times 10^{-4}\beta - .002525\end{aligned}$$

Elevator Control Coefficients

Figures A-14 through A-16 are representations of the elevator control data and the straight line curve fits of that data. The curve fits are done by hand since it is desired that the curves approximate the values around the origin more accurately than those at the limits of the elevator deflection. The reason for this weighting is that the elevator seldom approaches the deflection limits, but instead typically remains within 5° of the neutral position.

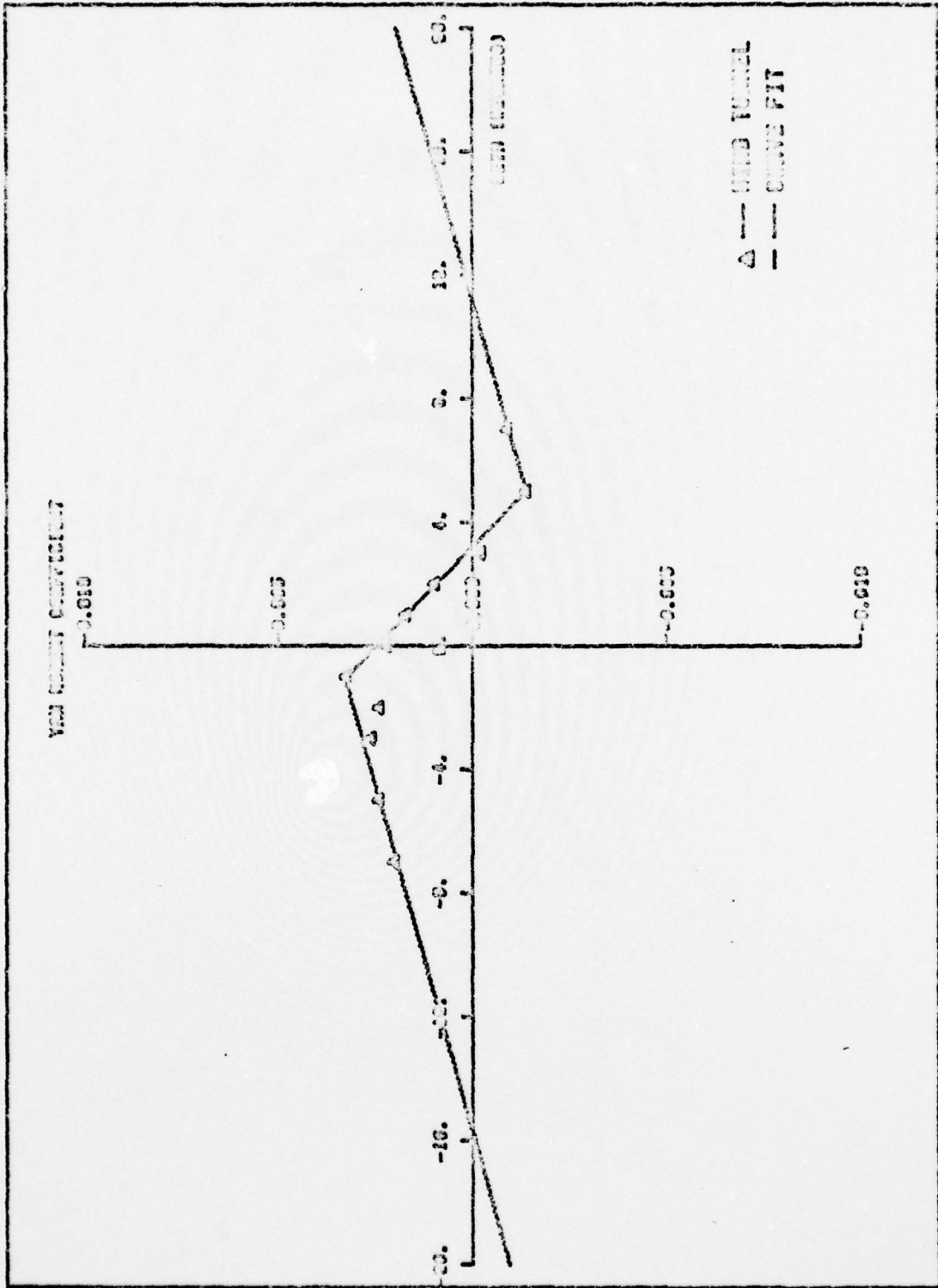


FIG. A-19 YAW MOMENT COEFFICIENT VERSUS SIDESLIP ANGLE (FLOPC 60MM)

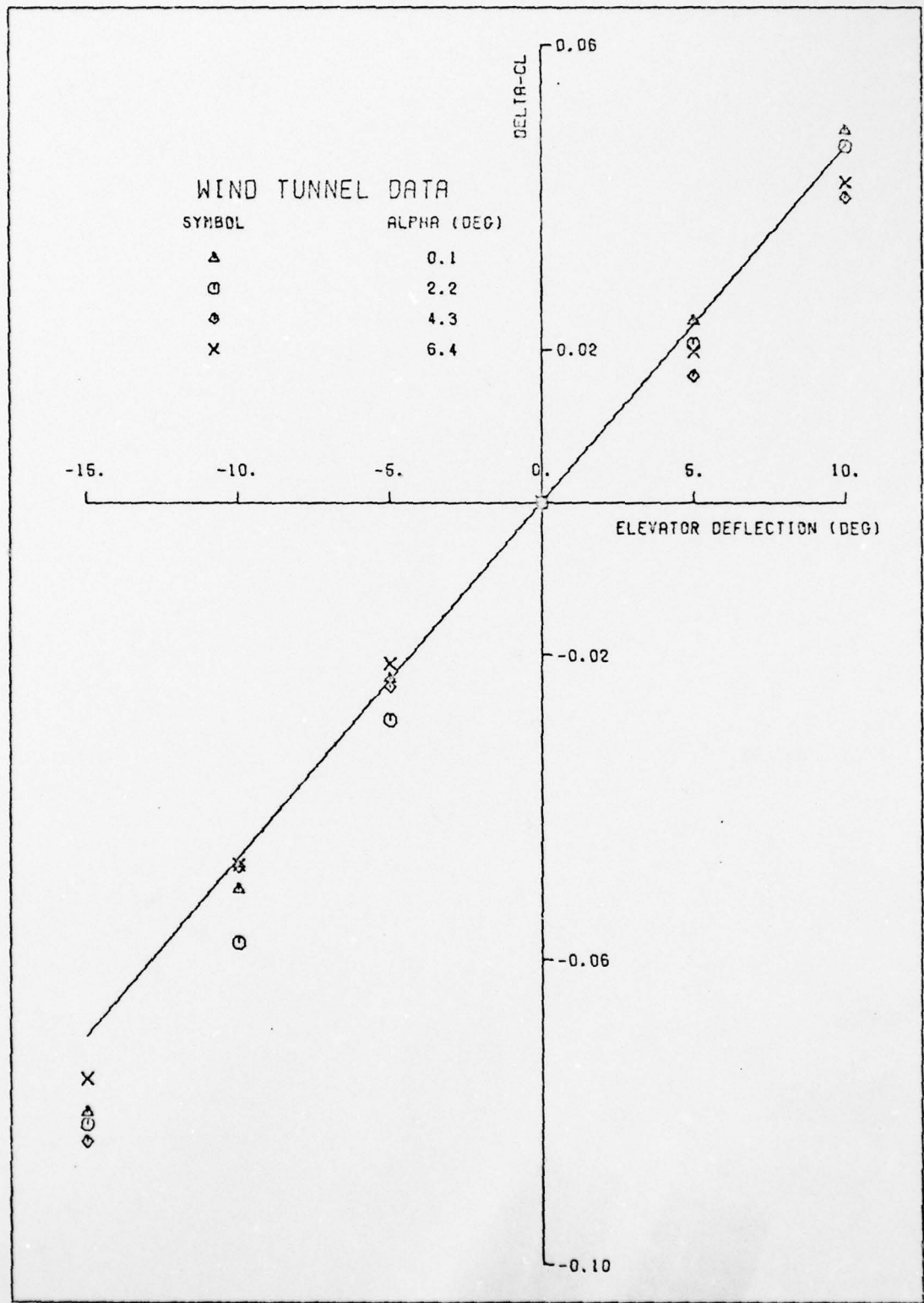


FIG. A-14 CHANGE IN LIFT COEFFICIENT VERSUS ELEVATOR DEFLECTION

AD-A057 434

AIR FORCE INST OF TECH WRIGHT-PATTERSON AFB OHIO SCH--ETC F/G 1/3
AN ANALYSIS OF THE STABILITY OF AN AIRCRAFT EQUIPPED WITH AN AI--ETC(U)
MAR 78 M A STAFFORD

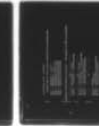
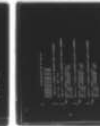
UNCLASSIFIED

AFIT-GGC-EE-78M-5

NL

3 OF 3

AD
A057434



END
DATE
FILMED
9-78

DDC

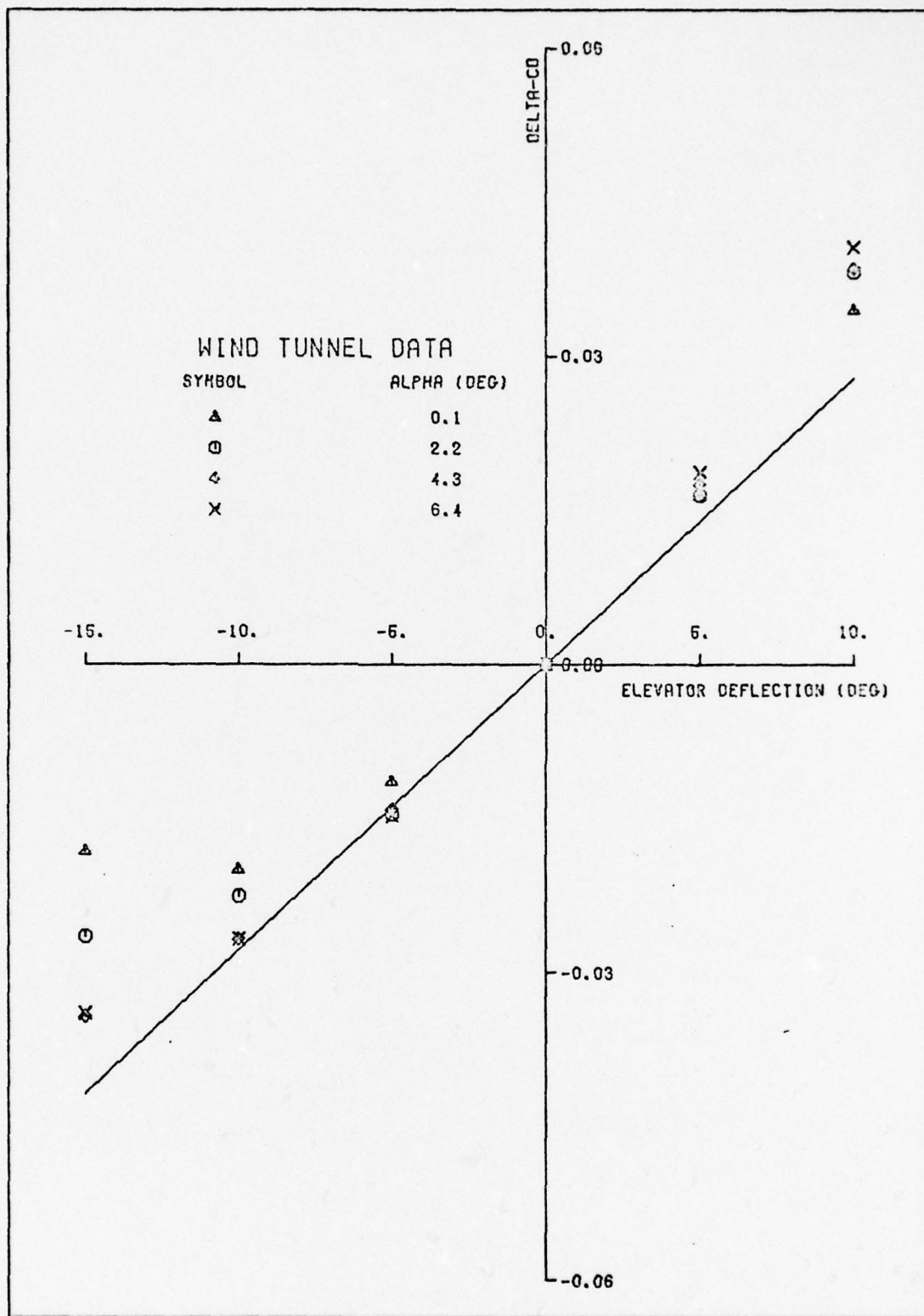


FIG. A-15 CHANGE IN DRAG COEFFICIENT VERSUS ELEVATOR DEFLECTION (DEG)

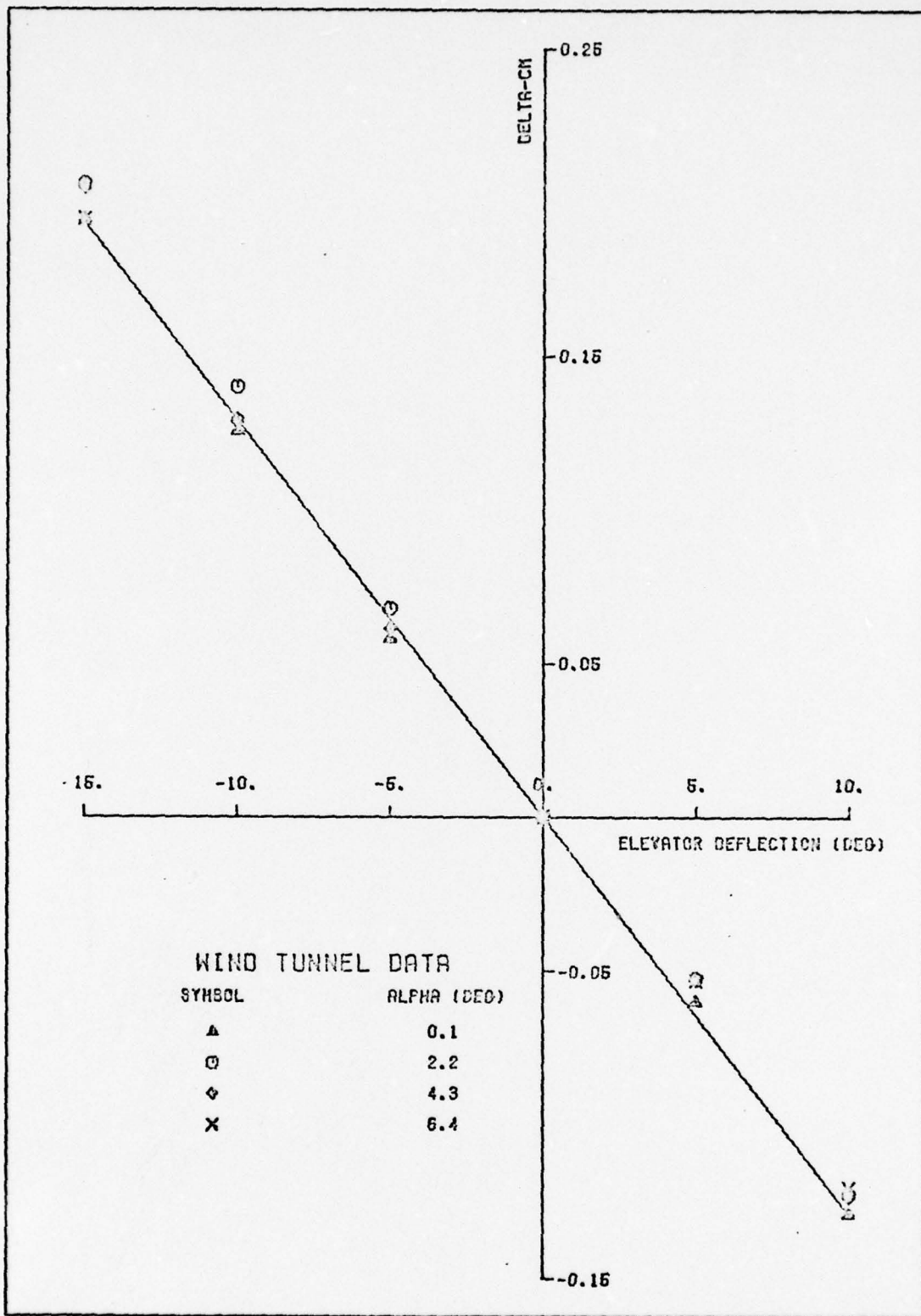


FIG. A-16 CHANGE IN PITCHING COEFFICIENT VERSUS ELEVATOR DEFLECTION

SECTION II

Additional Aerodynamic Data Provided

Some additional data was obtained from Reference 1. Specifically, the following dimensionless stability derivatives were given: C_{l_p} , C_{l_r} , C_{n_p} , C_{n_r} , $C_{l_{\delta_A}}$, and $C_{n_{\delta_A}}$. Unfortunately, these derivatives are available for the basic aircraft (i.e., without an ACRS installed). As a first approximation, these values are used directly with no modification. This is claimed to be a reasonable approximation for the latter three derivatives since, 1) the vertical stabilizer is typically the largest contributor to C_{n_r} (Ref 164.95), and 2) the distance of the ailerons from the fuselage precludes any appreciable effects of the fuselage on the aileron control derivatives. No claim is made as to the accuracy of the approximation for the first three derivatives, however. Table XV-A is a compilation of the stability derivatives along with their definitions.

Derived Aerodynamic Parameters

Four parameters were calculated from aerodynamic data and the geometry of the airframe: $C_{L_{\dot{\alpha}}}$, $C_{M_{\dot{\alpha}}}$, C_{L_q} , and C_{M_q} . These stability derivatives are expected to be significantly affected by the presence of the trunk, since the trunk lies generally in front of the horizontal tail. The horizontal tail plays a major role in determining the values of these four stability derivatives, as will be seen below, and hence the trunk's existence must be accounted for.

Consider first the $\dot{\alpha}$ stability derivatives. An equation for $C_{L_{\dot{\alpha}}}$ and $C_{M_{\dot{\alpha}}}$ (Reference 16) is

Table XV-A

SOME STABILITY DERIVATIVES FROM REFERENCE

(Note: Units of V_T are ft/sec)

Stability Derivative	Value or Algebraic Relation	Definition
C_{lp}	-.370	$C_{lp} = \frac{4}{\rho S b V_T} \frac{\partial L}{\partial P}$
C_{lr}	$-.06C_L + .459$	$C_{lr} = \frac{4}{\rho S b V_T} \frac{\partial L}{\partial R}$
$C_{l\delta A}$	$-.193 \left[1 - \left(\frac{V_T}{892.6} \right)^2 \right]$	$C_{l\delta A} = \frac{2}{\rho S b V_T^2} \frac{\partial L}{\partial \delta A}$
C_{np}	$-.125C_L + .0209$	$C_{np} = \frac{4}{\rho S b V_T} \frac{\partial N}{\partial P}$
C_{nr}	-.1545	$C_{nr} = \frac{4}{\rho S b V_T} \frac{\partial N}{\partial R}$
$C_{n\delta A}$	$.0166 - .009C_L$	$C_{n\delta A} = \frac{2}{\rho S b V_T^2} \frac{\partial N}{\partial \delta A}$

$$C_{L\dot{\alpha}} = 2C_{L\alpha H} \eta_H \bar{V}_H \frac{d\epsilon}{d\alpha} \quad (A-13)$$

$$C_{M\dot{\alpha}} = 2C_{L\alpha H} \eta_H \bar{V}_H \frac{x_H}{\bar{c}} \frac{d\epsilon}{d\alpha} \quad (A-14)$$

The constants are defined as

$C_{L\alpha H}$ - lift curve slope of the horizontal tail

η_H - efficiency factor of the horizontal tail

\bar{V}_H - horizontal tail volume coefficient

x_H - distance between the center of gravity and the horizontal tail aerodynamic center

\bar{c} - the mean aerodynamic chord

$\frac{d\epsilon}{d\alpha}$ - the rate of change of downwash angle with respect to angle of attack

Detailed information on each of these quantities can be found in Reference 16.

By techniques given in Reference 16 each of the quantities in equations A-13 and A-14 can be evaluated. The results are

$$C_{L\dot{\alpha}} = .02465/^\circ$$

$$C_{M\dot{\alpha}} = -.0604/^\circ$$

The remaining two stability derivatives can also be evaluated by techniques described in Chapter 4 of Reference 16. The necessary equations are

$$C_{Lq} = 2C_{L\alpha H} \eta_H \bar{V}_H$$

$$C_{Mq} = -2C_{L\alpha H} \eta_H \bar{V}_H \frac{x_H}{\bar{c}}$$

where the definitions of the parameters on the RHS of these two equations are the same as above. The results are

$$C_{Lq} = .0441/^\circ$$

$$C_{Mq} = -.108/^\circ$$

Appendix B

Salient Features

of the

EASY Aircraft Modeling and Analysis Program

A computer software package, EASY, is used throughout this report to facilitate programming of the mathematical models as well as to aid in the analysis of those models. This appendix discusses two main modes of operation of EASY, the modeling mode and the analysis mode, after which a source listing of the model used for simulations of the Jindivik slideout is presented. A detailed description of the use of EASY is given in the user's handbook, Reference 6.

Table I-B

DESCRIPTIONS OF SOME OF THE BLOCKS IN THE EASY MODELING PROGRAM

Block	Description
SD	Computes linear and angular velocities, linear and angular accelerations, and altitude by integrating the six equations of motion.
AV	Computes the aerodynamic variables (e.g., α , β , ρ , etc.)
LO	Computes longitudinal forces and moment (X_b , Z_b and M_b) from aerodynamic variables, gravitational force, and external forces.
LD	Computes lateral-direction force and moments (Y_b , L_b , and N_b) from aerodynamic variables, gravitational force, and external forces.
IT	Integrates the input variable.
MC	Multiplies input variables by constants and sums the products.
LG	First order lag transfer function.
TF	Second-order denominator transfer function.
AF	Analytic function generator (generates exponential or polynomial functions of time).
TG	Computes forces and torques produced by engine thrust.

Table II-B

DESCRIPTIONS OF SOME OF THE EASY ANALYSIS COMMANDS

EASY COMMAND	DESCRIPTION
SIMULATE	This command initiates a computer simulation from specified initial conditions to a specified final time.
STEADY STATE	This command initiates the calculation of the system steady state.
LINEAR ANALYSIS	This command initiates the calculation of a linear approximation to the model at a specified operating point.
TRANSFER FUNCTION	This command initiates the calculation of the frequency response function between any two specified points in the model.

The Modeling Mode

A mathematical model of 1) the aerodynamic and external forces acting on a vehicle, 2) the equations of motion of a vehicle, and 3) the control system of a vehicle, is converted into a single FORTRAN program by EASY in the modeling mode of operation. A user of the EASY modeling program provides information to the EASY precompiler through simple control statements that define which of several functional blocks are to be used and how they are to be connected. Some of these blocks are listed in Table I-B along with a description of the function of each block.

In addition to the functional blocks, FORTRAN statements may be entered between these blocks. This is a powerful feature of EASY since this increases the flexibility of the model significantly. The computer listing towards the end of this appendix demonstrates this feature since many FORTRAN statements are needed to generate the Jindivik slideout model.

The Analysis Mode

The final product of the modeling program discussed above is a binary object deck which is in a suitable form for the analysis program. In addition to simulations, several other means of analyzing the system described by the modeling program are available. Table II-B provides a list of some of the analysis commands which are available.

The Jindivik Slideout Model

A computer listing of the input commands to the EASY modeling program is presented in the following pages.

```

MODEL DESCRIPTION      JINDIVIK MODEL FOR SLIDEOUT SIMULATIONS/ACRS #2
ADD PARAMETERS
BX11, BX2P, BX2S, BX3P, BX3S, BX4P, BX4S, BX5P, BX5S, BX6P, BX6S, BX7P, BX7S, BX88
BY11, BY2P, BY2S, BY3P, BY3S, BY4P, BY4S, BY5P, BY5S, BY6P, BY6S, BY7P, BY7S, BY88
BZ, ZEQ, KPIT, KROL, CPIT, CROL, KH, CH, FSOP, FSOR, FHEQ, COFF, COFA, EQTH
CK1, CK2, CK3, CK4
UWE, VWE, WUE
ADD VARIABLES
ZD, Z11, ZD11, SP11, GAM11, FBX11, FBY11, TX11, TY11, TZ11
SFX, SFY, SFZ, STX, STY, STZ
XE, YE, DELD
ADD PARAMETERS
CL, CD, CM, CY, CLL, CN, CNB
ISYM, ICNB, ICHK, IFLAP, IGE
DPHID, DPHI, DTHETD, DTHET, ELETRIM, AILTRIM
OMEGA, A1, A2, A3
ADD VARIABLES
S1, UCON, Z1, Z2
LOCATION=55      TG
LOCATION=35      AV      INPUTS=SD
FORTRAN STATEMENTS
C
C      LIMIT ALPHA AND BETA
C
IF(AL AV.LT.-5.)AL AV=-5.
IF(AL AV.GT.7.5)AL AV=7.5
IF(BE AV.LT.-30.)BE AV=-30.
IF(BE AV.GT.30.)BE AV=30.

```

C C CALCULATE THE TRANSCENDENTALS

ALPHA=AL AU
 ARG=ALPHA/57.3
 SA = SIN(ARG)
 CSA = COS(ARG)
 SA2 = SA**2
 CSA2 = CSA**2
 EGTHR=(1.046-EGTH)/57.3
 SPIT=SIN(EGTHR)
 ROL=ROLSD/57.3
 PIT=PITSD/57.3
 YAU=YAUSD/57.3
 SR = SIN(ROL) \$CR = COS(ROL)
 SP = SIN(PIT) \$CP = COS(PIT)
 SY = SIN(YAU) \$CYY= COS(YAU)

C C ///TRANSFORMATION MATRIX///

C11=CYY*CP \$C12=CYY*SP*SR-SY*CP \$C13=CYY*SP*CR+SY*SR
 C21=SY*CP \$C22=SY*SP*SR+CYY*CR \$C23=SY*SP*CR-CYY*SR
 C31=-SP \$C32=CP*SR \$C33=CP*CR

C C OBTAIN NECESSARY VARIABLES FROM EASY

QS=QS AU \$Q = QC AU \$UT = UT AU \$BETA = BE AU
 U=UO AU \$U = UO AU \$SU = UO AU
 P=PO AU \$QO = QO AU \$R = R0 AU
 PRAD = P/57.2958 \$ORAD = QO/57.2958 \$RRAD = R/57.2958
 RHO = .0023768*\$IGAU
 S = S AU \$ B = B LD \$ C = C LO

SPRING/DAMPER UNIT **

C
C
C

BZ** = BZ - (BX**-.5)*SPIT
E**=CRAD*EZ** - RRAD*BY**
F**=RRAD*BX** - PRAD*BZ**
G**=FRAD*BY** - CRAD*BX**

C

Z** = -ALTS + C31*DX** + C32*BY** + C33*BZ**

C

XD** = XD SD + C11*E** + C12*F** + C13*G**
YD** = YD SD + C21*E** + C22*F** + C23*G**
ZD** = ZD + C31*E** + C32*F** + C33*G**

C
C
C
C

DIRECTION OF VELOCITY

SQR = (XD**)*XD** + (YD**)*YD**
IF(SQR.EQ.0.)GO TO 70
CANTX = ATAN2(YD**,XD**)
GO TO 71
CANTY = 0.
70 CONTINUE

70
71

C
C
C
C

SPRING FORCE

SP** = -KPIT*(ZEG+Z**) - CPIT*ZD** - FSOP

C
C
C
C
C

TEST FOR NEGATIVE SPRING FORCE

A** = FSOP + KPIT*(ZEG+Z**)
IF(A**<.0.)SP** = 0.

```

C C C
FRICION FORCES
=====
FRX** = COS(GAM**)*COFA*SP**
FRY** = SIN(GAM**)*COFA*SP**
C C C
RESOLVE FORCES INTO BODY AXIS SYSTEM
*****
FBX** = C11*FRX** + C21*FRY** + C31*SP**
FBY** = C12*FRX** + C22*FRY** + C32*SP**
FBZ** = C13*FRX** + C23*FRY** + C33*SP**
C C C
COMPUTE MOMENT ARMS FOR TORQUES
=====
PX** = BX** - C31*Z**
PY** = BY** - C32*Z**
PZ** = BZ - C33*Z**
C C C
CALCULATE TORQUES IN BODY AXIS SYSTEM
*****
TX** = (PY**)*FBZ** - (PZ**)*FBY**
TY** = (PZ**)*FBX** - (PX**)*FBZ**
TZ** = (PX**)*FBY** - (PY**)*FBX**

```

C+++++++SUM OF ACRS FORCES AND TORQUES+++++++
C

SFX=FBX11+FBX2P+FBX2S+FBX3P+FBX3S+FBX4P+FBX4S+FBX5P+FBX5S+FBX6P+
CFBX6S + Fbx7P + Fbx7S + Fbx88
SFY=FBY11+FBY2P+FBY2S+FBY3P+FBY3S+FBY4P+FBY4S+FBY5P+FBY5S+FBY6P+
CFBY6S + FBY7P + FBY7S + FBY88
SFZ=FBZ11+FBZ2P+FBZ2S+FBZ3P+FBZ3S+FBZ4P+FBZ4S+FBZ5P+FBZ5S+FBZ6P+
CFBZ6S + FBZ7P + FBZ7S + FBZ88
STX=TX11+TX2P+TX2S+TX3P+TX3S+TX4P+TX4S+TX5P+TX5S+TX6P+TX6S+
CTX7P + TX7S + TX88
STY=TY11+TY2P+TY2S+TY3P+TY3S+TY4P+TY4S+TY5P+TY5S+TY6P+TY6S+
CTY7P+TY7S + TY88
STZ=TZ11+TZ2P+TZ2S+TZ3P+TZ3S+TZ4P+TZ4S+TZ5P+TZ5S+TZ6P+TZ6S+
CTZ7P+TZ7S + TZ88


```

C      //SIDE FORCE COEFFICIENT///
C      CY = -.0101*BETA+ .00792
C      //ROLLING MOMENT COEFFICIENT///
C      CL1 = -(1.1483E-03)*BETA - 2.3545E-03
C      CL2 = -(1.5011E-03)*BETA - 1.2603E-03
C      CL3 = -(1.8773E-03)*BETA - 1.5545E-03
C      CL4 = -(2.3017E-03)*BETA - 1.4454E-03
C      //YAWING MOMENT COEFFICIENT///
C      IF(BETA.LT.-6.2)GO TO 201
C      IF(BETA.LE.10.4)GO TO 202
C      CN1 = (4.42E-04)*BETA - 8.97E-04 $GO TO 203
202  CN1 = -(5.8187E-08)*(BETA**5) + (1.2552E-07)*(BETA**4)
C      C+ (1.063E-05)*(BETA**3) + (1.9791E-06)*(BETA**2)
C      C-(2.09735E-04)*BETA - 7.0296E-04
C      GO TO 203
201  CN1 = (4.42E-04)*BETA + 1.54E-03
203  CONTINUE
C
C      IF(BETA.LT.-5.915)GO TO 204
C      IF(BETA.LE.6.05)GO TO 205
C      CN2 = (4.3E-04)*BETA - 5.89E-03
C      GO TO 206
205  CN2 = -(2.1346E-07)*(BETA**5) - (9.655E-07)*(BETA**4)
C      C+(2.9057E-05)*(BETA**3) + (6.8406E-05)*(BETA**2)
C      C-(1.3031E-03)*BETA - 1.3046E-03
C      GO TO 206
204  CN2 = (4.3E-04)*BETA + 5.673E-03
206  CONTINUE

```

```

IF(BETA.LT.-6.5)GO TO 207
IF(BETA.LE.6.267)GO TO 208
CN3=(4.5E-04)*BETA - 5.785E-03
GO TO 209
208 CN3 = -(4.142E-07)*(BETA**5) - (7.8671E-07)*(BETA**4)
C+(4.3616E-05)*(BETA**3) + (6.538E-05)*(BETA**2)
C-(1.471E-03)*BETA - 1.8538E-03
GO TO 209
207 CN3 = (4.5E-04)*BETA + 4.815E-03
209 CONTINUE
C
IF(BETA.LT.-5.585)GO TO 211
IF(BETA.LE.5.5)GO TO 212
CN4 = (4.24E-04)*BETA - 4.3E-03
GO TO 213
212 CN4 = -(2.3415E-07)*(BETA**5) - (6.1189E-07)*(BETA**4)
C+(2.7203E-05)*(BETA**3) + (4.7378E-05)*(BETA**2)
C-(9.6721E-04)*BETA -8.4685E-04
GO TO 213
211 CN4 = (4.24E-04)*BETA + .00453
213 CONTINUE
C
C** IF ISYM IS 1, REMOVE BIAS FROM LATERAL COEFFICIENTS**
IF(ISYM.EQ.0)GO TO 500
CY = CY - 7.92E-03
CL1 = CL1 + 2.3545E-03
CL2 = CL2 + 1.2603E-03
CL3 = CL3 + 1.5545E-03
CL4 = CL4 + 1.4454E-03
CN1 = CN1 + .70296E-03
CN2 = CN2 + 1.3046E-03
CN3 = CN3 + 1.8538E-03
CN4 = CN4 + .84685E-03
500 CONTINUE

```

```

C C INTERPOLATION FOR CLL AND CN
C C IF(ALPHA.LT.0.1)GO TO 301
C C IF(ALPHA.LE.2.2)GO TO 302
C C IF(ALPHA.LE.4.3)GO TO 303
C C IF(ALPHA.LE.6.4)GO TO 304
C C CASE A-----ALPHA IS GREATER THAN 6.4 DEGREES
C C CLL = CL4 $CN = CN4
C C CASE B-----ALPHA IS BETWEEN 4.3 AND 6.4 DEGREES
C C 304 RATIO = (ALPHA - 4.3)/2.1
C C CLL = CL3 + RATIO*(CL4-CL3)
C C CN = CN3 + RATIO*(CN4 - CN3)
C C GO TO 305
C C CASE C-----ALPHA IS BETWEEN 2.2 AND 4.3 DEGREES
C C 303 RATIO = (ALPHA-2.2)/2.1
C C CLL = CL2 + RATIO*(CL3 - CL2)
C C CN = CN2 + RATIO*(CN3 - CN2)
C C GO TO 305
C C CASE D-----ALPHA IS BETWEEN 0.1 AND 2.2 DEGREES
C C 302 RATIO = (ALPHA - .1)/2.1
C C CLL = CL1 + RATIO*(CL2 - CL1)
C C CN = CN1 + RATIO*(CN2 - CN1)
C C GO TO 305

```

```

C      CASE E-----ALPHA IS LESS THAN 0.1 DEGREES
C
C      301  CLL = CL1
C      305  CN = CN1
C      CONTINUE
C
C      * * * * * //FOR FLAPS DOWN///// * * * * *
C
C      IF(IFLAP.EQ.0)GO TO 750
C      CL = CL + .4
C      CD = (1.653E-03)*ALPHA**2 + (5.18E-03)*ALPHA + .16445
C      IF(ALPHA.LT..33)CN=-.0062 + (4.3E-04)*ALPHA
C      IF(ALPHA.GE..33)CN=-.005 - (3.4E-03)*ALPHA
C      CK1 = 1.299 + .1365*ALPHA
C      CLL = .0012 + CK1*(-.0014)*BETA
C      IF(BETA.LT.-1.05)GO TO 850
C      IF(BETA.LT.5.)GO TO 851
C      CN = (2.25E-04)*BETA - 25.25E-04
C      GO TO 855
C      851  CN = (-7.75E-04)*BETA + 24.75E-04
C      GO TO 855
C      850  CN = (2.25E-04)*BETA + 35.25E-04
C      855  CONTINUE
C      750  CONTINUE
C

```

IF(ICNB.EQ.1)CN = CNB*BETA

CALCULATION OF DIMENSIONAL-STABILITY-AXIS-DERIVATIVES

CNP = -.00218*CL + .000365
CLR = -.00105*CL + .008
TLPS = .25*RRHO*S*U*(B**2)*CLP
TNRS = .25*RRHO*S*U*(E**2)*CNR
TNPS = .25*RRHO*S*U*(E**2)*CNP
TLRS = .25*RRHO*S*U*(E**2)*CLR

C***** CO-EFFICIENTS FOR EASY / FOR BLOCKS LO AND LD *****

FX
X0 LO = QS*(-CD*CSA + CL*SA)
XDELO = (.00467*SA - .00279*CSA)*QS
FZ
Z0 LO = -QS*(CL*CSA + CD*SA)
ZDELO = (-.00467*CSA - .00279*SA)*QS
ZG LO = -.25*RRHO*S*U*C*CLQ*CSA
ZADLO = -.25*RRHO*S*U*C*CLAD*CSA2
TY

MQ LO = CM*QS*C
MDELO = -.0129*QS*C
MADLO = .25*RRHO*S*(C**2)*CMAD*CSA
MO LO = .25*RRHO*S*(C**2)*CMQ

```

C      - - - - - FY - - - - -
C
C *** NOTE, YDRLD IS USED TO INPUT THE Y-FORCE, WITH RUULD = 1 *****
C      YDRLD=CY*QS
C
C      - - - - - TX - - - - -
C
C ***NOTE, LDRLD IS USED TO INPUT THE X-TORQUE, WITH RUULD = 1. ****
C      LDRLD = CLL*QS*B
C      LDALD=(-.193*(1.-(VT**2)/(815366.)))/57.3)*QS*B
C      LP LD=TLPS*CSA2 - (TLRS + TNPS)*SA*CSA + TNRS*SA2
C      LR LD = TLRS*CSA2 - (TNRS - TLPS)*SA*CSA - TNPS*SA2
C
C      - - - - - T2 - - - - -
C
C ***NDRLD IS USED TO INPUT THE Z-TORQUE, WITH RUULD = 1. *****
C      NDRLD = CN*QS*B
C      NDALD = (.0166 - .009*CL)*QS*B/57.3
C      NP LD = TNPS*CSA2 - (TNRS-TLPS)*SA*CSA - TLRS*SA2
C      NR LD = TNRS*CSA2 + (TLRS+TNPS)*SA*CSA + TLPS*SA2
C      IF(ICHK.EQ.0)GO TO 510
C      NDALD= 0.      $NP LD = 0.
C
C      510 CONTINUE

```

```

C *****AILERON AUTOPILOT*****
  PHI = ROLSD
  ROLL = ROLSD/57.3
  PITCH = PITSD/57.3
  PHID = P + (Q* SIN(ROLL)+R* COS(ROLL))*TAN(PITCH)
  X1 MC A = PHI - DPHI
  X2 MC A=PHID-DPHID
  X3 MC A = CK1*U SD+CK2*ROLSD+CK3*P SD+CK4*R SD
  IF(X4 MC A.LT.-10.)X4 MC A = -10.
  IF(X4 MC A.GT.10.)X4 MC A = 10.
C *****ELEVATOR AUTOPILOT*****
  PHIR = PHI/57.3
  THETD = Q* COS(PHIR) - R* SIN(PHIR)
  THET = PITSD
  IF(X4 MC E.LT.-15.)X4 MC E = -15.
  IF(X4 MC E.GT.10.)X4 MC E = 10.
  X1 MC E = THET - DTHET
  X2 MC E = THETD - DTHETD
  X3 MC E = ELETRIN
C * * * * * OPTIMAL CONTROL LOGIC * * * * *
  Z1 = X4 MCZ1
  Z2 = X4 MCZ2
  IF(Z2.LT.0.)S1=A1*OMEGA*(1. - (OMEGA/(A2*Z1 + OMEGA)))*A3)
  IF(Z2.GE.0.)S1=-A1*OMEGA*(1. - (-OMEGA/(A2*Z1-OMEGA)))*A3)
  IF(Z2.LT.S1)UCON = -OMEGA
  IF(Z2.GE.S1)UCON = +OMEGA
C ++++++TOTAL EXTERNAL FORCES AND TORQUES+++++
  FX1LO = SFX + FX TG
  FY1LO = SFY + FY TG + UCON
  FZ1LO = SFZ + FZ TG
  TX1LO = STX + TX TG
  TY1LO = STY + TY TG
  TZ1LO = STZ + TZ TG - 10.*UCON

```

```

C BYPASS AILERON AND/OR ELEVATOR AUTOPILOTS
  VB1SW A = AILTRIM
  VB1SW E = ELETRIM
* * * * *
LOCATION = 323 AF U
LOCATION = 343 AF U
LOCATION = 326 SU U
LOCATION = 346 SU U
LOCATION = 217 TF E
LOCATION = 219 LG E
LOCATION = 215 SU E
LOCATION = 213 MC E
LOCATION = 244 MCZ1
LOCATION = 247 MCZ2
LOCATION = 113 MC A
LOCATION = 117 TF A
LOCATION = 119 LG A
LOCATION = 115 SU A
LOCATION = 3 LO
LOCATION = 15 LD
LOCATION = 17 SD
FORTRAN STATEMENTS
  XE = X2 ITXX
  YE = -X2 ITYY
LOCATION = 29 ITXX
LOCATION = 40 ITYY
END OF MODEL
PRINT
* * * * *
INPUTS = AF U(X=UB1)
INPUTS = AF U(X=VB1)
INPUTS = SU E(V01=X)
INPUTS = TF E
INPUTS = MC E(X=VA1)
INPUTS=SD(U=X,R=X)
INPUTS=SD(V=X,R=X)
INPUTS=SU A(V01=X)
INPUTS=TF A
INPUTS=MC A(X=VA1)
INPUTS=AV, LG E(X=ELE)
INPUTS=AV, LO, LG A(X=AIL)
INPUTS=LO, LD
INPUTS=SD(XD=X)
INPUTS=SD(YD=X)

```

Bibliography

1. Aerodynamic Derivatives and Autopilot/Servo Transfer Functions for Mk.203A Short Span Jindivik Fitted with Mk.7/8 Wing Tip Fuel Pods. Appendix to an unpublished report by Government Aircraft Factories, Australia, date unknown.
2. Athans, Michael, and Peter L. Falb. Optimal Control. New York, McGraw-Hill Book Company, 1966.
3. Bauer, Frederick C. Air Cushion Landing System Drop Dynamics Theory (Mechanical). MS thesis. Wright-Patterson AFB, Ohio: Air Force Institute of Technology, December 1973.
4. Blakelock, John H. Automatic Control of Aircraft and Missiles. New York: John Wiley and Sons, Inc., 1965.
5. Boghani, A. B., K. M. Captain, and D. A. Wormley. Heave-Pitch-Roll Analysis and Testing of Air Cushion Landing Systems. NASA Contract No. NAS1-12403. Langley Research Center: Hampton, Virginia. circa 1977.
6. Burroughs, J. D., and A. W. Warren. Application of the EASY Dynamic Analysis Program to Aircraft Modeling. Users Manual. Seattle, Washington: Boeing Computer Services, November 1976.
7. Cole, Neil R. Experimental Determination of Lift and Drag for a Coanda Yaw Thruster. MS thesis. Wright-Patterson AFB, Ohio: Air Force Institute of Technology, December 1975.
8. Coles, A. V. Air Cushion Landing System CC-115 Aircraft. AFFDL-TR-72-4 Part I. Wright-Patterson AFB, Ohio: Air Force Flight Dynamics Laboratory, May 1972.
9. D'Azzo, John J. and Constantine H. Houppis. Feedback Control System Analysis and Design: Conventional and Modern. New York: McGraw-Hill Book Company, 1975.
10. DeRusso, Paul M., Rob J. Roy, and Charles M. Close. State Variables for Engineers. New York: John Wiley and Sons, Inc., 1965.
11. Hudson, James P. Polynomial Least Square Curve Fit (PLSQ). AFIT subroutine. Wright-Patterson AFB, Ohio: Computer Science Division, October 1970.

Bibliography (Cont'd)

12. Husson, M. A. A Differential Thrust Controller for Air Cushion Landing System Aircraft. MS thesis. Wright-Patterson AFB, Ohio: Air Force Institute of Technology, December 1974.
13. Kirk, Donald E. Optimal Control Theory---An Introduction. Englewood Cliffs: Prentice-Hall, Inc., 1970.
14. McRuer, Duane, Irving Ashkenas, and Dunstan Graham. Aircraft Dynamics and Automatic Control. Princeton, Princeton University Press, 1973.
15. Mulhauser, C. W. Results of Tethered and Taxi Testing of an Air Cushion Landing and Take-off System Fitted to a Mk.203A Jindivik Target Drone. GAF Project Report Jindivik No. B3BL/77. Port Melbourne, Australia. September 1976.
16. Roskam, Jan. Flight Dynamics of Rigid and Elastic Airplanes. Lawrence: Roskam Aviation and Engineering Corporation, 1972.
17. Ryken, John M. Design of an Air Cushion Recovery System for the Jindivik Drone Aircraft. AFFDL-TR-74-38. Wright-Patterson AFB, Ohio: Air Force Flight Dynamics Laboratory, March 1974.
18. Solnick, R. J. (Draftsman). Air Cushion Recovery Skirt - Jindivik (sheet 1). blueprint: code identification number 03481. BF Goodrich Aerospace and Defense Products, June 25, 1974.
19. Stauffer, C. L. Ground/Flight Test Report of Air Cushion Landing Gear (IA-4). AFFDL-TR-69-23. Wright-Patterson AFB, Ohio: Air Force Flight Dynamics Laboratory, September 1969.
20. Troy, A. C. A Simulation Experiment to Verify Differential Thrust Controller Designs for an Air Cushion Vehicle. MS thesis. Wright-Patterson AFB, Ohio: Air Force Institute of Technology, March 1976.
21. Vaughan, John C., James T. Steiger, David J. Pool, and Shade Campbell. Laboratory Tests of an Air Cushion Recovery System for the Jindivik Aircraft. AFFDL-TR-74-64. Wright-Patterson AFB, Ohio: Air Force Flight Dynamics Laboratory, April 1974.
22. Wilt, et al. OPTCON, Solution of Linear Quadratic Optimal Control Problem. AFIT Subprogram. Wright-Patterson AFB, Ohio. Revised 1976.
23. Wrigley, Walter, and Walter M. Hollister, and William G. Denhard. Gyroscopic Theory, Design, and Instrumentation. Cambridge, The M.I.T. Press, 1969.

VITA

Max Allen Stafford was born on 16 November 1947 in Maryville, Tennessee. Upon graduation from Maryville High School, Maryville, Tennessee, in 1965 he attended the University of Tennessee. In August, 1970 he was awarded a Bachelor of Science degree in Aerospace Engineering and a Bachelor of Science degree in Electrical Engineering. In April, 1971 he received a commission in the USAF, after completing Officers Training School. He received undergraduate pilot training at Williams AFB, Arizona, earning his wings in April, 1972. From 1972 until 1976 he served as a KC-135 pilot in the 71st Air Refueling Squadron, Barksdale AFB, Louisiana. In June, 1976 he entered the School of Engineering at the Air Force Institute of Technology, Wright-Patterson AFB, Ohio.

Permanent Address: 904 Rennborro Road
Knoxville, Tennessee 37919

REPORT DOCUMENTATION PAGE		READ INSTRUCTIONS BEFORE COMPLETING FORM	
1. REPORT NUMBER AFIT/GGC/EE/78-5 ✓	2. GOVT ACCESSION NO.	3. RECIPIENT'S CATALOG NUMBER	
4. TITLE (and Subtitle) An Analysis of the Stability of an Aircraft Equipped with an Air Cushion Recovery System		5. TYPE OF REPORT & PERIOD COVERED	
		6. PERFORMING ORG. REPORT NUMBER	
7. AUTHOR(s) Max A. Stafford Captain, USAF		8. CONTRACT OR GRANT NUMBER(s)	
9. PERFORMING ORGANIZATION NAME AND ADDRESS Air Force Institute of Technology (AFIT-EN) Wright-Patterson AFB, Ohio 45433		10. PROGRAM ELEMENT, PROJECT, TASK AREA & WORK UNIT NUMBERS	
11. CONTROLLING OFFICE NAME AND ADDRESS Air Force Flight Dynamics Laboratory (FEM) Wright-Patterson AFB, Ohio 45433		12. REPORT DATE March 1978	
		13. NUMBER OF PAGES 202	
14. MONITORING AGENCY NAME & ADDRESS (if different from Controlling Office)		15. SECURITY CLASS. (of this report) Unclassified	
		15a. DECLASSIFICATION/DOWNGRADING SCHEDULE	
16. DISTRIBUTION STATEMENT (of this Report)			
<table border="1"> <tr> <td> <p>DISTRIBUTION STATEMENT A</p> <p>Approved for public release Distribution Unlimited</p> </td> </tr> </table>			<p>DISTRIBUTION STATEMENT A</p> <p>Approved for public release Distribution Unlimited</p>
<p>DISTRIBUTION STATEMENT A</p> <p>Approved for public release Distribution Unlimited</p>			
17. DISTRIBUTION STATEMENT (of the abstract entered in Block 20, if different from Report)			
Approved for public release; distribution unlimited			
18. SUPPLEMENTARY NOTES			
Approved for public release; IAW AFR 190-17 Jerral F. Guess, Captain, USAF Director of Information			
19. KEY WORDS (Continue on reverse side if necessary and identify by block number)			
Air Cushions Switching Control Jindivik Optimal Control			
20. ABSTRACT (Continue on reverse side if necessary and identify by block number)			
<p>✓ The stability of an aircraft equipped with an air cushion recovery system (ACRS) was investigated both in-flight and during the landing (slideout) phase of flight. Digital computer simulations were used to identify unstable tendencies of a specific aircraft (the Jindivik drone). Control system designs are proposed to eliminate the instabilities.</p> <p>A nonlinear, six degree of freedom, aerodynamic model is developed based on available wind-tunnel data. The model is used in a computer software</p>			

Block 20 - Contd

package, EASY, to simulate the vehicle in flight. The vehicle is shown to be unstable in flight due to lateral-directional characteristics created by the installation of the ACRS. A time optimal control design is developed using a coanda-effect yaw thruster. The design is verified by computer simulations which indicate that the controller performs adequately for reasonably small deviations in sideslip angle.

A model of the air cushion recovery system is also developed. The model is generated by matching experimental data obtained from an actual ACRS with 14 spring/damper units. The model is verified by computer simulation, and the slideout simulations are performed. These simulations reveal a lateral-directional instability in the slideout. An optimal control design is proposed and verified, after which it is shown that the stability of the system is dramatically enhanced by the addition of an optimal controller.

Unclassified